OFFICE OF CIVILIAN RADIOACTIVE WASTE MANAGEMENT
MODEL COVER SHEET

1. QA: QA
Page: 1 of: 2

Complete Only Applicable Items

2. Type of Mathematical Model

[X] Process Model [ ] Abstraction Model [ ] System Model

Describe Intended Use of Model:
The Thermal Conductivity of the Potential Repository Horizon Model Report provides the distribution and means values, matrix and lithophysal porosity, dry bulk density, wet and dry matrix thermal conductivity, and the wet and dry bulk thermal conductivity, for the stratigraphic units that may host the proposed repository. These units for which representations have been provided are the Tptpul, Tptpmn, Tptpll, and the Tptpln.

Technical Contact/Department:
James Ramsey, Natural Systems (505) 844-1331, Clinton Lum, Natural Systems (702) 295-3401

3. Title:
Thermal Conductivity of the Potential Repository Horizon Model Report

4. DI (including Rev. No. and Change No., if applicable):
MDL-NBS-GS-000005, Rev 00

5. Total Attachments:
Five.

6. Attachment Numbers - No. of Pages in Each:
I-6 pages, II-46 pages, III-6 pages, IV-4 pages, V-4 pages.

	Printed Name	Signature	Date
7. Originator	Ernest Hardin for James Ramsey	Ernest Hardin for	8/28/02
8. CSO	Bruce Kirstein	B. E. Kirstein	8/28/02
9. Checker	Nancy Brodsky		8/29/02
10. QER	James Graff		08/29/02
11. Responsible Manager/ Lead	Clinton Lum	Ernest Hardin for	8/29/02
12. Responsible Manager	Paul Dixon		8/29/02

13. Remarks:

Checker	Norma Biggar		8/28/02
Checker	Dwight Hoxie		08/29/02

OFFICE OF CIVILIAN RADIOACTIVE WASTE MANAGEMENT

QA: QA MRS 9/26

MODEL REVISION RECORD

2. Model Title:
Thermal Conductivity of the Potential Repository Horizon Model Report

3. DI (including Rev. No. and Change No., if applicable):
MDL-NBS-GS-000005, Rev. 00

4. Revision/Change No.	5. Description of Revision/Change
00	Initial issue.

CONTENTS

Page

CONTENTS (Continued)

Page

FIGURES

Page

FIGURES (Continued)

Page

FIGURES (Continued)

Page

INTENTIONALLY LEFT BLANK

TABLES

Page

INTENTIONALLY LEFT BLANK

1. PURPOSE

The purpose of this report is to assess the spatial variability and uncertainty of thermal conductivity in the host horizon for the proposed repository at Yucca Mountain. More specifically, the lithostratigraphic units studied are located within the Topopah Spring Tuff (Tpt) and consist of the upper lithophysal zone (Tptpul), the middle nonlithophysal zone (Tptpmn), the lower lithophysal zone (Tptpll), and the lower nonlithophysal zone (Tptpln). The Tptpul is the layer directly above the repository host layers, which consist of the Tptpmn, Tptpll, and the Tptpln. Current design plans indicate that the largest portion of the repository will be excavated in the Tptpll (Board et al. 2002 [157756]).

The main distinguishing characteristic among the lithophysal and nonlithophysal units is the percentage of large scale (cm-m) voids within the rock. The Tptpul and Tptpll, as their names suggest, have a higher percentage of lithophysae than the Tptpmn and the Tptpln. Understanding the influence of the lithophysae is of great importance to understanding bulk thermal conductivity and perhaps repository system performance as well.

To assess the spatial variability and uncertainty of thermal conductivity, a model is proposed that is functionally dependent on the volume fraction of lithophysae and the thermal conductivity of the matrix portion of the rock. In this model, void space characterized as lithophysae is assumed to be air-saturated under all conditions, while void space characterized as matrix may be either water- or air-saturated. Lithophysae are assumed to be air-saturated under all conditions since the units being studied are all located above the water table in the region of interest, and the relatively strong capillary forces of the matrix will, under most conditions, preferentially retain any moisture present in the rock.

Furthermore, since experimental data regarding matrix thermal conductivity are quite limited, three published models of thermal conductivity developed for porous media applications are investigated in this report. Based on the criteria and evaluation described in Section 6.1.7 of this report, the Hsu et al. (1995 [158073]) three-dimensional (3-D) cubic model was ultimately selected and subsequently used to model the spatial variability of matrix thermal conductivity. In this model, matrix thermal conductivity is a function of matrix porosity, the thermal conductivity of the saturating fluid, the thermal conductivity of the solid minerals, and the geometry and connectivity of the solid. The thermal conductivity of the saturating fluid is treated as constant, but the remaining model parameters are treated as spatially uncertain random functions. The geostatistical method known as sequential Gaussian simulation is used to develop 50 independent, equally likely realizations of these uncertain properties. Available measurements from core samples and borehole petrophysical logs are used to derive models of spatial continuity and to condition the geostatistical simulations. These 3-D property sets then serve as inputs to the matrix thermal conductivity model yielding 3-D geostatically-based realizations of matrix thermal conductivity.

The spatial heterogeneity and uncertainty of lithophysal porosity is addressed in a similar manner. A method of characterizing lithophysal porosity from borehole petrophysical data is developed and applied in this endeavor. The results are used to derive models of spatial continuity and to condition geostatistical simulations of this property.

The geostatistical modeling conducted in this work follows closely the methodologies and thought processes developed in the *Rock Properties Model Analysis Model Report* (BSC 2002a [159530]). In an effort to create a self-contained document, much of the introductory text concerning geostatistics (Sections 6.1.2 and 6.1.3) has been paraphrased and in some places copied directly from the *Rock Properties Model Analysis Model Report* (BSC 2002a [159530]) report. Readers interested in acquiring a greater understanding of the application and limitations of the geostatistical methods applied in this work are encouraged to read that report.

This model report addresses activities described in *Technical Work Plan for: The Integrated Site Model* (BSC 2002b [158075]) with regard to thermal conductivity. The limitation of the model is that because there are limited actual thermal conductivity data, the spatial distribution of thermal conductivity shown by the model is based on the input parameters of matrix and lithophysal porosity. This is a conduction-only model, and the bulk thermal conductivity values provided are for saturated and dry conditions. Interpolations for intermediate saturation conditions can be performed by any user of the model. The geostatistical method of developing the model provides the range of expected values of thermal conductivity over a 3-D volume. Predictions of future repository performance would want to consider the range of values applied to the repository volume.

2. QUALITY ASSURANCE

The modeling effort was evaluated in accordance with AP-2.21Q, *Quality Determinations and Planning for Scientific, Engineering, and Regulatory Compliance Activities,* and was determined to be quality affecting and subject to the Yucca Mountain Site Characterization Project (YMP) quality assurance program (BSC 2002b, Attachment 1 [158075]). Accordingly, efforts to develop this report have been conducted in accordance with quality assurance procedures identified in *Technical Work Plan for: The Integrated Site Model* (BSC 2002b [158075]).

Electronic management of data was evaluated in accordance with procedure AP-SV.1Q, *Control of the Electronic Management of Information*, and the applicable controls are discussed in the *Technical Work Plan for: The Integrated Site Model* (BSC 2002b [158075]). This model report reports on natural barriers that are included in the *Q-List* (YMP 2001 [154817]) as items important to waste isolation. However, this model report contributes to the analysis and modeling of data for performance assessment and site characterization; it does not directly impact engineering, construction, or operational tasks associated with the Q-list items as discussed in AP-2.22Q, *Classification Criteria and Maintenance of the Monitored Geologic Repository Q-List*.

3. USE OF SOFTWARE

3.1 SOFTWARE TRACKED BY CONFIGURATION MANAGEMENT

The parameters documented in this report were constructed using geostatistical algorithms that are part of the public-domain GSLIB geostatistical software library (Deutsch and Journel 1992 [100567], 1998 [102895], and other internally developed codes). The codes subject to Software

Configuration Management are listed in Table 3-1, together with a brief description of their functionality. These software packages were obtained from Software Configuration Management and were judged appropriate for use in this type of modeling activity. The software was used within the range of validation. Most of the codes listed in Table 3-1 were run on an Intel personal computer under the Microsoft (MS) Windows 2000 or the MS Server 2000 operating system. The exceptions are GSLIB V. 1.4MNSCOREV1.201 (STN: 10109-1.4MNSCOREV1.201-02 [158222]), which was run on a HP 9000 workstation operating under the HP UX 10.20 operating system, and EARTHVISION V. 5.1 (EARTHVISION V. 5.1, STN: 10174-5.1-00 [152614]), which was run on a Silicon Graphics Octane workstation operating under the IRIX Version 6.5 operating system. Input and output files for the software are contained in the DTN: SN0208T0503102.007. The qualification status of the software is shown in the electronic Document Input Reference System.

3.2 EXEMPT SOFTWARE

Software products such as operating systems, utilities, compilers and their associated libraries, spreadsheets, desktop database managers, graphical representations of data, computer aided design systems, and acquired software that is embedded in the test and measurement equipment and the standard functions of commercial off-the-shelf software products are exempt software products in accordance with Section 2.1 of AP-SI.1Q, *Software Management*.

AFPL Ghostscript Version 7.04 is a set of software that provides an interpreter for the PostScript language with the ability to convert PostScript language files to many raster formats, view them on displays, print them on non-postscript printers, and act as an interpreter for Portable Document Format. Ghostscript also has the ability to convert back and forth between PostScript language to Portable Document Format files and provides a set of C procedures that implement the graphics capabilities that appear as primitive operations in the PostScript language.

Compaq Visual Fortran Version 6.1A is a Fortran 95 compiler for Windows. Compaq Visual Fortran is a complete development system that includes Compaq's Fortran 95 compiler, the latest visual development environment from Microsoft, and support for numerous industry standard Fortran language extensions.

Cygwin Version 1.3.9 tools are ports of the GNU development tools and utilities for Windows NT, 9x, and Windows 2000. They function through the use of the Cygwin library, which provides the UNIX system calls and the environment that these programs require.

GSView Version 4.2 is a graphical interface for Ghostscript. Ghostscript is an interpreter for the PostScript page description language used by laser printers. For documents following the Adobe PostScript Document Structuring Conventions, GSView allows selected pages to be viewed or printed. GSview requires AFPL Ghostscript.

MS Excel 2000 was used to calculate matrix and lithophysal porosity. Standard functions were used in these calculations.

Table 3-1. Software Tracked by Configuration Management

Code Name	Version	STN Number	Platform	Operating System	Brief Description
EARTHVISION [152614]	V. 5.1	10174-5.1-00	SGI INDIGO R4000	IRIX 6.5	3-D earth science modeling package used to produce visualizations of this report and to project stratigraphic contacts.
GSLIB V. 1.4MBACKTR [113642]	V1.20	10108-1.4MBACKTRV1.20-01	PC	MS Server	Transforms a standard-normal distribution (GSLIB format) to match a reference histogram (from the software library, GSLIB; inverse of program NSCORE).
GSLIB V. 1.0MGAMV2 [158221]	V1.201	10087-1.0MGAMV2V1.201-02	PC	MS Server and MS 2000	A geostatistical software utility that is used to calculate variograms and related statistical measures for (up to) 3-D data sets. Designed for use with non-gridded data.
GSLIB V. 1.4MNSCORE [158222]	V1.201	10109-1.4MNSCOREV1.201-02	PC and HP 9000	MS Server and HP UX 10.20	Transforms a distribution of values to standard-normal form while preserving quantile relationships (from the software library, GSLIB).
GSLIB HISTPLT [158223]	V. 2.01	10802-2.01-00	PC	MS Server and MS 2000	Generates univariate statistical summaries and histograms that are compatible with a PostScript display device (from the software library, GSLIB).
GSLIB V. 1.4SGSIM [158224]	V1.41	10110-1.4SGSIMV1.41-00	PC	MS Server	Generates conditional or unconditional Gaussian simulations of a continuous variable; optional normal-score forward and back transformation (from the software library, GSLIB).
Etype [159417]	V. 2.01	10731-2.01-00	PC	MS Server	Reads a set of simulation output (GSLIB format) files and computes mean and standard deviation of simulations.
HsuInv [158228]	V. 1.0	10804-1.0-00	PC	MS Server	The code solves the inverse problem for Hsu et al. (1995 [158073]) 3-D cube model of matrix thermal conductivity. The inverse problem consists of simultaneously solving two non-linear equations.
LITHO [158256]	V. 1.0	10800-1.0-00	PC	MS Server	Designed to process data from geophysical logs and core data to generate “GEO-EAS” formatted files that can be input into GSLIB programs. The formatted output consists of the measured data as a function of stratigraphic elevation.

Table 3-1. Software Tracked by Configuration Management (Continued)

Code Name	Version	STN Number	Platform	Operating System	Brief Description
MODGEOM [158257]	V. 1.02	10597-1.02-01	PC	MS Server	A software utility program that modifies the random seed for a SGSIM parameter file.
SMOOTH [158258]	V. 1.0	10734-1.0-01	PC	MS Server	A software utility that reads in external data that varies as a function of depth (such as borehole data), computes the mean of a moving window.
POINT [158336]	V. 1.0	10826-1.0-00	PC	MS Server	A utility program that extracts point data from multiple GSLIB-formatted realizations.
TCOND [158260]	V. 1.0	10801-1.0-00	PC	MS Server	Computes an effective wet and dry bulk thermal conductivity for porous rock that includes both small scale (< 1mm) intergranular porosity and much larger scale (cm to m.) void spaces.

NOTES: EARTHVISION was run on an Octane model CPU (barcode 700800) manufactured by Silicon Graphics. All other software was run on a 530 Work Station model CPU (barcode 436032) manufactured by Dell.

3-D = three-dimensional; CPU = central processing unit; MS = Microsoft; PC = personal computer.

MS Visual C++ Version 6.0 provides the development environment for compiling C and C++ computer software.

MS Word 2000 is an office automation system word processor used to author, format, edit, and review project documents.

Sigma Plot Version 8.0 was used to plot the figures presented in this report.

4. INPUTS

The model of bulk thermal conductivity developed in this report is highly dependent on the existing data collected at Yucca Mountain from well-log and laboratory core analyses. These data appear to be high-quality measurements and are used directly as inputs to the model. There are data, however, which, if not removed from the input data set, could lead to inappropriate model predictions. Examples for which this might be the case include data obtained over an insufficient range of conditions or outside the calibrated range of the measuring device. For this reason, a significant effort was devoted to examining input data and removing unsuitable data from the input set.

Attachments II and III document data usage decisions and summarize model inputs. Attachment II consists of plots of processed well-log data and, where available, comparisons with laboratory core measurements. Data use restrictions, if any, are discussed on the same page on which the data are presented in Attachment II. Attachment III discusses thermal conductivity measurements acquired from laboratory core samples. Several of these data are excluded from the analysis. The reasons for excluding certain thermal conductivity measurements are discussed in Attachment III. Often these decisions are subjective and based on limited information. Therefore, all decisions regarding data quality usage are subject to interpretation and may change as new information becomes available.

4.1 DATA AND PARAMETERS

Laboratory core measurements of porosity, particle density, water saturation, and thermal conductivity are used in this report to develop geostatistically based models of thermal conductivity (Table 4-1) and various other important rock properties. Petrophysical well-log measurements, from a total of 37 different boreholes that, at a minimum, penetrated the top of the Tptpul (Table 4-2), are used to characterize the spatial variability of both lithophysae and matrix porosity. The locations of the boreholes used in this work are depicted graphically in Figure 4-1.

Table 4-1. Source of Laboratory Core Physical Properties Data

Data Source Description	Reference
Particle Density, Water Saturation, and Porosity data	DTN: MO0109HYMXPROP.001 [155989][1]
Particle Density, Water Saturation, and Porosity data	DTN: GS980808312242.014 [106748][2]

1) Boreholes: USW SD-7, USW SD-9, USW SD-12, USW NRG-7/7a, USW UZ-7a, USW NRG-6, and USW UZ-1/USW UZ-14

2) Borehole: USW SD-6

Table 4-2. Source of Input Petrophysical Data

Data Source Description	Reference
Neutron porosity and bulk density data	DTN: MO0010CPORGLOG.002 [155229]
Neutron porosity and bulk density data	DTN: MO0010CPORGLOG.003 [155959]

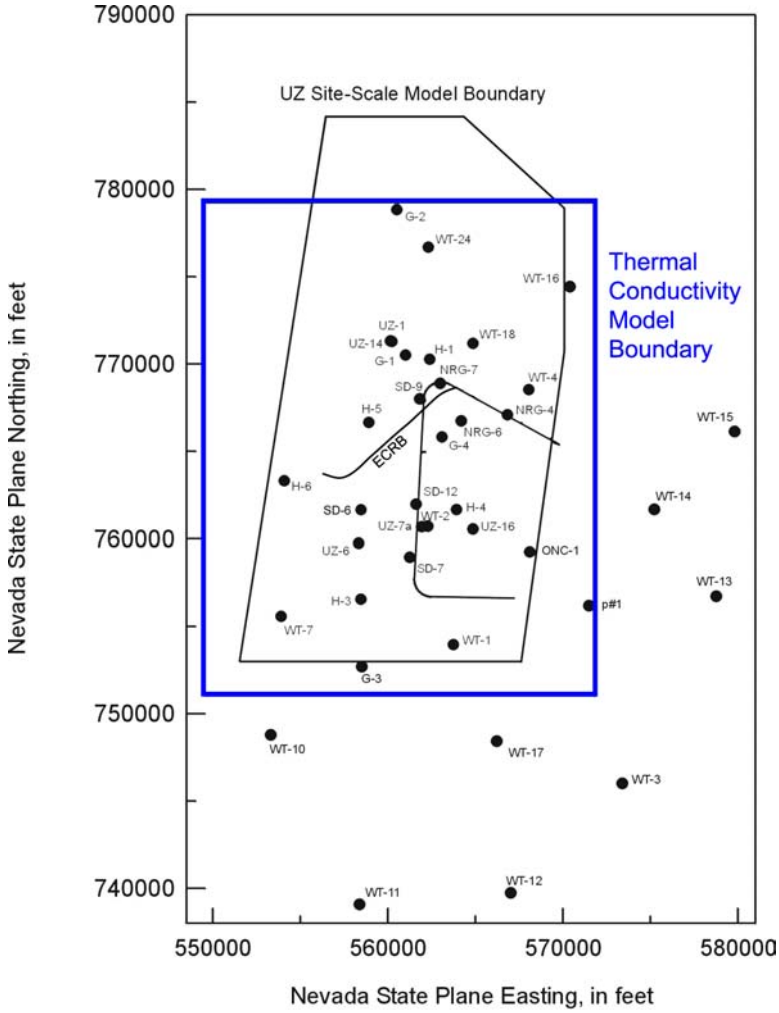

DTN: MO0012MWDGFM02.002 [153777]

Figure 4-1. Yucca Mountain Boreholes that Penetrate the Tptpul

A second type of data required in this work consists of borehole locations and borehole stratigraphic contacts. The sources of these data are given in Sections 4.1.5 through 4.1.7. Data tracking numbers (DTNs) associated with each type of data are provided in the following tables.

4.1.1 Laboratory Core Physical Property Data

Laboratory core measurements of particle density, water saturation, and porosity from eight different boreholes are used in this work. The DTNs associated with these measurements are presented in Table 4-1. These DTNs are appropriate because the core data contained within them are specific to the lithostratigraphic units and spatial region for which this model is being developed.

4.1.2 Petrophysical Data

Borehole petrophysical measurements of bulk density and neutron porosity are used to make quantitative estimates of matrix and lithophysal porosity. These data provide substantial information regarding the spatial heterogeneity of porosity across the entire site (Figure 4-1). This is particularly true for regions distant from the proposed repository block where no core samples have been acquired. Data from regions outside the model boundaries are useful for identifying patterns of long-range spatial correlation. The DTNs associated with borehole petrophysical data are presented in Table 4-2. These DTNs are appropriate because the petrophysical data contained within them are specific to the lithostratigraphic units and spatial region for which this model is being developed.

Data acquired from the Technical Data Management System must first be partitioned into model units and then reformatted to accommodate the input configuration used by the GSLIB software suite. Furthermore, to obtain a consistent scale of measurement between core and petrophysical data, the petrophysical data are smoothed and re-sampled on an interval equal to the nominal length of core, which happens to be three feet. Two software utility codes are used in this pre-processing step: SMOOTH (SMOOTH V. 1.0, STN: 10734-1.0-01 [158258]) and LITHO V. 1.0 (LITHO V. 1.0, STN: 10800-1.0-00 [158256]). The code SMOOTH is applied only to borehole petrophysical data, and the code LITHO V. 1.0 is a pre-processor applied to both core and smoothed petrophysical data.

4.1.3 Matrix Thermal Conductivity Data

There are a total of four sources of laboratory matrix thermal conductivity measurements that were used in this study. These four sources plus the matrix porosity data associated with the borehole core samples are listed in Table 4-3. The first three DTNs include data that were used to calibrate the matrix thermal conductivity model, and the last two DTNs include data that were used to validate the model. A detailed discussion of these data including the rationale for excluding certain data is provided in Attachment III. The first three DTNs are appropriate because the thermal conductivity data contained within them are specific to the lithostratigraphic units. In addition, the three DTNs provide wet and dry thermal conductivity (as explained in Attachment III) and porosity values on the same samples or sample splits.

Table 4-3. Source of Matrix Thermal Conductivity Data

Data Source Description	Reference
Borehole Core Samples	DTN: SNL01A05059301.005 [109002]
Borehole Sample Porosity	DTN: SNL01A05059301.007 [108980]
Alcove 5 Core Samples	DTN: SNL22100196001.006 [158213]
Drift Scale Test Core Samples *	DTN: SNL22100196001.001 [109733]
Alcove 7 Core Samples *	DTN: SNL22100196001.002 [153138]

*Used only for model validation.

4.1.4 In situ Bulk Thermal Conductivity Test Results

Preliminary analyses from two recent in situ thermal conductivity tests are used to validate the bulk thermal conductivity model in Section 6.1.4. The DTNs associated with this work are given in Table 4-4.

Table 4-4. Source of Bulk Thermal Conductivity Data

Data Source Description	Reference
Two-hole Test *	DTN: SN0206F3504502.012 [159145]
Three-hole Test *	DTN: SN0206F3504502.013 [159146]

*Used only for model validation.

4.1.5 Borehole Coordinates

The Nevada State plane coordinates of borehole wellheads are obtained from the DTN listed in Table 4-5. The locations of the boreholes used in this study are shown in Figure 4-1 and also listed in Attachment IV.

Table 4-5. Source of Borehole Coordinate Data

Data Source Description	Reference
Borehole Wellhead Coordinates	DTN: MO9906GPS98410.000 [109059]

4.1.6 Observed Lithostratigraphic Contacts

The geostatistic models produced in this report are developed using a stratigraphic coordinate system, which represents the relative vertical position of each measured property value within a model unit. The conversion from natural (x,y,z) coordinates to stratigraphic coordinates requires the upper and lower contact of each aggregate model unit in each borehole. This process is described in Section 6.1.2. Typically, the required depth values are observed, either in core specimens, petrophysical logs, or downhole video records. The DTNs associated with observed lithostratigraphic contact data are presented in Table 4-6, and the contacts themselves are reproduced in Attachment IV. These DTNs are appropriate because the lithostratigraphic contacts contained within them are specific to the units and spatial region being modeled. They

represent the compilation of borehole data that are used as input to the Geologic Framework Model (GFM2000) (DTN: MO0012MWDGFM02.002 [153777]).

Table 4-6. Source of Input for Observed Lithostratigraphic Contacts

Data Source Description	Reference
Lithostratigraphic Contacts	DTN: MO0004QGFMPICK.000 [152554]
Contacts for SD-6	DTN: SNF40060298001.001 [107372]

4.1.7 Lithostratigraphic Contacts

Most of the lithostratigraphic contacts were obtained from observed contacts defined in the Geologic Framework Model (GFM2000) (DTN: MO0012MWDGFM02.002 [153777]). A small number of these contacts are, however, projected using this same model. Projected contacts are sometimes required when a borehole only partially penetrates the region of interest or crosses a fault. The DTN for the data obtained from the Geologic Framework Model is given in Table 4-7. The projected lithostratigraphic contacts are presented in Attachment IV. The DTN is appropriate because the model results provide a 3-D geologic representation of the units and spatial region being modeled.

Table 4-7. Source of Input for Lithostratigraphic Contacts

Data Source Description	Reference
Geologic Framework Model 2000	DTN: MO0012MWDGFM02.002 [153777]

4.2 CRITERIA

This report complies with subparts of 10 CFR 63 [156605] pertaining to the characterization of the Yucca Mountain site (Subpart B, Section 63.15), the compilation of information regarding geology of the site in support of the License Application (Section 63.21[c][1][ii]), and the definition of the geologic parameters and conceptual models used in performance assessment (Subpart E, Section 63.114[a]).

4.3 CODES AND STANDARDS

No codes or standards are applicable to the modeling documented in this report.

5. ASSUMPTIONS

1. The principle assumption applied in this work is that the properties of geologic strata may be represented by stationary random functions. A random function is a set of spatially distributed random variables whose dependence on one another is specified by some probabilistic mechanism. The term “stationary” implies that the probabilistic mechanism is independent of spatial location. Stationary random functions are widely used and commonly found in most geostatistical estimation procedures. Isaaks and Srivastava (1989,

p. 198 to 236 [109018]) introduce the concept of random function models and discuss the use of those models in the field of geostatistics. This is a commonly accepted assumption applied in geostatistical modeling and does not require justification. This assumption is used throughout Section 6.

2. Justification of this assumption can be provided by evaluating the impact of the assumption over the range of observed matrix saturation values for the Tpt units (Tptpul, Tptmn, Tptpll, and Tptpln) that have been modeled as part of the analysis of thermal conductivty presented in this report. As indicated by the data for boreholes SD-7 and SD-9 plotted in Figures 3 and 4 of Flint (1998 [100033]), matrix saturation within these units ranges from 80 to 100 percent with an average saturation of about 90 percent.

   To evaluate the assumption, data from three sample depths from borehole USW H-6 were selected. These include data that were used in this analysis to generate the matrix and bulk thermal conductivity values discussed in Sections 6.1.7 and 6.1.8 of this report. Calculations that show the impact of changing the matrix saturation from 100 to 80 percent are presented in Table 5-1. These borehole samples were selected to bracket the range of matrix and lithophysal porosities observed in the borehole.

Table 5-1. Change in Calculated Porosity Caused by Changing Matrix Saturation from 100 to 80 Percent.

Sample USW H-6	Saturation 100%		Saturation 80%		Percent Change		Magnitude Change	
	Matrix Porosity	Lithophysal Porosity	Matrix Porosity	Lithophysal Porosity	Matrix Porosity	Lithophysal Porosity	Matrix Porosity	Lithophysal Porosity
541 ft	0.128	0.291	0.155	0.268	+21%	-8%	+0.027	-0.023
586 ft	0.083	0.137	0.102	0.119	+23%	-13%	+0.019	-0.018
625 ft	0.187	0.128	0.223	0.087	+19%	-32%	+0.036	-0.041

DTN: SN0208T0503102.007

The results of the calculation indicate that changing the saturation from 100 to 80 percent results in a relative change in matrix porosity of about 19 to 21 percent (which is consistent with the definition of matrix porosity presented in Attachment I). The relative change in lithophysal porosity is –8 to –32 percent. The change in matrix porosity ranges from 1.9 to 3.6 percent and in lithophysal porosity from 1.8 to 4.1 percent. Applying the methodology described in Section 6.1.7, specifically Equations 6-6 and 6-7, the impact of the results presented in Table 5-1 on dry and wet matrix thermal conductivity was calculated. The results of these calculations are presented in Table 5-2. To calculate the matrix thermal conductivity values, the following inputs for the HsuInv V. 1.0 model for the Tptpul layer were used: a solid thermal conductivity of 2.6011 W/mK and a geometry factor (gamma c) of 0.8517, which are the same values that were used in the modeling described in Section 6.1.7 for the Tptpul unit.

Table 5-2. Change in Calculated Matrix Thermal Conductivity Caused By Changing Matrix Saturation from 100 to 80 Percent.

Sample USW H-6	Saturation 100%		Saturation 80%		Percent Change		Magnitude Change	
	Dry Matrix Thermal K (W/mK)	Wet Matrix Thermal K (W/mK)	Dry Matrix Thermal K (W/mK)	Wet Matrix Thermal K (W/mK)	Dry Matrix Thermal K (Percent)	Wet Matrix Thermal K (Percent)	Dry Matrix Thermal K (W/mK)	Wet Matrix Thermal K (W/mK)
541 ft	1.490	2.125	1.406	2.047	-5.64%	-3.67%	-0.084	-0.078
586 ft	1.649	2.266	1.578	2.204	-4.31%	-2.74%	-0.071	-0.062
625 ft	1.316	1.962	1.223	1.873	-7.07%	-4.54%	-0.093	-0.089

DTN: SN0208T0503102.007

These results indicate that the change in dry matrix thermal conductivity ranges from -4.31 to –7.07 percent, while the change in wet thermal conductivity values ranges from –2.74 to –4.54 percent W/mK. These percentage differences are of the same magnitude as the experimental error of ± 5 percent associated with thermal conductivity values determined from core samples (SNL 1998, p. 10 [118788]) and represent an acceptable range of uncertainty.

In order to completely evaluate the effect of this assumption, the impact on the calculation of bulk thermal conductivity was examined using the parallel model of thermal conductivity described in Section 6.1.8. The results of this impact evaluation are shown in Table 5-3.

Table 5-3. Change in Calculated Bulk Thermal Conductivity Caused By Changing Matrix Saturation from 100 to 80 Percent.

Sample USW H-6	Saturation 100%	Saturation 80%	Percent Change Bulk Thermal Conductivity (Percent)	Magnitude Change Bulk Thermal Conductivity (W/mK)
	Bulk Thermal Conductivity (W/mK)	Bulk Thermal Conductivity (W/mK)		
541 ft	1.329	1.252	-5.79%	-0.077
586 ft	1.838	1.735	-5.60%	-0.103
625 ft	1.615	1.530	-5.26%	-0.085

DTN: SN0208T0503102.007

These results indicate that the change in bulk thermal conductivity due to the difference in assumed matrix saturation values range from –5.26 to –5.79 percent. This percentage change in bulk thermal conductivity is also of the same magnitude as the experimental error of ± 5 percent associated with determining thermal conductivity on core samples (SNL 1998, p. 10 [118788]) and is within the acceptable limit of uncertainty.

On the basis of this evaluation of impact, it is concluded that assuming a matrix saturation of 1.0 to evaluate thermal conductivity from borehole data for which no direct measurements of matrix saturation are available leads to calculated thermal conductivity values that are within expected and acceptable ranges of uncertainty.

3. For computing matrix and lithophysal porosity from petrophysical measurements, the particle density is assumed to be constant in each of the four lithostratigraphic units studied. This assumption is supported by evaluating Figures 3 and 4 from Flint (1998 [100033]). The figures indicate that the particle density for the Tptpul, Tptpmn, Tptpll, and Tptpln lithostratigraphic units is quite constant and varies from 2.5 to 2.6 g/cc. This homogeneity can be compared to the variable density for the formations underlying the repository zones. No further justification of this assumption is required. This assumption is used in Sections 6.1.4 and 6.1.5.

   It is also assumed that the particle density and the grain density are equivalent in these units. In general, particle density is lower than grain density because of occluded pores but approaches it for rocks having small occluded pore space. Comparison of mean particle and grain density data in Table 5-4 verifies that this assumption is valid. This assumption is used in Sections 6.1.4, 6.1.5, 6.1.6, as well as in Attachment I.

Table 5-4. Mean Particle Density in the Four Lithostratigraphic Layers

Lithostratigraphic Unit	Particle Density[1] (g/cc)	Grain Density[2] (g/cc)
Tptpul	2.51	2.53
Tptpmn	2.53	2.53
Tptpll	2.55	2.56
Tptpln	2.55	2.56

[1]See Section 6.1.6.
[1]CRWMS M&O 1996, pp. 5-30 to 5-31 [111105]

4. It is further assumed that any water present in the rock is contained within the small-scale pore space of the matrix. This assumption is an application of basic capillary principles that under steady state conditions, in less than saturated conditions, large-scale voids (centimeter-scale lithophysae and fractures) will be unsaturated (Hillel 1980, pp. 196 to 197 [101134]). No further justification of this assumption is required. Evidence specific to the proposed site is provided by the texture of calcite and opal coating in the interior of the lithophysae that indicates that the lithophysae within the welded tuffs exposed in the Exploratory Studies Facility have been open and air-filled throughout the geologic period of record (Paces et al. 2001, p. 66 [156507]). This assumption is used in Sections 6.1.4 and 6.1.5.

5. In the absence of data proving otherwise, it is assumed that the spatial correlation models developed for matrix porosity are applied to other uncertain model parameters (solid thermal conductivity, k_s, and solid connectivity, γ_c) in the matrix thermal conductivity model. The assumption is that all matrix properties behave similarly in terms of spatial correlation (Section 6.1.7). No further justification of this assumption is required. This assumption is used in Sections 6.1.3 and 6.1.7.

6. The upper bound form of Maxwell's model of heat conduction in a solid body containing dilute inclusions of fluid (1954 [158165]) is assumed in the development of the bulk thermal conductivity model. This implies a parallel model of heat flow through the matrix and

lithophysae. The rationale for the selection of this model is provided in Section 6.1.8. No further justification of this assumption is required. This assumption is used in Section 6.1.8.

6. ANALYSIS/MODEL

6.1 MODEL DISCUSSION

Energy transport within the proposed nuclear waste repository at Yucca Mountain is a complex phenomenon dependent on many physical processes. These processes include heat conduction through the surrounding rock, fluid migration and phase changes, radiative heat transport, natural convection cells, energy storage changes, and perhaps other processes. Heat conduction is considered to be one of the more dominant energy transport mechanisms and is controlled principally by the thermal conductivity of the rock surrounding the repository. Furthermore, recent studies show that thermal conductivity is one of the most important parameters when considering the performance of the proposed repository (BSC 2001a, Section 5.3.1.4.8 [155950]). The purpose of this report is to investigate the spatial distribution of thermal conductivity and assess its uncertainty in the repository host horizon.

The geologic stratigraphy of Yucca Mountain is shown in Figure 6-1 (DTN: MO9510RIB00002.004 [103801]). In the current design plans the repository host rock is located within the Tpt in the Paintbrush Group. This report develops 3-D, geostatistically based representations of thermal conductivity for certain lithostratigraphic layers of the Tpt. These layers are the Tptpul, Tptpmn, Tptpll, and Tptpln. The complete names and a brief description (Buesch et al. 1996, pp. 41 to 43 [100106]) of these units are provided in Table 6-1.

Numerous scientists have studied heat transfer through porous media over many years. Indeed, books have been written on this topic. Kaviany (1991, pp. 1 to 5, 123 to 127 [148383]) summarizes the historical development of this field and reviews many predictive models of thermal conductivity. Yucca Mountain, however, presents a unique and interesting challenge due to the presence of large-scale (cm-m) void spaces not typically encountered in porous media applications. These voids are called lithophysae and can be found to varying degrees in all four of the lithostratigraphic layers studied.

In this work the rock is conceptualized as being a composition of matrix and lithophysae. The term lithophysae is used in this work to refer only to air-filled large-scale voids. Vapor-phase alteration or other mineral deposits commonly associated with lithophysae are conceptualized as matrix. The matrix component consists of solid minerals and their associated intergranular pore space. Matrix materials possess strong capillary forces that preferentially retain water in comparison to the same forces in lithophysae. This important matrix property is used to differentiate matrix from lithophysal porosity using well-log measurements of bulk density and neutron porosity.

Bulk thermal conductivity is defined as the effective value of thermal conductivity, which satisfies Fourier's law of heat conduction (Rohsenow and Choi 1961, p. 5 [158324]) for a system composed of two or more materials with different heat transfer characteristics. Bulk thermal conductivity for the Tpt is calculated by considering that the matrix and lithophysae act in

parallel with respect to energy transport, as described in Section 6.1.8. Applying Fourier's equation of heat conduction to a parallel system yields the following expression (Hadley 1986, p. 914, Equation 18 [153165]):

$$k_b = \phi_L k_a + (1 - \phi_L) k_m \quad \text{(Eq. 6-1)}$$

The derivation of Equation 6-1 is provided in Section 6.1.8. In Equation 6-1, ϕ_L is the volume fraction of the lithophysae, k_b and k_m are the bulk and matrix thermal conductivities, respectively, and k_a is the thermal conductivity of air.

Matrix thermal conductivity is a function of matrix porosity, water saturation, the geometry and packing of the solid, and the thermal conductivity of the solid minerals. The 3-D Cubic Model, developed by Hsu et al. (1995 [158073]) and described in Section 6.1.7, is used to predict matrix thermal conductivity from these fundamental rock properties. With the exception of matrix water saturation, these fundamental properties are treated as spatially uncertain random functions. The geostatistical method known as sequential Gaussian simulation is used to generate 50 equally likely independent realizations of these properties in order to provide a sufficient statistical sample for each property. Available measurements from core samples and petrophysical logs are used to derive models of spatial continuity and to condition the geostatistical simulations. The spatial heterogeneity and uncertainty in lithophysal porosity is addressed in the same manner.

Matrix water saturation, S_w, is expected to vary both spatially and temporally due to thermal loading. Therefore, thermal conductivity is presented only at the two end states, $S_w = 1$ (wet) and $S_w = 0$ (dry), as explained in Attachment III. The user of these data should apply some method of interpolation for the saturation state of their particular application. The report *Laboratory Measurements of Thermal Conductivity as a Function of Saturation State for Welded and Nonwelded Tuff Specimens* (SNL 1998 [118788]) investigates two commonly used interpolation methods for estimating matrix thermal conductivitiy at intermediate saturation states: linear interpolation and square root interpolation. It is shown that these same interpolation methods may also be applied to bulk thermal conductivity (Section 7.4.1).

6.1.1 Overview of Model Development

The purpose of this analysis is to assess the spatial heterogeneity and uncertainty of bulk thermal conductivity for selected units of the Tpt. At the present time however, there are simply too few experimental data regarding this property to estimate the spatial distribution or uncertainty directly. This lack of data results from the fact that bulk thermal conductivity cannot be measured in a controlled laboratory setting due to the size of the sample that would be required to incorporate the effects of lithophysae. The project has initiated a series of in situ thermal conductivity field tests that will certainly contribute to the understanding of the energy transport processes and bulk thermal conductivity in the Tpt. The quantity of these measurements will, however, be necessarily small in number due to the substantial cost associated with in situ testing and the limited access to the units of concern. Consequently, direct simulation of bulk thermal conductivity at the mountain scale will likely never be feasible. For these reasons, a theoretical

Stratigraphic Unit						Abbreviation
Group	Formation	Member	Zone	Subzone		
	Alluvium and Colluvium					Qal, Qc
Timber Mountain Group						Tm
Paintbrush Group						Tp
	Tiva Canyon Tuff					Tpc
		Crystal-Rich Member				Tpcr
		Crystal-Poor Member				Tpcp
			Vitric zone			Tpcpv
				Densely welded subzone		Tpcpv3
				Moderately welded subzone		Tpcpv2
				Nonwelded subzone		Tpcpv1
		Pre-Tiva Canyon bedded tuff				Tpbt4
	Yucca Mountain tuff					Tpy
		Pre-Yucca Mountain bedded tuff				Tpbt3
	Pah Canyon Tuff					Tpp
		Pre-Pah Canyon bedded tuff				Tpbt2
	Topopah Spring Tuff					Tpt
		Crystal-Rich Member				Tptr
			Vitric zone			Tptrv
				Nonwelded subzone		Tptrv3
				Moderately welded subzone		Tptrv2
				Densely welded subzone		Tptrv1
			Nonlithophysal zone			Tptm
			Lithophysal zone			Tptrl
		Crystal-Poor Member				Tptp
			Upper lithophysal zone			Tptpul
			Middle nonlithophysal zone			Tptpmn
			Lower lithophysal zone			Tptpll
			Lower nonlithophysal zone			Tptpln
			Vitric zone			Tptpv
				Densely welded subzone		Tptpv3
				Moderately welded subzone		Tptpv2
				Nonwelded subzone		Tptpv1
		Pre-Topopah Spring bedded tuff				Tpbt1
	Calico Hills Formation					Ta
		Bedded tuff				(Tacbt)
Crater Flat Group						Tc
	Prow Pass Tuff					Tcp
		Pre-Prow Pass bedded tuff				(Tcbbt)
	Bullfrog Tuff					Tcb
		Pre-Bullfrog Tuff bedded tuff				(Tcbbt)
	Tram Tuff					Tct
		Bedded tuff				(Tctbt)

DTN: MO9510RIB00002.004 [103801]

Figure 6-1. Yucca Mountain Stratigraphy

Table 6-1. Lithostratigraphic Units Studied

Lithostratigraphic Unit	Name	Description
Tptpul	Topopah Spring Tuff Crystal-poor upper lithophysal zone	The crystal-poor upper lithophysal zone is moderately to densely welded, devitrified, and composed of 70 to 90 percent matrix groundmass, 1 to 3 percent phenocrysts, 0 to 25 percent pumice clasts, 2 to 40 percent lithophysae, and trace amounts of volcanic lithic fragments.
Tptpmn	Topopah Spring Tuff Crystal-poor middle nonlithophysal zone	The middle nonlithophysal zone is densely welded, devitrified, and composed of 90 to 99 percent matrix groundmass, 1 to 2 percent phenocrysts, 0 to 5 percent lithophysae, 1 to 5 percent pumice clasts, and 1 to 5 percent lithic fragments.
Tptpll	Topopah Spring Tuff Crystal-poor lower lithophysal zone	The lower lithophysal unit is densely welded, devitrified, and composed of 70 to 96 percent groundmass, 1 to 7 percent lithophysae (locally 20 percent), 1 to 3 percent phenocrysts, 1 to 10 percent pumice clasts, and 1 to 5 percent lithic clasts (locally 10 percent).
Tptpln	Topopah Spring Tuff Crystal-poor lower nonlithophysal zone	The lower nonlithophysal zone is densely welded, devitrified, and composed of 75 to 97 percent groundmass, 1 to 2 percent phenocrysts, 1 to 15 percent pumice clasts, and 1 to 10 percent lithic clasts (locally 10 to 20 percent). Lithophysae abundance ranges from 0 to 5 percent[1].

Source: Buesch et al. 1996, pp. 41 to 43 [100106]
[1]Mongano et al. 1999, p. 34 [149850]

model of bulk thermal conductivity was developed during this study and subsequently used to calculate bulk thermal conductivity from the more easily measured rock properties of lithophysal porosity and matrix thermal conductivity (Equation 6-1).

Lithophysal porosity is calculated from the relatively abundant well-log petrophysical measurements of bulk density and neutron porosity. In this calculation it is necessary to make certain assumptions regarding the state of matrix water saturation. These calculations are discussed in detail in Section 6.1.4 and Attachment I. The resulting values of lithophysal porosity are used to develop spatial correlation models and condition geostatistical simulations of this rock property.

Matrix thermal conductivity has been measured on a limited number of laboratory core samples. Unfortunately, many of these measurements do not span the range of possible saturation states, and in some cases the data cannot be used as discussed in Section 5. Consequently, the spatial heterogeneity and uncertainty in matrix thermal conductivity cannot be determined solely from laboratory core measurements at this time. Alternatively, there is a large volume of literature addressing the thermal conduction properties of porous media. Many researchers have developed theoretical models of thermal conductivity that may be applied at Yucca Mountain. After examining several of these models, the 3-D Cubic Model developed by Hsu et al. (1995 [158073]) was selected to calculate matrix thermal conductivity based on the criteria set forth in Section 6.1.7.

Having chosen an appropriate theoretical model for matrix thermal conductivity, parameter distributions specific to the chosen model were developed based on core thermal conductivity measurements extracted from the Tpt. Geostatistical representations of these model parameters,

namely, matrix porosity, mineral thermal conductivity, and solid connectivity, were then developed using the sequential Gaussian simulation procedure described in Section 6.1.3.

Lastly, dry bulk density is another important rock property in energy transport calculations due to a strong correlation with heat capacity. This property is calculated directly from simulated values of matrix and lithophysal porosity and unit-specific estimates of grain density as described in Section 6.1.6.

6.1.2 Model Domain and Discretization

The model domain chosen for this study is shown in Figure 6-2. The modeled region extends from the vicinity of Fatigue Wash in the west to the middle of Midway Valley in the east and from central Yucca Wash in the north to the middle of Dune Wash in the south. In Nevada State plane coordinates, the model domain extends from 167,500 m to 174,300 m (549,541 ft to

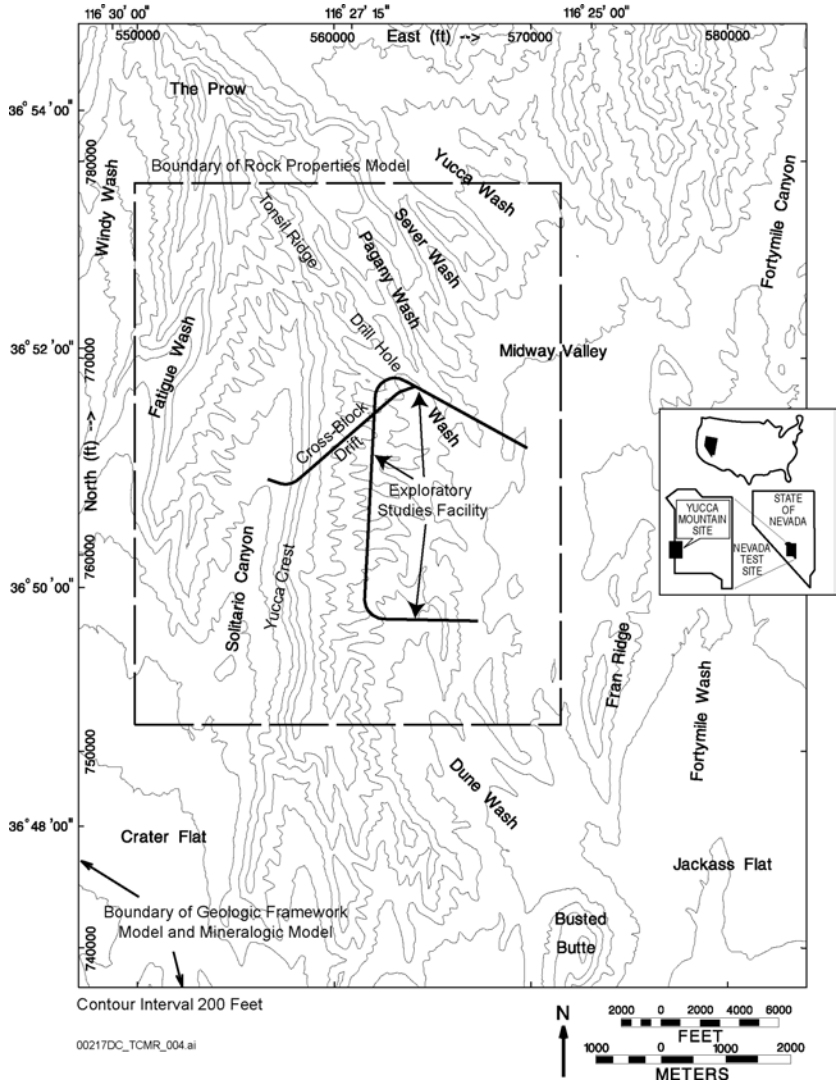

Figure 6-2. Map Showing the Model Domain Relative to Geologic Features and Constructed Tunnels

571,850 ft) in the east and from 228,900 m to 237,500 m (750,984 ft to 779,199 ft) in the north (DTN: SN9910T0501399.001 [129717]). This same model domain has been used previously in the *Rock Properties Model Analysis Model Report* (BSC 2002a [159530]).

Each of the four lithostratigraphic intervals is modeled in a stratigraphic coordinate system that reflects the original, pre-faulted depositional continuity of these ash-flow tuffaceous deposits (Figure 6-3). This coordinate system uses Nevada State plane coordinates in the east-west and north-south direction; however, the vertical coordinate represents the fractional elevation relative to the thickness of the lithologic unit. The use of a stratigraphic coordinate system effectively repositions the rock back to its original point of deposition, removing the effect of depositional thinning and post-depositional features such as faulting and deformation. The process of constructing such a coordinate system is illustrated graphically in Figure 6-3.

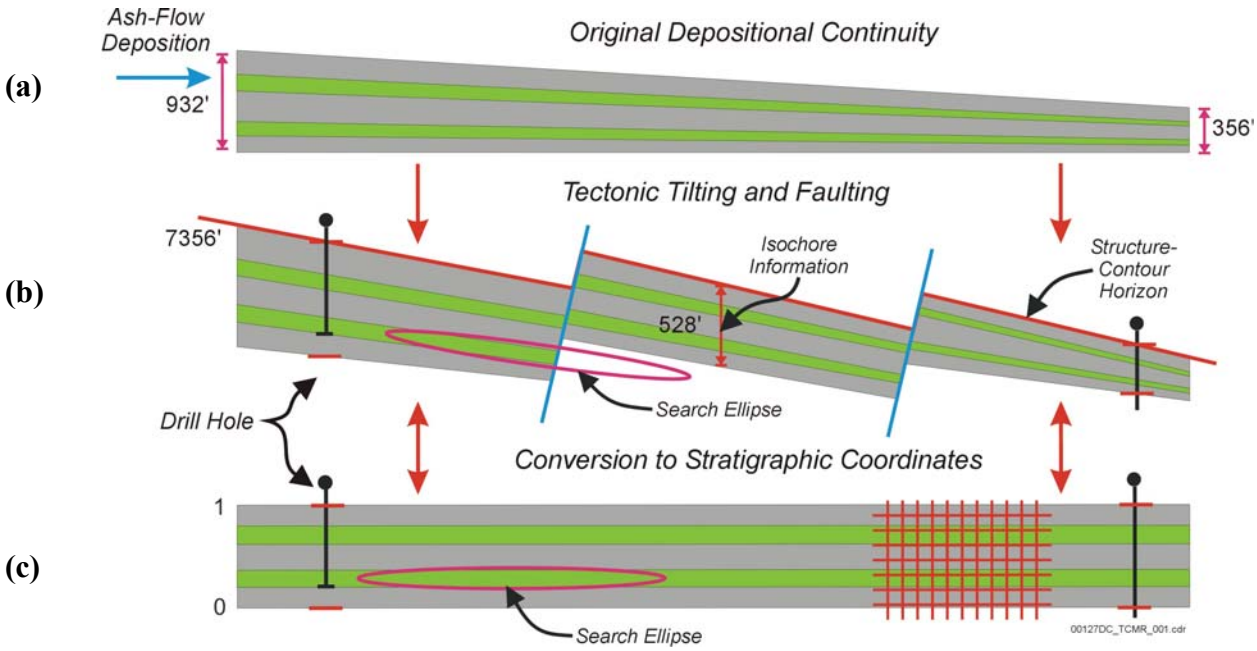

Source: BSC 2002a, Figure 8 [159530]

NOTES: Conceptual illustration of the construction and use of stratigraphic coordinates. (a) Rock unit is formed by areally extensive volcanic (or sedimentary) processes. Zones of differing rock properties (shaded colors) are formed in a stratiform manner. (b) Tectonic deformation tilts and disrupts original stratiform continuity by faulting. (c) Modeling unit is returned to an approximation of original continuity in a rectangular coordinate system in which all vertical distances are measured as a fractional position measured from the top or bottom of the rock unit.

Figure 6-3. Illustration of the Process of Converting to Stratigraphic Coordinates

At Yucca Mountain, regions of varying material properties have been emplaced or otherwise formed in an essentially stratiform manner. The volumetrically dominant rocks were formed by pyroclastic flows deposited in thick ash-flow sheets that thin laterally away from their source. Since rocks formed under similar depositional, pressure, and temperature conditions tend to have similar material properties, there is a tendency for rock of the same unit and relative vertical

elevation to have similar material properties. This behavior is illustrated in part (a) of Figure 6-3.

Later, faulting as part of Basin and Range tectonism disrupted the originally continuous volcanic rocks and tilted the rock units as indicated in part (b). To exploit the observed and measurable spatial continuity of material properties with respect to depositional environment, the measured data must first be translated to a relative deposition position. This is accomplished through the conversion to stratigraphic coordinates, which is illustrated in part (c). In this translation, the vertical location of data is specified as the fractional elevation from the base of the unit, which is assigned a distance of zero, to the top of the unit, which is assigned a distance of one. This value is then multiplied by the nominal thickness of the unit in order to ensure meaningful parameters in the vertical variography.

As suggested by the mesh of intersecting dotted lines in the right-hand portion of Figure 6-3(c), a regular rectangular modeling grid is defined within each stratigraphic coordinate system. Note that the various material property zones have been stretched or compressed vertically so that the overall stratigraphic thickness of the unit is constant. Defining the modeling grid within this framework positions rock with similar material properties in a stratigraphically horizontal plane. This repositioning greatly simplifies the search methods required for data in the geostatistcal modeling, as shown conceptually by the search ellipse in part (c). Although it is possible to rotate the principal direction of the search ellipse to match the overall tectonic dip of the unit as shown in part (b), it is virtually impossible to modify the search strategy to account for the vertical displacement of material property zones through faulting.

After completing the modeling exercise, the transformation from the stratigraphic coordinate system to standard Nevada State plane coordinates is achieved by computing the vertical elevation of each node in the grid. This reverse transformation requires knowledge of the spatially varying structure contour and thickness for each unit. This information and the transformation itself are obtained from the independently developed Geologic Framework Model (GFM2000) (DTN: MO0012MWDGFM02.002 [153777]).

Implementation of the stratigraphic coordinate system is slightly more complicated than the example discussed in Figure 6-3. This is primarily because sample locations are typically specified in terms of depth and are specific to a particular drill hole. These depths must be converted to stratigraphic elevations using lithologic contact data (observed or predicted) obtained from the Geologic Framework Model (GFM2000) (DTN: MO0012MWDGFM02.002 [153777]). The software routine LITHO V. 1.0 was written to extract pertinent well-log or core data from the original data source, compute stratigraphic elevations, and then assemble the data extracted from multiple sources into a single file formatted according to GSLIB specifications.

The Equation 6-2 for calculating the stratigraphic elevation, E_s, from depth is:

$$E_s = \left[1 - \left(\frac{D - T}{B - T}\right)\right] \cdot H \qquad \text{(Eq. 6-2)}$$

where D is the measured depth, H is the nominal thickness of the lithologic unit, and B and T are the measured or projected depths to the bottom and top lithologic contacts of the unit, respectively.

Due to differences in nominal thickness, each of the four lithostratigraphic units utilizes a different model domain vertically. Horizontally, the model domains are identical and are therefore all discretized using a uniform, 50 x 50 m (164.042 x 164.042 ft) grid. The value of 50 m was chosen to closely match the resolution required by the Engineered Barrier System Lower-Temperature Operating Mode study (BSC 2001b [158204]). Vertically, the domain is discretized using 3.048 m (10 ft) elements in all units except the Tptpll, which is discretized using 4.572 m (15 ft) elements. Larger elements are used in Tptpll to moderate the computational burden of this relatively thick unit. As before, the vertical resolution was chosen to meet the needs of the Engineered Barrier System Lower-Temperature Operating Mode study (BSC 2001b [158204]). This information is summarized in Table 6-2.

Table 6-2. Model Discretization

Grid Dimension		Origin (ft/m)	Spacing (ft/m)	No. of Nodes	Nominal Thickness (ft/m)	Total Nodes
Model X (Easting)		549540.68/ 167,500	164.042/ 50.0	136	---	---
Model Y (Northing)		750984.25/ 228,900	164.042/ 50	172	---	---
Model Z (Stratigraphic Vertical)	Tptpul	0.0	10.0/ 3.048	20	200/ 60.96	467,840
	Tptpmn	0.0	10.0/ 3.048	12	120/ 36.58	280,704
	Tptpll	0.0	15.0/ 4.572	20	300/ 91.44	467,840
	Tptpln	0.0	10.0/ 3.048	15	150/ 45.72	350,880

DTN: SN0208T0503102.007

6.1.3 Sequential Gaussian Simulation

Geostatistics offers a method of distributing isolated measurements in space and quantifying their uncertainty. A fundamental characteristic underlying all geostatistical techniques is the idea of spatial correlation. Spatial correlation may informally be defined as the degree to which samples that are close to one another resemble each other in a certain attribute or material property.

Within the field of geostatistics there are two broad classes of algorithms used to predict material properties at unsampled locations: estimation and simulation. Geostatistical estimation is focused on the prediction of property values most likely to be encountered at a given spatial location, and it may be thought of as modeling the expected value of a variable of interest. Estimation in the field of geostatistics is known as “kriging,” and it is simply a weighted-average interpolation method invoking neighboring nearby data. A common feature among all

estimation techniques (including non-geostatistical ones) is that estimated values generally grade smoothly away from the locations of known values.

The other broad class of geostatistical methods consists of simulation algorithms. Simulation may be thought of as expanding the information available in a stochastic manner that is consistent with the data ensemble and spatial context of those data. The process builds on the intuition that unsampled locations near a known value tend to resemble that value, whereas unsampled locations at increasing distances progressively resemble that value less and less. In contrast to estimation, geostatistical simulation attempts to reproduce not only the known data but also the overall statistical character of those data, including the specified spatial correlation. Property sets produced by geostatistical simulation do not typically grade smoothly between measured data. Where spatial correlations are weak or in the vicinity of conflicting measurements, predicted property values may fluctuate greatly over short distances.

Deutsch and Journel (1998, p. 119 [102895]) state that Gaussian-related simulation algorithms "are the algorithms of choice for most continuous variables." Sequential Gaussian simulation is perhaps the most popular and widely used member of this family. These simulations may be conditional or unconditional. Conditional simulations are anchored numerically to a specific set of measured data and exhibit three important attributes that are useful in evaluating geologic heterogeneity. Specifically, conditional simulations:

1. Reproduce known data values at the location they were measured

2. Reproduce the full range of measurement variability, as represented by histogram and univariate descriptive statistics of the known data

3. Reproduce the bivariate statistics (or two-point spatial correlation structure) of the known data

Unconditional simulations are similar, except that they are not spatially anchored to any particular data, and thus Item 1 does not apply. Simulations produced using sequential Gaussian simulation cannot be distinguished statistically from the data ensemble they were derived from or from each other. Consequently, they serve as alternative, equally likely stochastic realizations of an incompletely sampled reality.

The sequential Gaussian simulation program GSLIB V. 1.4SGSIMV1.41 (Table 3-1; GSLIB V. 1.4SGSIMV1.41, STN: 10110-1.4SGSIMV1.41-00 [158224]; Deutsch and Journel 1992, pp. 123 to 125 and 164 to 167 [100567]) is used to generate a sufficient statistical sample based on 50 realizations of each of the four uncertain model parameters (lithophysal porosity, matrix porosity, solid thermal conductivity, and solid connectivity). Realizations of lithophysae and matrix porosity are conditioned to available well-log and core measurements. Realizations of solid thermal conductivity and solid connectivity are unconditioned.

The sequential modeling process is relatively straightforward and is implemented as follows:

1. Conditioning data are first transformed into a univariate standard-normal distribution ($\mu = 0$, $\sigma^2 = 1$) using a normal-score transformation (Figure 6-4). The normal-score

transform is implemented using the program GSLIB V. 1.4MNSCOREV1.201 (Table 3-1; GSLIB V. 1.4MNSCOREV1.201, STN: 10109-1.4MNSCOREV1.201-02 [158222]; Deutsch and Journel 1992, pp. 138 and 209 to 211 [100567]). This transformation does not alter the structure of spatial correlation since the transformation is quantile-preserving.

2. The spatial correlation structure is identified using the normal-score transformed values and modeled using standard variography.

3. A sequential random path is defined that stops at each node in the grid once.

4. At each node along this path, a search is conducted for nearby data including any previously simulated nodes. The search parameters specified in this study require that the full range of the spatial continuity model (variogram) be searched for data.

5. The user-specified N closest data within the search radius are identified and subsequently used to compute a conditional expected value and variance through simple kriging.

6. A random value is drawn (in standard-normal space) from a conditional Gaussian probability distribution defined by the mean and variance obtained in Step 5. This value is assigned to the current node and the simulation proceeds to the next location on the random path. Steps 4 through 6 are repeated until all nodes have been simulated.

7. Once the random path has been completed, the simulated values must be back-transformed from standard-normal space to their original space. This inverse transform is conducted using the program GSLIB V. 1.4MBACKTR (Table 3-1; GSLIB V. 1.4MBACKTRV1.20, STN: 10108-1.4MBACKTRV1.20-01 [113642]).

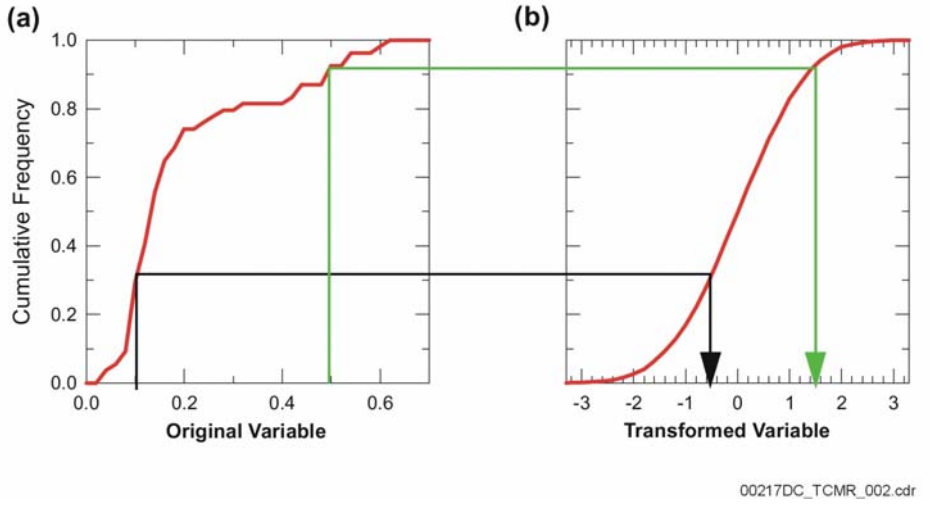

Figure 6-4. Graphical Representation of the Quantile-Preserving Normal-Score Transformation

Because there is a certain degree of randomness in the simulation algorithm, simulated values depend on both the random path followed and the seed to the random number generator. Independent realizations utilize different random paths and different random seeds. Simple logic dictates that independent realizations will have different simulated values. However, at locations that are well constrained by consistent measured data, the variability in simulated values tends to be small. On the other hand, at locations far from measured data, or at grid nodes that are in the vicinity of conflicting measurements, the spread of simulated values can be quite broad. Such variability may approach the univariate variance of the property being simulated, indicating that the spatial attributes of the conditioning data provide no additional knowledge of the property being simulated at that particular location. This information is quite valuable in assessing spatial uncertainty.

6.1.4 Lithophysal Porosity

Lithophysal porosity is defined as the fractional volume of large-scale (cm-m) void space per unit volume of rock. Recent mappings of this property in the Enhanced Characterization of the Repository Block (ECRB) Cross-Drift show that lithophysae vary in size, shape, and abundance throughout all four lithostratigraphic layers (Mongano et al. 1999, pp. 16 to 35 [149850]). The abundance of lithophysae, as suggested by their given names, is greater in the upper and lower lithophysal zones than in the middle and lower nonlithophysal zones.

The measurement of lithophysal porosity is somewhat challenging since what constitutes large-scale versus small-scale void space must first be established. Mongano et al. (1999, pp. 16 to 35 [149850]) report that lithophysal spaces vary in size from as small as 1 cm to as large as 100 cm. Conversely, capillary pressure measurements from the core suggest that the intergranular size of matrix voids is substantially less than 1 cm by at least an order of magnitude. This considerable difference in scale is quite useful in interpreting well-log petrophysical measurements and ultimately serves as the basis for distinguishing lithophysae from matrix porosity.

Since capillary forces in porous media are directly related to pore size, it is safe to assume that under unsaturated, equilibrium, or near equilibrium conditions, the water present in units of the Tpt will preferentially reside within the small-scale pore space of the matrix. This fact is used to develop equations to calculate matrix and lithophysal porosity from petrophysical and, where available, core measurements.

Bulk density, defined in Attachment I, is the principle petrophysical measurement used to calculate lithophysal porosity. In theory, petrophysical measurements of bulk density account for all contributions of mass to the system (liquid, solid, gas). Lithophysal porosity can be calculated directly from bulk density (Attachment I) when certain properties of the matrix (porosity and saturation) have been established either through direct measurement (i.e., core samples) or assumption. Depending on the availability of direct measurements, one of three methods is used. These can be summarized as follows:

> **Method A**. In boreholes where core samples were collected and measurements of matrix porosity obtained, depth-matched bulk density values are linearly interpolated from the smoothed bulk density data set (Section 4.1.2). Lithophysal porosity is calculated using

Equation I-14 from the core matrix porosity, interpolated bulk density, unit-specific particle density (Table 5-4), and an assumed matrix water saturation of unity.

Method B. In boreholes where core samples were not collected but neutron porosity petrophysical data exist and appear reasonable, Equation I-23 is used to calculate lithophysal porosity. In this case the smoothed neutron porosity data (Section 4.1.2) are used to calculate the volumetric water content of the composite rock. As in Method A, the unit-specific particle density (Table 5-4) and an assumed matrix water saturation of unity are applied, as discussed in Section 5, Assumption 2.

Method C. In boreholes where core samples were not collected and neutron porosity data either do not exist or do not appear reasonable, Equation I-14 is used to calculate lithophysal porosity. In such circumstances, matrix porosity, particle density, and water saturation are all assumed in the calculation of lithophysal porosity. Matrix porosity is assumed equal to 0.10, particle density is obtained from Table 5-4, and water saturation is once again assumed equal to unity.

The equations used in Method A and Method B are developed in Attachment I. The equations used in Method C are identical to those of Method A when the assumptions noted above are invoked.

Of the three calculations, Method A is considered to be the most reliable, followed by Method B, and then Method C. Method B was applied most often since most older boreholes were not cored, and Method C was applied the least since neutron porosity data are nearly as abundant as bulk density. Attachment II provides comments pertaining to the specific choice of calculation method including plots of the smoothed petrophysical data and computed porosities for each borehole.

In all three methods, the matrix continuum is assumed to be water saturated (Section 5, Assumption 2). Setting S_w to unity may lead to smaller calculated matrix porosities; however, the calculated values of lithophysal porosity are not highly dependent on the values of matrix saturation (See Attachment I, Equations I-14 and I-23).

All three methods also utilize the values of particle density given in Table 5-4. These are the unit-specific mean values from corresponding histograms, presented later in Section 6.1.6. The narrowness of these histograms justifies the use of constant values. For comparison, the mean grain density for each unit is also given in Table 5-4.

Histogram plots of calculated lithophysal porosity are depicted in Figure 6-5 for each of the four lithostratigraphic units. The data from as many as 37 boreholes are used in the construction of these plots. Consequently, these distributions reflect the spatial variability of lithophysal porosity across the entire mountain. For a number of boreholes (e.g., Figure II-3), negative values of lithophysal porosity are calculated over some intervals. This is the result of the possible measurement errors associated with the petrophysical measurements and the analytical methods applied to calculate lithophysal porosity. These nonphysical negative values are plotted in the figures in Attachment II; however, the negative values are treated as zeros in the construction of the lithophysal porosity distributions. This can be verified by examining the

minimum values of lithophysal porosity tabulated in Figure 6-5. As discussed in Section 6.1.1, these distributions and their associated statistical measures agree reasonably well with the ECRB observations of Mongano et al. (1999, pp. 16 to 35 [149850]).

Variogram models of spatial continuity were then developed from the normal-score transformed lithophysal porosity data. The computer program GSLIB V. 1.0MGAMV2 (Table 3-1; GSLIB V. 1.0MGAMV2V1.201, STN: 10087-1.0MGAMV2V1.201-02 [158221]) is used to generate experimental semivariogram data that are then fit to traditional spherical models (Deutsch and Journel 1998, p. 25 [102895]). The experimental data and resulting models are presented graphically in Figure 6-6. The lithophysal porosity model semivariograms shown in Figure 6-6 are a linear combination of an isotropic nugget effect and two spherical semivariogram models. The specific parameters that implement these models in the GSLIB V. 1.4SGSIMV1.41 software are provided in Table 6-3. The horizontal and vertical search radii specify that only data falling within the search ellipsoid are to be considered in the Gaussian simulations. The sill, the horizontal and vertical range parameters, and the three rotation angles defining the geometric anisotropy are required to define each spherical model component (Deutsch and Journel 1998, pp. 25 to 28 [102895]). These parameters are estimated to provide an accurate approximation to the experimental semivariogram data. In this work, the three rotation angles were set equal to zero, indicating the principal directions of the semivariogram model are aligned with the stratigraphic coordinate directions.

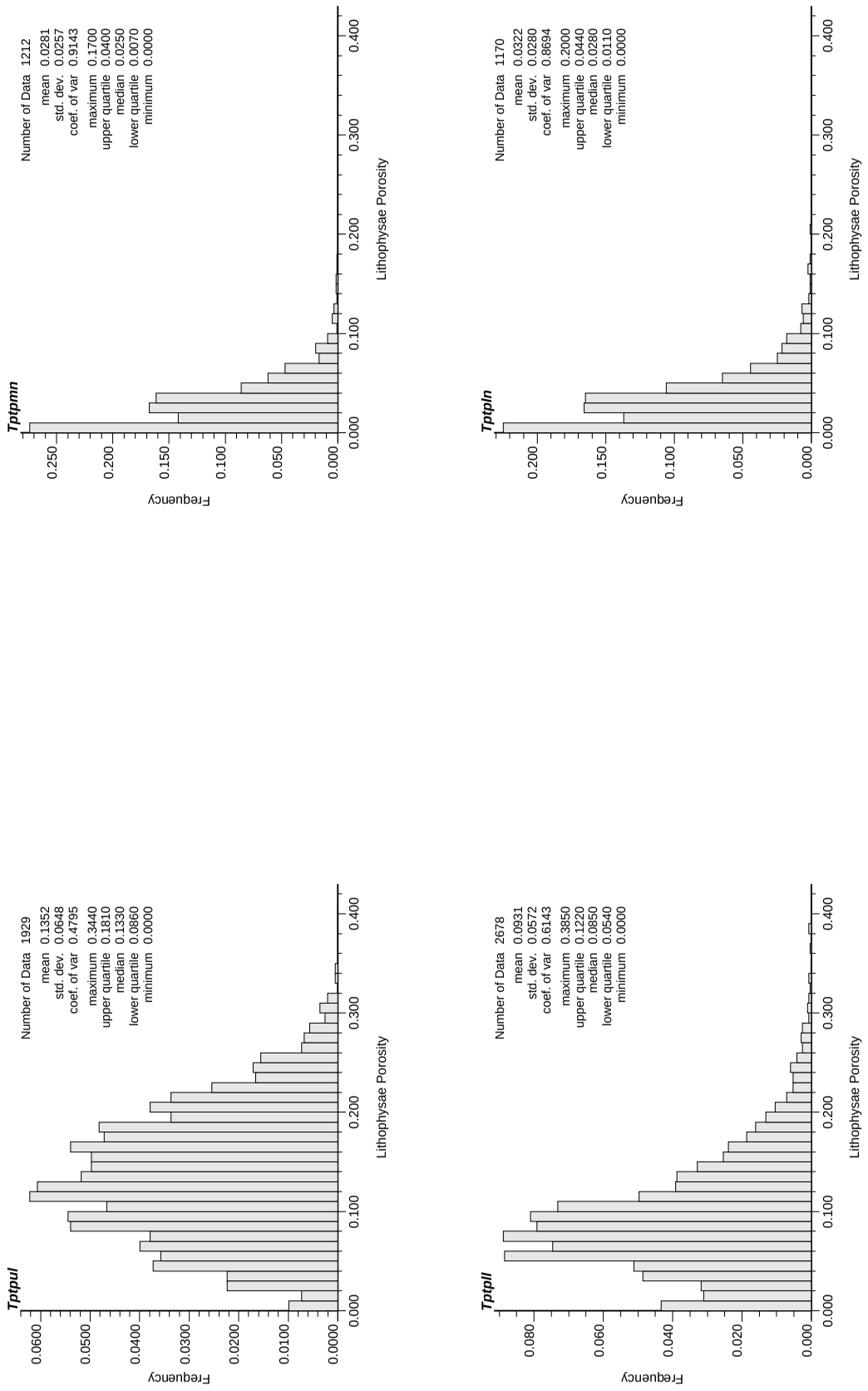

DTN: SN0208T0503102.007

Figure 6-5. Histogram of Lithophysal Porosity Conditioning Data

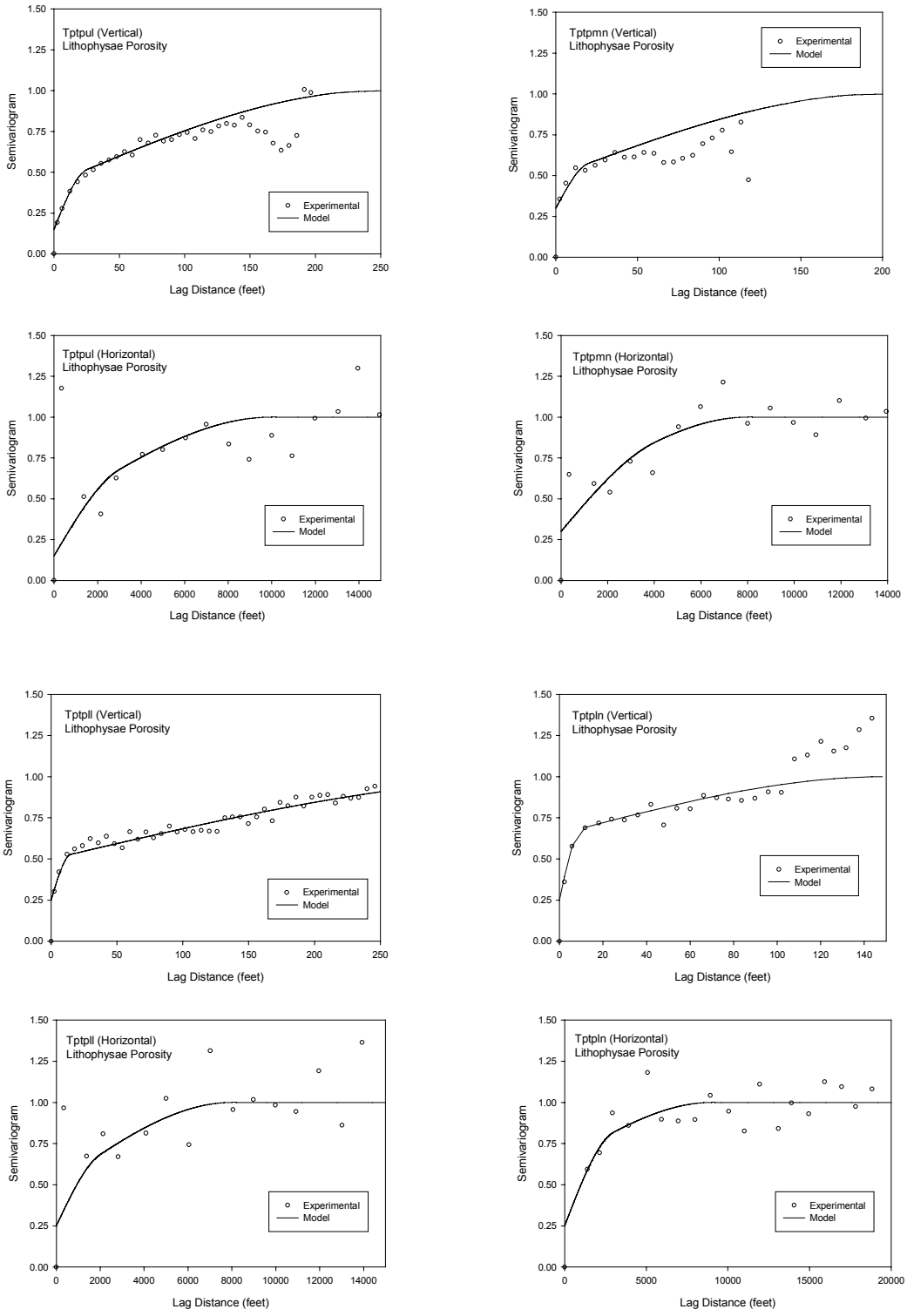

DTN: SN0208T0503102.007

Figure 6-6. Lithophysal Porosity Semivariograms

Table 6-3. Lithophysal Porosity Model Variogram Parameters

Nest No.	Model Type	Range/*Search Radius* (feet)		Sill	Rotation Angles (degrees)			Anisotropy Ratio	
		Horizontal (Maximum)	Vertical (Minimum)		1	2	3	1	2
Tptpul Unit									
0	Nugget	*10,000*	*200*	0.15	---	---	---	*1.0*	*0.0200*
1	Spherical	3,000	25	0.28	0	0	0	1.0	0.0083
2	Spherical	10,000	250	0.57	0	0	0	1.0	0.0250
Tptpmn Unit									
0	Nugget	*8,000*	*120*	0.30	---	---	---	*1.0*	*0.0150*
1	Spherical	4,000	20	0.20	0	0	0	1.0	0.0050
2	Spherical	8,000	200	0.50	0	0	0	1.0	0.0250
Tptpll Unit									
0	Nugget	*8,000*	*300*	0.25	---	---	---	*1.0*	*0.0300*
1	Spherical	2,000	15	0.25	0	0	0	1.0	0.0050
2	Spherical	8,000	400	0.50	0	0	0	1.0	0.0400
Tptpln Unit									
0	Nugget	*9,000*	*100*	0.25	---	---	---	*1.0*	*0.0111*
1	Spherical	3,000	10	0.40	0	0	0	1.0	0.0033
2	Spherical	9,000	150	0.35	0	0	0	1.0	0.0167

DTN: SN0208T0503102.007

The anisotropy ratios given in the last two columns of Table 6-4 correspond to the horizontal and vertical planes, respectively. A value of one in the horizontal plane implies the maximum and minimum horizontal ranges are identical and is equivalent to isotropy in this plane. The anisotropy ratio in the vertical plane is computed as the ratio of the vertical to horizontal values.

The reliability of the experimental semivariogram data decreases as the lag distance increases. The distance at which the semivariogram approaches a value equal to one defines the scale at which two measurements of a variable are essentially uncorrelated. The deviations between the model and the experimental semivariogram at large lag distances are acceptable because the search radii are chosen to control the extent of data inclusion. The emphasis on determining model parameters is aimed at lag distances for which sufficient data and meaningful correlations exist.

Table 6-4. Matrix Porosity Variogram Parameters

Nest No.	Model Type	Range/*Search Radius* (feet)		Sill	Rotation Angles (degrees)			Anisotropy Ratio	
		Horizontal (Maximum)	Vertical (Minimum)		1	2	3	1	2
Tptpul Unit									
0	Nugget	*5000*	*150*	0.05	---	---	---	*1.0*	*0.0300*
1	Spherical	500	25	0.20	0	0	0	1.0	0.0500
2	Spherical	5000	600	0.75	0	0	0	1.0	0.1200
Tptpmn Unit									
0	Nugget	*8000*	*120*	0.08	---	---	---	*1.0*	*0.0150*
1	Spherical	4000	25	0.20	0	0	0	1.0	0.0063
2	Spherical	8000	240	0.72	0	0	0	1.0	0.0300
Tptpll Unit									
0	Nugget	*4000*	*200*	0.10	---	---	---	*1.0*	*0.0500*
1	Spherical	600	17	0.28	0	0	0	1.0	0.0283
2	Spherical	4000	800	0.62	0	0	0	1.0	0.2000
Tptpln Unit									
0	Nugget	*6000*	*90*	0.20	---	---	---	*1.0*	*0.0150*
1	Spherical	2500	25	0.13	0	0	0	1.0	0.0100
2	Spherical	6000	90	0.67	0	0	0	1.0	0.0150

DTN: SN0208T0503102.007

6.1.5 Matrix Porosity

Geostatistical representations of matrix porosity are developed based on laboratory core and well-log petrophysical measurements. Matrix porosity can be calculated either by comparing saturated and dry bulk densities or by comparing dry bulk and grain densities. Reports of laboratory core measurements produced for the YMP generally include two values of dry bulk density. The first dry density is obtained by drying the sample in a relative humidity (RH) oven at elevated temperature and humidity levels (60°C and 65 percent RH), and the second is obtained by drying the sample in a 105°C oven at ambient but very low RH. Oven-dried (OD) calculations of porosity are almost always greater than RH calculations since water that is bound to minerals or otherwise trapped in unconnected pores is displaced in the OD measurements but remains behind in RH measurements. Consequently, the OD value is a better measure of the total potential water content and, therefore, more appropriate for the purpose of calculating matrix thermal conductivity.

Applying many of the same concepts discussed in the previous section, a method of calculating matrix porosity from bulk density and neutron porosity is presented in Attachment I, Equation I-22. This equation is applied at locations where petrophysical data are available, but core data are not (Method B). Where core data are available (Method A), matrix porosity is

measured directly from the core; therefore, it is unnecessary to calculate. Finally, where bulk density measurements are the only reliable data available (Method C), matrix porosity is set equal to 0.10, but solely for the purpose of estimating lithophysal porosity. Bulk density measurement alone provides inadequate information to estimate matrix porosity. Therefore, data sets classified as Method C are simply ignored with respect to matrix porosity.

One important distinction between matrix and lithophysal porosity is that the two properties are defined with respect to different reference volumes. Consequently, these properties cannot be added directly, and care must be exercised when applying the geostatistical results. This difference in definition is necessitated by the fact that core measurements do not account for the volume of lithophysae and, hence, are not based on the total volume. Instead, matrix porosity is measured and, therefore, defined as the volume fraction of small-scale void space with respect to the matrix volume, V_m, where the matrix volume is simply the total volume, V_t, less the lithophysae volume, V_L:

$$V_m = V_t - V_L . \qquad \text{(Eq. 6-3)}$$

This same definition of matrix porosity is used in the derivation of Equation I-22, so it is appropriate to combine the petrophysically derived calculated values of matrix porosity with the laboratory measured values into a composite data set.

Histogram plots of this composite data set are depicted in Figure 6-7 for each of the four lithostratigraphic units. As was the case for lithophysal porosity, these distributions reflect the spatial variability of matrix porosity across the entire mountain. It should be noted that both the mean and the variance are greater in the lithophysal zones than in the nonlithophysal zones.

This indicates that the lithophysal zones have higher matrix porosity values than nonlithophysal zones. This higher matrix porosity is likely caused by the formation lithophysae and the associated vapor phase alteration.

Variogram models of spatial continuity were then developed from the normal-score transformed matrix porosity data. The computer program GSLIB V. 1.0MGAMV2V1.201 [158221] (Table 3-1) is used to generate experimental semivariogram data that are then fit to traditional spherical models (Deutsch and Journel 1998, p. 25 [102895]). The experimental data and resulting models are presented graphically in Figure 6-8. Finally, the specific parameters that implement these models in the GSLIB V. 1.4SGSIMV1.41 software are provided in Table 6-4.

6.1.6 Dry Bulk Density

Dry bulk density, ρ_{bd}, is defined as the mass per unit volume of an air-saturated porous rock. In lithophysae bearing units, ρ_{bd} can be expressed as a function of matrix porosity, ϕ_m; lithophysal porosity, ϕ_L; and the particle density, ρ_g:

$$\rho_{bd} = (1 - \phi_L)(1 - \phi_m)\rho_g \qquad \text{(Eq. 6-4)}$$

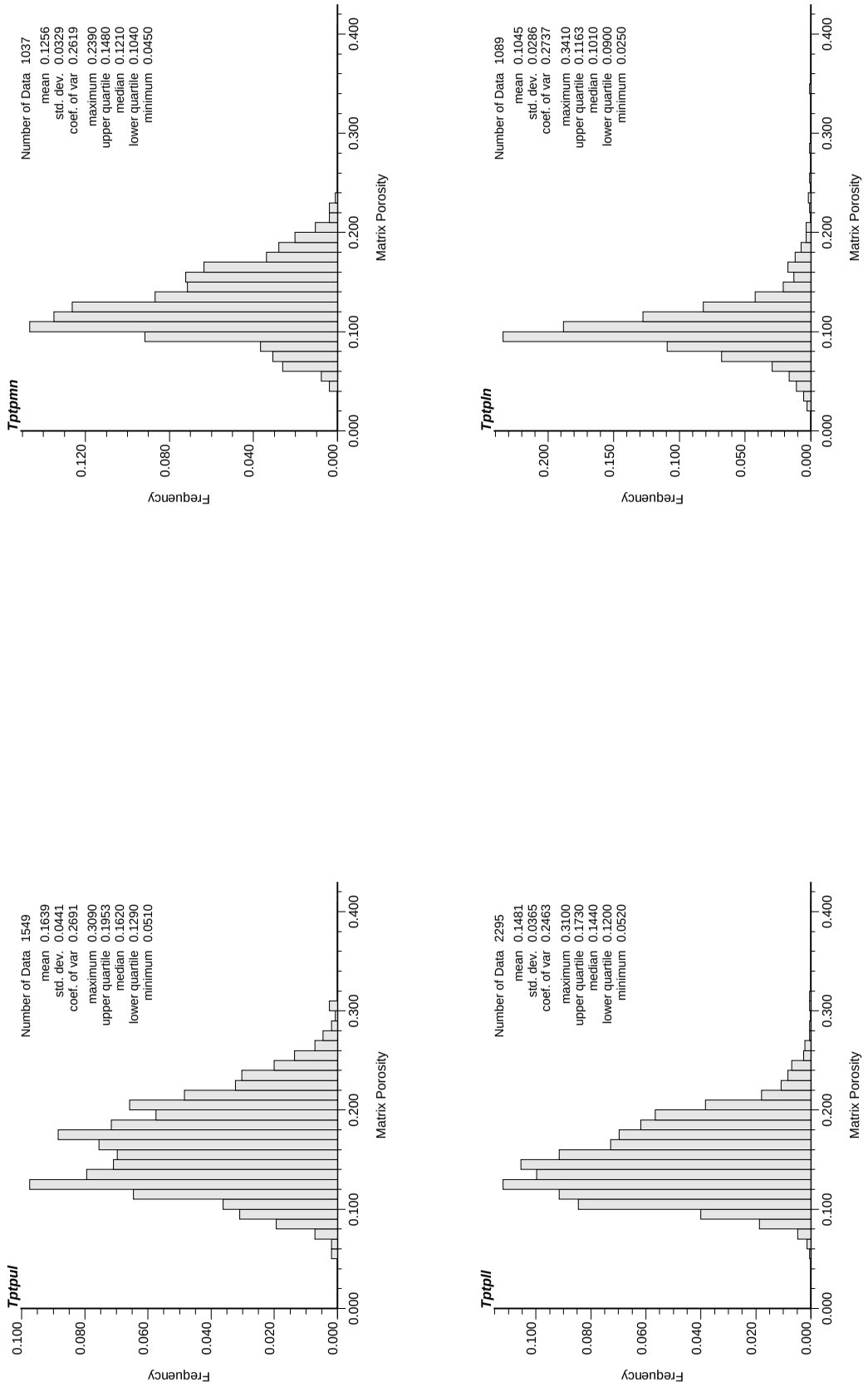

DTN: SN0208T0503102.007

Figure 6-7. Histogram of Matrix Porosity Conditioning Data

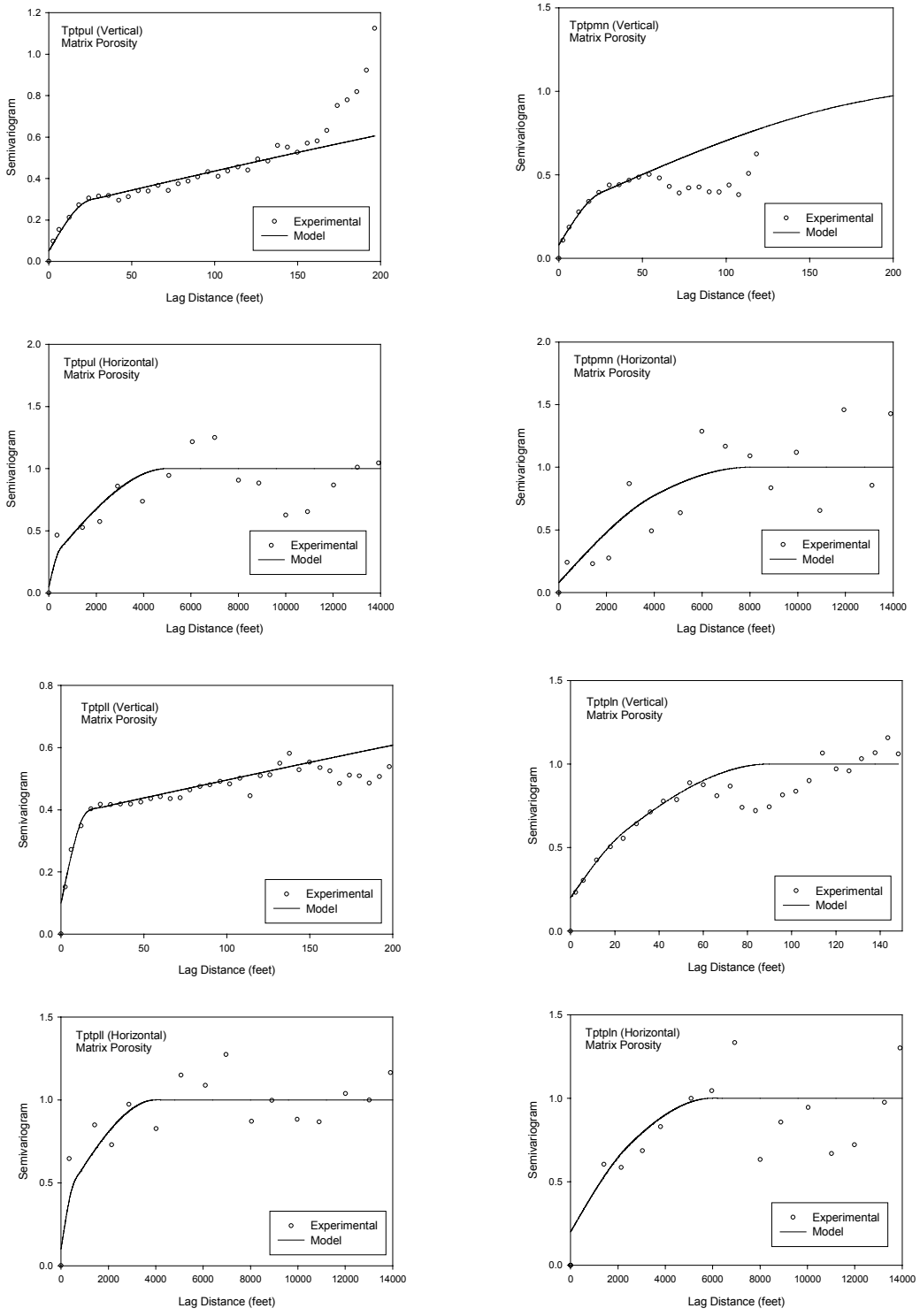

DTN: SN0208T0503102.007

Figure 6-8. Matrix Porosity Semivariograms

In Equation 6-3 the density of air has been neglected, and the term $1-\phi_L$ represents the volume of matrix, V_m, per unit total volume, V_t. The term $1-\phi_m$ represents the volume of rock per unit volume of matrix, and ρ_g is the mass, M, per unit volume of rock. In terms of these more fundamental properties, Equation 6-4 can be written as:

$$\rho_{bd} = \frac{V_m}{V_t}\frac{V_r}{V_m}\frac{M}{V_r} = \frac{M}{V_t} \qquad \text{(Eq. 6-5)}$$

which demonstrates that ρ_{bd} is correctly defined.

Histogram plots of particle density derived from core measurements are presented in Figure 6-9. These plots illustrate the observation that particle density gradually increases with depth over these four units. The variance of these data within a given unit is, however, reasonably small, indicating that for the purpose of computing dry bulk density, it is appropriate to ignore sub-unit spatial variability and simply use a constant value of particle density. The unit-specific mean particle density values shown in Figure 6-9 are used for this purpose and are tabulated in Table 5-4.

Unlike matrix and lithophysal porosity, dry bulk density is not simulated explicitly but rather computed at each node in the model grid from simulated values of $\phi_L(x,y,z)$ and $\phi_m(x,y,z)$ by applying Equation 6-3. This calculation is performed using the program TCOND (Table 3-1; TCOND V. 1.0, STN: 10801-1.0-00 [158260]) and yields 50 equally likely realizations of dry bulk density that are spatially consistent with the corresponding realizations of matrix and lithophysal porosity.

6.1.7 Matrix Thermal Conductivity

The spatial variability and uncertainty in matrix thermal conductivity is addressed by first selecting one of several thermal conductivity models from the literature. The decision to apply a theoretical model rather than conditionally simulate matrix thermal conductivity is based on the quantity, quality, and type of available data. At the present time there are relatively abundant data regarding fundamental rock properties such as matrix porosity but only a handful of the more difficult measurements of thermal conductivity. Consequently, it was decided to implement a model that utilizes the more abundant fundamental property data sets. This is not to say that the information from laboratory thermal conductivity measurement was neglected.

Indeed, these measurements are used to constrain and calibrate the selected model through the development of model parameter values and uncertainty distributions.

The thermal conductivity of porous materials has been the subject of considerable study over several decades. Consequently, many analytical and empirical models have been developed for this property. This research is beneficial from the perspective of finding a predictive model that may be applied at Yucca Mountain. However, the task of selecting the “best” model from all those proposed is a substantial and difficult one. Much of the early work in this field (prior to 1960) pertains mostly to unconsolidated substances and is, therefore, not particularly suited to the welded tuff of the Tpt. More recent models tend to address consolidated porous media but

may also include additional model parameters and varying degrees of complexity. In general, those parameters associated with pore structure or geometry must be evaluated experimentally.

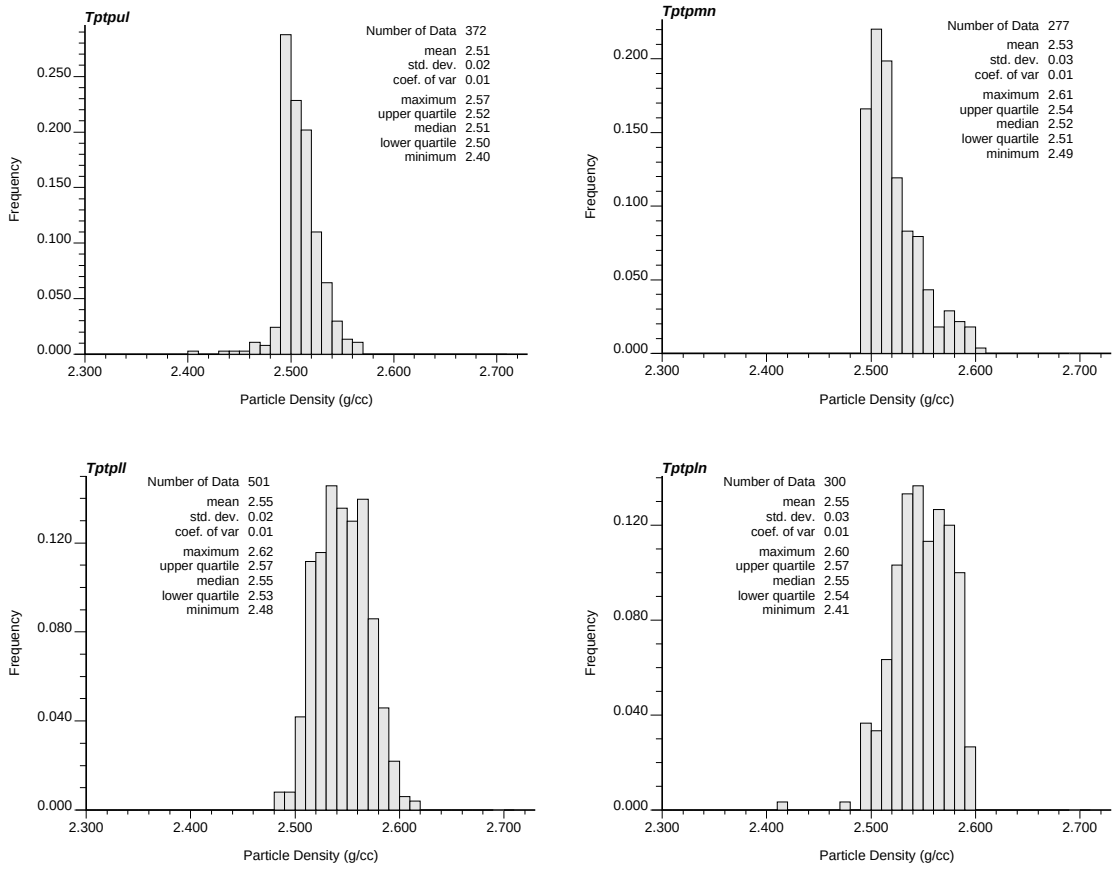

DTN: SN0208T0503102.007

Figure 6-9. Histogram Plots of Particle Density Obtained from Core Measurement

In this work, three candidate models are examined for application at Yucca Mountain. The proposed models are Kunii and Smith (1960 [153166]), Hadley (1986 [153165]), and Hsu et al. (1995 [158073]). All three models address consolidated porous media and in theory are good candidates for this work. One of the three was ultimately selected based on the following screening criteria:

1. The theoretical development must be well documented, relatively easy to comprehend, and appropriate for consolidated porous media.

2. The model must be capable of reproducing experimental results within the estimated range of experimental error.

3. The model parameters and their uncertainty must be easily derived through existing qualified data.

Kunii and Smith (1960 [153166]) assume that the thermal conductivity of a porous medium can be represented by a layer of fluid acting in parallel with a composite layer consisting of both fluid and solid phases. Parameters that dictate the geometry of the composite layer are derived based on an analytical solution of heat flow between two spheres. The authors extrapolate this solution to approximate multiple spheres by considering additional contact points and the orientation of these contacts for various packing arrangements. The theory is then extended to consolidated porous media by introducing an additional parameter with additional assumptions.

The fundamental premise behind the Kunii and Smith model is that the analytical solution of heat flux between two spheres can be stretched and approximated to the point that it is applicable to consolidated porous substances. This argument is fairly convincing for unconsolidated granular substances but not so convincing for consolidated media. This model was, therefore, not selected based on Criteria 1.

The Hadley (1986 [153165]) model is derived from volume-averaging theory and makes use of the pioneering work of Maxwell (1954 [158165]). This is a versatile model that is applicable over the complete range of potential pore structures. In addition, the model is unique in that it is not explicitly tied to a specific geometry or packing arrangement. The model was not selected, however, due to the difficulty of quantifying model parameter uncertainty from existing data.

In the Hadley model there are three parameters that must be calibrated to experimental data or otherwise estimated. These parameters consist of a geometry factor f_0, a consolidation parameter α, and the thermal conductivity of the mineral solids k_s. Hadley (1986 [153165]) derives equations for α and f_0 from experimental data; however, it is not clear that the specimens used in these experiments are representative of welded tuff. Therefore, it was decided that Hadley's representation of α and f_0 should not be used unless they could be proven valid for welded tuff.

The Yucca Mountain experimental data set generally consists of one to two measurements of thermal conductivity for a given sample at a specific temperature. Often, thermal conductivity is measured after saturating the sample with water (wet) and then again with the sample saturated with air (dry) or by measuring saturated and dry thermal conductivities on a matched pair of specimens where the two specimens are taken from adjacent locations on a single piece of core. In some cases the mineralogy has also been determined using x-ray diffraction. There are a total of eleven samples, all from USW NRG-6, where all three measurements exist, and the data are usable. For many samples, however, there are only one or two constraints and three unknowns in the Hadley model. It may be possible to calibrate the Hadley model from existing data, but it would be difficult, and the resulting parameter distributions would be highly uncertain. For this reason, the Hadley model was not selected.

The final model examined and ultimately selected is the 3-D Cubic Model developed by Hsu et al. (1995 [158073]). This model is conceptually similar to that proposed by Kunii and Smith (1960 [153166]) in that a simplified geometrical representation of the porous medium is proposed and then the effective thermal conductivity of the simplified problem is derived through resistance analogues. In the case of the 3-D Cubic Model, the porous medium is represented by a periodic array of in-line cubes with connecting nodules. The unit cell of the 3-D periodic array is shown in Figure 6-10.

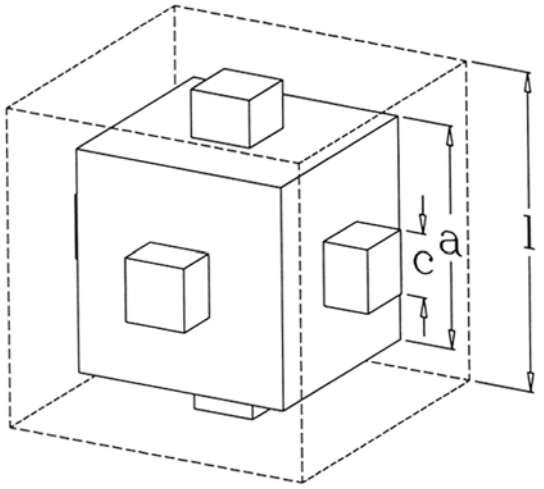

Source: Hsu et al. 1995, Figure 8 [158073]

Figure 6-10. 3-D Cubic Model

Hsu et al. 1995 [158073] derive the following equation for this geometry:

$$\frac{k_m}{k_f} = 1 - \gamma_a^2 - 2\gamma_c\gamma_a + 2\gamma_c\gamma_a^2 + \frac{\gamma_c^2\gamma_a^2}{\lambda} + \frac{\gamma_a^2 - \gamma_c^2\gamma_a^2}{1 - \gamma_a + \gamma_a\lambda} + \frac{2\left(\gamma_c\gamma_a - \gamma_c\gamma_a^2\right)}{1 - \gamma_c\gamma_a + \gamma_c\gamma_a\lambda} \qquad \text{(Eq. 6-6)}$$

where $\gamma_a = a/l$; $\gamma_c = c/a$; $\lambda = k_f / k_s$; and k_s, k_f, and k_m are the thermal conductivities of the solid, fluid, and composite matrix, respectively, and where the scales *a*, *c*, and *l* are as shown in Figure 6-10. As illustrated in Figure 6-10, *l* is the length of the unit cell cube shown, *a* is the length of one side of the solid square cylinder, and *c* is the width of the connecting plate. It should be noted that the connecting nodules are square but are not cubes. The connecting nodule protrudes from the face of the solid cube a distance defined by $(l-a)/2$.

For the 3-D Cubic Model unit cell illustrated in Figure 6-10, the pore-volume may be computed by subtracting the volume of the solid cube, a^3, and the 6 connecting nodules, each having a volume of $c^2(l-a)/2$, from the unit cell volume, l^3. Furthermore, from geometrical considerations it can be shown that γ_a and γ_c are functionally dependent. This dependency may be written as:

$$1 - \phi_m - \gamma_a^3 - 3\gamma_c^2\left(\gamma_a^2 - \gamma_a^3\right) = 0 \qquad \text{(Eq. 6-7)}$$

It is apparent from Equations 6-5 and 6-6 that the effective matrix thermal conductivity may be expressed as a function of four independent variables:

$$k_m = f\left(k_f, k_s, \phi_m, \gamma_c\right) \qquad \text{(Eq. 6-8)}$$

The wet and dry laboratory thermal conductivity measurements extracted from the Tpt were used to calibrate this model. The change in sample mass from the air-saturated state to the water-saturated state is used to calculate ϕ_m, and the thermal conductivities of the saturating fluids are known sufficiently that they are assumed constant. The thermal conductivity of water,

k_w, was selected to be 0.64 (W m^{-1} K^{-1}) (Holman 1997, p. 650 [101978]) and air, k_a, to be 0.028 (W m^{-1} K^{-1}) (Holman 1997, p. 646 [101978]). This leaves two equations and two unknowns (k_s and γ_c) for each sample:

$$k_m(\text{wet}) = f(k_w, k_s, \phi_m, \gamma_c) \quad \text{(Eq. 6-9)}$$

$$k_m(\text{dry}) = f(k_a, k_s, \phi_m, \gamma_c) \quad \text{(Eq. 6-10)}$$

The program HsuInv V. 1.0 was used to solve the resulting system of nonlinear equations for each sample for which porosity and wet and dry values were available. Given the wet and dry matrix thermal conductivity, thermal conductivity of air and water, and matrix porosity, HsuInv V. 1.0 iteratively solves these two nonlinear equation for the parameters k_s and γ_c. The resulting values obtained for k_s and γ_c are tabulated in Table 6-5 and plotted in the form of histograms in Figure 6-11.

The histograms plotted in Figure 6-11 were created by selecting a suitable uniform bin size, Δx, for the data set and assigning each parameter value of the set to the appropriate bin. The number of data values in any bin, Δx_i, is the frequency, f_i, for that particular bin. The bin size used for the solid connectivity parameter, γ_c, was chosen to be 0.05, while the bin size for the solid thermal conductivity parameter, k_s, was chosen to be 0.2 W/m-K. The probability that the data lie within bin Δx_i is simply $f_i/(\Delta x N)$ where N is the total number of data points in the entire set. The probability is plotted on the y-axis of Figure 6-11.

At the bottom of Table 6-5 are six measurements for samples obtained from Alcove 5. The first three Alcove 5 samples were cored horizontally and the last three cored vertically at three different locations. In order to avoid over-weighting the results from Alcove 5, only the first three horizontal samples were used in the development of the histogram plots in Figure 6-11.

Also presented in Figure 6-11 are plots of the parameter distributions chosen to represent the spatial uncertainty for γ_c and k_s. The solid connectivity parameter, γ_c, is represented by a folded normal distribution with a mode of 1.0 and a standard deviation of 0.2, and the solid thermal conductivity parameter, k_s, is represented by log-normal distribution with a mean of 0.95 and a standard deviation of 0.14 in natural log space.

It should be noted that in the histogram for γ_c in Figure 6-11, there is a large population of values equal to unity. This spike is somewhat artificial since it results from the treatment of γ_c when the 3-D Cubic Model could not reproduce a specific pair of experimental results precisely.

To explain the limitations of the 3-D Cubic Model and the procedures implemented to address these limitations, a plot of predicted wet and dry thermal conductivity as a function of γ_c is shown in Figure 6-12. In this plot, the matrix porosity and solid thermal conductivity are held constant at values representative of welded tuff. It should be noted that the wet thermal conductivity is relatively insensitive to γ_c and, therefore, to the geometry of the model.

This is because the 3-D Cubic Model prediction is insensitive to the relative difference between the thermal conductivity of the solid and the thermal conductivity of the water filling the matrix pore-space (0.64 W/mK) (Holman 1997, p. 650 [101978]). The 3-D Cubic Model prediction of

dry thermal conductivity shows a greater sensitivity to γ_c, due to the somewhat greater relative difference between the solid thermal conductivity and the thermal conductivity of air (0.028 W/mK) (Holman 1997, p. 646 [101978]) filling the matrix pore-space. Figure 6-12 illustrates that the differences between the 3-D Cubic Model predictions of wet and dry matrix thermal conductivity depend on γ_c and have definite upper and lower bounds. The maximum difference is located at or near $\gamma_c = 0$, and the minimum difference is located at or near $\gamma_c = 1$.

There are several pairs of experimental wet and dry thermal conductivity measurements in the current data set that the 3-D Cubic Model is unable to replicate. The reason for this difficulty, in all cases, is that the wet and dry pairs of thermal conductivity measurements are simply too close to one another to be reproduced by the model. In such circumstances, γ_c is set equal to one, and k_s is calculated such that the dry thermal conductivity measurement is satisfied exactly. The dry measurement is satisfied rather than the wet because dry measurements are easier to control experimentally and, therefore, are presumed to be more reliable. Setting γ_c to one minimizes the difference between the experimentally measured and the model-predicted wet thermal conductivity. These differences, relative to their measured data, are presented graphically in Figure 6-13. *Laboratory Measurements of Thermal Conductivity as a Function of Saturation State for Welded and Nonwelded Tuff Speciments* (SNL 1998, p. 21 [118788]), cites that the differences between wet and dry thermal conductivity may, in fact, be smaller than experimentally measured due to the calibration procedures used in testing. As new data become available, the model's ability to match experimental data may be further evaluated.

The relative differences reported in Figure 6-13 raise questions regarding the fit of the model to the experimental data. With values up to 20 percent, and the model unable to replicate 15 of 33 experimental data, it seems reasonable to question the applicability of the model (Criteria 2). However, close examination of the experimental data reveals that most of the wet and dry pairs were collected from different samples extracted from the same physical core. One would expect similar results from these samples; however, there is no way to be certain of this or to estimate the error introduced because of it.

For those cases where the wet and dry thermal conductivity measurements were acquired from the same sample, the 3-D Cubic Model (Hsu et al. 1995 [158073]) is capable of replicating the experimental results quite well. In these cases, model parameters were identified that reproduced both the wet and the dry experimental results exactly, except for five of the six samples collected from Alcove 5 (Table 6-5). In the case of the Alcove 5 data, the dry measurements are reproduced precisely, and the difference between the measured wet thermal conductivity and the model prediction is roughly 2 percent. Such differences are well within the reported experimental error of ± 5 percent (SNL 1998, p. 10 [118788]) and are tolerable. Therefore, after considering all possible sources of experimental error, it was decided that the 3-D Cubic Model (Hsu et al. 1995 [158073]) was the most appropriate at this time.

Table 6-5. Model Parameters for the 3-D Cubic Model

Specimen ID Dry/Wet	Porosity	Dry Thermal Conductivity ($W\ m^{-1}\ K^{-1}$)	Wet Thermal Conductivity ($W\ m^{-1}\ K^{-1}$)	k_s Solids Thermal Conductivity ($W\ m^{-1}\ K^{-1}$)	γ_c Solid Connectivity Parameter
NRG4-529.0B/529.0A	0.1650	1.160	1.670	2.0483	0.9429
NRG4-586.2B/586.2A	0.1944	0.945	1.640	2.1010	0.7533
NRG4-654.0B/654.0A	0.1369	1.155	1.800	2.1648	0.7986
NRG5-781.8A/781.8A	0.1571	1.000	1.920	2.4185	0.6628
NRG5-791.6A/791.3A	0.2459	0.820	1.780	2.5691	0.6165
NRG5-834.8B/834.8A	0.0891	1.655	1.920	2.4188	1.0000
NRG5-843.5A/843.5A	0.0877	1.650	2.200	2.5335	0.8882
NRG5-853.8A/852.5B	0.0873	1.705	2.260	2.6102	0.8916
NRG5-874.9B/874.3B	0.0862	1.675	2.320	2.6867	0.8451
NRG5-886.5B/886.5B	0.1236	1.370	2.530	3.1932	0.6624
NRG6-277.5E/277.5D	0.1000	1.255	1.680	1.8944	0.9455
NRG6-321.1E/321.1D	0.1500	1.165	1.710	2.0698	0.8742
NRG6-354.9C/354.9B	0.1500	1.135	1.490	1.9142	1.0000
NRG6-392.1D/392.1C	0.0400	1.185	1.550	1.6171	0.8431
NRG6-416.0K/416.0J	0.0900	1.285	1.550	1.8686	1.0000
NRG6-421.8D/421.8C	0.1269	1.190	1.700	1.9911	0.8837
NRG6-425.3B/425.3A	0.1380	1.260	1.820	2.1940	0.8701
NRG6-451.2B/451.2A	0.1852	1.290	1.700	2.3748	1.0000
NRG6-693.1C/693.1C	0.1363	1.370	1.930	2.3462	0.8891
NRG6-757.0B/757.0A	0.0960	1.610	2.020	2.3956	1.0000
NRG6-778.1B/778.1A	0.0840	1.710	1.850	2.4663	1.0000
NRG6-787.5B/787.5A	0.1123	1.600	1.720	2.4843	1.0000
NRG6-802.7D/802.7C	0.0945	1.670	1.780	2.4773	1.0000
NRG6-900.4D/900.4C	0.1445	1.500	2.230	2.8417	0.8140
NRG6-926.3E/926.3-D	0.1287	1.540	2.150	2.6388	0.8733
NRG6-987.0B/987.0A	0.1175	1.550	2.040	2.4367	1.0000
NRG7-312.8D/312.8C	0.1061	1.330	1.630	2.0211	1.0000
Alcove5/SPC00515193-G-H	0.0967	1.810	2.300	2.7063	1.0000
Alcove5/SPC00515196-G-H	0.0986	1.720	2.250	2.6425	0.9243
Alcove5/SPC00515199-G-H	0.0955	1.870	2.330	2.7892	1.0000
Alcove5/SPC00515193-C-V	0.0922	1.820	2.280	2.6889	1.0000
Alcove5/SPC00515196-C-V	0.0993	1.810	2.270	2.7251	1.0000
Alcove5/SPC00515199-C-V	0.1014	1.800	2.270	2.7248	1.0000

Highlighted fields indicate the same sample was used in both the wet and dry experiments.

DTN: SNL01A05059301.005 [109002], SNL01A05059301.007 [108980], SNL22100196001.006 [158213]

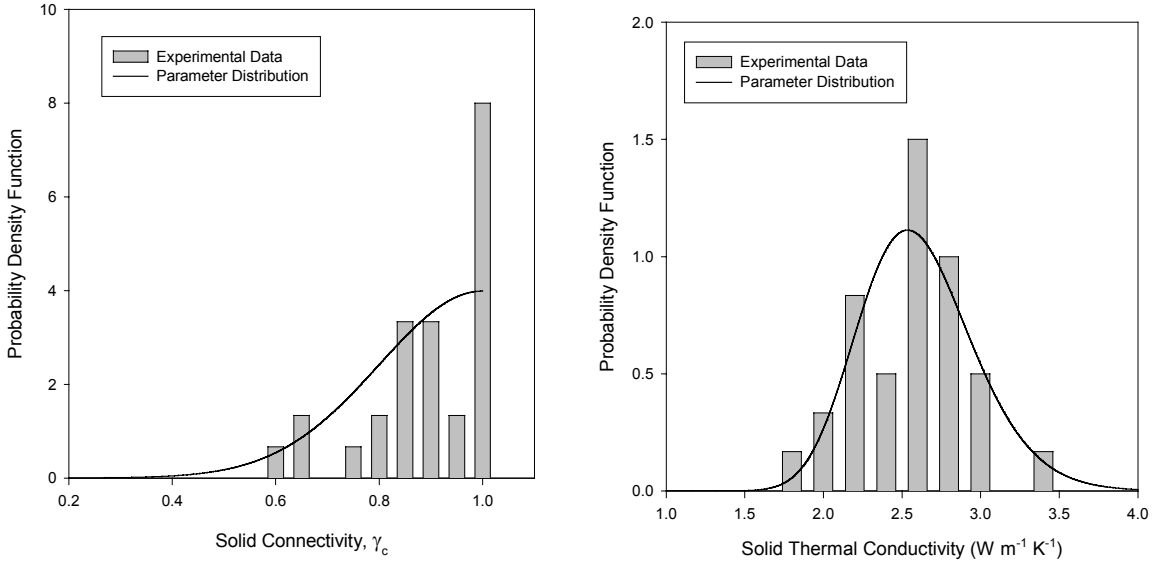

DTN: SN0208T0503102.007

Figure 6-11. Parameter Distributions for the 3-D Cubic Model

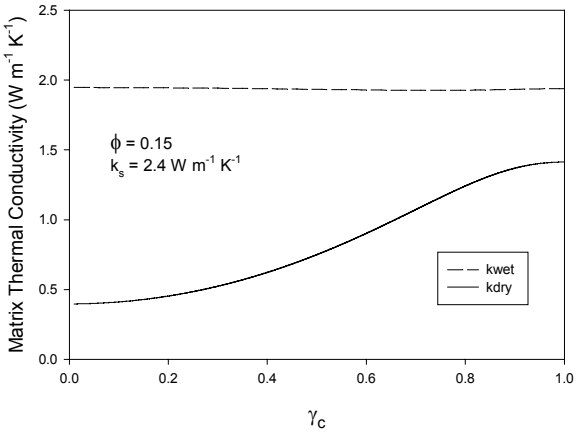

Figure 6-12. Matrix Thermal Conductivity as a Function of Solid Connectivity

Having selected the theoretical model for matrix thermal conductivity and developed corresponding model uncertainty parameter distributions, the next task was to create spatial realizations of all uncertain model parameters. In the 3-D Cubic Model (Hsu et al. 1995 [158073]), the uncertain parameters are matrix porosity, solid connectivity, and solid thermal conductivity. Matrix porosity was discussed previously in Section 6.1.5, leaving γ_c and k_s to be addressed here.

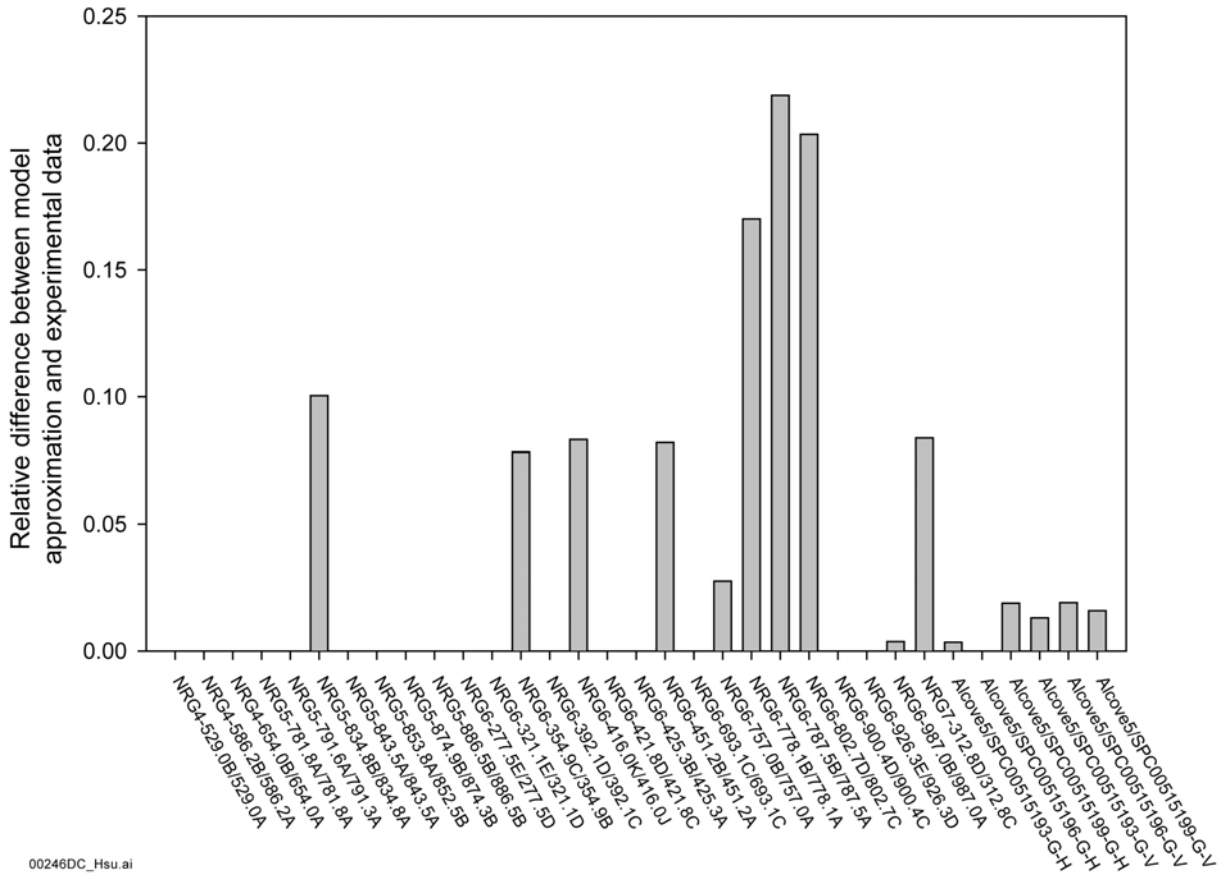

DTN: SN0208T0503102.007

Figure 6-13. Relative Difference in Wet Thermal Conductivity Between Model Predictions and Experimental Measurement

Solid thermal conductivity is theoretically solely dependent on mineralogy. In version 3.0 of the Mineralogic Model (BSC 2002c, p. II-4 [158730]), the four units of the Tpt studied are described as devitrified rhyolitic tuff with relatively constant feldspar content but highly variable ratios of tridymite, cristobalite, and quartz. The feldspar content averages 58 percent with a standard deviation of 6 percent in the middle nonlithophysal zone (BSC 2002c, p. 74 [158730]). Tridymite, cristobalite, and quartz are all silica polymorphs in which quartz is the stable species (BSC 2002c, p. 58[158730]). Though it is uncertain what if any change in thermal conductivity takes place when tridymite and cristobalite convert to quartz, it is clear that even small variations in the combined silica content may influence thermal conductivity. This is true because the thermal conductivity of rock high in quartz content (quartzite) is greater than that of rock having high feldspar content such as tuff and granite, as shown in Figure 6-14 (Stephens and Sinnock 1979 [158151]).

Ideally, realizations of k_s should be correlated with or conditioned to measurements of mineralogy or mineralogic models such as the one mentioned above. This, however, is quite an arduous task, and it is not clear that this level of effort is warranted at the present time.

Consequently, k_s is simulated unconditionally in this work, and the spatial correlations (variograms) developed for matrix porosity are applied to k_s as well.

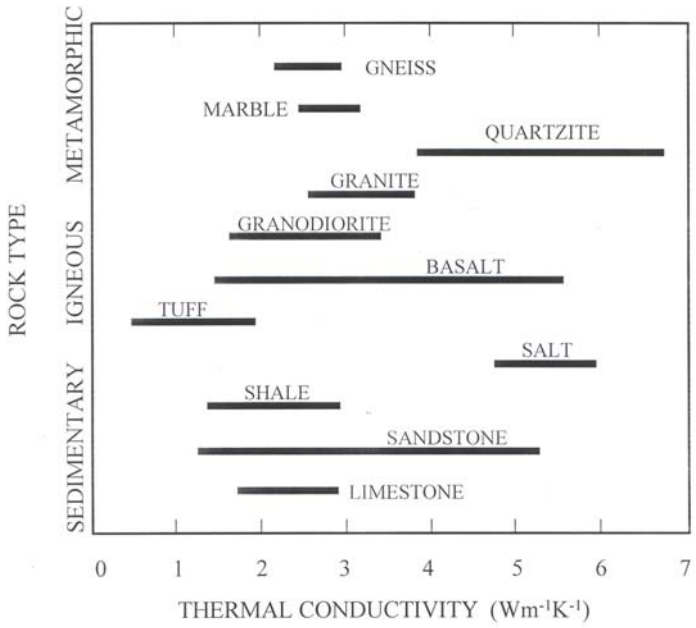

Source: Stephens and Sinnock 1979, Figure 4 [158151]

Figure 6-14. Ranges of Thermal Conductivities for Various Materials

Lastly, γ_c could be conditioned to the experimentally derived values given in Table 6-5, yet there are so few data that the results would be largely unconditioned anyway. For this reason, γ_c is also simulated unconditionally. Once again, the variography developed for matrix porosity is applied to γ_c.

6.1.8 Bulk Thermal Conductivity

For bulk thermal conductivity, a parallel model is selected to incorporate the effects of lithophysal porosity on the composite matrix conductivity. The selection is based on several criteria:

1. General description of lithophysae as spheroidal
2. Minimizing the number of model parameters to describe the composite medium
3. Maxwell's model (1954, pp. 440 to 441 [158165]) for the effects of spherical cavities on conductivity
4. Comparison of predictions to direct measurement of bulk thermal conductivity in the field.

A general description of lithophysae in the Tptpll unit is given by Mongano et al. (1999, p. 29, Table 3 [149850]). Based on visual inspection of exposed surfaces in the ECRB Cross-Drift excavation, cavity shapes range from spherical to lenticular, often irregular. As stated in the report, for the interval from Station 22+82 to 23+26, "smaller cavities tend to be lenticular or gash-like features, whereas larger cavities generally have ellipsoidal to spherical or irregular

shapes" (p. 29). For purposes of conceptual development, it is inferred that lithophysae are generally not planar or tabular features and that where lithophysal porosity is greater, the cavities are likely to be larger, with more open shapes (e.g., ellipsoidal or spheroidal, irregular cavities). Thus, where the effect of lithophysal porosity on conduction is greatest (i.e., greatest lithophysal porosity), open shapes are likely to be present and may predominate.

As stated in the controlling technical work plan (BSC 2002b [158075]), the criteria for conceptual model selection shall include limiting the number of model input parameters. For models of the type under discussion here, additional parameters are used to express the effects of non-ideal geometry (e.g., Hadley 1986 [153165] and Kunii and Smith 1960 [153166]). For spherical voids (an idealization of spheroidal), no geometrical parameters are required, as shown by Maxwell (1954 [158165]). The Maxwell model is, therefore, the simplest representation available for lithophysal porosity with highly uncertain geometry. The Maxwell model is described in this section, where it is shown that for media such as lithophysal tuff (solid conductivity >> void conductivity), the Maxwell model is equivalent to a parallel model. Accordingly, the parallel model is selected to represent the effects of lithophysae. This selection incorporates the generalization of sphericity and non-interference between the effects of adjacent voids (a condition of the Maxwell model). To validate the parallel model, comparison of model predictions with field testing is used in this report (Section 7.4).

The appropriateness of the parallel heat flow representation of Equation 6-1 can be justified through the early work of Maxwell (1954, pp. 440 to 441 [158165]).

Maxwell (1954 [158165]) formulated an expression for the bulk thermal conductivity of a solid body containing dilute inclusions of fluid. Hadley (1986 [153165]) refers to this formula as the Maxwell upper bound and shows that it may be written as:

$$\frac{k_b}{k_f} = \frac{\phi f + \kappa(1-\phi f)}{1-\phi(1-f)+\kappa\phi(1-f)} \qquad \text{(Eq. 6-11)}$$

In Equation 6-11, k_b is the bulk thermal conductivity, k_f is the thermal conductivity of the fluid, ϕ is the volume fraction of fluid inclusions, and $\kappa \equiv k_{sb}/k_f$, where k_{sb} is the thermal conductivity of the solid body. To obtain the Maxwell upper bound formula, the parameter f is defined by:

$$f = \frac{2\kappa}{2\kappa+1} \qquad \text{(Eq. 6-12)}$$

Hadley (1986 [153165]) also shows that f is theoretically bounded on the interval [0,1]. When f = 0, Equation 6-11 reduces to a series formula that is the lower bound of a two-component system. When f = 1, Equation 6-11 reduces to a parallel formula that is the theoretical upper bound.

The Maxwell upper bound formula can be applied in the Tpt by conceptualizing the matrix as the solid body and the lithophysae as dilute air-filled voids. Mathematically, this is achieved by letting $k_{sb} = k_m$, and $k_f = k_a$, $\phi = \phi_L$. If f is then computed for a representative case within the Tpt for which $k_m = 1.8$, $k_a = 0.028$, and $\kappa = 64.3$ the result obtained from Equation 6-12 is:

$$f = \frac{2(64.3)}{2(64.3)+1} = 0.992 \qquad \text{(Eq. 6-13)}$$

It is evident that $f \approx 1.0$ for almost any case imaginable. This is verified by calculating f for the average dry thermal conductivity of 1.443, f = 0.990, and for the average wet thermal conductivity of 1.948, f = 0.993. Since the Maxwell upper bound formula essentially reduces to a parallel flow representation for this specific application, it is justifiable to utilize the much simpler parallel representation instead. Applying the parallel model to the same matrix/lithophysae conceptualization yields,

$$k_b = \phi_L k_a + (1-\phi_L) k_m \qquad \text{(Eq. 6-14)}$$

Equation 6-14 is invoked by the program TCOND (Table 3-1; TCOND V.1.0, STN: 10801-1.0-00 [158260]) to produce 50 realizations of $k_b(x,y,z)$. TCOND operates on the realization of $\phi_L(x,y,z)$ developed in Section 6.1.4 and $k_m(x,y,z)$ developed in Section 6.1.7.

7. MODEL VALIDATION

This section presents evidence that the spatially dependent realizations of bulk thermal conductivity are valid and appropriate for their intended use. To support this proposition, calculated values of matrix (Section 6.1.1) and lithophysal porosity (Section 6.1.2) are examined to show that these values are reasonable and consistent with other measurements. Next, the model of matrix thermal conductivity is validated (Section 6.1.3) by comparing model results with thermal conductivity measurements obtained from laboratory core samples. Finally, the bulk thermal conductivity model (Section 6.1.4) is validated by comparing model results with analysis of in situ thermal conductivity field tests.

In addition, by validating matrix and lithophysal porosity, realizations of dry bulk density are inherently validated as well. This is true because dry bulk density is calculated directly from these parameters as discussed in Section 6.1.6.

7.1 PARAMETER VALIDATION: MATRIX POROSITY

Matrix porosity is used in the determination of matrix thermal conductivity and thus indirectly in the estimation of bulk thermal conductivity. The purpose of this section is to validate petrophysically derived values of matrix porosity. The approach taken is to compare values of matrix porosity determined from laboratory core measurements with values derived from in situ petrophysical measurements for selected boreholes.

Two types of matrix porosity measurements are available from laboratory core testing: RH porosity and OD porosity. The RH porosity allows some water to remain in the pores, while the

OD porosity is determined by drying in a oven until the interstitial water has been eliminated from the samples pores. Of the two, the OD measurement is theoretically more consistent with the petrophysical measurement since this measurement better represents the total water content of the sample, which is what the logging tool measures.

In order to validate matrix porosity, data from two wells were examined (USW SD-7 and USW SD-12). These boreholes are useful in the validation process because they extend through the layers of interest and core samples are available from them. Matrix porosity determined from laboratory testing of the core samples will be compared with matrix porosity values obtained from petrophysical measurement using the calculation Method B described in Section 6.1.4 and Attachment I. The model will be considered valid if the difference between the calculated matrix porosity and the measured matrix porosity value on core is within a few percentage points. This criteria will be applied in the nonlithophysal zones as the presence of lithophysae and associated vapor-phase alteration can affect the calculation and measurement of matrix porosity. The porosity measurements on the core samples are the best and most reliable technique to determine matrix porosity.

7.1.1 USW SD-7

Figure 7-1(a) shows neutron porosity measurements for USW SD-7. As noted in Section 6.1.4, neutron porosity is assumed to reflect the volumetric water content of the rock. For comparison, the volumetric water content measured from core samples is also shown. It should be noted that there is good agreement between the neutron porosity measurements and the core volumetric water content data in all four layers.

Figure 7-1(b) shows the variation in bulk density from petrophysical logging of USW SD-7. As expected, the bulk density is the lowest in the lithophysal zones, Tptpul and Tptpll, due to the larger fraction of voids in these regions. The bulk density log generally increases with depth, with some local variations.

Figure 7-1(c) shows matrix and lithophysal porosity calculated using Method B. In the Tptpul, the calculated matrix porosity decreases from top to bottom in the layer. The calculated matrix porosities are relatively constant in the lower three layers: Tptpmn, Tptpll, and Tptpln.

Figure 7-2 shows the comparison of the calculated matrix porosity with the RH and OD core porosity data. The agreement between the Method B calculation and the core measurement is very good in all four layers, with the calculation more closely matching the OD data. Therefore, the model of matrix porosity is considered valid. Below the Tptpln, the calculated matrix porosity differs from the measured core data due to a change in the particle density that is not accounted for in the calculation.

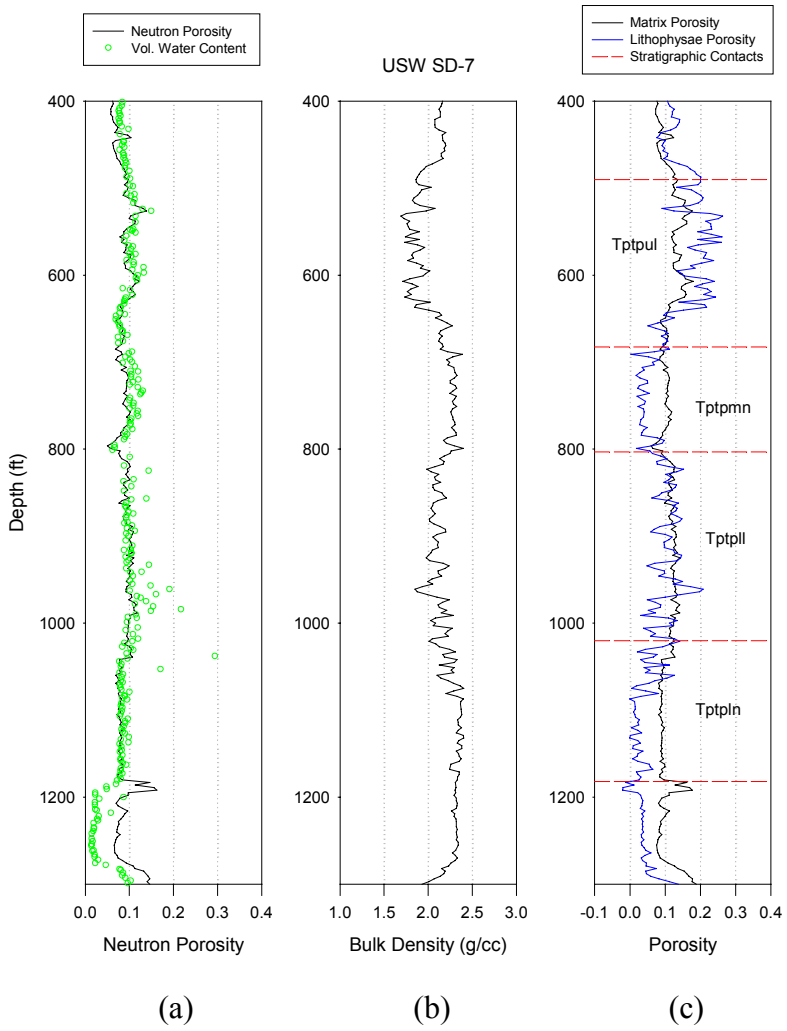

(a) (b) DTN: MO0010CPORGLOG.003 [155959]

(c) DTN: SN0208T0503102.007

Figure 7-1. USW SD-7 (a) (b) Core and Petrophysical Data; (c) Method B Porosity

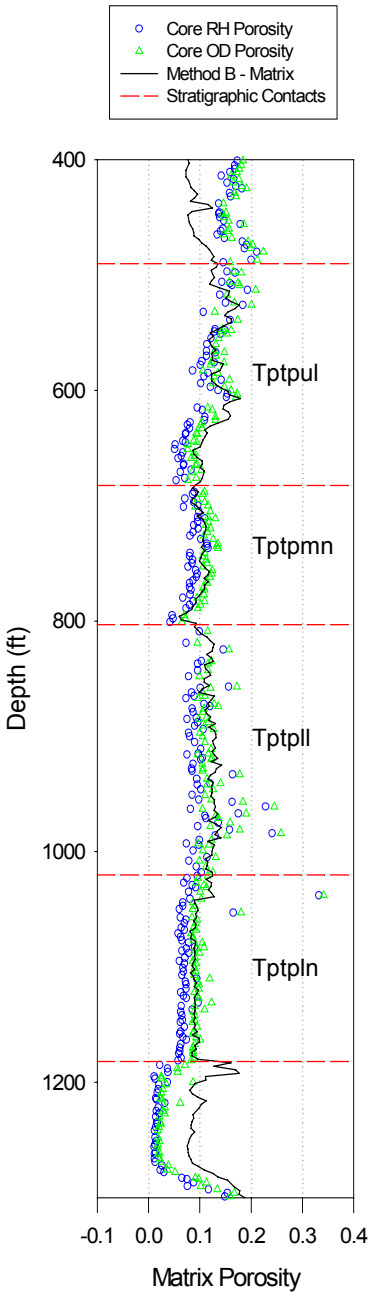

Core RH and OD: DTN: MO0109HYMXPROP.001 [155989], Method B matrix DTN: SN0208T0503102.007

NOTES: OD = oven dried, RH = relative humidity.

Figure 7-2. USW SD-7 Comparison of Core and Method B Matrix Porosity

7.1.2 USW SD-12

Figure 7-3(a) shows the neutron porosity measurements for USW SD-12. For comparison, the volumetric water content measured from core samples is also shown. The agreement between the neutron porosity measurements and the core volumetric water content data in all four layers is not quite as good as that seen in USW SD-7. In general the neutron porosity data over predict the volumetric water content in USW SD-12.

Figure 7-3(b) shows the variation of bulk density from petrophysical logging for USW SD-12. The bulk density is the lowest in the upper lithophysal zone, Tptpul, and generally increases with depth. An uncharacteristic region of low density is also observed near the middle of the Tptpmn.

Figure 7-3(c) shows the calculated values of matrix and lithophysal porosity for USW SD-12. The calculated matrix porosities are generally higher in the lithophysal units than in the nonlithophysal units. Also, the calculated matrix porosities are relatively constant with depth in each of the four units.

Figure 7-4 shows the comparison of calculated matrix porosity with core measurements of the same property. Both RH and OD measurements are presented. The agreement between the calculated matrix porosity and the core measurements, while not as good as for USW SD-7, are still reasonably close in all four layers. The tendency of neutron porosity to be slightly high in this borehole leads to higher calculated matrix porosity. In the Tptpmn, where the neutron porosity and volumetric water content are in better agreement, the matrix porosity is also in agreement, matching the OD porosity measurements quite well. Therefore, the model of matrix porosity is considered valid.

7.1.3 Matrix Porosity Validation Summary and Conclusions

Matrix porosity data, based on core samples from the Tptpul, Tptpmn, Tptpll, and Tptpln, are unavailable for most of the exploration boreholes. Petrophysical measurements of neutron porosity and bulk density are frequently more common and can be used to estimate matrix porosity using the formula given in Attachment I. Matrix porosity calculated with this approach is shown to provide satisfactory agreement with core measurements for the units of interest in two boreholes, USW SD-7 and USW SD-12. This validation provides confidence in the procedure for estimating matrix porosity based on petrophysical measurements. Further confidence is attained by recognizing that the equations developed in Attachment I simply account for the solid and liquid mass and pore volumes in the bulk rock mass.

7.2 PARAMETER VALIDATION: LITHOPHYSAL POROSITY

In order to validate lithophysal porosity, data from two boreholes (USW NRG-6 and USW H-6) are examined. Calculations of lithophysal porosity for the two lithophysal layers, Tptpul and Tptpll, as well as for the two nonlithophysal layers, Tptpmn and Tptpln, are examined. The calculated lithophysae porosities are compared with estimates obtained from a mapping of the

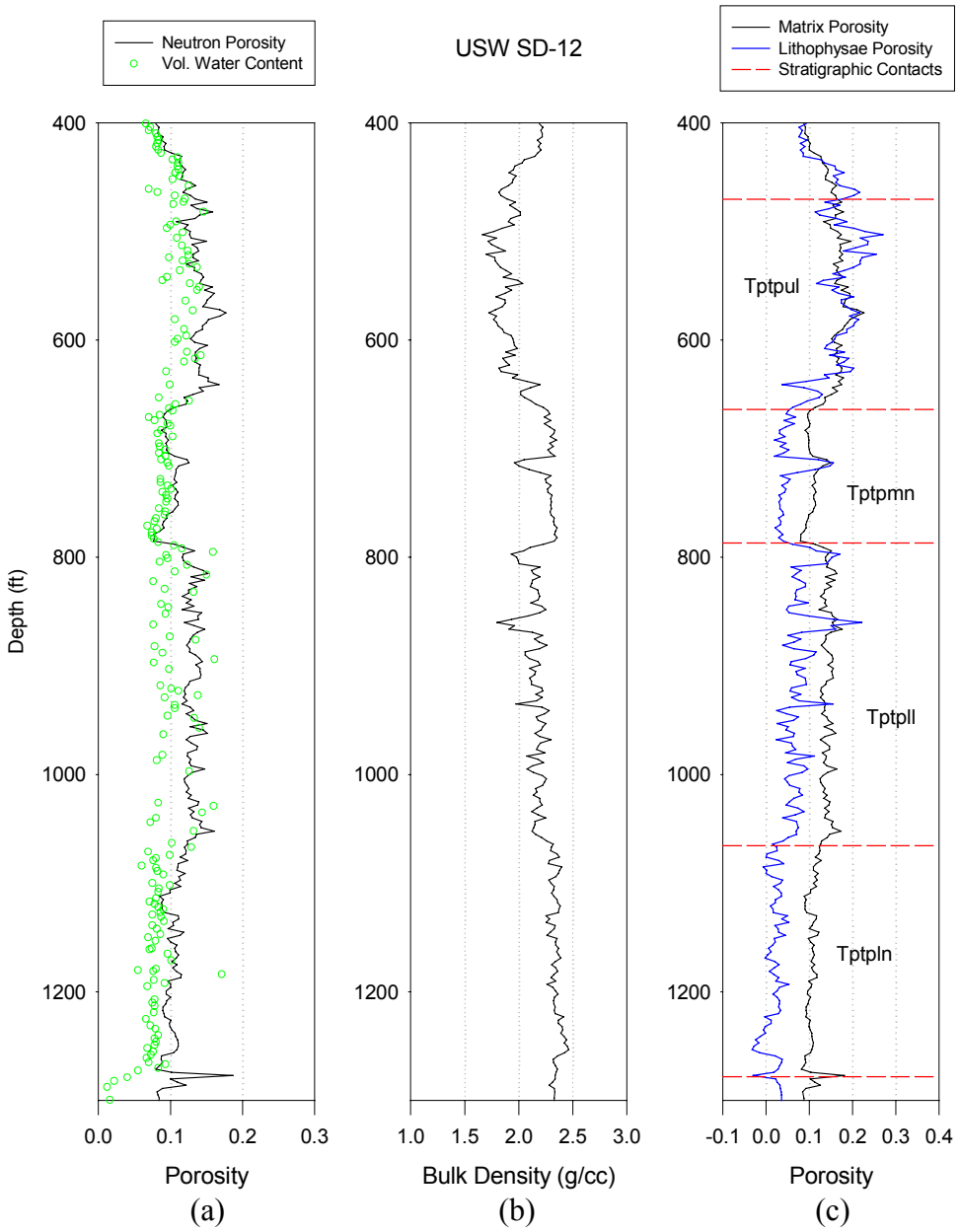

(a) (b) DTN: MO0010CPORGLOG.003 [155959]

(c) DTN: SN0208T0503102.007

Figure 7-3. USW SD-12 (a) (b) Core and Petrophysical Data; (c) Method B Porosity

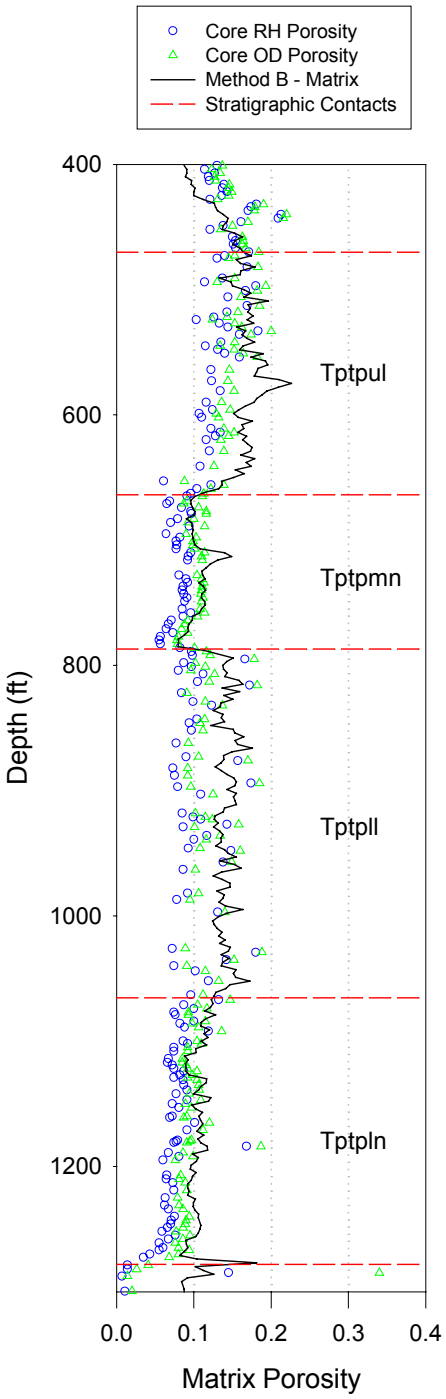

Core RH and OD: DTN: MO0109HYMXPROP.001 [155989], Method B matrix DTN: SN0208T0503102.007

NOTES: OD = oven dried, RH = relative humidity.

Figure 7-4. USW SD-12 Comparison of Core and Method B Matrix Porosity

ECRB Cross-Drift. Recent lithophysal porosity measurements, DTN: SN0205F3504502.010 [159144], obtained from video observation of lithophysae in boreholes drilled in support of the ECRB Thermal Conductivity Tests 1 and 3 (Howard 2002 [159152]) are also compared with geostatistically derived lithophysal porosity for each test site. Model validation criteria for lithophysal porosity will be met when the calculated values are found to be within one standard deviation of the observed or measured determinations of lithophysal porosity.

The data from the ECRB Cross-Drift mapping and the borehole video are not used to develop or calibrate the realizations of lithophysal porosity and, thus, provide an appropriate comparison for validation. The ECRB Cross-Drift is a 2.7-km-long, 5-m-diameter tunnel excavated entirely in the Topopah Spring Tuff (Mongano et al. 1999, p. 3 [149850]). The ECRB Cross-Drift begins in the upper-central portion of the upper lithophysal zone and descends geologically through all four lithostratigraphic units of interest before encountering a fault near the end of the drift. The Tptpul is exposed in the first kilometer (station 0+00 to 10+15) of the tunnel. The middle nonlithophysal zone, Tptpmn, is exposed over approximately 0.4 km (station 10+15 to 14+44) of the tunnel, while approximately 0.9 km of the tunnel (station 14+44 to 23+26) exposes the lower lithophysal zone, Tptpll. Between stations 23+26 and 25+85, the lower nonlithophysal zone, Tptpln, is exposed. The uppermost portion of the Tptpul is exposed at the end of the excavation (station 25+90 to 26+57.5) in the hanging wall of the eastern strand of the Solitario Canyon fault zone (SCFZ). Table 7-1 summarizes the four units and where they were encountered in the tunnel excavation.

The boreholes selected to validate lithophysal porosity, USW NRG-6 and USW H-6, were chosen because they are relatively close to the ECRB Cross Drift, as shown in Figure 4-1. USW NRG-6 is located near the beginning of the drift while USW H-6 is near the far end.

Table 7-1. ECRB Cross-Drift Tunnel: Lithostratigraphic Units and Stations

Unit	Stations
Tptpul	0+00 to 10+15 and 25+90 to 26+57.5
Tptpmn	10+15 to 14+44
Tptpll	14+44 to 23+26
Tptpln	23+26 and 25+85

Source: Mongano et al. 1999, Table 1 [149850]

Figure 7-5 illustrates the percentage of lithophysae mapped as a function of Cross Drift stationing. These data are based on 10-meter station increments and are adapted from Mongano et al. (1999, p. 77, Figure 13 [149850]). It is impossible to directly compare measurements of lithophysal porosity made in the ECRB with calculated values from nearby boreholes since the ECRB is oriented horizontally, and boreholes are, for the most part, vertical. It is possible to qualitatively compare general trends in lithophysal porosity observed in the ECRB with those observed in nearby boreholes. Furthermore, statistical comparisons of the different data sets permit one to draw conclusions regarding the quantitative value of the petrophysically derived values.

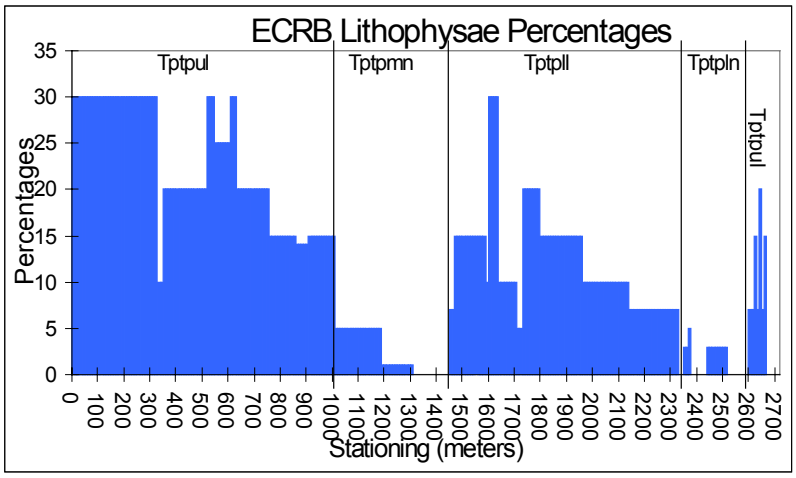

Source: Mongano et al. 1999, Figure 13 [149850]

Figure 7-5. ECRB Lithophysae Percentages versus Stationing

The data used in the construction of Figure 7-5 (DTN: GS991108314224.015) were processed using Microsoft Excel to calculate statistical measures (mean, median, standard deviation, minimum, and maximum) of the ECRB mapped lithophysal porosity for each of the four layers (DTN: SN0208T0503102.007). The ECRB statistics were then compared with statistics calculated for the petrophysically derived lithophysal porosities from the boreholes. This statistical comparison is provided in Tables 7-2 through 7-5, and a discussion follows. In addition, the general trends shown in Figure 7-5 were compared with those calculated from petrophysical data for each layer.

Table 7-2. Comparison of Tptpul Lithophysal Porosity Statistics for Boreholes USW H-6, USW NRG-6, and ECRB Cross-Drift Mapping

Tptpul Lithophysal Porosity			
	H-6[1]	NRG-6[1]	Mongano[2]
Mean	1.56E-01	1.39E-01	2.13E-01
Median	1.50E-01	1.57E-01	2.00E-01
Standard Deviation	6.76E-02	4.83E-02	7.51E-02
Minimum	2.68E-02	3.16E-02	0.00E+00
Maximum	2.96E-01	2.17E-01	3.00E-01

[1]DTN: SN0208T0503102.007; [2]DTN: GS991108314224.015

Table 7-3. Comparison of Tptpll Lithophysal Porosity Statistics for Boreholes USW H-6, USW NRG-6, and ECRB Cross-Drift Mapping

Tptpll Lithophysal Porosity			
	H-6[1]	NRG-6[1]	Mongano[2]
Mean	1.20E-01	8.80E-02	1.25E-01
Median	1.05E-01	8.38E-02	1.00E-01
Standard Deviation	7.14E-02	4.16E-02	5.57E-02
Minimum	7.89E-03	0.00E+00	5.00E-02
Maximum	3.18E-01	2.71E-01	3.00E-01

[1]DTN: SN0208T0503102.007; [2] DTN: GS991108314224.015

Table 7-4. Comparison of Tptpmn Lithophysal Porosity Statistics for Boreholes USW H-6, USW NRG-6, and ECRB Cross-Drift Mapping

Tptpmn Lithophysal Porosity			
	H-6[1]	NRG-6[1]	Mongano[2]
Mean	1.80E-02	3.91E-02	2.19E-02
Median	1.65E-02	3.81E-02	1.00E-02
Standard Deviation	1.25E-02	1.71E-02	2.27E-02
Minimum	0.00E+00	1.19E-02	0.00E+00
Maximum	6.65E-02	7.21E-02	5.00E-02

[1]DTN: SN0208T0503102.007; [2] DTN: GS991108314224.015

Table 7-5. Comparison of Tptpln Lithophysal Porosity Statistics for Borehole USW H-6 and ECRB Cross-Drift Mapping

Tptpln Lithophysal Porosity		
	H-6[1]	Mongano[2]
Mean	2.37E-02	1.30E-02
Median	2.15E-02	0.00E+00
Standard Deviation	1.63E-02	1.64E-02
Minimum	0.00E+00	0.00E+00
Maximum	5.24E-02	5.00E-02

[1]DTN: SN0208T0503102.007; [2] DTN: GS991108314224.015

Figure 7-5 illustrates the following general features (These observations are specific to the ECRB and may or may not be true at other locations within the mountain):

1. Lithophysal porosity in the upper part of the Tptpul (stations 25+90 to 26+57.5) has a lower value than the central and lower portions (0+00 to 10+44). Lithophysal porosity generally decreases with depth in the Tptpul to the contact with Tptpmn.

2. The lithophysal porosity in Tptpmn varies between 0 and 5 percent and decreases with depth.

3. The lithophysal porosity in the Tptpll is typically less than 20 percent, with a local region of 30 percent. Compared to the Tptpul, the lithophysal porosity is generally lower in the Tptpll. Lithophysal porosity also decreases in the Tptpll from near the center of the unit to its contact with the Tptpln.

4. Lithophysal porosity in the Tptpln varies between 0 and 5 percent.

7.2.1 USW H-6

Figures 7-6(a) and 7-6(b) show the neutron porosity and bulk density logs for USW H-6. Core data are not available for this borehole; therefore, Method B (Attachment I) is used to compute matrix and lithophysal porosity. The calculated values are shown in Figure 7-6(c).

In Figure 7-6(c), the location of the contacts between the lithophysal zones and the nonlithophysal zones are identified (Attachment IV). These contacts are not based on the calculated lithophysal porosity and, therefore, provide an independent basis for identifying the transition from one layer to the next. The lithophysal porosity calculated using petrophysical measurements is highly effective in identifying both the middle and lower nonlithophysal zones. Furthermore, the magnitude of the calculated lithophysal porosity for these zones is in good agreement with the data obtained from the ECRB (DTN: GS991108314224.015). Tables 7-4 and 7-5 compare the statistical properties of these layers. The mean lithophysal porosity in the Tptpmn for USW H-6 is 1.8 percent, compared with 2.2 percent from the ECRB. In the Tptpln, the mean is 2.4 percent, compared with 1.3 percent from the ECRB. The ECRB trend of lithophysal porosity decreasing with depth in the Tptpmn is not, however, observed in the calculated values for USW H-6.

Figure 7-6(c) and Table 7-2 show that the calculated lithophysal porosity for the Tptpul varies between 2.7 and 30 percent. Comparing lithophysae statistics in Table 7-2 results in a calculated mean of 15.6 percent for USW H-6 and 21.3 percent for the ECRB. The ECRB data, therefore, show a somewhat higher mean lithophysal porosity compared with the petrophysically derived mean value. The maximum lithophysal porosity for both data sets is 30 percent. There is also a general decrease in the lithophysal porosity of the Tptpul with depth over the bottom half of the layer. This is in agreement with the trend observed in Figure 7-5.

From Figure 7-6(c) and Table 7-3, the lithophysal porosity calculated for the Tptpll varies between approximately 1 and 32 percent, with a mean value of 12 percent. The ECRB data vary between 5 and 30 percent, with a mean lithophysal porosity of 12.5 percent. In the upper third of the Tptpll, the calculated lithophysal porosity varies between 10 and 30 percent, in the middle third it varies between 3 and 20 percent, and in the bottom third it varies between 0 and 14 percent. In the upper third there are two significant zones of higher lithophysal porosity. The calculated mean lithophysal porosity for the Tptpll is in good agreement with the ECRB data, and the trend of decreasing porosity with depth is observed in both data sets.

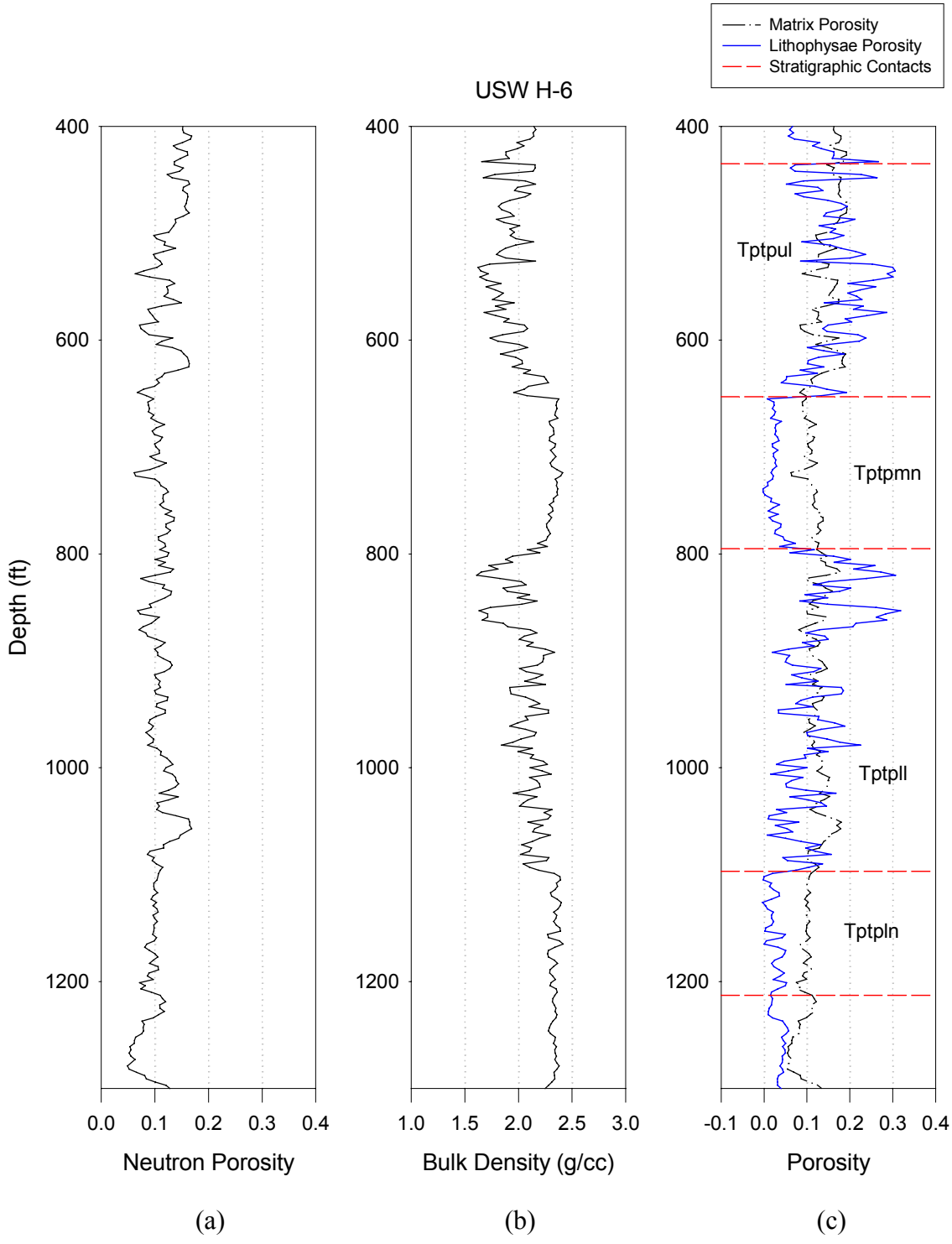

DTN: MO0010CPORGLOG.002 [155229], SN0208T0503102.007

Figure 7-6. USW H-6 (a) (b) Petrophysical Data; (c) Method B Porosity

7.2.2 USW NRG-6

USW NRG-6 has volumetric water content and matrix porosity available from core samples as well as neutron porosity and bulk density measurements. Calculation Method A is, therefore, applied to compute lithophysal porosity for this borehole (Section 6.1.4). For comparison, matrix and lithophysal porosity are also calculated and examined using Method B.

The neutron porosity and bulk density logs for USW NRG-6 are shown in Figure 7-7(a) and 7-7(b), respectively. Neutron porosity agrees well with the volumetric water content from core measurements, as shown in Figure 7-7(a). The calculated matrix and lithophysae porosities presented in Figure 7-7(c) are derived from neutron porosity and bulk density measurements using Method B. Figure 7-8(a) shows the RH and OD core matrix porosity data available for this borehole. Included for comparison in this figure is matrix porosity, calculated using Method B. The Method B calculations of matrix porosity underestimate the core data in the upper half of the Tptpul but are in good agreement with the core data throughout the Tptpmn and the Tptpll. Figure 7-8(b) compares lithophysal porosity, calculated using both Method A and Method B. The Method B calculations of lithophysal porosity are slightly greater than the Method A calculations in the upper portion of the Tptpul. This is the same portion in which matrix porosity is slightly underestimated using Method B.

The remaining discussion for USW NRG-6 pertains to the Method A lithophysal porosity calculations. Of the two methods of calculating lithophysal porosity, Method A is believed to be more accurate since laboratory core measurements of matrix porosity are often more reliable than well-log neutron porosity measurements.

In Figure 7-8(b) the Tptpul-Tptpmn contact in this borehole is easily identified. However, the Tptpmn–Tptpll contact is less well defined. From Figure 7-8(b), the calculated lithophysal porosity in the Tptpmn varies in the 1 to 2 percent range over the top half of the layer with somewhat higher values, up to 7 percent, over the bottom half of the layer. The mean calculated lithophysal porosity is 3.9 percent compared to 2.2 percent from the ECRB data set, as summarized in Table 7-4. Similar to USW H-6, there is no discernable decrease in lithophysal porosity with depth in the Tptpmn. There are no petrophysical measurements for the lower nonlithophysal unit for this borehole since the borehole was not drilled into this layer.

In the upper lithophysal unit, Tptpul, the predicted lithophysal porosity over much of the top half of the unit is fairly constant at 17 percent (plus or minus 3 percent) and steadily decreases to about 5 percent at contact with the Tptpmn. The overall decrease from the middle of the Tptpul to contact with the Tptpmn is consistent with the observations in the ECRB. The calculated mean lithophysal porosity for the Tptpul (Table 7-2) was 13.9 percent compared to 15.6 percent from USW H-6 and 21.3 percent from the ECRB.

In the lower lithophysal unit, Tptpll, the calculated lithophysal porosity varies between 0 and 27 percent compared to data from the ECRB (DTN: GS991108314224.015) values of 5 to 30 percent (Table 7-3). The mean calculated lithophysal porosity in the Tptpll is 8.8 percent, compared to 12 percent in USW H-6 and 12.5 percent from the ECRB.

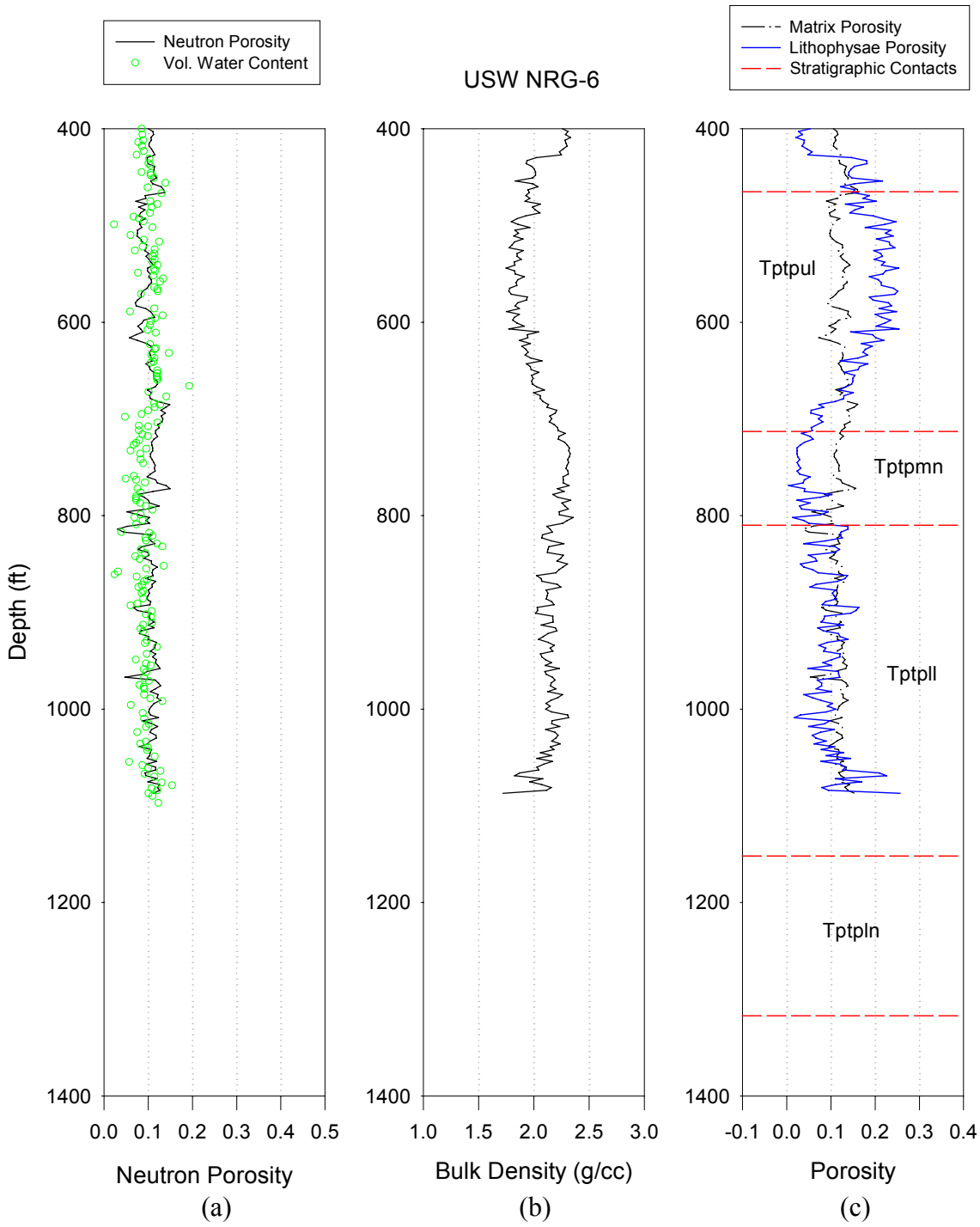

DTN: MO0010CPORGLOG.003 [155959], SN0208T0503102.007

Figure 7-7. USW NRG-6 (a) (b) Core and Petrophysical Data; (c) Method B Porosity

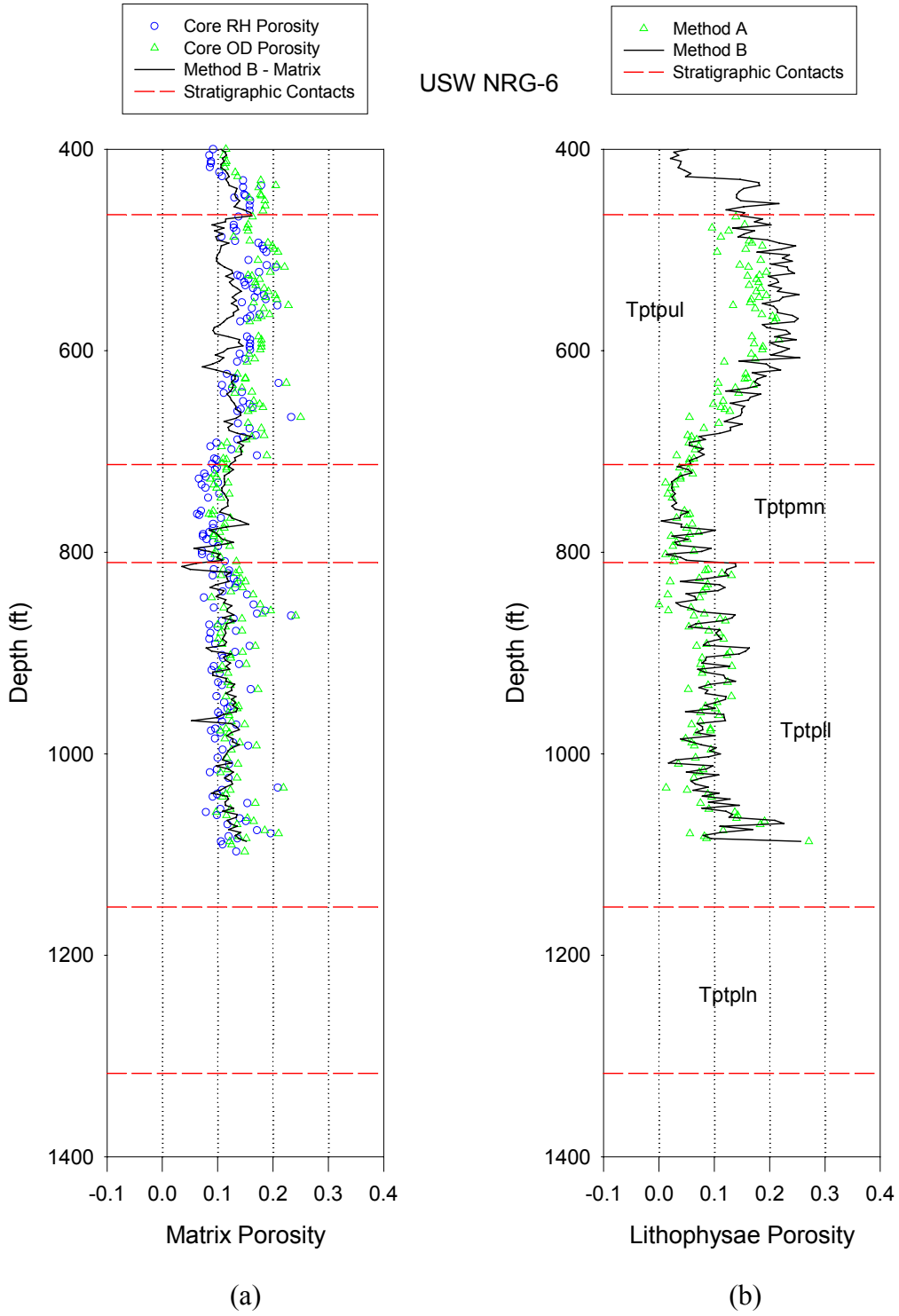

NOTES: OD = oven dried, RH = relative humidity.

DTN: MO0109HYMXPROP.001 [155989], SN0208T0503102.007

Figure 7-8. USW NRG-6 (a) Core and Method B Matrix Porosity; (b) Method A and Method B Lithophysal Porosity

7.2.3 Lithophysal Porosity in Thermal Conductivity Test Areas

In this section, lithophysal porosity data (DTN: SN0205F3504502.010 [159144]) are examined based on video recording of lithophysae features in the boreholes drilled in support of thermal conductivity field tests: ECRB Thermal Conductivity Tests 1 and 3 (Howard 2002 [159152]). A total of five boreholes were examined for this evaluation: ECRB-THERMK-001 and ECRB-THERMK-002 for the ECRB Thermal Conductivity Test 1, and ECRB-THERMK-009, ECRB-THERMK-010, and ECRB-THERMK-011 for ECRB Thermal Conductivity Test 3.

Both tests were performed in the Tptpll and are similar in construction (Howard 2002 [159152]). In ECRB Test 1, the holes ECRB-THERMK-001 (for the heater element) and ECRB-THERMK-002 (for the thermocouple assembly) are oriented perpendicularly to each other and are separated in elevation by approximately 0.1 m. Figure 7-9 illustrates the heater and thermocouple arrangement used in the two-hole heater test performed in the lower lithophysal unit. The heater, 5 m in length, was inset 3 m from the ECRB drift wall. A 5-m-long array of 30 thermocouples was placed in a second borehole.

In ECRB Test 3, ECRB-THERMK-009 (the heater element) is located between and oriented perpendicularly to the two boreholes, ECRB-THERMK-010 and ECRB-THERMK-011, containing the thermocouple assemblies. Approximately 0.4 m of distance separates the central borehole, ECRB-THERMK-009, from the other two holes. In the plan view ECRB-THERMK-010 and ECRB-THERMK-011 overlay each other. The locations and mean lithophysal porosities are presented for each of the holes in Table 7-6.

The mean lithophysal porosity data from the borehole video are compared with predictions based on the geostatistically derived realizations. To perform this comparison it is necessary to determine the discretized grid element in which the borehole resides. The resolution of the grid elements is 50 m x 50 m x 4.57 m in the Tptpll (Table 6-2). This is accomplished by first converting the borehole coordinates into stratigraphic coordinates as discussed in Section 6.1.2. Using these coordinates, the utility software POINT (Table 3-1; POINT V. 1.0, STN: 10826-1.0-00 [158336]) locates the desired grid element and then reports the parameter values for all 50 realizations. Statistical measures of the resulting data are used to characterize the local expected value and uncertainty of the lithophysal porosity model. Figures 7-10 and 7-11 illustrate the histograms for lithophysal porosity at each test location, along with relevant statistics for each data set.

For ECRB Test 1, the mean lithophysae porosities for ECRB-THERMK-001 and ECRB-THERMK-002 were 8.1 percent and 18.9 percent, respectively (Table 7-6). The large difference in mean values for these boreholes illustrates the possible variability of lithophysal porosity over relatively short distances. It is also plausible that the interval over which the video was taken is insufficient to obtain a statistically representative sample of the lithophysae. The geostatistically derived mean lithophysal porosity for the ECRB Test 1 site was 11.6 percent, with a standard deviation of 5.6 percent. For the 50 realizations the lithophysal porosity ranged from a minimum value of 2.1 percent to a maximum of 26.5 percent (Figure 7-10).

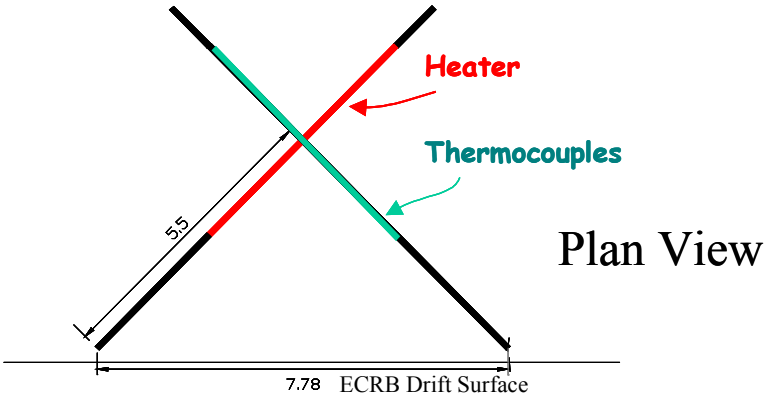

Source: Howard 2002, p. 38 [159152]

Figure 7-9. ECRB Thermal Conductivity Test 1 Layout

Table 7-6. Borehole Locations and Mean Lithophysal Porosity for ECRB Thermal Conductivity Tests 1 and 3

Borehole	Northing[1] m	Easting[1] m	Elevation[1] m	ECRB Station[1] m	Mean Lithophysal Porosity[2] %
ECRB-THERMK-001	233311.0	170706.1	1107.8	15+62.2	8.1
ECRB-THERMK-002	233305.8	170700.2	1107.9	16+69.9	18.9
ECRB-THERMK-009	233195.7	170573.7	1109.3	17+37.7	24.8
ECRB-THERMK-010	233190.6	170567.9	1109.6	17+45.4	20.0
ECRB-THERMK-011	233190.7	170567.8	1109.1	17+45.5	31.5

[1]Survey data provided by DTN: MO0205GSC02070.000 [159148]
[2]Lithophysal porosity data provided by DTN: SN0205F3504502.010 [159144]

For ECRB Test 3, the mean lithophysal porosity for ECRB-THERMK-009 was 24.8 percent, for ECRB-THERMK-010 the mean was 20 percent, and for ECRB-THERMK-011 the mean was 31.5 percent (Table 7-6). Similar to ECRB Test 1, the mean lithophysal porosity shows variability. The geostatistically derived mean lithophysal porosity for this test site was 15.6 percent, with a standard deviation of 7.7 percent. For all 50 realizations, lithophysal porosity ranged from a minimum value of 4.5 percent to a maximum of 33.7 percent (Figure 7-11).

At both test site locations, the histogram plots show a high degree of uncertainty in model predictions of lithophysal porosity. The model predictions are somewhat lower at ECRB Test 1 than at ECRB Test 3, which is consistent with the video logs.

7.2.4 Lithophysal Porosity Validation Summary and Conclusions

Lithophysal porosity for the four layers (Tptpul, Tptpmn, Tptpll, and Tptpln) was calculated for borehole USW H-6 and for Tptpul, Tptpmn, and Tptpll in borehole USW NRG-6. These calculations, based on mass conservation equations developed in Attachment I, are compared with estimates of lithophysal porosity made in the ECRB Cross-Drift (DTN: GS991108314224.015).

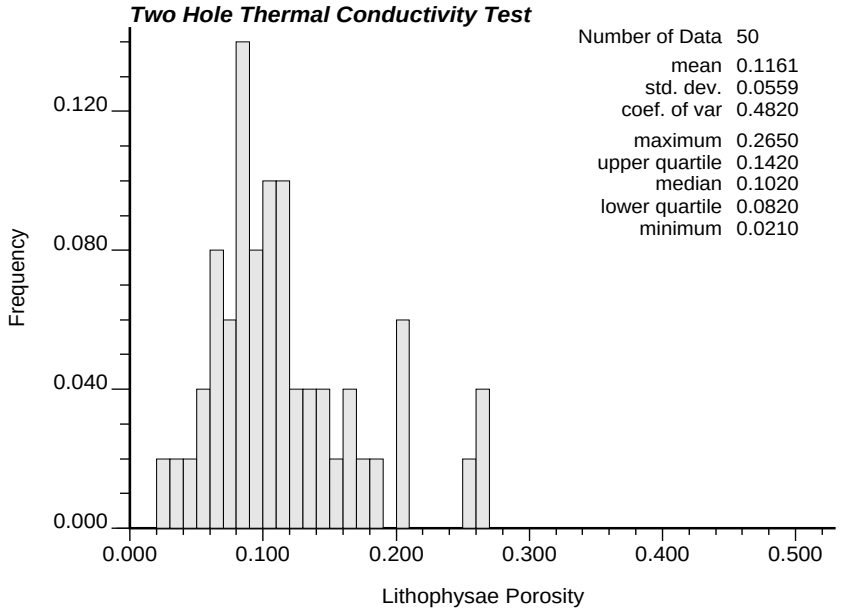

DTN: SN0208T0503102.007

Figure 7-10. Model Prediction of Lithophysal Porosity at Site of ECRB Thermal Conductivity Test 1

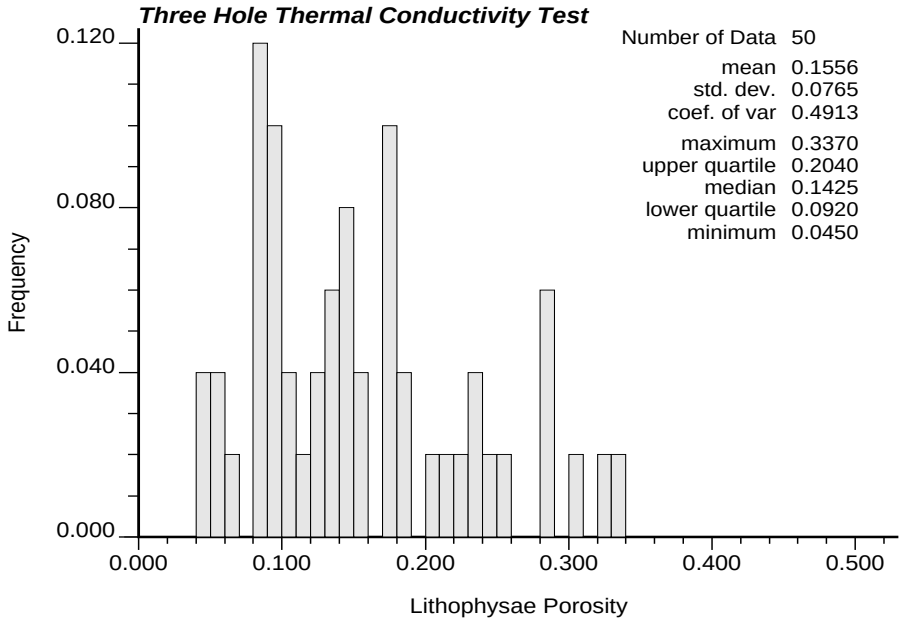

DTN: SN0208T0503102.007

Figure 7-11. Model Prediction of Lithophysal Porosity at Site of ECRB Thermal Conductivity Test 3

The two methods used to calculate lithophysal porosity were both found to be consistent with the independently identified lithostratigraphic contacts. This statement is true for nearly all boreholes used in this study and can be verified by examining the data presented in

Attachment II. General trends and the overall magnitude of lithophysal porosity derived through petrophysical measurement were found to agree reasonably well with those observed in the ECRB (DTN: GS991108314224.015). Differences are primarily in magnitude and are likely due to measurement error, differences in scale, and natural spatial variations. Substantial variations in lithophysal porosity over short distances are apparent in all sources of data.

Geostatistically derived values of lithophysal porosity are also compared to data obtained from video observations (DTN: SN0205F3504502.010 [159144]) of five boreholes drilled for the ECRB Thermal Conductivity Tests 1 and 3 (Howard 2002 [159152]). The video data fall within the range of values predicted by the model, and the high degree of spatial variability demonstrated by the video data supports the large range of possible values predicted by the model and the underlying model uncertainty at both locations.

7.3 MODEL VALIDATION: MATRIX THERMAL CONDUCTIVITY

To validate the matrix thermal conductivity model, a comparison of experimental measurements is made with the geostatistically derived realizations of matrix thermal conductivity. The experimental data used in this comparison are not used to calibrate the model or to condition the geostatistic realizations. These data are, therefore, appropriate for model validation. The data consist of 10 samples acquired from Alcove 7 (DTN: SNL22100196001.002 [153138]) and 20 samples acquired from the Drift Scale Test area in Alcove 5 (DTN: SNL22100196001.001 [109733]). The Alcove 7 samples were measured under OD conditions at 110°C, and the Alcove 5 samples were measured after being saturated with water at 70°C. Model predictions under both wet and dry conditions are, therefore, examined in this validation exercise. The matrix thermal conductivity model will be considered valid if the modeled values are found to be within one standard deviation of measured values of matrix thermal conductivity.

To compare laboratory experimental results with model predictions, it is first necessary to determine the discretized grid element in which the core sample resides. This is accomplished by first converting the sample coordinates into stratigraphic coordinates as discussed in Section 6.1.2. Using these coordinates, the utility software POINT (Table 3-1) locates the desired grid element and then reports the parameter values for this element for all realizations. Statistical measures of the resulting output are used to characterize the models' local expected value and local uncertainty.

Both Alcove 5 and Alcove 7 are located within the middle nonlithophysal zone, Tptpmn. The conversion to stratigraphic coordinates thus requires estimates of the upper and lower lithostratigraphic contacts for the Tptpmn. The required inputs and the computed stratigraphic elevations are tabulated in Table 7-7.

Table 7-7. Stratigraphic Coordinates of Alcove 5 and Alcove 7 Core Samples

Location	Northing [1] (feet)	Easting [1] (feet)	Elevation [1] (feet)	Top of Tptpmn [2] (feet)	Bottom of Tptpmn [2] (feet)	Stratigraphic Elevation (feet)
End centerline (face) at invert of the Alcove 5 Turnaround Niche	767869.9	562125.8	3489.5	3516.2	3397.9	92.9
Right Rib Alcove 7, Station 0+88, on invert[3]	760592.0	561952.6	3610.6	3680.3	3543.8	58.7

1. Survey data provided by DTN: MO0205GSC02068.000 [159147]
2. Lithostratigraphic contacts derived from the Geologic Framework Model (GFM 2000) (DTN: MO0012MWDGFM02.002 [153777]).
3. Location data Alcove 7 samples provided by YMP 1997 [159151].

Histogram plots of matrix thermal conductivity, specific to the coordinates provided in Table 7-7, are presented in Figure 7-12. These plots show model predictions of matrix thermal conductivity from all 50 realizations for the discretized locations that represent Alcove 5 and Alcove 7. In Figure 7-12(a), the water saturated (wet) matrix thermal conductivity for Alcove 5 is presented, and in Figure 7-12(b), the OD (dry) matrix thermal conductivity for Alcove 7 is presented. At both locations the spread in the data is rather broad, reflecting a high degree of uncertainty in the model predictions of matrix thermal conductivity at these particular locations.

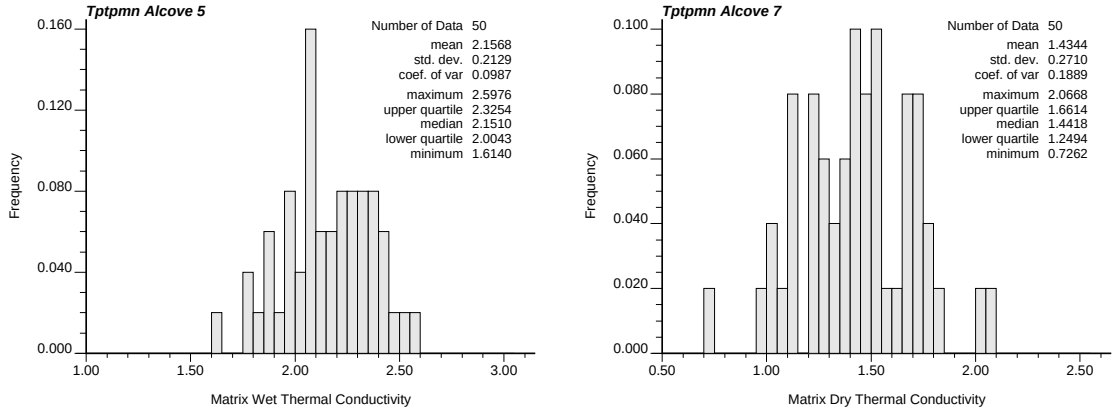

(a) (b)

DTN: SN0208T0503102.007

Figure 7-12. Model Predictions of Matrix Thermal Conductivity (W m^{-1} K^{-1}) at (a) Alcove 5 and (b) Alcove 7

The laboratory measurements from both Alcove 5 and Alcove 7 are fairly consistent across all specimens. Consequently, the specimen means may be interpreted as the "true" value of matrix thermal conductivity at their respective locations. These mean values and their associated standard deviations are given in Table 7-8.

Table 7-8. Statistical Measures of Alcove 5 and Alcove 7 Thermal Conductivity Measurements

Location	Number of Samples	Mean Thermal Conductivity ($W m^{-1} K^{-1}$)	Standard Deviation ($W m^{-1} K^{-1}$)
Alcove 5	20	2.1 (wet)	0.1
Alcove 7	10	1.66 (dry)	0.01

DTN: SNL22100196001.001 [109733], SNL22100196001.002 [153138]).

Comparisons of the experimentally derived mean values with the model predictions are quite good. In the case of Alcove 5, the experimental value of 2.1 is nearly equal to the mean prediction of 2.16 (Figure 7-12(a)). For Alcove 7, the experimental value of 1.66 is equal to the lower bound of the upper quartile and is also within one standard deviation, 0.27, of the mean, 1.43 (Figure 7-12(b)).

7.3.1 Matrix Thermal Conductivity Model Validation Summary and Conclusions

Experimental thermal conductivity measurements of samples extracted from Alcoves 5 and 7 are compared with model predictions of wet and dry thermal conductivity. At both locations, the range in predictions is quite broad, indicating a relatively high level of model uncertainty. Measurements from Alcove 5 are nearly equal to the mean prediction, and measurements from Alcove 7 are within one standard deviation of the mean; therefore, the matrix thermal conductivity model satisfies the validation criterion.

7.4 MODEL VALIDATION: BULK THERMAL CONDUCTIVITY

To validate the bulk thermal conductivity model, predictions of bulk thermal conductivity at the approximate locations of the ECRB Thermal Conductivity Test 1 and Test 3 (Howard 2002 [159152]) are compared with experimentally derived values from these tests results. The model will be considered valid if the difference between the modeled values are found to be within one standard deviation of measured values of bulk thermal conductivity.

7.4.1 ECRB Thermal Conductivity Tests 1 and 3

Figure 7-9 illustrates the heater and thermocouple arrangement used in ECRB Thermal Conductivity Test 1 (Howard 2002 [159152]) performed in the lower lithophysal unit, Tptpll. The heater, 5 m in length, was inset 3 m from the ECRB drift wall. A 5-m-long array of 30 thermocouples was placed in a second borehole. The thermocouple borehole was located 12 cm above the heater borehole. The thermocouple and heater boreholes were oriented to be perpendicular to each other. Insulation was placed in front of and after the heater and thermocouple assemblies to prevent heat loss from the boreholes. The data available from the test consist of temperatures as a function of time at the thermocouple locations.

ECRB Thermal Conductivity Test 3 (Howard 2002 [159152]) is very similar to Test 1. In this test, two boreholes were drilled for emplacement of thermocouple assemblies. The thermocouple boreholes were drilled approximately 0.4 m above (ECRB-THERMK-010) and below (ECRB-THERMK-011) the heater borehole (ECRB-THERMK-009). Each thermocouple assembly consisted of 30 thermocouples.

The heater assembly used in the ECRB Thermal Conductivity Tests can be mathematically represented as a finite line heat source. The temperatures around a finite-length line source heater may be computed by representing the heater as a series of small overlapping spheres, each with a diameter equal to the borehole diameter. Using the principle of superposition (Carslaw and Jaeger 1959, p. 262 [100968]), the temperature at a specified time and location is calculated by summing the contributions from each sphere. Under the assumption that heat conduction is the only significant mode of heat transfer and that the rock is both homogeneous and isotropic, the temperature at any distance from a heated sphere can be calculated using Equation 7-1 (Carslaw and Jaeger 1959, p. 248, Equation 4 [100968]).

$$v = \frac{a^2 F_0}{Kr}\left\{ erfc\frac{r-a}{2(kt)^{1/2}} - \exp\left[\frac{r-a}{a} + \frac{kt}{a^2}\right] erfc\left[\frac{r-a}{2(kt)^{1/2}} + \frac{(kt)^{1/2}}{a}\right]\right\} \qquad \text{(Eq. 7-1)}$$

where:

v = Temperature (K)
a = Radius of sphere (m)
F_0 = Heat flux at surface of sphere (W/m^2)
K = Thermal conductivity (W/mK)
r = Distance from center of sphere to measurement point (m)
k = Thermal diffusivity (m^2/s)
t = Time (s).

A total of 1,312 spheres were used to represent the 5-m-long heater element. The average measured heat output was 433W in Test 1 (DTN: SN206F3504502.012 [159145]) and 505.5W in Test 3 (DTN: SN0265F3504502.013 [159146]), and the radius of each borehole was 0.0381 m (1.5 in). Table 7-9 summarizes the values of bulk thermal conductivity determined for each thermocouple string.

Table 7-9. Summary of Results of ECRB Thermal Conductivity Tests 1 and 3

Test	Borehole	Bulk Thermal Conductivity (W/mK)
1	ECRB-THERMK-002	1.74[1]
3	ECRB-THERMK-010 ECRB-THERMK-011	1.74[2]

1. Data provided by DTN: SN206F3504502.012 [159145]
2. Data provided by DTN: SN0265F3504502.013 [159146]. A single value of thermal conductivity was calculated using data from both ECRB-THERMK-010 and ECRB-THERMK-011.

Following the procedures described in Section 6.1.8, values of wet and dry bulk thermal conductivity were obtained for all 50 realizations at both test locations. Histogram plots of these data are presented in Figures 7-13(a) and (b) and 7-14(a) and (b) for Tests 1 and 3, respectively.

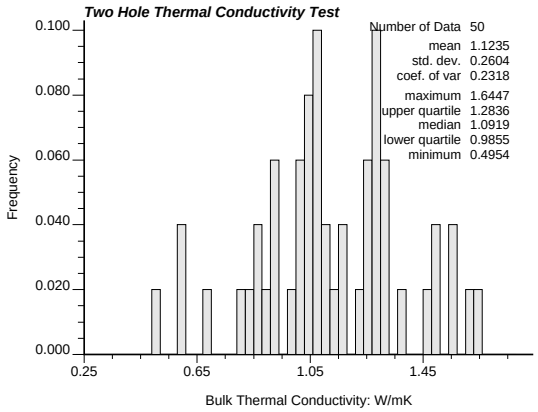

(a) dry

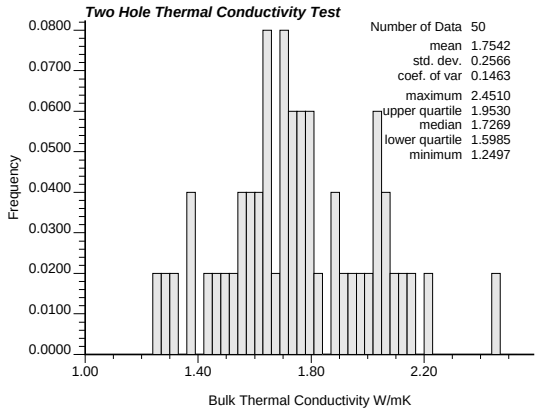

(b) wet

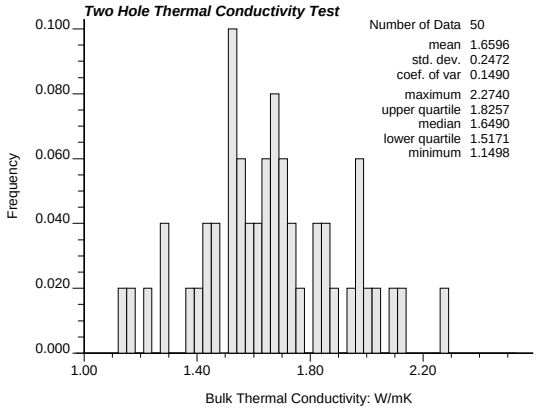

(c) 85% saturation

DTN: SN0208T0503102.007

Figure 7-13. Model Predictions of Bulk Thermal Conductivity (W/mK) ECRB Thermal Conductivity Test 1

To allow comparison of the experimental results given in Table 7-9 with the model predictions, an equation for bulk thermal conductivity can be derived that accounts for the influence of liquid saturation in the matrix. Expressions for wet and dry bulk thermal conductivity are obtained by substituting the appropriate wet or dry matrix thermal conductivity (k_m^{wet}, k_m^{dry}) into Equation 6-10.

$$k_b^{wet} = \phi_L k_a + (1-\phi_L) k_m^{wet} \quad \text{(Eq. 7-2)}$$

$$k_b^{dry} = \phi_L k_a + (1-\phi_L) k_m^{dry} \quad \text{(Eq. 7-3)}$$

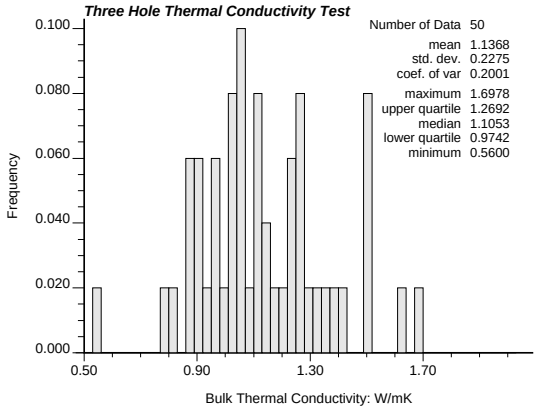

(a) dry

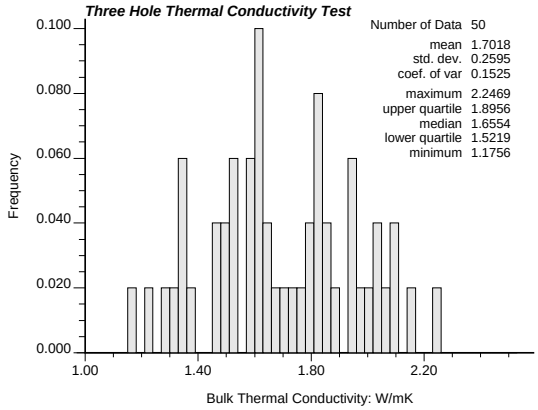

(b) wet

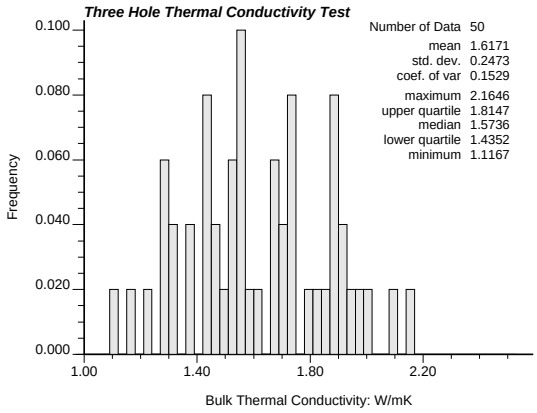

(c) 85% saturation

DTN: SN0208T0503102.007

Figure 7-14. Model Predictions of Bulk Thermal Conductivity (W/mK) ECRB Thermal Conductivity Test 3

In the absence of data for intermediate saturation states, the matrix thermal conductivity, k_m, was taken to be a linear function of the matrix water saturation, S_w, to perform this validation.

$$k_m = k_m^{dry} + S_w (k_m^{wet} - k_m^{dry}) \quad \text{(Eq. 7-4)}$$

Substituting Equation 7-4 into Equation 6-10 gives:

$$k_b = \varphi_L k_a + (1 - \varphi_L)\left\{k_m^{dry} + S_w \left(k_m^{wet} - k_m^{dry}\right)\right\} \quad \text{(Eq. 7-5)}$$

Using Equation 7-3 allows Equation 7-5 to be written as:

$$k_b = k_b^{dry} + S_w (1 - \phi_L)\left(k_m^{wet} - k_m^{dry}\right) \quad \text{(Eq. 7-6)}$$

Solving Equations 7-2 and 7-3 for the term $\left(k_m^{wet} - k_m^{dry}\right)$ and substituting the result into Equation 7-6 gives the mathematical relationship for bulk thermal conductivity in terms of matrix water saturation and wet and dry bulk thermal conductivity.

$$k_b = k_b^{dry} + S_w\left(k_b^{wet} - k_b^{dry}\right) \qquad \text{(Eq. 7-7)}$$

In order to use Equation 7-7, a value of matrix water saturation representative of the field experiments must be chosen. Since test-site-specific matrix water saturation information was not available, data from core samples taken from the Tptpll were examined (DTN: MO0109HYMXPROP.001 [155989] and DTN: GS980808312242.014 [106748]). A histogram plot of the matrix water saturation based on these core samples is presented in Figure 7-15. Note that the Tptpll is generally highly saturated. Consequently, for the purpose of evaluating Equation 7-7, a representative matrix water saturation of 0.85 is chosen for both tests.

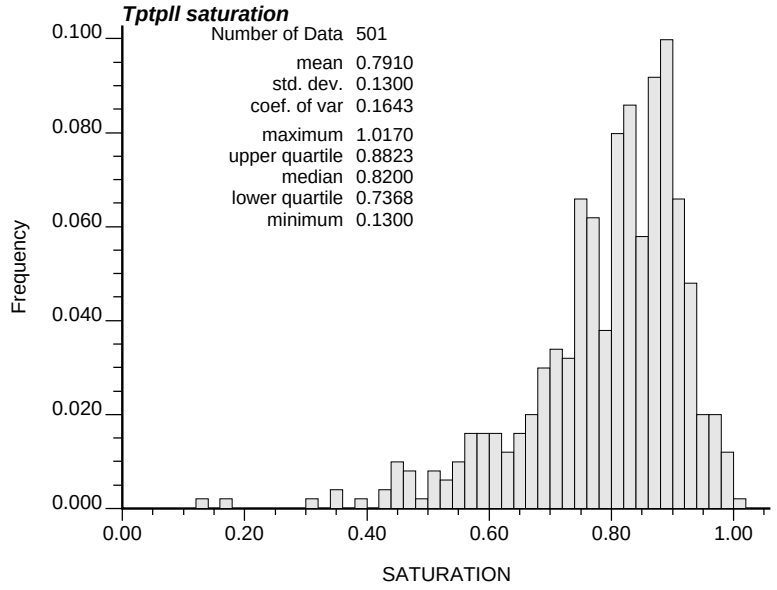

DTN: SN0208T0503102.007, MO0109HYMXPROP.001 [155989], and GS980808312242.014 [106748]

Figure 7-15. Histogram Plot of Matrix Water Saturation in the Tptpll

Applying Equation 7-7 to the model-predicted pairs of wet and dry bulk thermal conductivity provides values of bulk thermal conductivity that can be compared directly with those calculated from the field experiments (Table 7-9). These predictions are presented in the form of histograms in Figures 7-13(c) and 7-14(c).

For Test 1, the mean predicted bulk thermal conductivity at 85 percent saturation was 1.66 W/mK, with a standard deviation of 0.25 W/mK (Figure 7-13(c)), which is reasonably close to the experimental value of 1.74 W/mK. For Test 3, the mean predicted bulk thermal conductivity was 1.62 W/mK with a standard deviation of 0.25 W/mK, which is also reasonably close to the reported experimental value of 1.74 W/mK. In both cases the experimental values

fall within the range of predicted values and also within one standard deviation of the mean predictions (Figures 7-13 and 7-14).

7.4.2 Bulk Thermal Conductivity Model Validation Summary and Conclusions

Bulk thermal conductivity estimates from the ECRB Thermal Conductivity Tests 1 and 3 were compared with geostatistically derived estimates for the two sites. At both test locations, the range in predictions is quite broad, indicating a relatively high level of model uncertainty. The experimentally derived bulk thermal conductivity values fall within the range of model uncertainty and are also within one standard deviation of the model's mean predictions.

7.5 MODEL RESULTS AND DISCUSSION

The principal results of this study are the 3-D bulk thermal conductivity fields developed for four lithostratigraphic units of the Tpt. The spatial variability and uncertainty of this property is characterized using a total of 50 equally likely stochastic realizations. Each realization consists of a 3-D, discrete set of five rock properties (matrix porosity, lithophysal porosity, dry bulk density, wet bulk thermal conductivity, and dry bulk thermal conductivity) and four intermediate model parameters (matrix solid thermal conductivity, matrix solid connectivity, wet matrix thermal conductivity, and dry matrix thermal conductivity). At each node within the computational grid, these nine different model parameters and rock properties are developed such that they are both mathematically and physically consistent. Statistical summaries of model results are also provided, which may be used in analyses that do not require spatial heterogeneities.

7.5.1 Expected Value and Uncertainty

The spatially dependent expected value and uncertainty of modeled rock properties are estimated by computing the mean and the standard deviation of all 50 realizations at each node in the computational mesh. The resulting field of mean values represents the conditional expectation of central tendency and is referred to as the Etype V. 2.01 (Etype V. 2.01, STN: 10731-2.01-00 [159417]) estimate (Deutsch and Journel 1992, pp. 76 and 225 [100567]). The standard deviation is a familiar statistical property, used here to measure model uncertainty. Expected value and uncertainty models were generated for each of the nine properties modeled using the software Etype V. 2.01 (Table 3-1).

Surface diagrams of the expected value of dry and wet bulk thermal conductivity are presented in Figures 7-16 and 7-17, respectively, presented at the end of this section. The definition of the data used to provide these "dry" and "wet" thermal conductivity representations is presented in Attachment III. Each figure presents the results of all four lithostratigraphic units studied in the stratigraphic coordinate system. From the diagrams it is clear that bulk thermal conductivity is substantially less in the lithophysal zones (Tptpul, Tptpll) than in the nonlithophysal zones (Tptpmn, Tptpln), confirming the anticipated influence of lithophysae on thermal conductivity. Noting the change in scale between Figures 7-16 and 7-17, it is clear that bulk thermal conductivity depends on water saturation. There is some evidence of slightly lower values in the southern portions of the nonlithophysal zones, but the differences are not great.

Etype V. 2.01 models inherently reproduce values at the location of measured data. However, these models generally do not reproduce the univariate statistical characteristics or spatial correlation of the same measured data. Averaging across replicate simulations creates a univariate distribution that is, for the most part, void of the tails in the underlying distributions and compressed towards the mean. Etype V. 2.01 models also typically grade smoothly and continuously from one measured value to the next (in three dimensions). Thus, the spatial continuity of the Etype V. 2.01 model is naturally much greater than that observed in the data themselves. This is the so-called smoothing effect that is typical of virtually all interpolation (in contrast to simulation) algorithms, including kriging, nearest-neighbor estimation, and inverse-distance-to-a-power weighting methods.

The spatial uncertainty of dry and wet bulk thermal conductivity is presented in Figures 7-18 and 7-19, respectively. Interestingly, the uncertainty in the Etype V. 2.01 model is slightly greater in the nonlithophysae zones than in the lithophysae zones. This indicates that the uncertainties in matrix thermal conductivity are, for the most part, controlling the uncertainty of bulk thermal conductivity. This conclusion is based on the observation that the standard deviation of bulk thermal conductivity is approximately the same (0.25 Wm-1K-1) in both the lithophysae and the nonlithophysae zones (Table 7-10). Because the uncertainty in lithophysal porosity is lower in the nonlithophysae zones, one would expect the uncertainty in bulk thermal conductivity to be lower in the nonlithophysae zones as well. Since this is not the case, it may be concluded that uncertainty in lithophysal porosity does not play a significant role in the uncertainty estimate of bulk thermal conductivity. Furthermore, since the particular model of bulk thermal conductivity used in this report is only dependent on two uncertain inputs, lithophysal porosity and matrix thermal conductivity, the latter must be dominating to some extent. This conclusion may not be valid for other models of bulk thermal conductivity.

In the lithophysae zones there is some evidence of reduced uncertainty near the location of boreholes; however, there is little evidence of this in the nonlithophysae zones. A likely explanation is that the realizations of matrix thermal conductivity are largely unconditioned. Of the three spatially dependent inputs to the matrix thermal conductivity model, only matrix porosity is conditioned to field measurements. The other two matrix thermal conductivity parameters (solid thermal conductivity, k_s, and solid connectivity, γ_c) are simulated unconditionally. In addition, the parameter distributions that characterize the latter two parameters are rather broad, demonstrating a high degree of model uncertainty (Section 6.1.7, Figure 6-11).

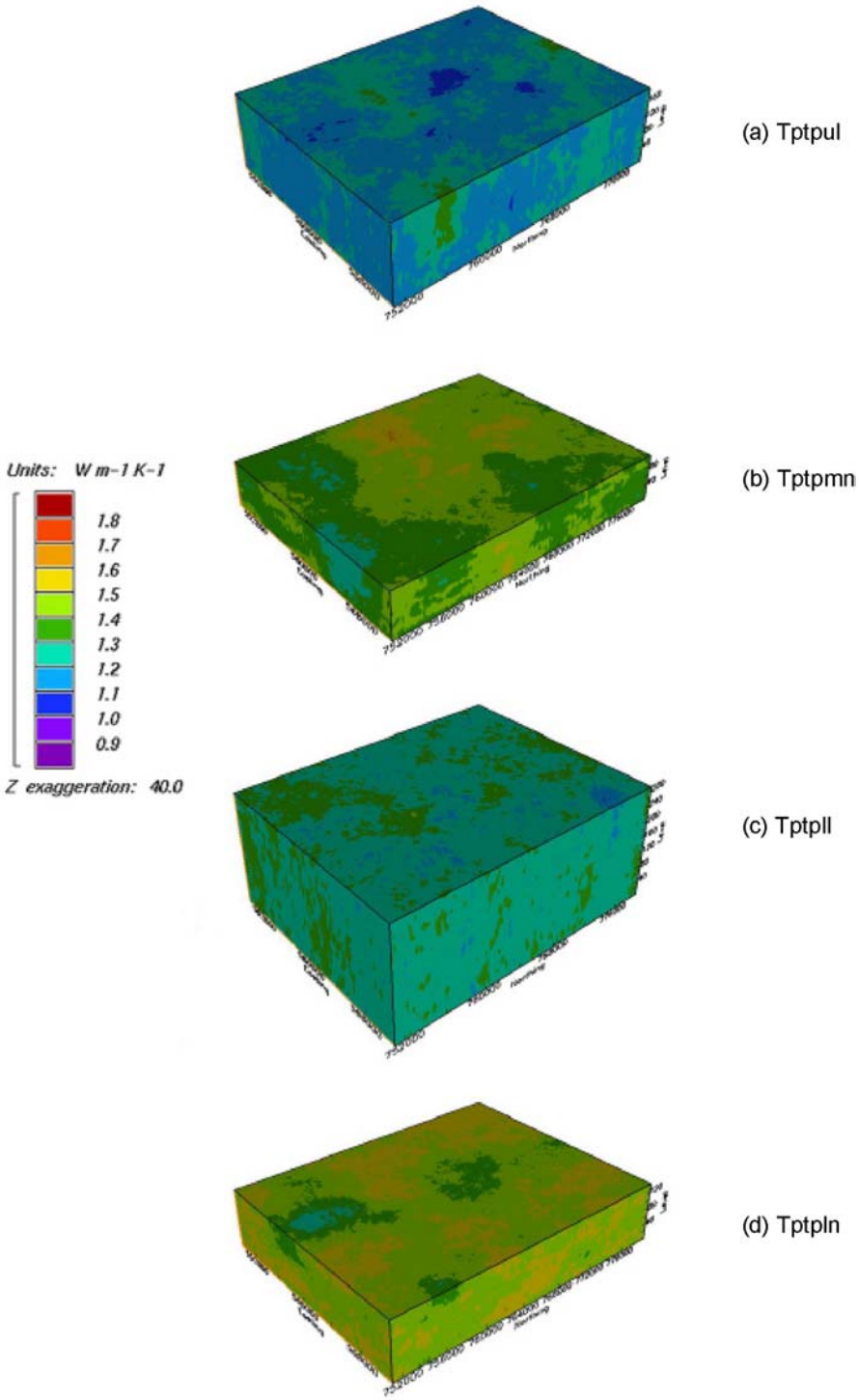

DTN: SN0208T0503102.007

Figure 7-16. Expected Dry Bulk Thermal Conductivity (W m^{-1} K^{-1})

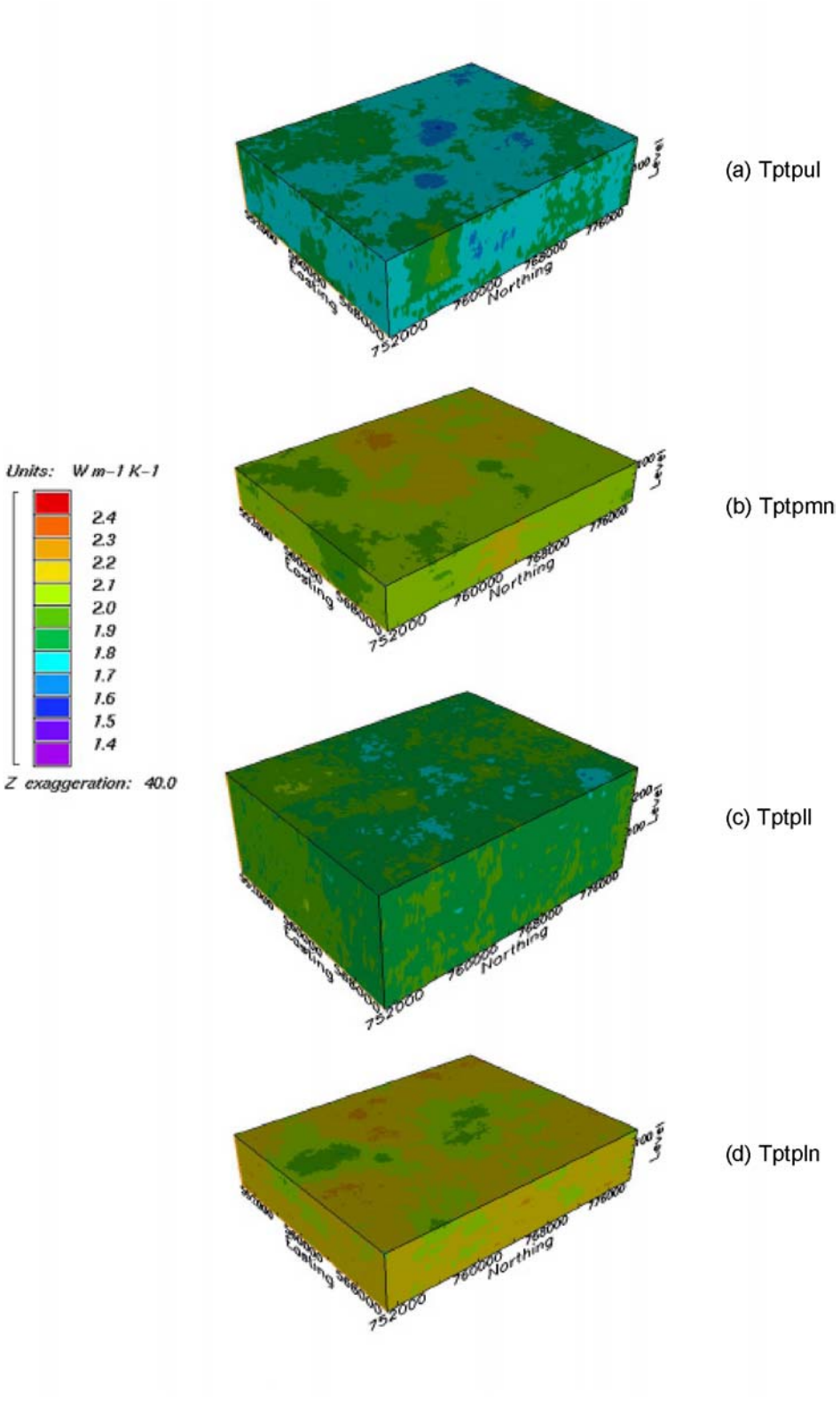

DTN: SN0208T0503102.007

Figure 7-17. Expected Wet Bulk Thermal Conductivity (W m^{-1} K^{-1})

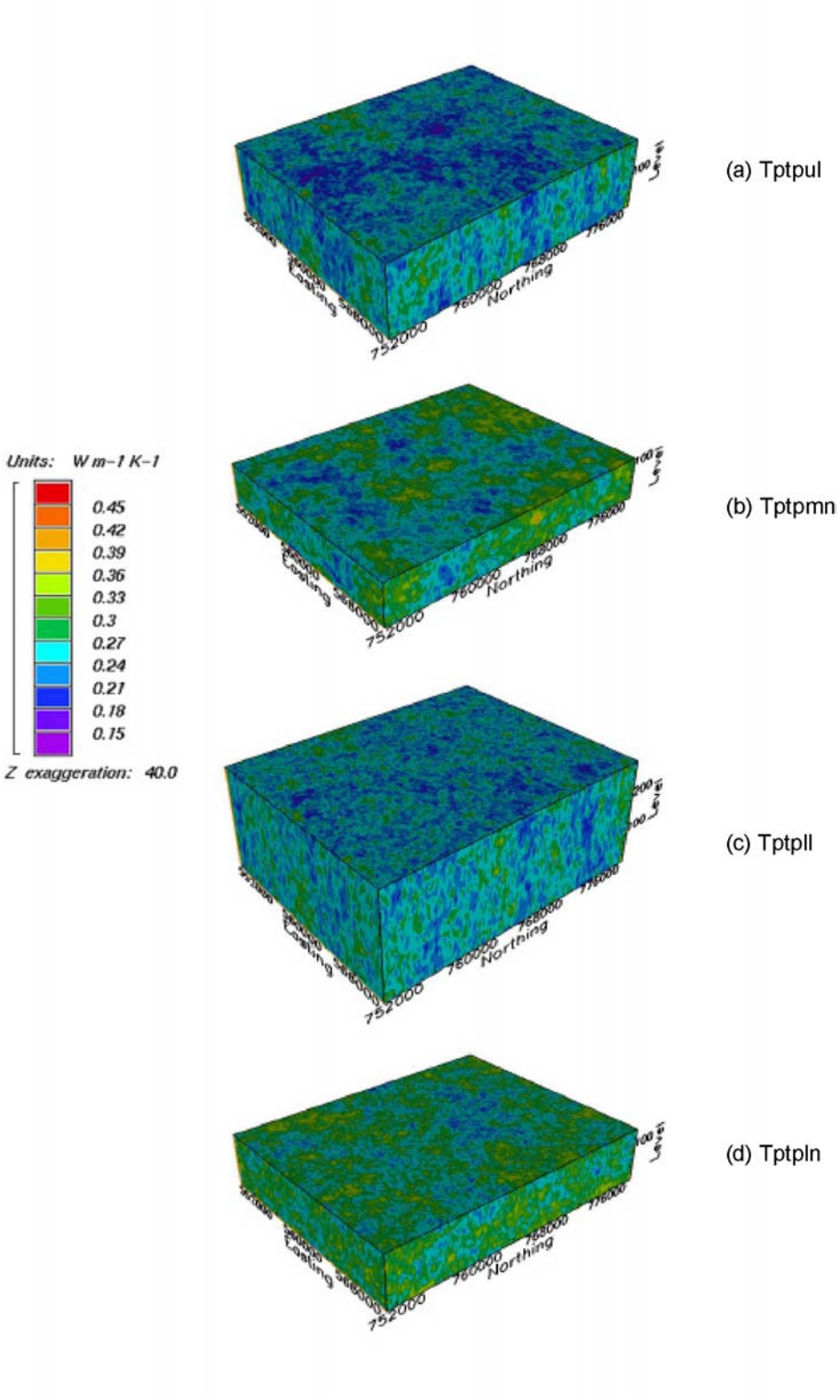

DTN: SN0208T0503102.007

Figure 7-18. Standard Deviation Dry Bulk Thermal Conductivity (W m^{-1} K^{-1})

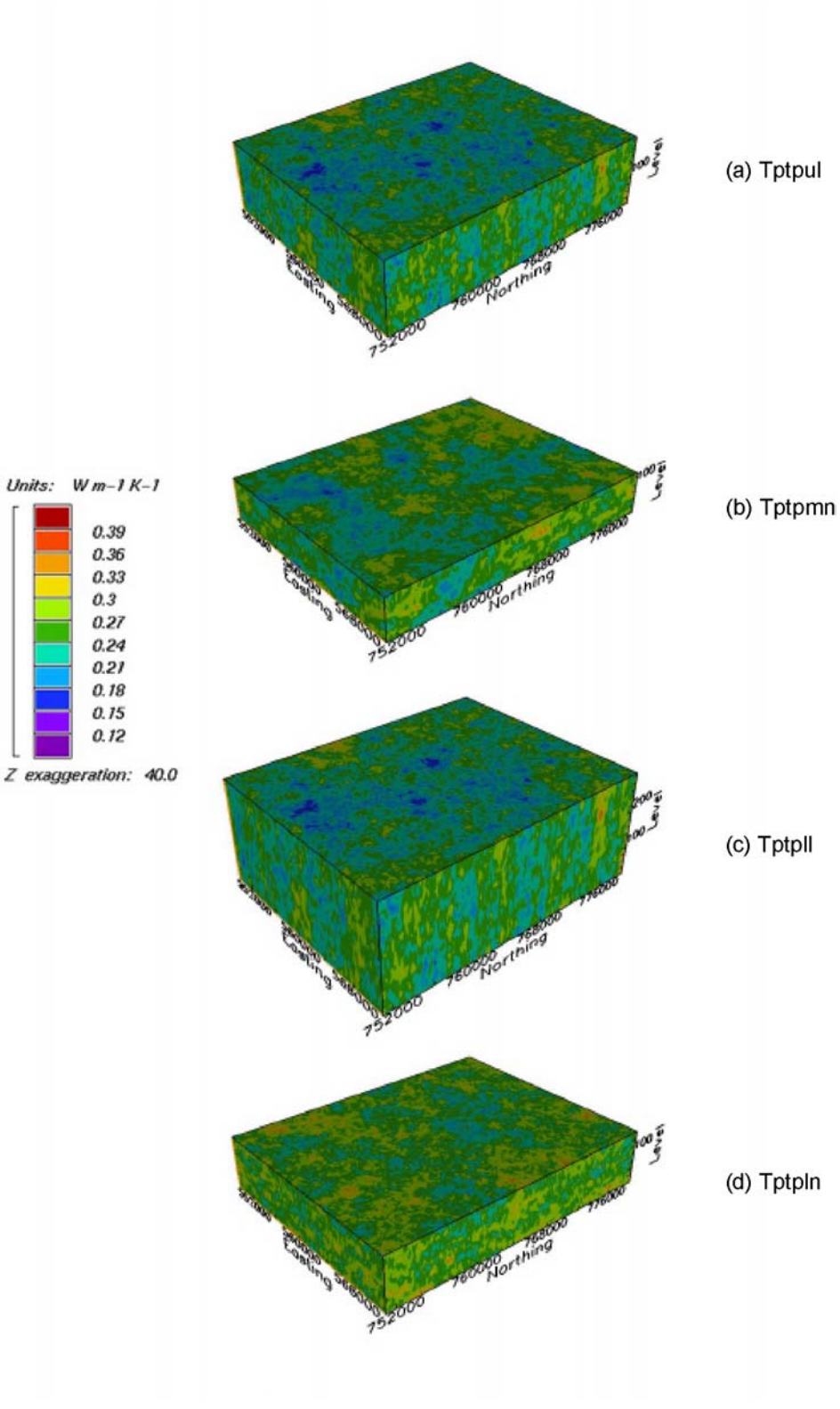

DTN: SN0208T0503102.007

Figure 7-19. Standard Deviation Wet Bulk Thermal Conductivity (W m^{-1} K^{-1})

Table 7-10. Summary of Primary Property Statistics

Stratigraphic Unit	Dry Bulk Thermal Conductivity [W/(m K)]		Wet Bulk Thermal Conductivity [W/(m K)]		Dry Bulk Density [g/cc]		Matrix Porosity		Lithophysal Porosity	
	mean	std. dev.	mean	std. Dev.	mean	std. dev.	mean	std. dev.	mean	std. dev.
Tptpul	1.1829	0.2440	1.7749	0.2474	1.8344	0.1496	0.1667	0.0412	0.1228	0.0613
Tptpmn	1.4189	0.2654	2.0741	0.2517	2.1483	0.0932	0.1287	0.0323	0.0254	0.0225
Tptpll	1.2784	0.2511	1.8895	0.2484	1.9793	0.1381	0.1486	0.0340	0.0883	0.0540
Tptpln	1.4900	0.2844	2.1303	0.2676	2.2114	0.0857	0.1058	0.0264	0.0302	0.0253

DTN: SN0208T0503102.007

7.5.2 Sample Realization

Surface plots of parameters of interest are presented in Figures 7-20 through 7-26. Once again, the stratigraphic coordinate system is used. These plots are for realization number 15, which was selected only because it is one of three realizations that are analyzed further in the following section. It is important to recognize that the vertical axis has been exaggerated by a factor of 40. This was done to illustrate heterogeneities oriented in the vertical plane. This distortion, however, gives the appearance of large vertical correlation lengths, which is simply not the case. This factor should be considered when viewing these diagrams.

Matrix porosity for realization 15 is presented in Figure 7-20. Matrix porosity tends to be higher in the lithophysal zones than in the nonlithophysal zones. This is presumably due to greater vapor phase alteration products in the lithophysal zones. Elevated matrix porosities are particularly apparent in the upper lithophysal zone, where lithophysal porosity also tends to be greatest.

Lithophysal porosity for realization 15 is presented in Figure 7-21. Both the middle and lower nonlithophysal zones have very low lithophysal porosity, with pockets of slightly elevated values. Lithophysal porosity is greatest in the upper portions of the upper lithophysal zone and tends to decrease with depth. Smaller pockets of high lithophysal porosity are observed in the lower lithophysal zone and also tend to occur in the upper portions of the unit.

Dry bulk density for realization 15 is presented in Figure 7-22. Dry bulk density is inversely proportional to matrix and lithophysal porosity. Consequently, the lithophysal zones, which have the highest porosities, also have the lowest bulk densities. The lowest values are located in the upper lithophysal zone, and there is a strong inverse resemblance with the plot of lithophysal porosity discussed previously.

Dry and wet values of matrix thermal conductivity are presented in Figures 7-23 and 7-24, respectively. In the case of the dry model predictions, values of matrix thermal conductivity are slightly lower in the two lithophysal zones due to higher matrix porosity in these zones. This difference is not quite as apparent in the wet predictions, though, due to the similarity between the thermal conductivity of water and the minerals that compose the matrix solid (Section 6.1.7).

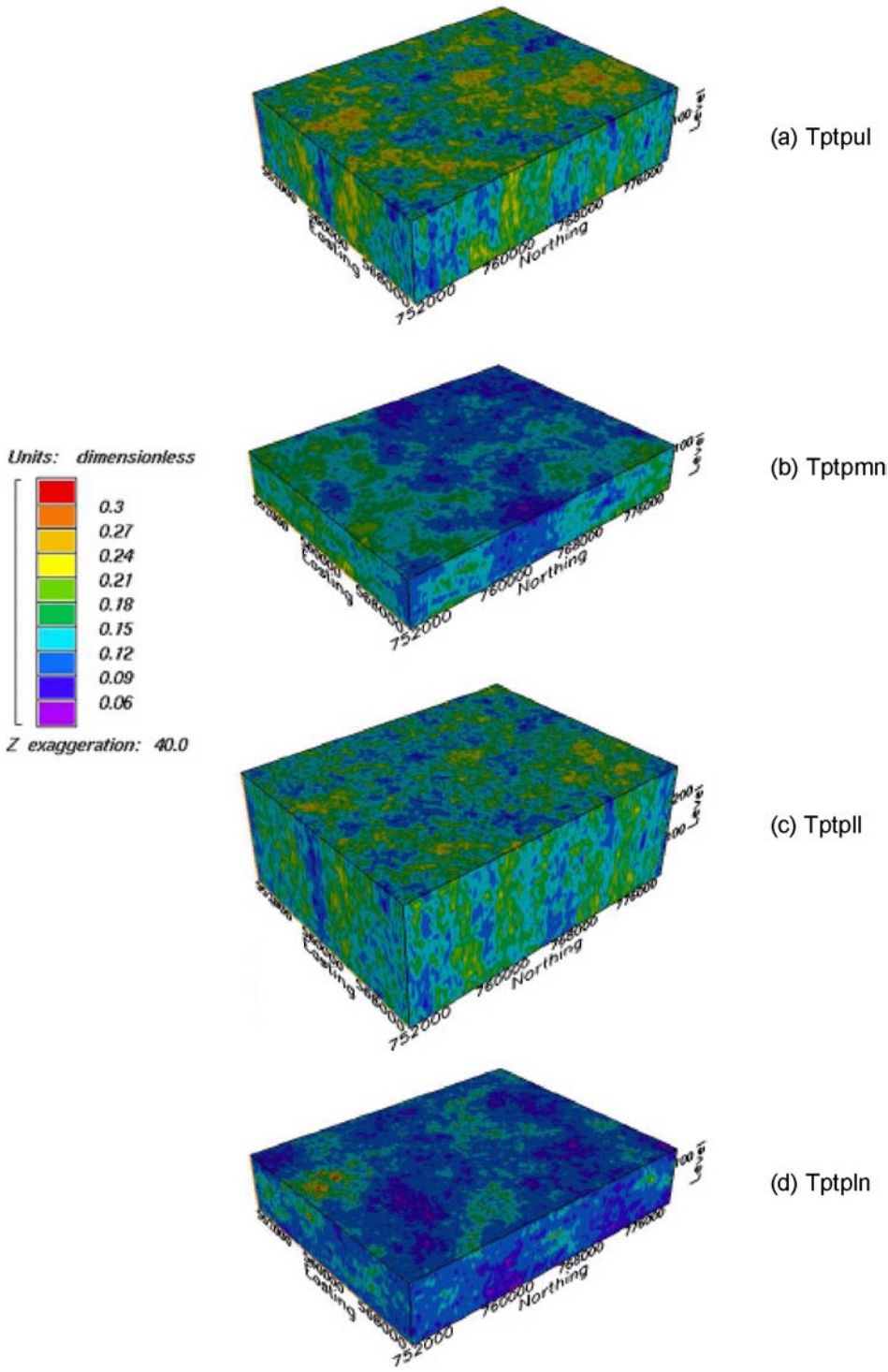

DTN: SN0208T0503102.007

Figure 7-20. Matrix Porosity Realization 15 (dimensionless)

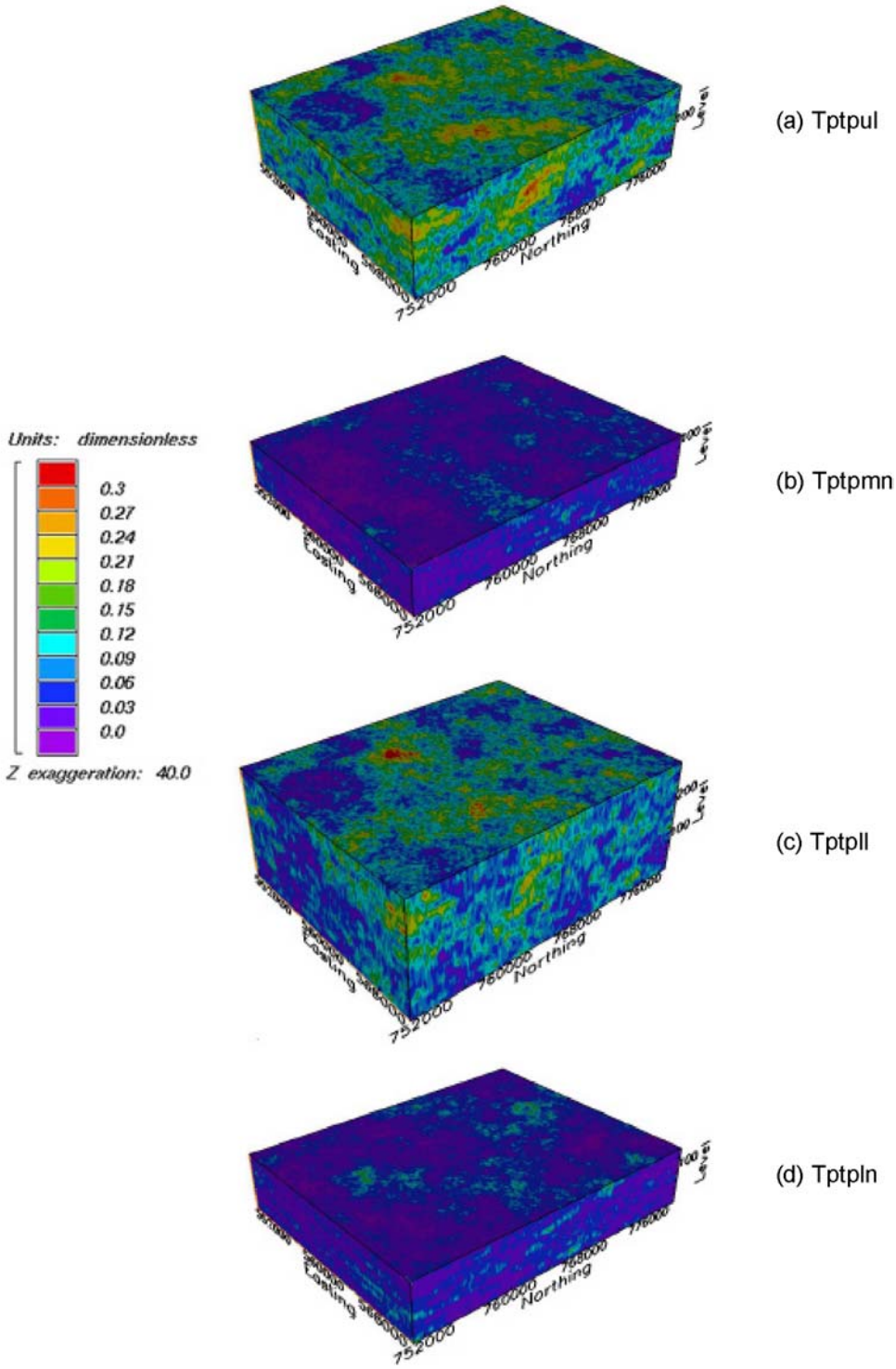

DTN: SN0208T0503102.007

Figure 7-21. Lithophysal Porosity Realization 15 (dimensionless)

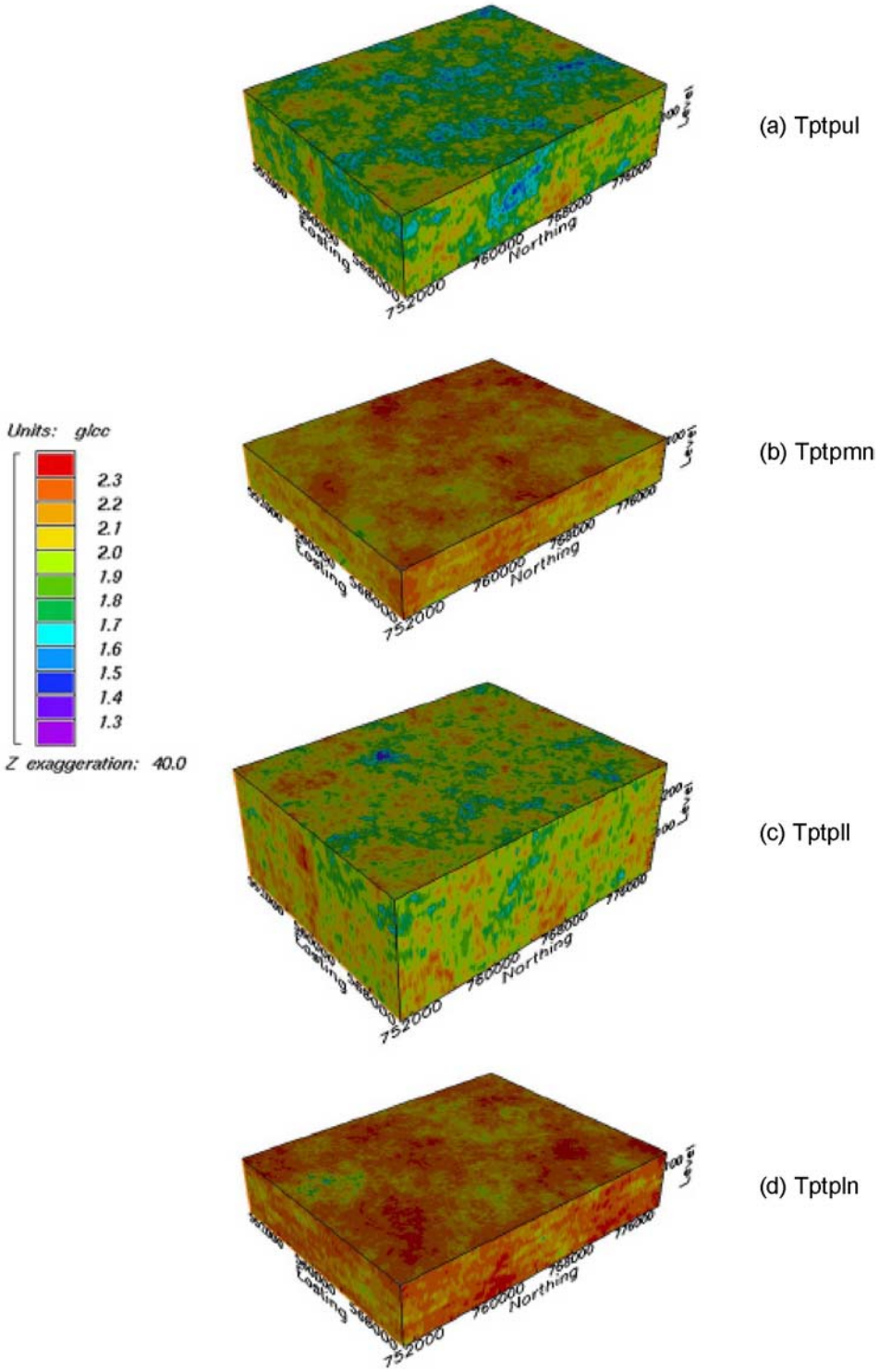

DTN: SN0208T0503102.007

Figure 7-22. Dry Bulk Density Realization 15 (g/cc)

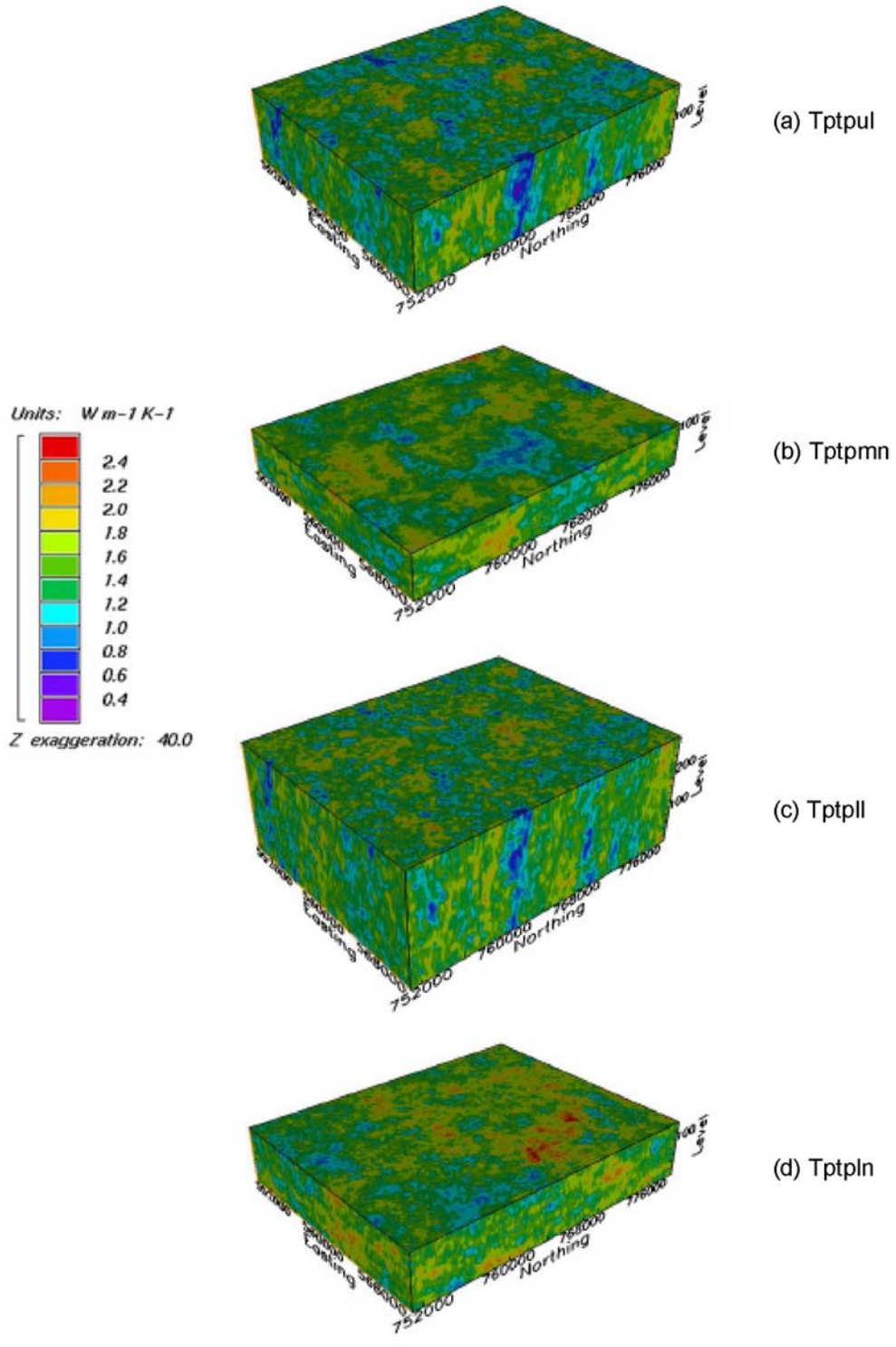

DTN: SN0208T0503102.007

Figure 7-23. Matrix Dry Thermal Conductivity Realization 15 (W m^{-1} K^{-1})

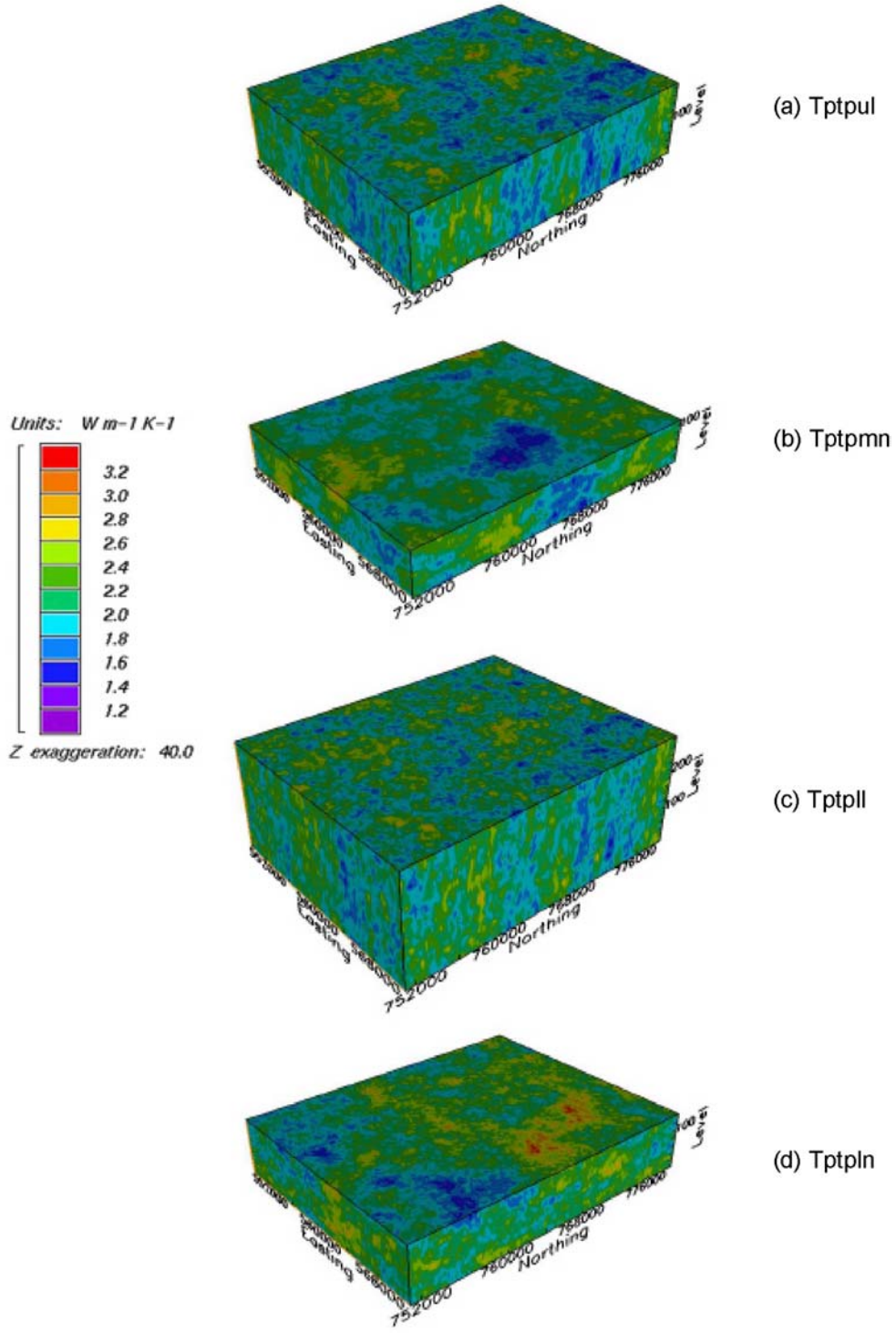

DTN: SN0208T0503102.007

Figure 7-24. Matrix Wet Thermal Conductivity Realization 15 (W m^{-1} K^{-1})

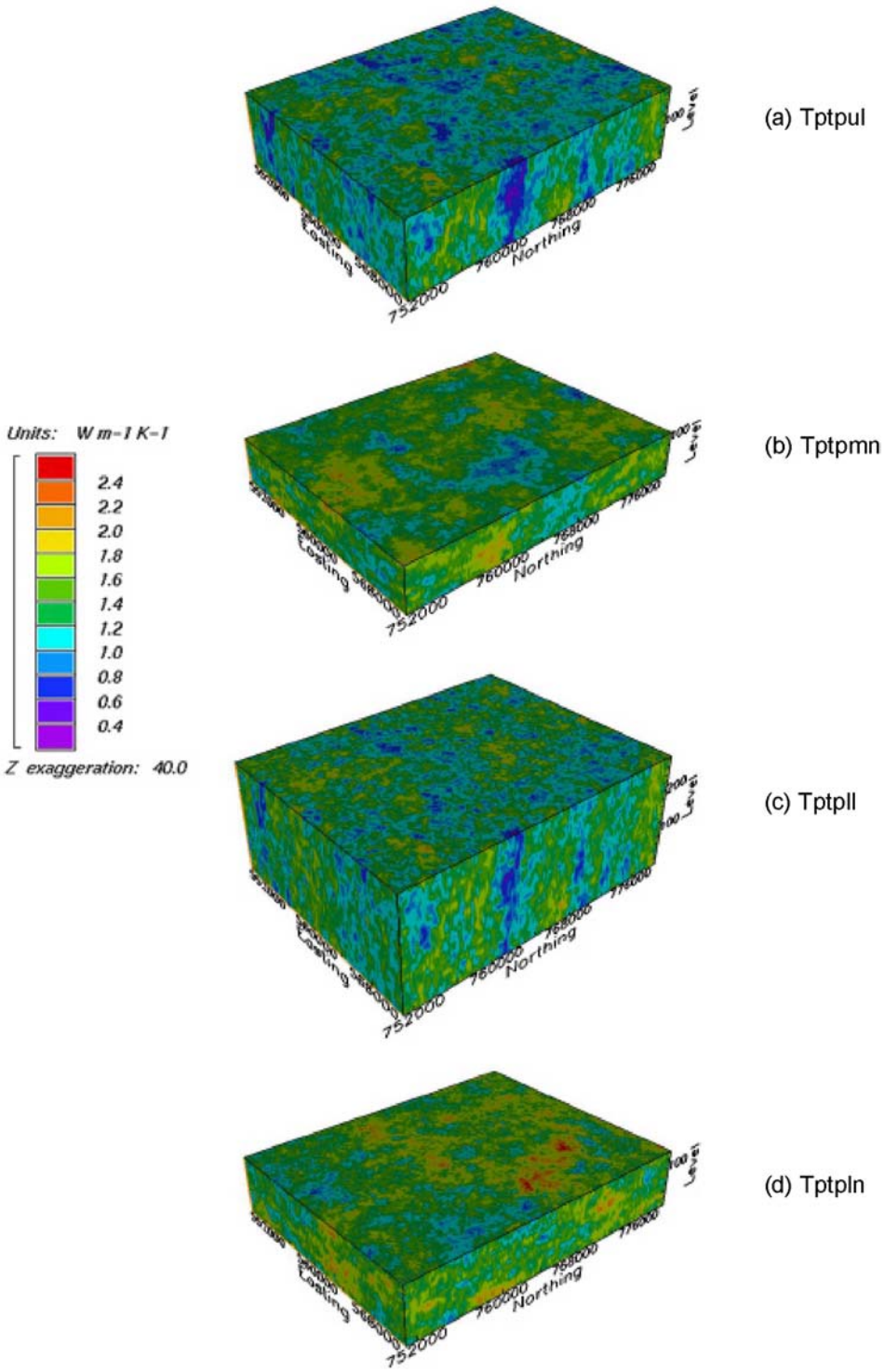

DTN: SN0208T0503102.007

Figure 7-25. Bulk Dry Thermal Conductivity Realization 15 (W m^{-1} K^{-1})

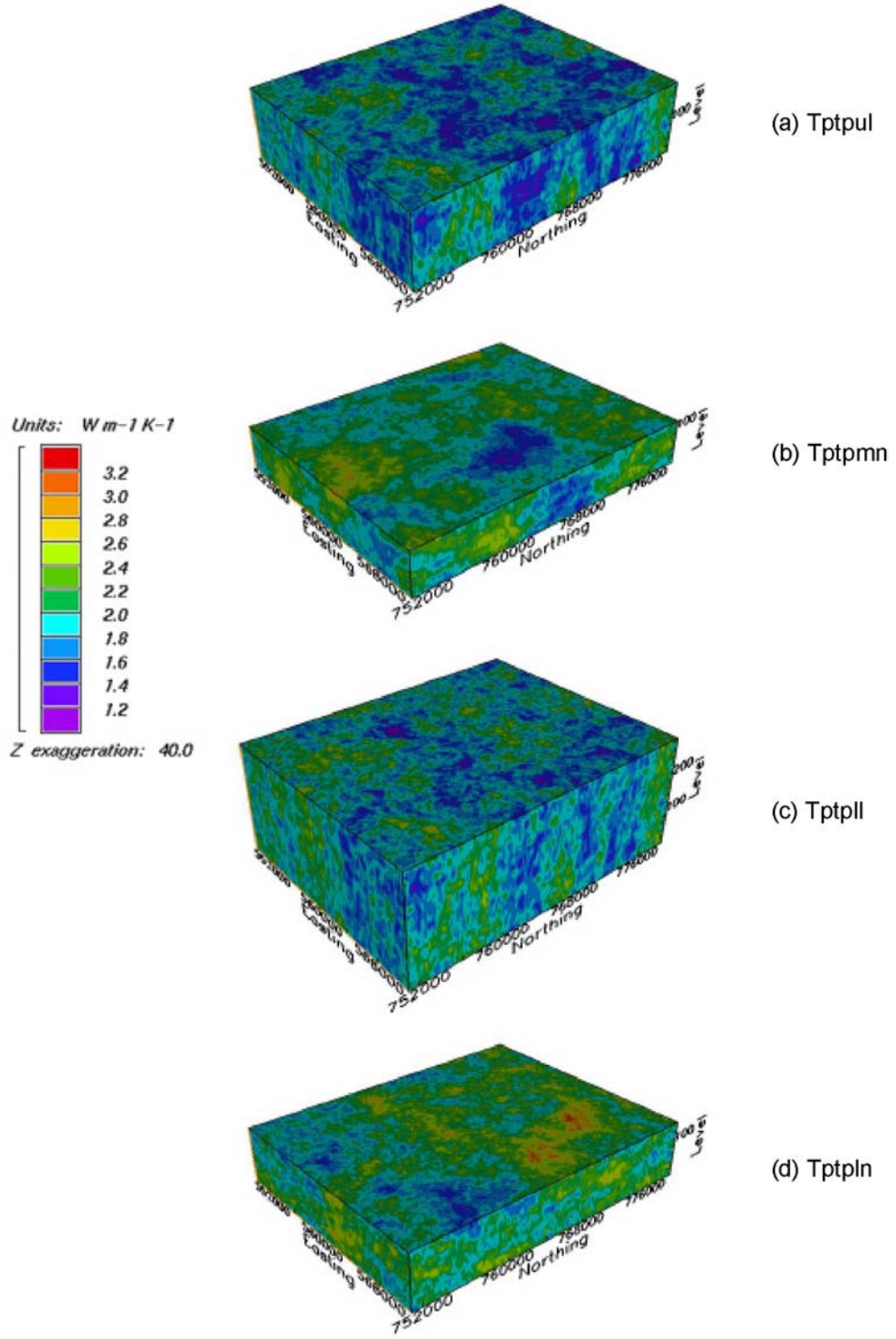

DTN: SN0208T0503102.007

Figure 7-26. Bulk Wet Thermal Conductivity Realization 15 (W m^{-1} K^{-1})

Finally, the realization 15 values of dry and wet bulk thermal conductivity are presented in Figures 7-25 and 7-26, respectively. These results are consistent with the discussion of the expected value results. It is important to notice the significant differences between the results of this individual realization and the expected value model depicted in Figures 7-16 and 7-17. In contrast to the relatively smooth and consistent values of the Etype V. 2.01 model, the actual realizations depict much greater variability, often over relatively short distances. The Etype V. 2.01 models are useful for identifying trends and regions of abnormal behavior. They are poor models, however, of the spatial heterogeneity and of the parameters' range and distribution.

7.5.3 Summary Statistics

Table 7-10 summarizes the mean and the standard deviation of the parameters most critical to thermal hydrologic modeling in each of the four units analyzed. Here the mean is taken as the mean value of the expected-value model. This value represents the mean value of all 50 realizations. The standard deviation reported in Table 7-10 is the average standard deviation from realizations 15, 30, and 45. As seen in the histogram plots that follow, the univariate statistical characteristics from one realization to the next are quite similar. Consequently, the average standard deviation of the three realizations is quite representative of parameter uncertainty for all realizations.

Similarly, Table 7-11 summarizes the mean and the standard deviation of intermediate model results. These values were obtained in the same manner as those of Table 7-10. It should be noted that the statistical measures for the matrix thermal conductivity model parameters of γ_c and k_s are nearly identically in all four units. This was expected and is a consequence of assuming the same univariate parameter distribution (Figure 6-11) for all four units. Slight differences in matrix thermal conductivity between the units are a consequence of higher matrix porosity in the lithophysal units (Table 7-10).

Table 7-11. Summary of Intermediate Property Statistics

Stratigraphic Unit	Solid Connectivity, γ_c		Solid Thermal Conductivity [W/(m K)]		Dry Matrix Thermal Conductivity [W/(m K)]		Wet Matrix Thermal Conductivity [W/(m K)]	
	mean	std. dev.	mean	std. dev.	mean	std. dev.	mean	std. dev.
Tptpul	0.8517	0.1158	2.6011	0.3493	1.3453	0.2639	2.0201	0.2484
Tptpmn	0.8476	0.1094	2.6033	0.3518	1.4553	0.2690	2.1276	0.2519
Tptpll	0.8531	0.1130	2.6030	0.3413	1.3998	0.2640	2.0707	0.2455
Tptpln	0.8492	0.1151	2.6017	0.3505	1.5356	0.2908	2.1958	0.2764

DTN: SN0208T0503102.007

7.5.4 Summary Histograms

Histogram plots for three of the 50 realizations and histogram plots of the expected-value model for each of the four lithostratigraphic units are shown in Figures 7-27 through 7-50. Realizations 15, 30, and 45 were chosen for this analysis simply because they are each a multiple of the number 15. They are statistically indistinguishable from the other realizations. The first

nine of these plots (Figures 7-27 through 7-35) present the complete set of spatially dependent properties studied for the Tptpul. These are followed by the five more important properties, summarized in Table 7–4, for each of the three remaining lithostratigraphic units.

8. CONCLUSIONS

The spatial variation and uncertainty of bulk thermal conductivity in the proposed repository horizon has been estimated through the application of selected theoretical models. Inputs to these models consist of the following stochastic, geostatistically simulated rock properties: matrix porosity, lithophysal porosity, matrix solid thermal conductivity, and matrix solid connectivity. Simulations of matrix and lithophysal porosity are conditioned to borehole measurements and thus anchor the subsequent calculations of matrix and bulk thermal conductivity for the repository host layers (Tptpul, Tptpmn, Tptpll, and Tptpln). The results of this modeling effort are found in DTN: SN0208T0503102.007. Simulations of solid thermal conductivity and solid connectivity, however, are both unconditioned, and their uncertainty parameter distributions are rather broad. Consequently, even at locations where matrix and lithophysal porosity are known precisely (neglecting measurement error), there is some degree of uncertainty in model prediction of bulk thermal conductivity.

Highly variable measurements of lithophysal porosity in the lithophysal zones also contribute to uncertainty in bulk thermal conductivity. However, for the model adopted in this report, the univariate statistical properties of individual realizations and plots of the standard deviation in the Etype V. 2.01 model suggests that the uncertainty in bulk thermal conductivity is dominated by uncertainty in matrix thermal conductivity.

The range and uncertainty of bulk thermal conductivity reported in this document may or may not be adequate for the purpose of predicting repository performance. It is ultimately the user's responsibility to determine whether the assumptions inherent in the model development and data distributions produced are appropriate for their use. The only way to determine this is to conduct a Monte Carlo analysis using the results of this study as input to thermal hydraulic simulations and then evaluate the results with respect to a specific performance metric (i.e., average repository temperature). If the uncertainty in the performance metric is within a specified tolerance, it can be concluded that the uncertainty in bulk thermal conductivity, and other input parameters, is justifiable.

If deemed necessary, it is believed that uncertainty can be reduced through systematic and thorough laboratory studies and field investigations of matrix thermal conductivity. Such a study should include samples collected from several different regions of the repository and consist of thermal conductivity measurements under both water-saturated and air-saturated conditions. Quantification of sample mineralogy would also be helpful and would, perhaps, lead to the incorporation of the existing mineralogy database into the model. Additional study of porous media thermal conductivity models available from the literature may also be warranted, resulting in improved model predictions and reduced model uncertainty.

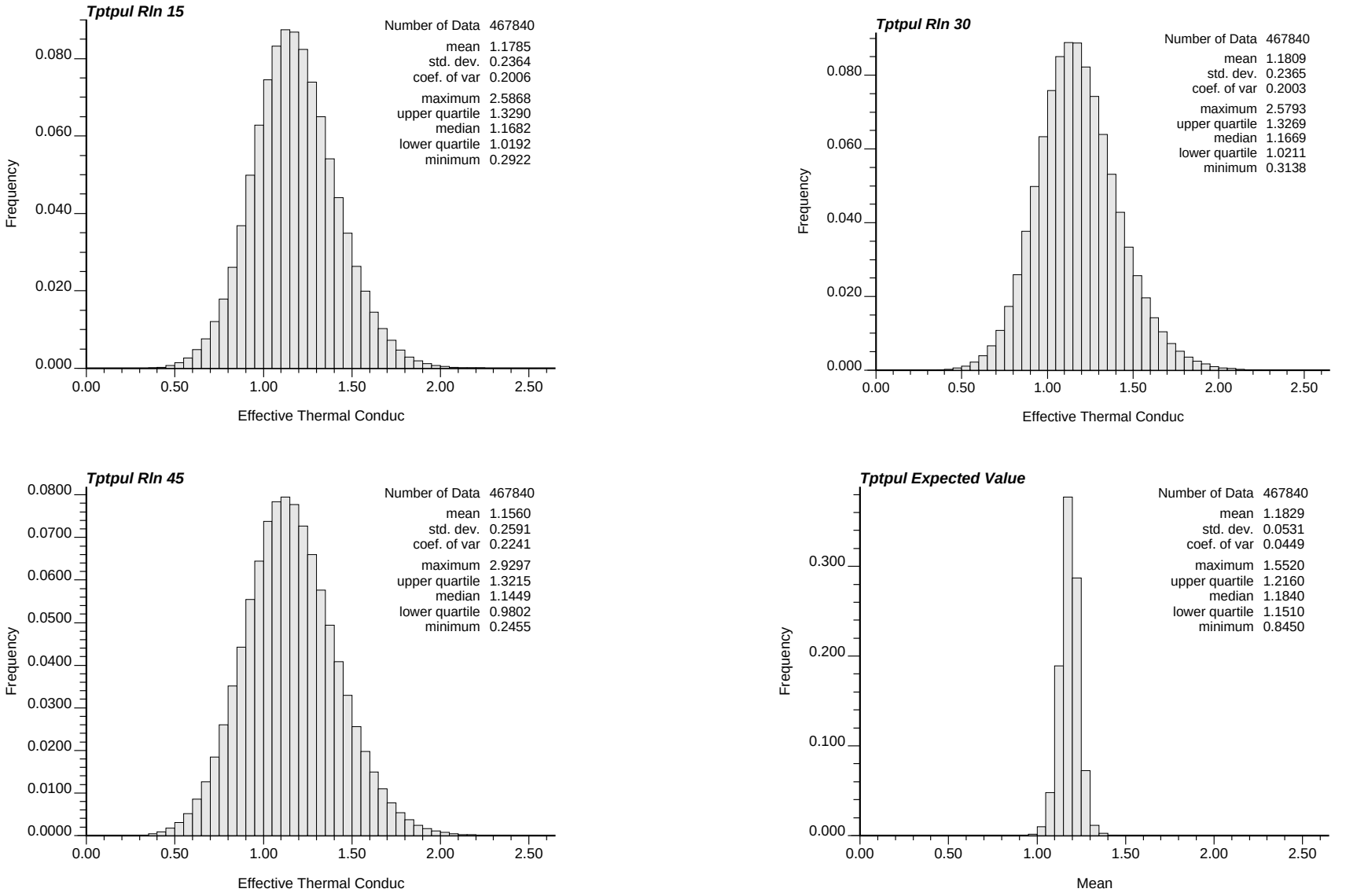

DTN: SN0208T0503102.007

Figure 7-27. Dry Bulk Thermal Conductivity (W m^{-1} K^{-1}) in the Tptpul

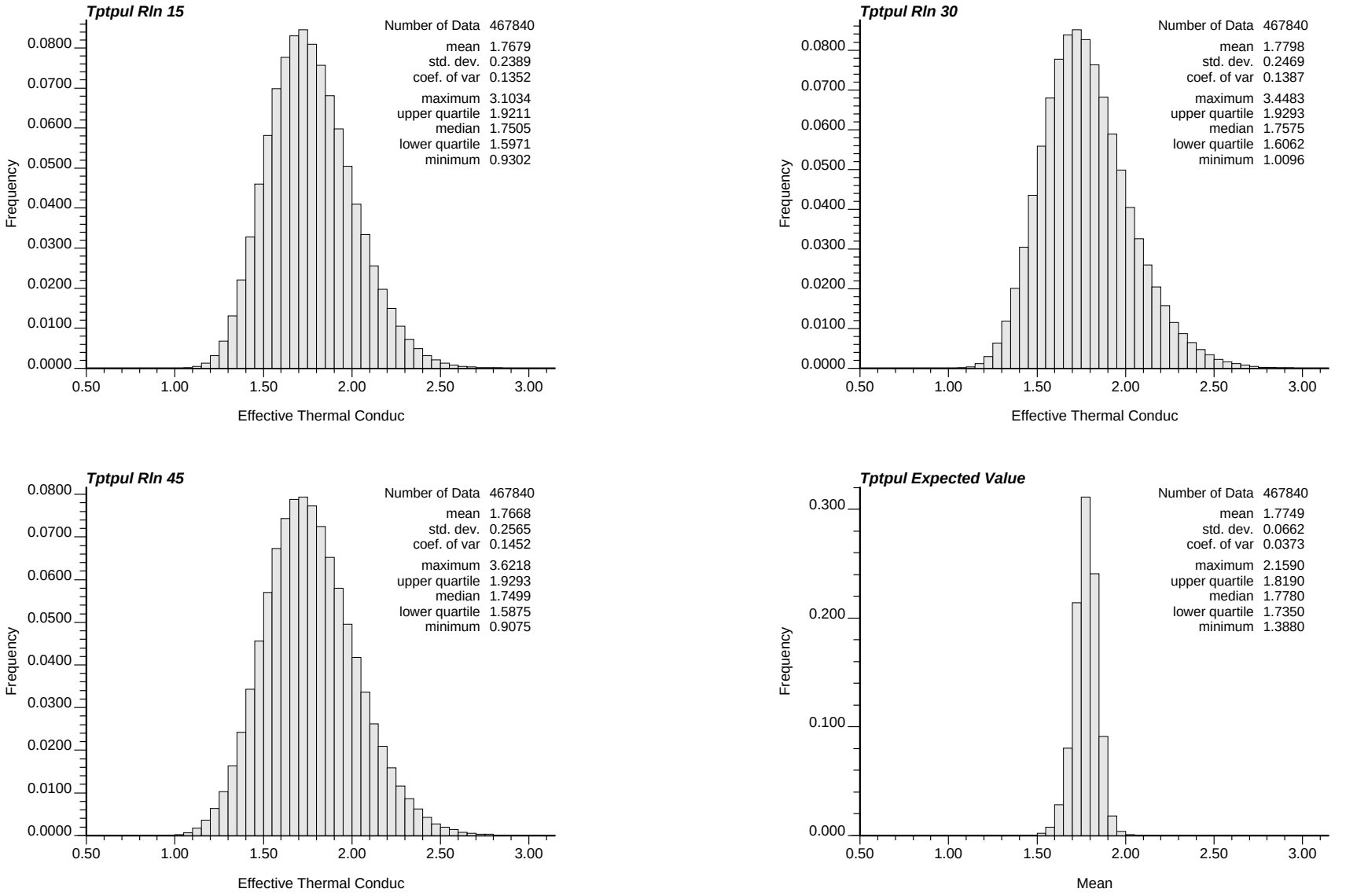

DTN: SN0208T0503102.007

Figure 7-28. Wet Bulk Thermal Conductivity (W m^{-1} K^{-1}) in the Tptpul

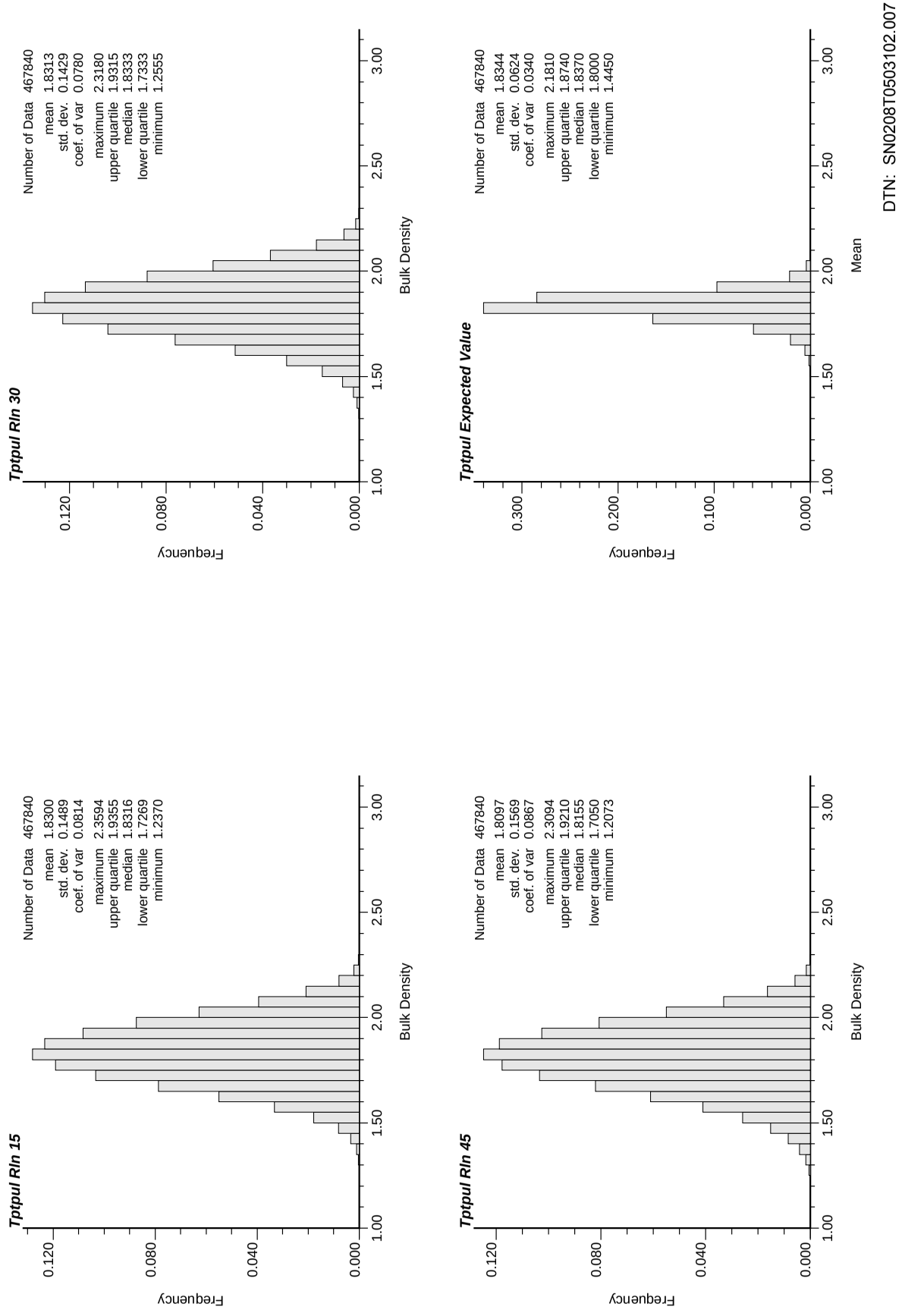

DTN: SN0208T0503102.007

Figure 7-29. Dry Bulk Density (g/cc) in the Tptpul

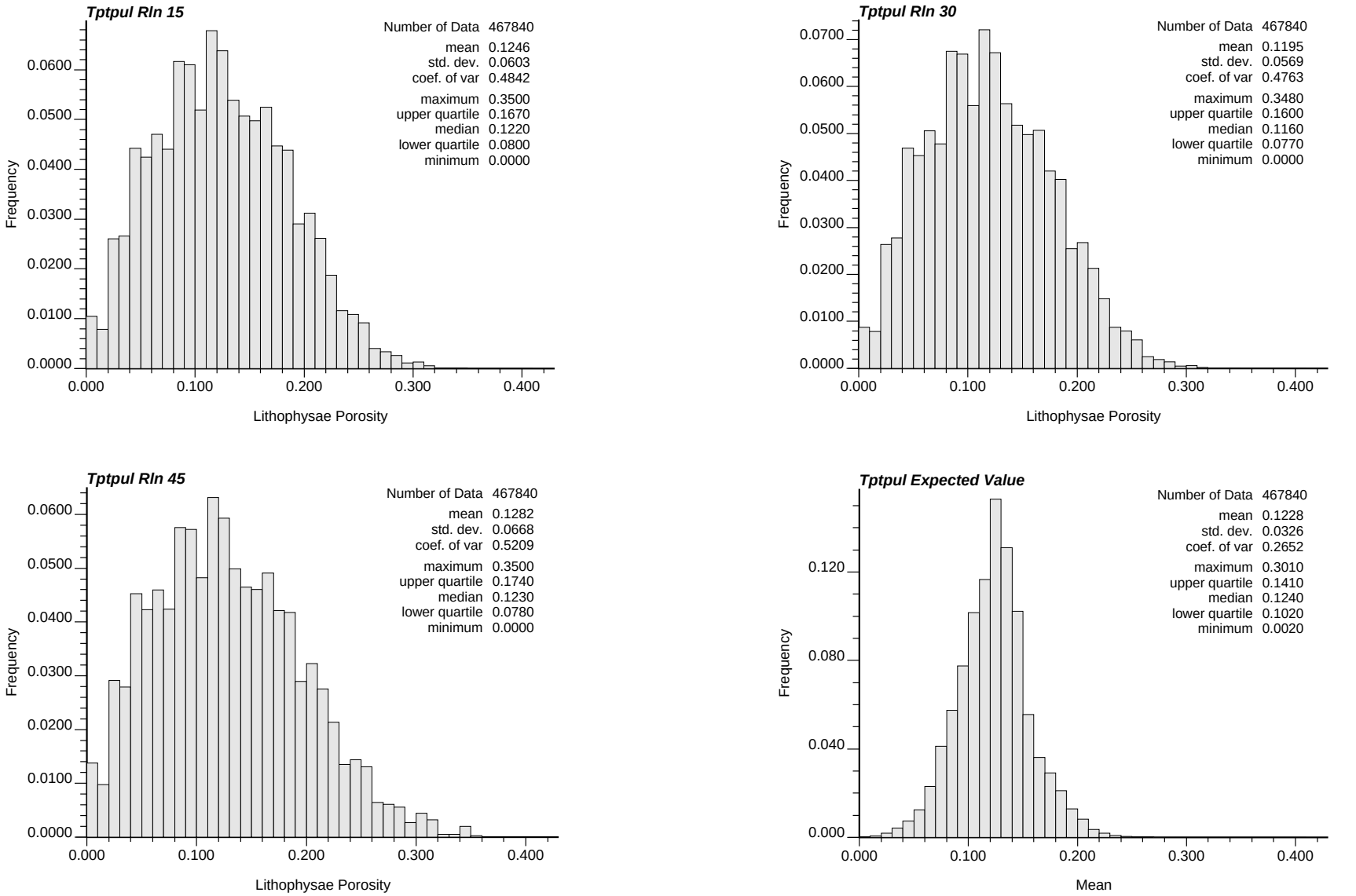

DTN: SN0208T0503102.007

Figure 7-30. Lithophysal Porosity in the Tptpul

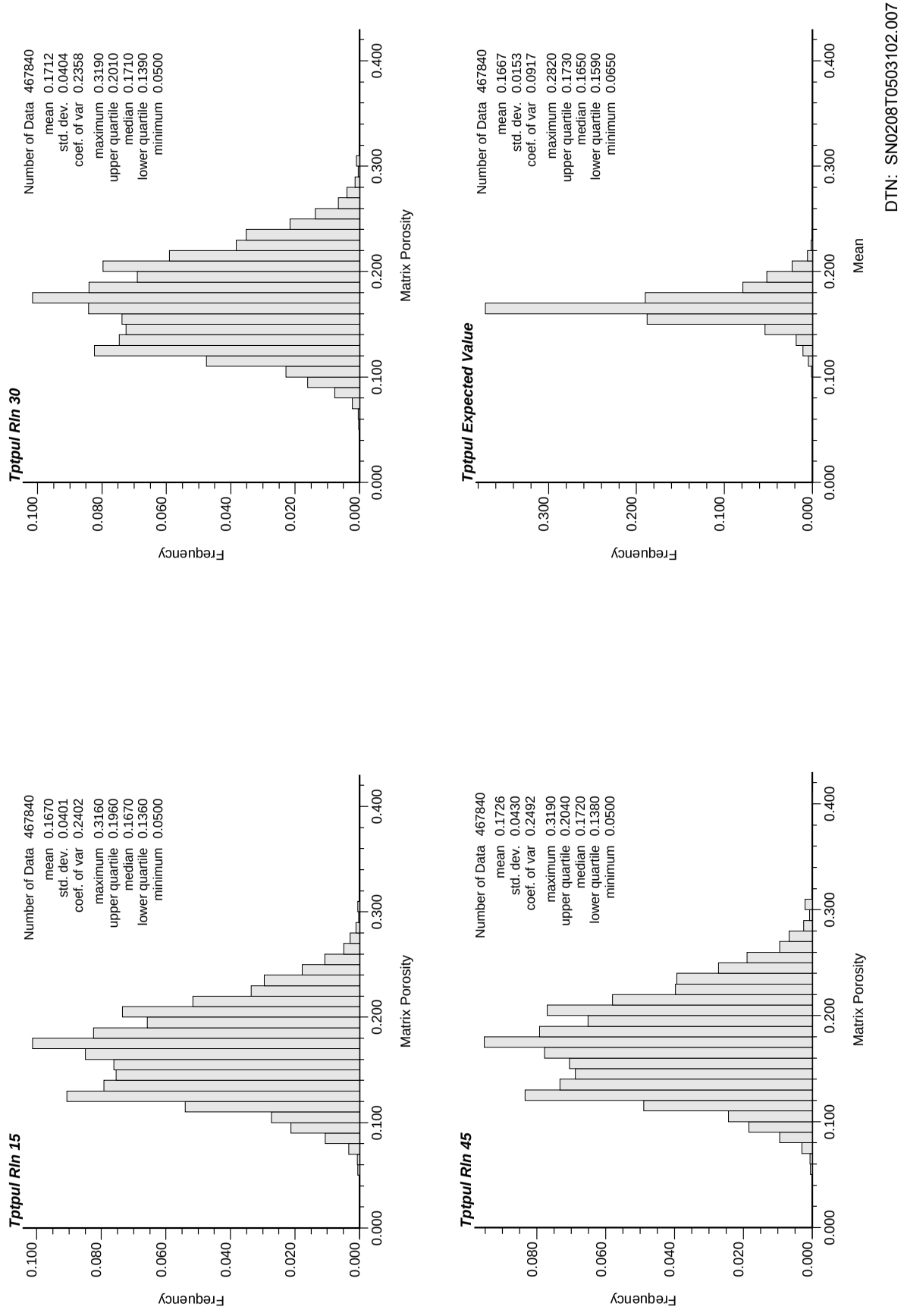

DTN: SN0208T0503102.007

Figure 7-31. Matrix Porosity in the Tptpul

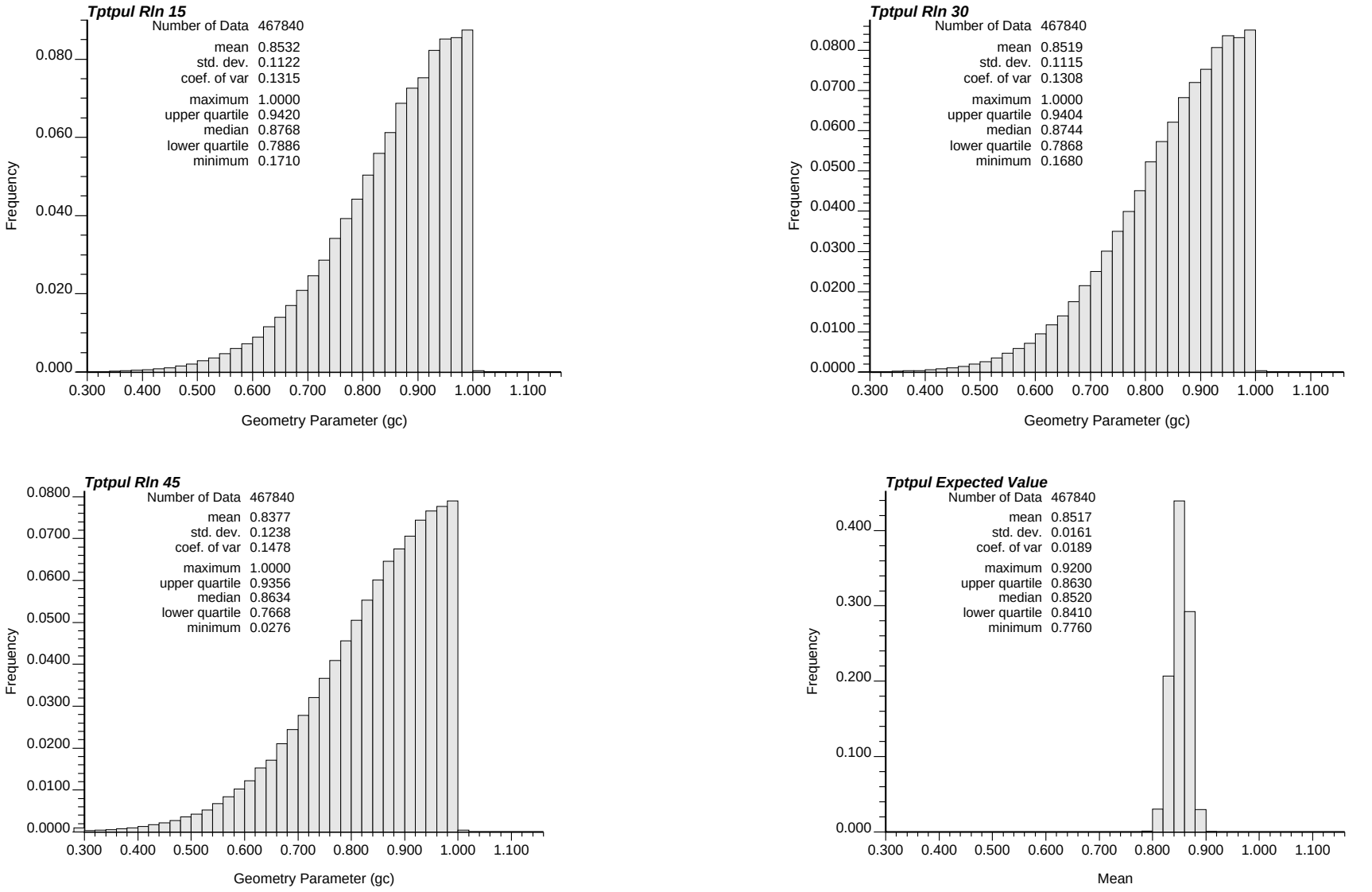

DTN: SN0208T0503102.007

Figure 7-32. γc in the Tptpul

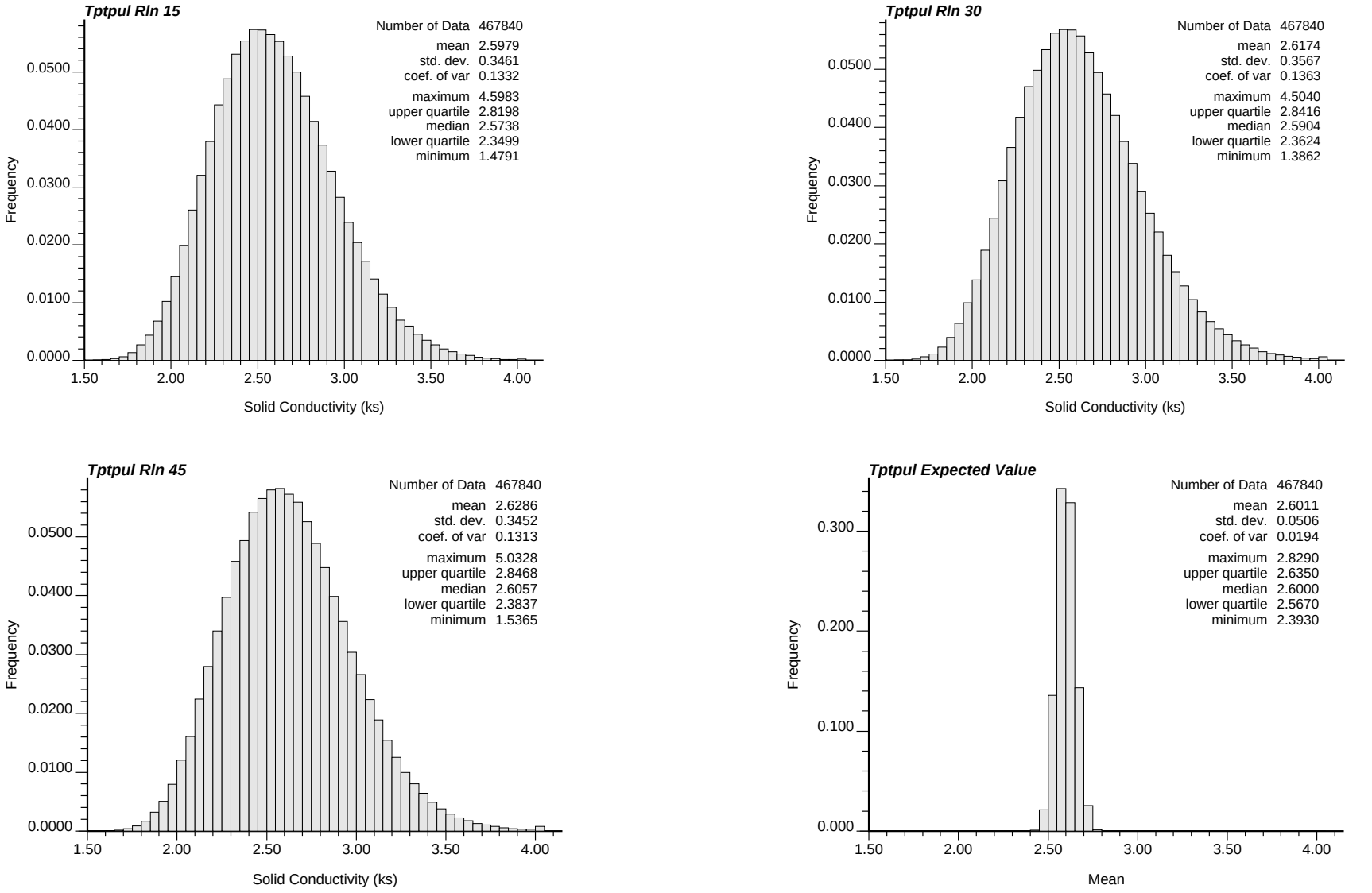

DTN: SN0208T0503102.007

Figure 7-33. ks in the Tptpul

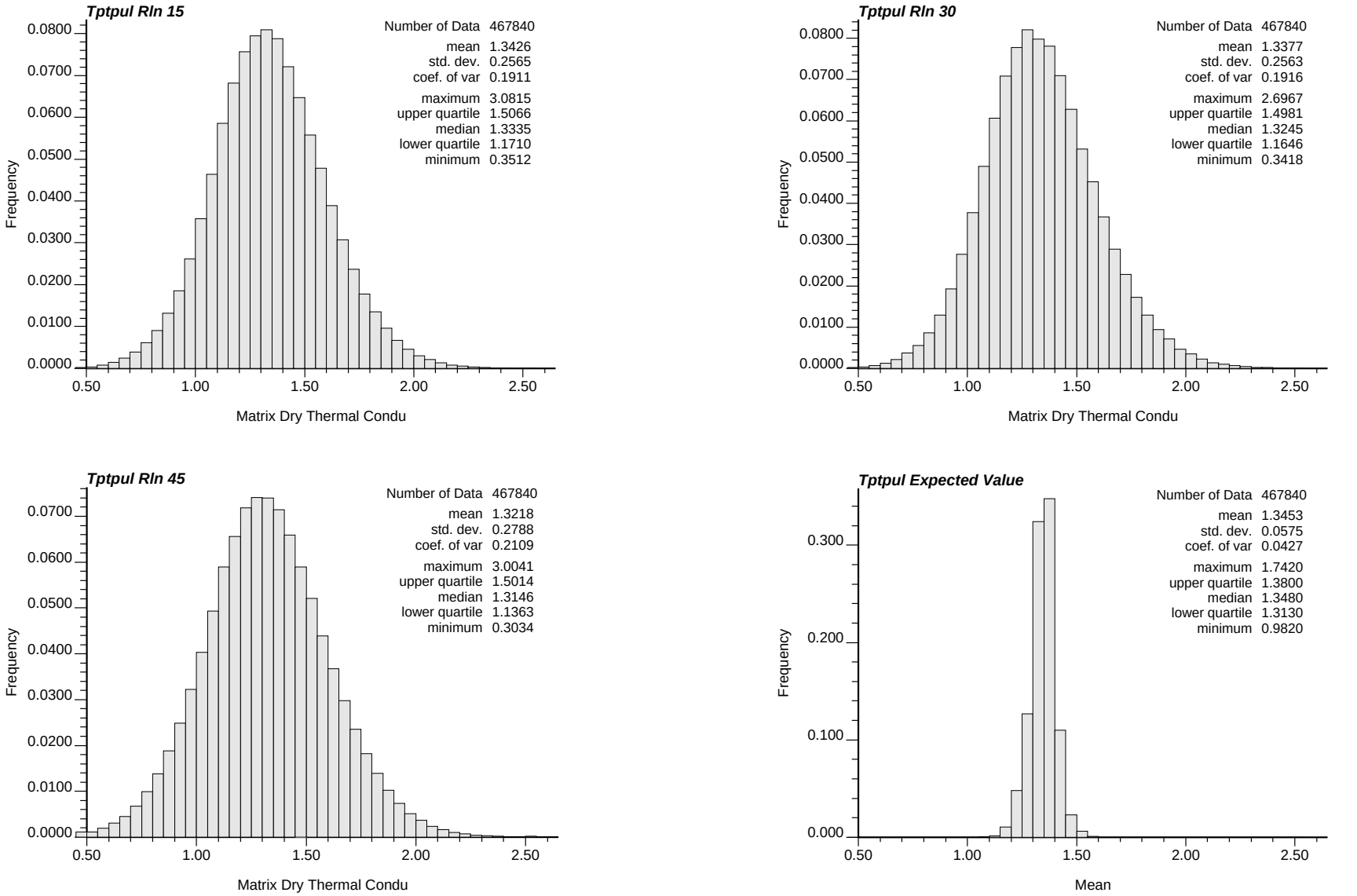

DTN: SN0208T0503102.007

Figure 7-34. Dry Matrix Thermal Conductivity (W m^{-1} K^{-1}) in the Tptpul

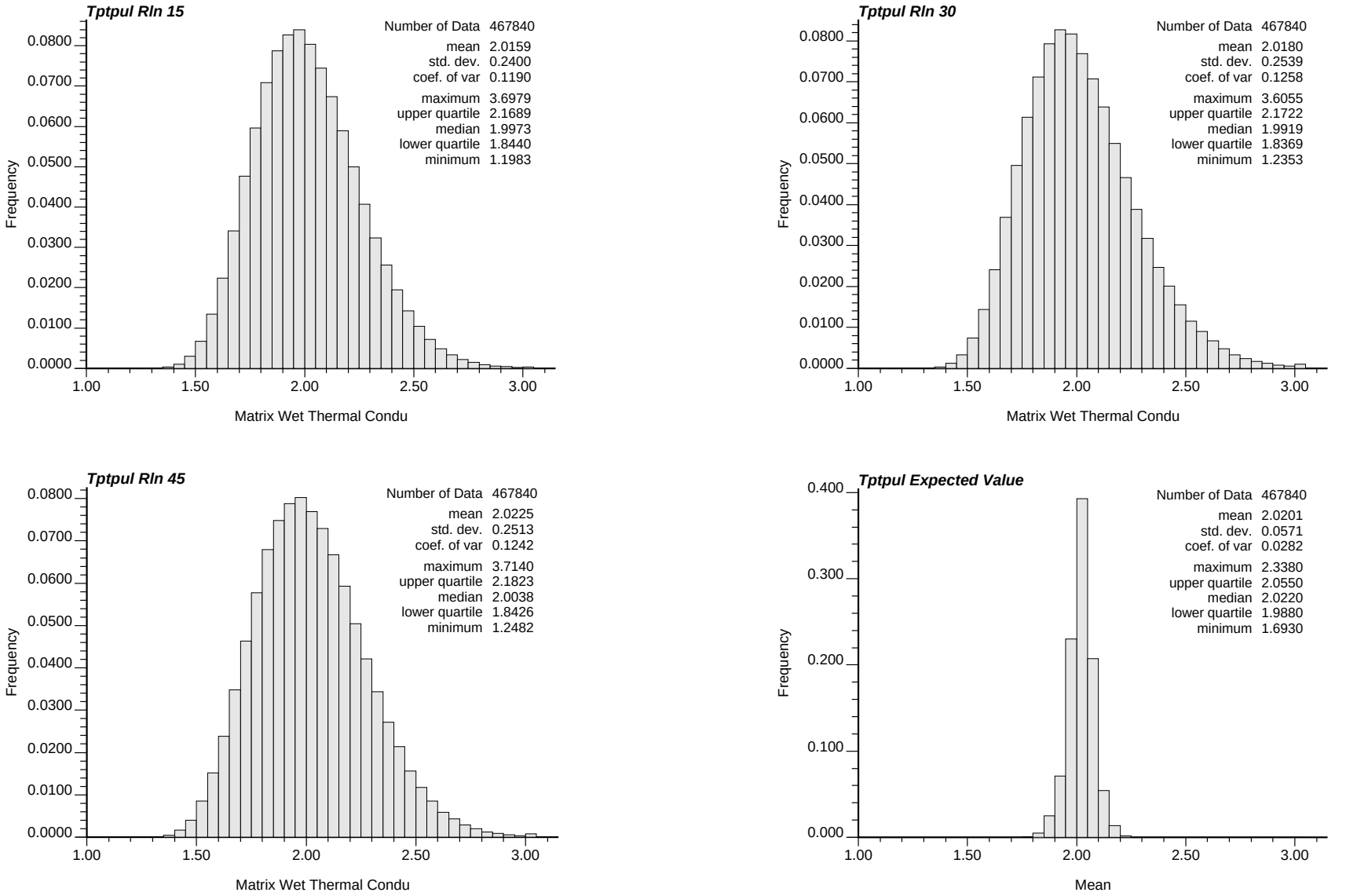

DTN: SN0208T0503102.007

Figure 7-35. Wet Matrix Thermal Conductivity (W m^{-1} K^{-1}) in the Tptpul

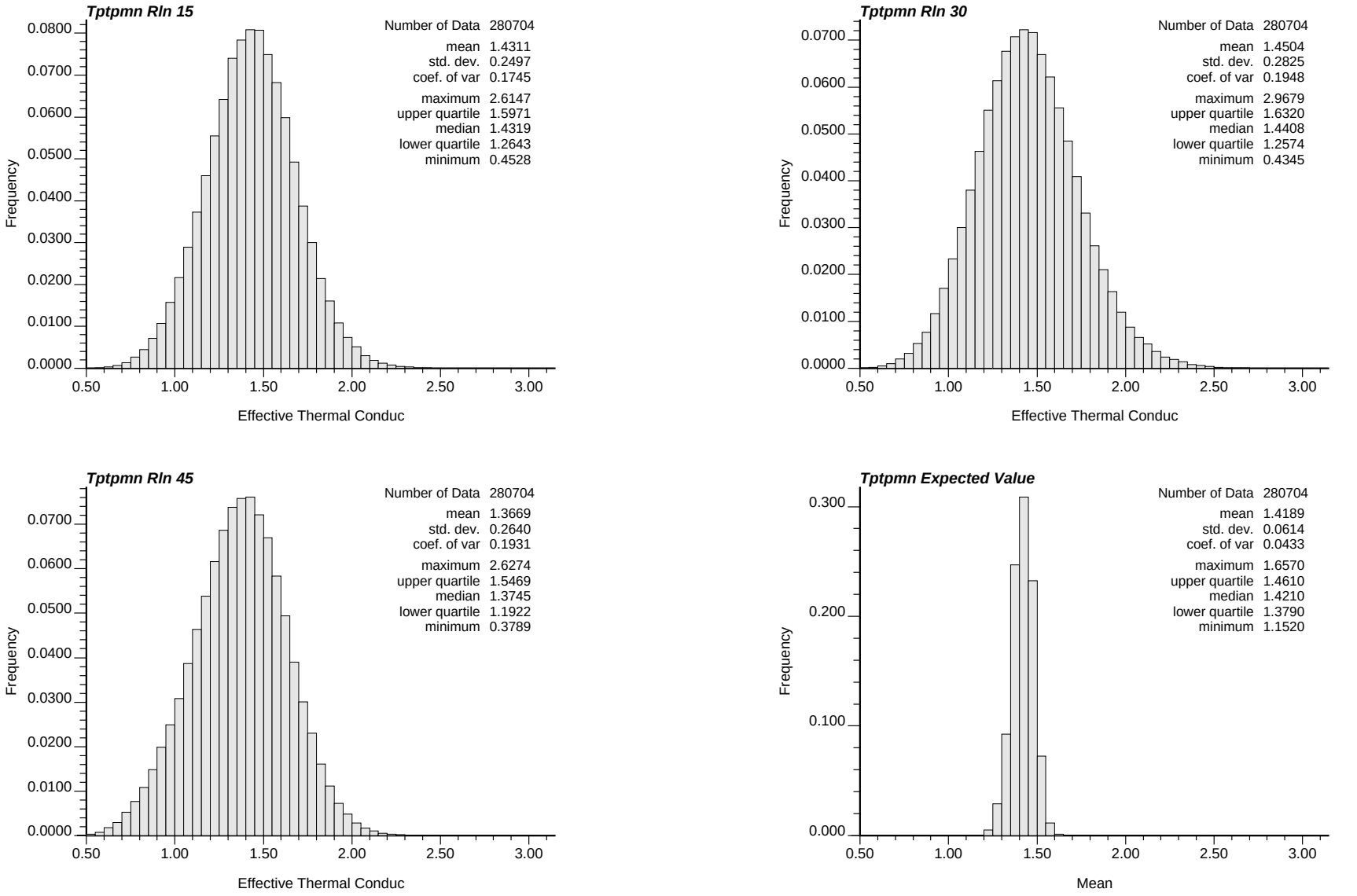

DTN: SN0208T0503102.007

Figure 7-36. Dry Bulk Thermal Conductivity (W m^{-1} K^{-1}) in the Tptpmn

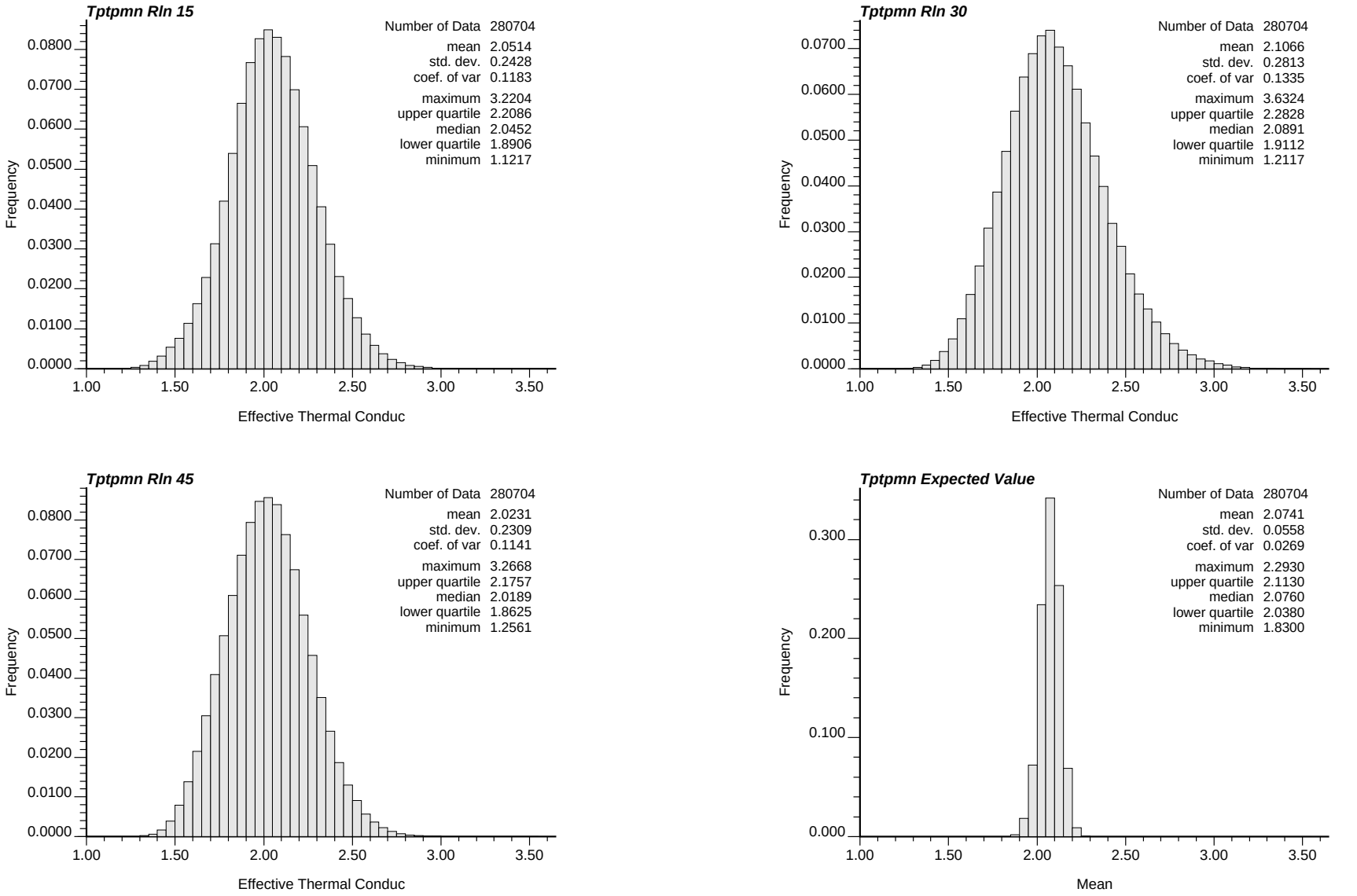

DTN: SN0208T0503102.007

Figure 7-37. Wet Bulk Thermal Conductivity (W m^{-1} K^{-1}) in the Tptpmn

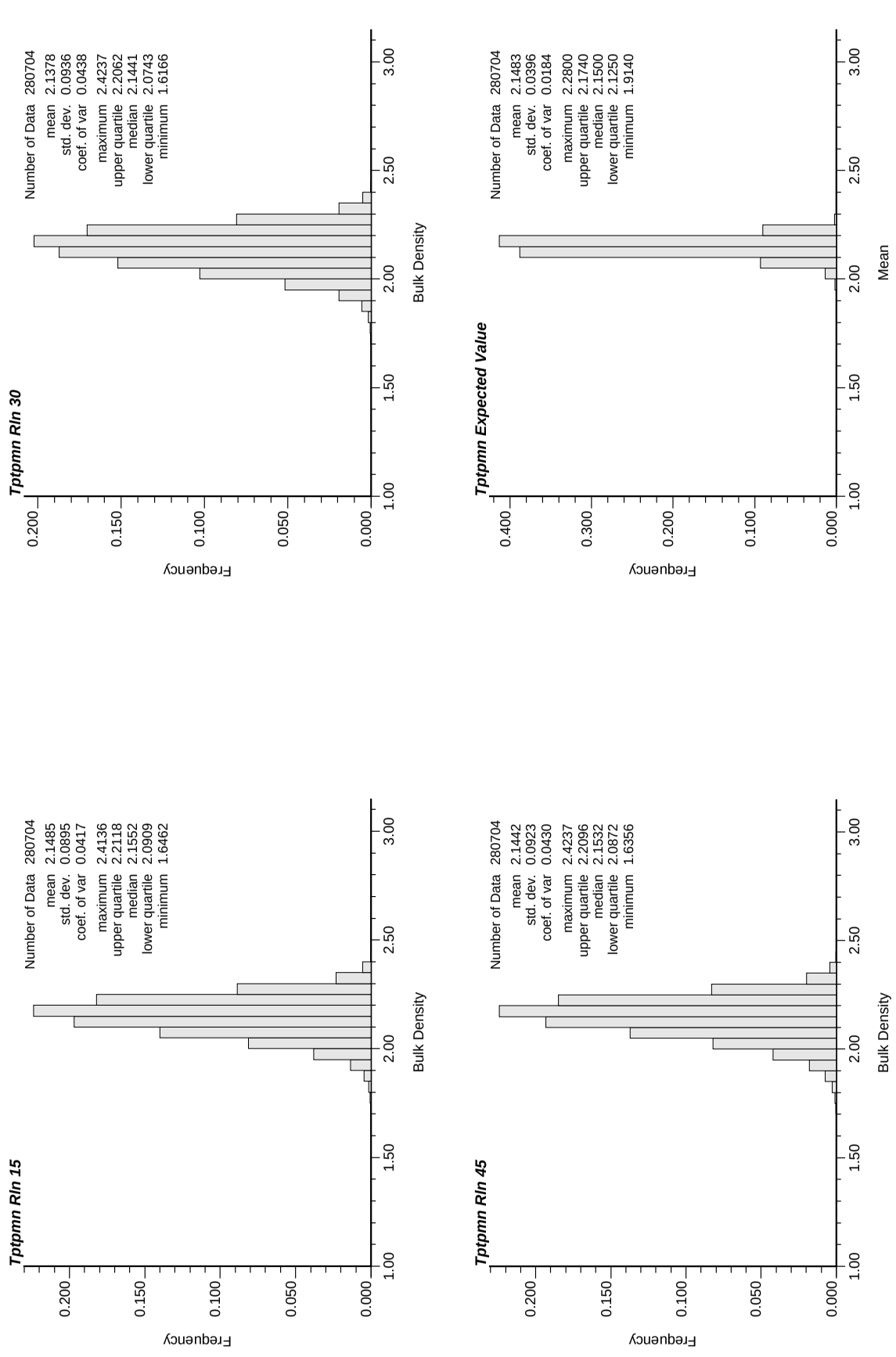

DTN: SN0208T0503102.007

Figure 7-38. Dry Bulk Density (g/cc) in the Tptpmn

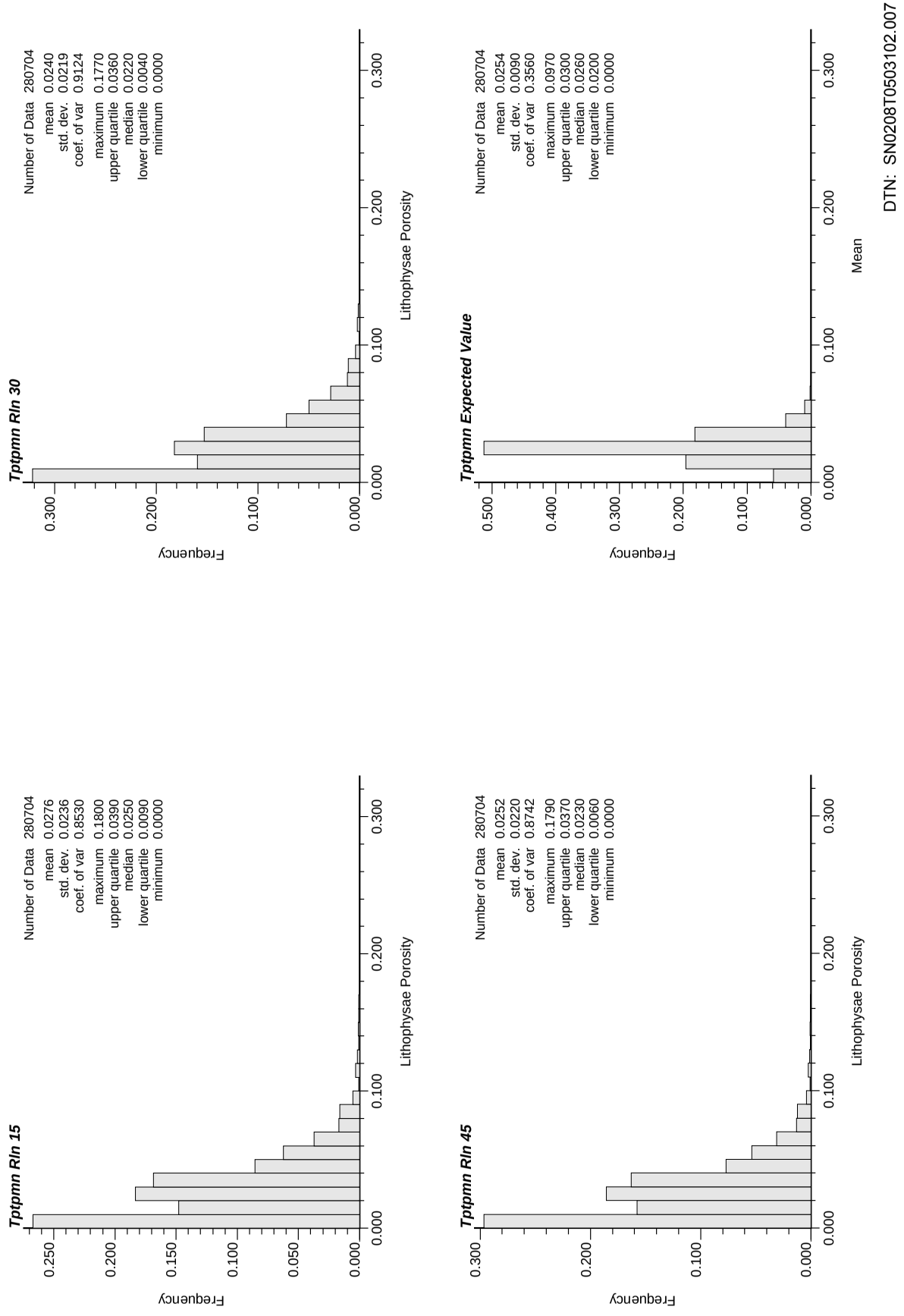

Figure 7-39. Lithophysal Porosity in the Tptpmn

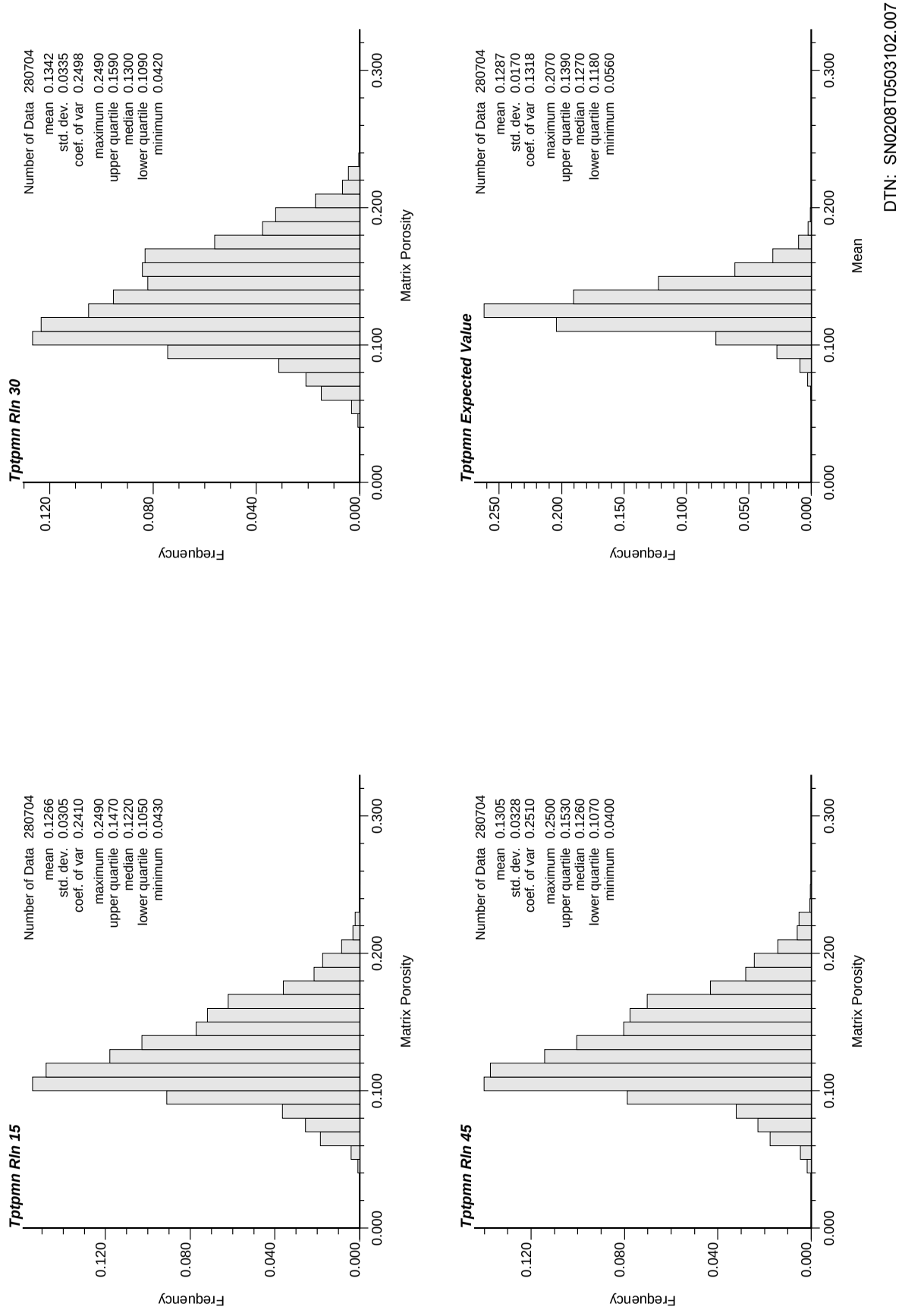

Figure 7-40. Matrix Porosity in the Tptpmn

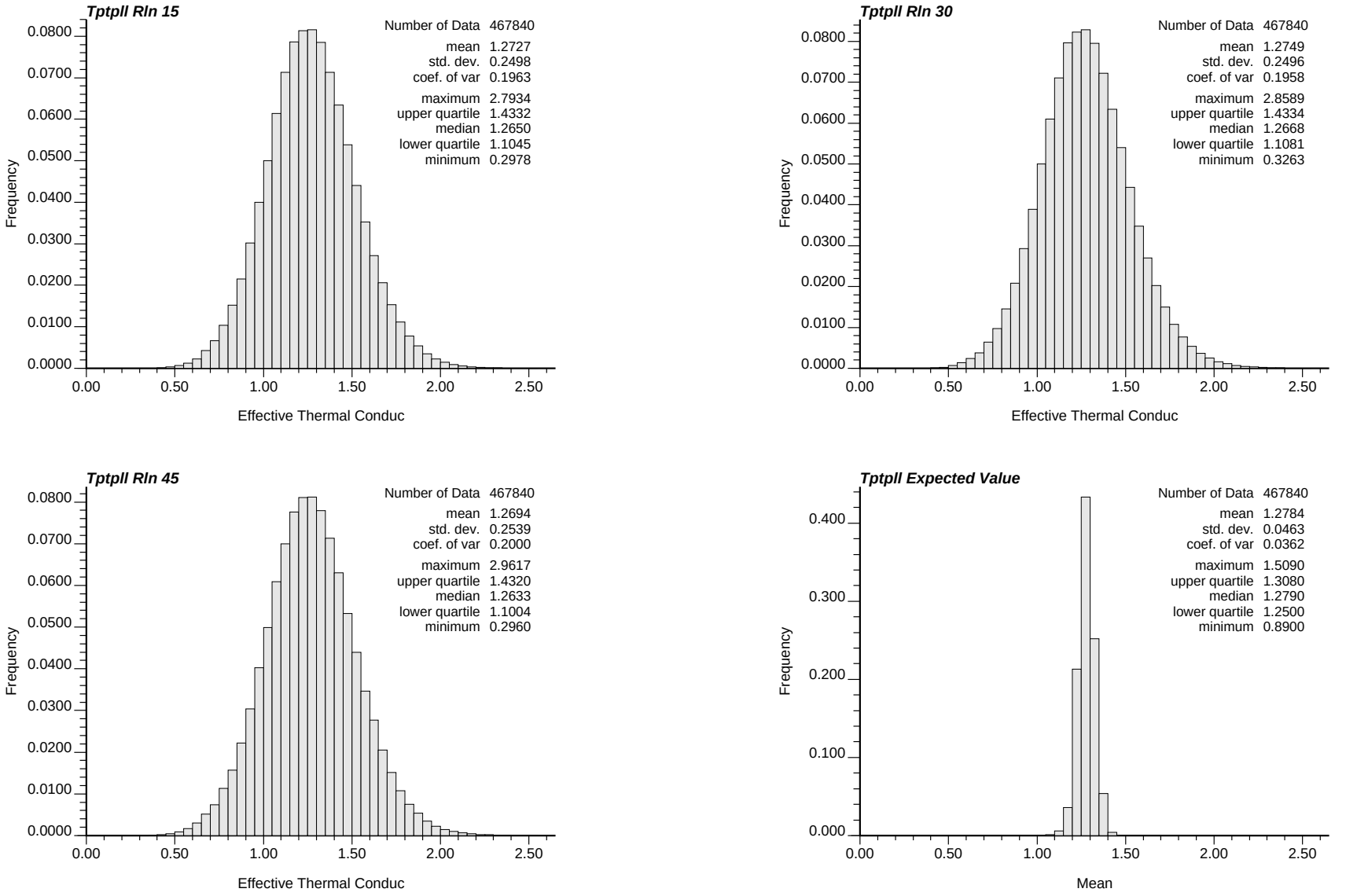

DTN: SN0208T0503102.007

Figure 7-41. Dry Bulk Thermal Conductivity (W m^{-1} K^{-1}) in the Tptpll

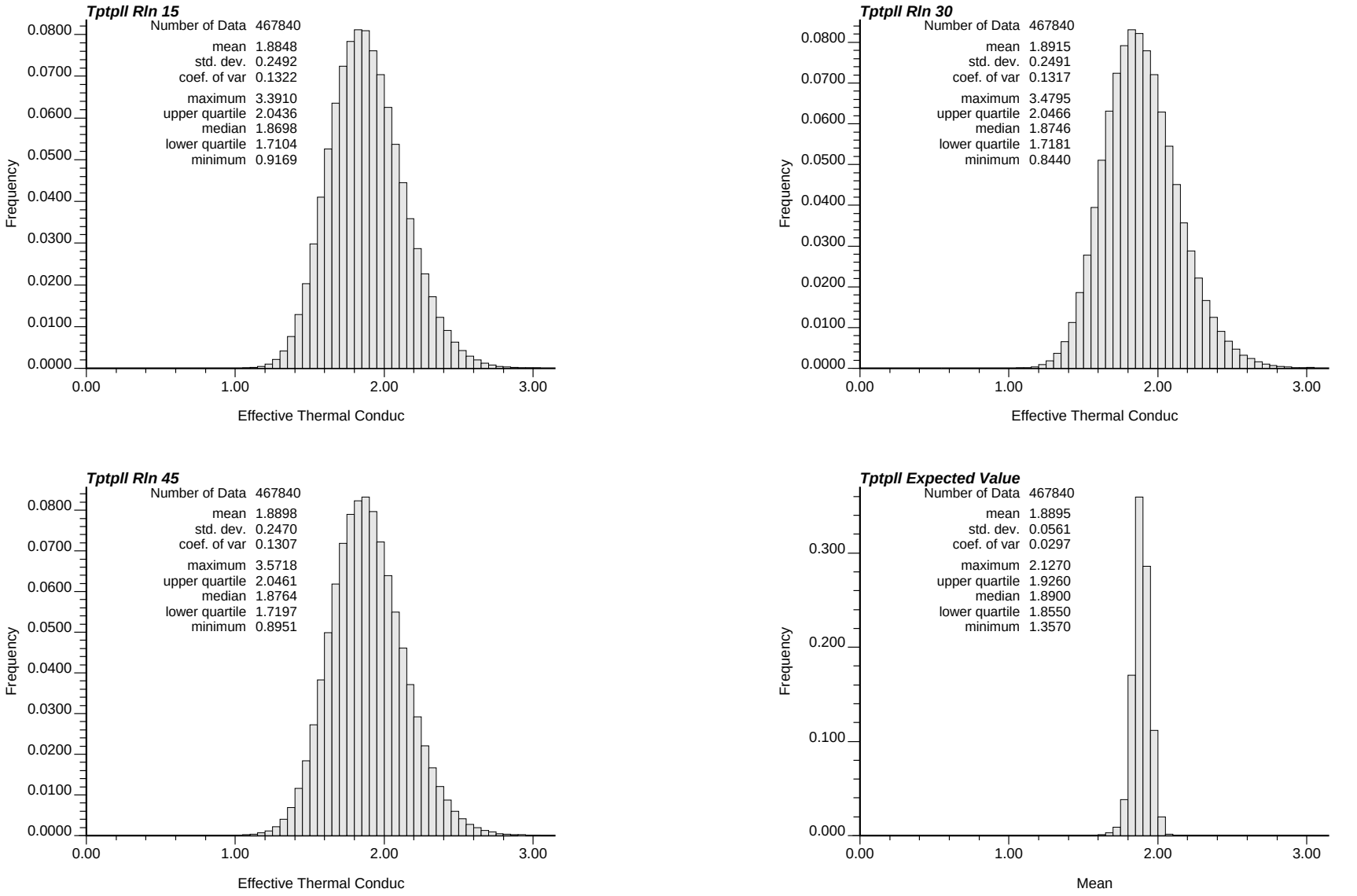

DTN: SN0208T0503102.007

Figure 7-42. Wet Bulk Thermal Conductivity (W m^{-1} K^{-1}) in the Tptpll

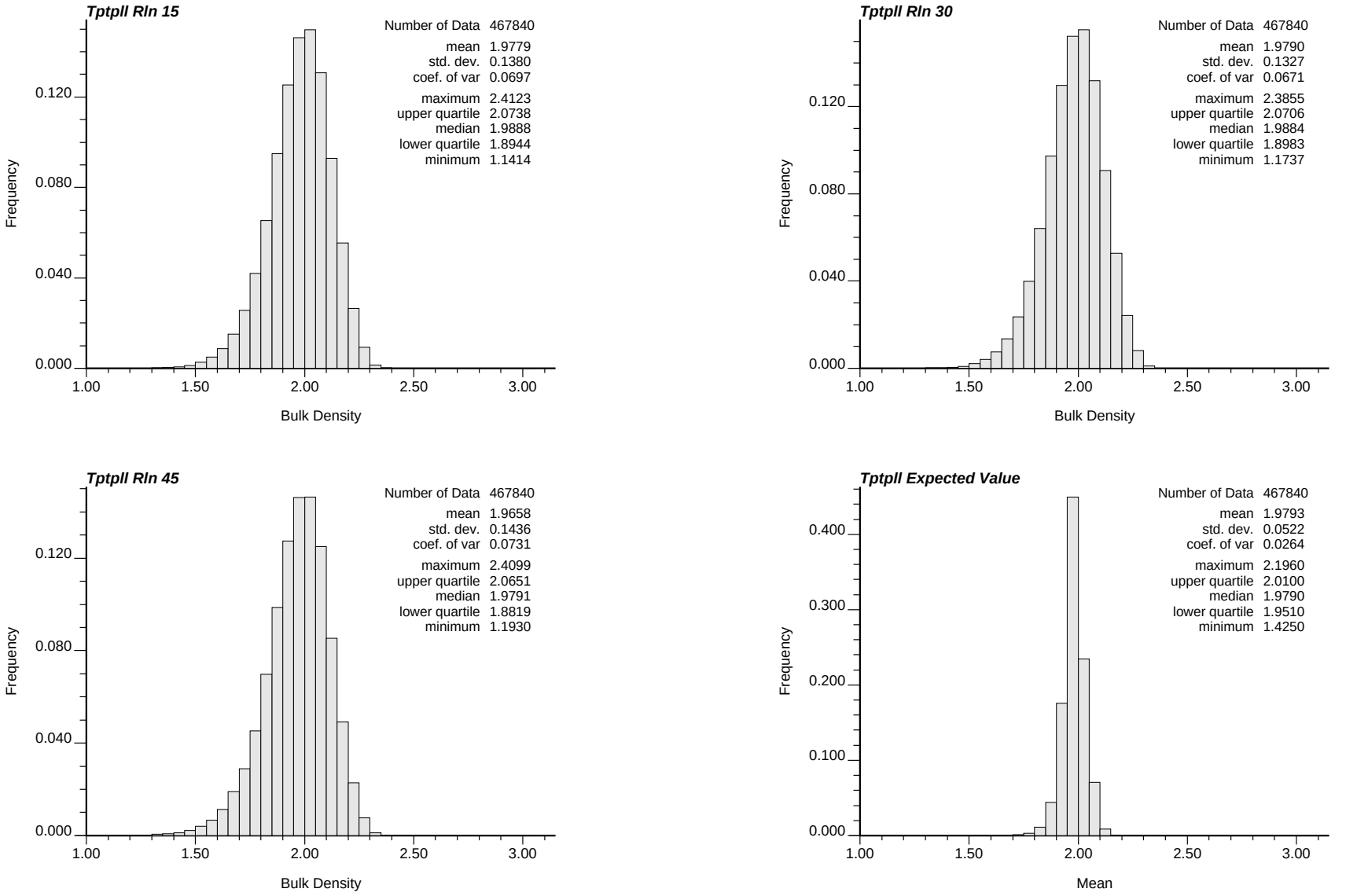

DTN: SN0208T0503102.007

Figure 7-43. Dry Bulk Density (g/cc) in the Tptpll

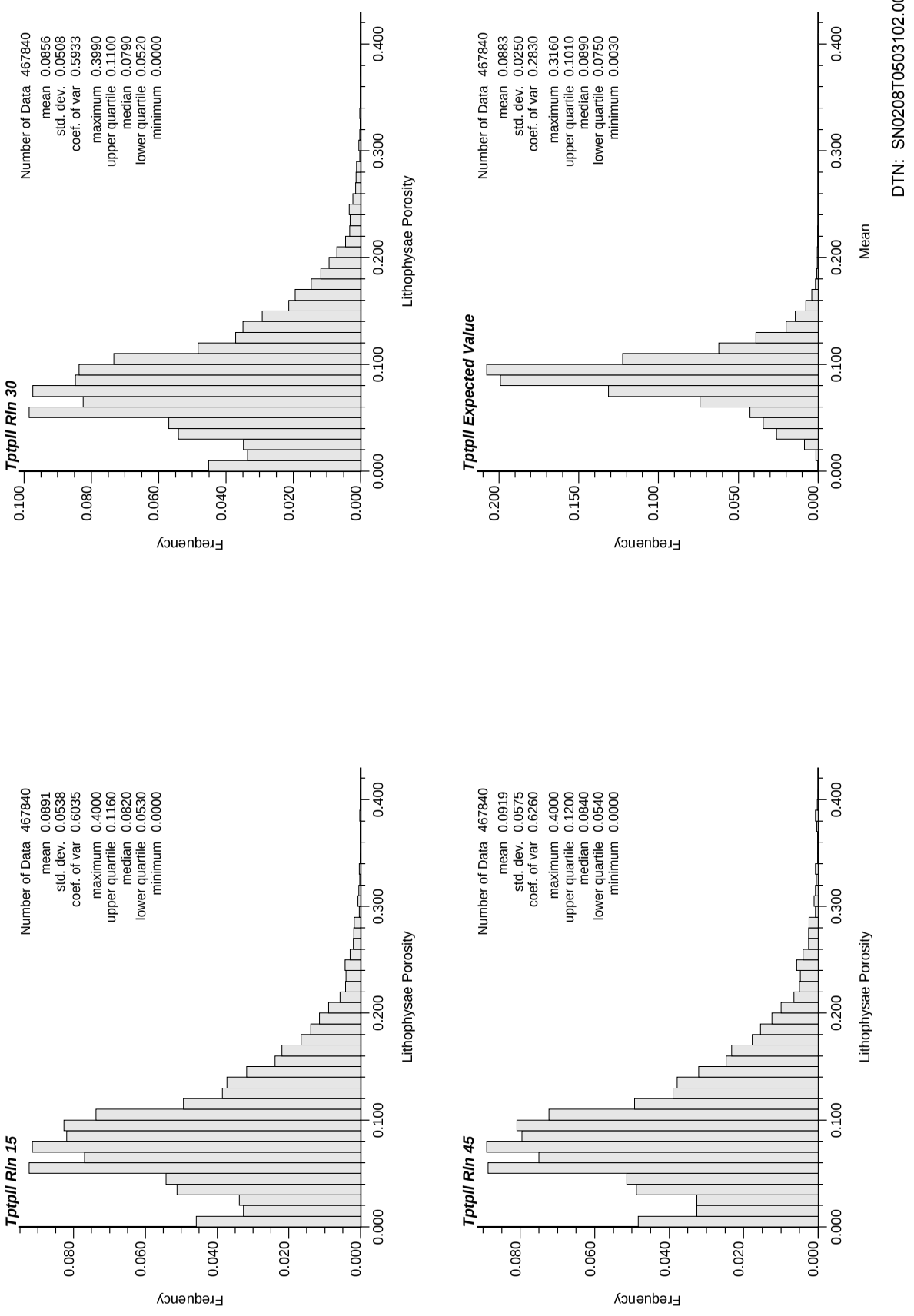

Figure 7-44. Lithophysal Porosity in the Tptpll

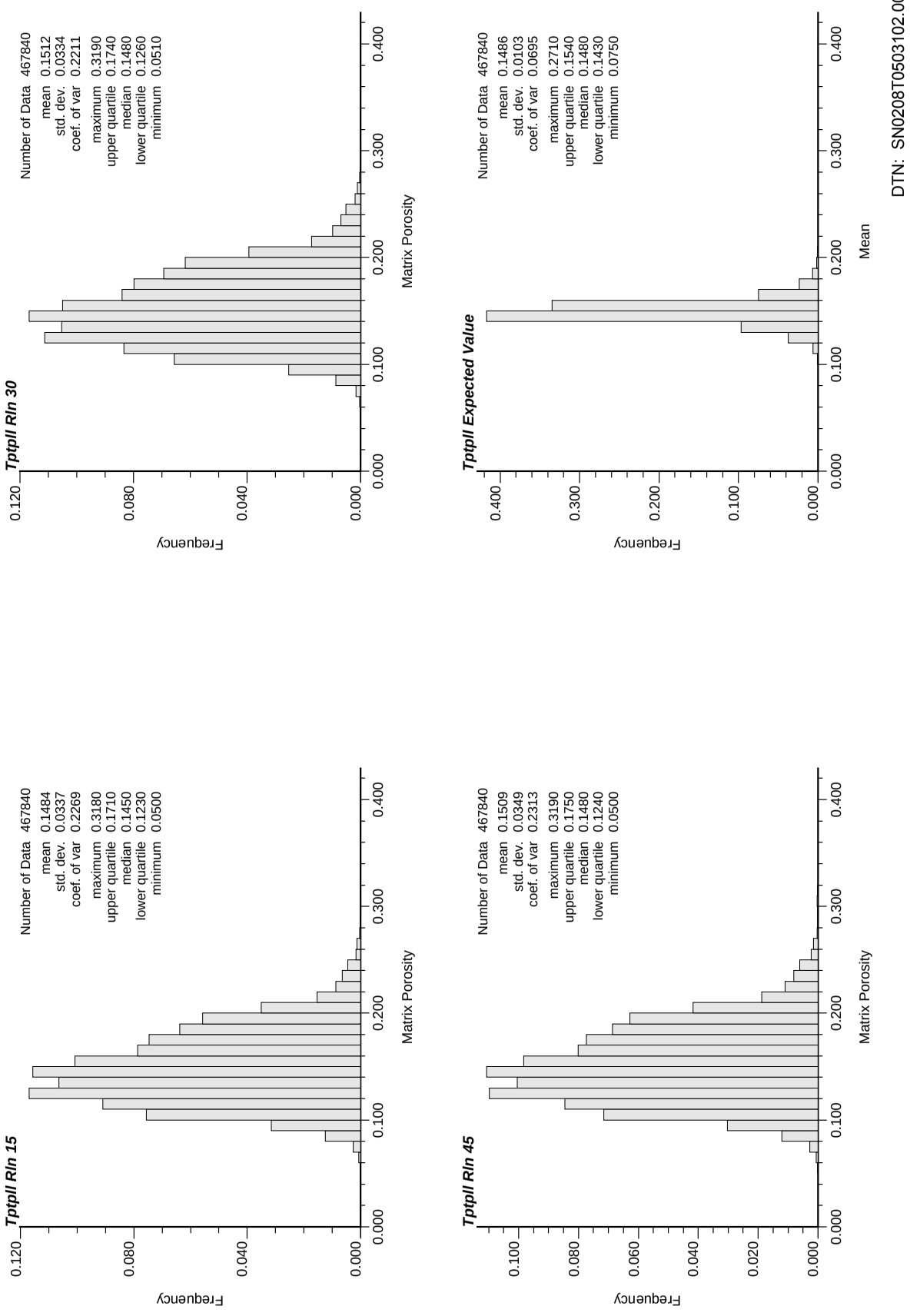

DTN: SN0208T0503102.007

Figure 7-45. Matrix Porosity in the Tptpll

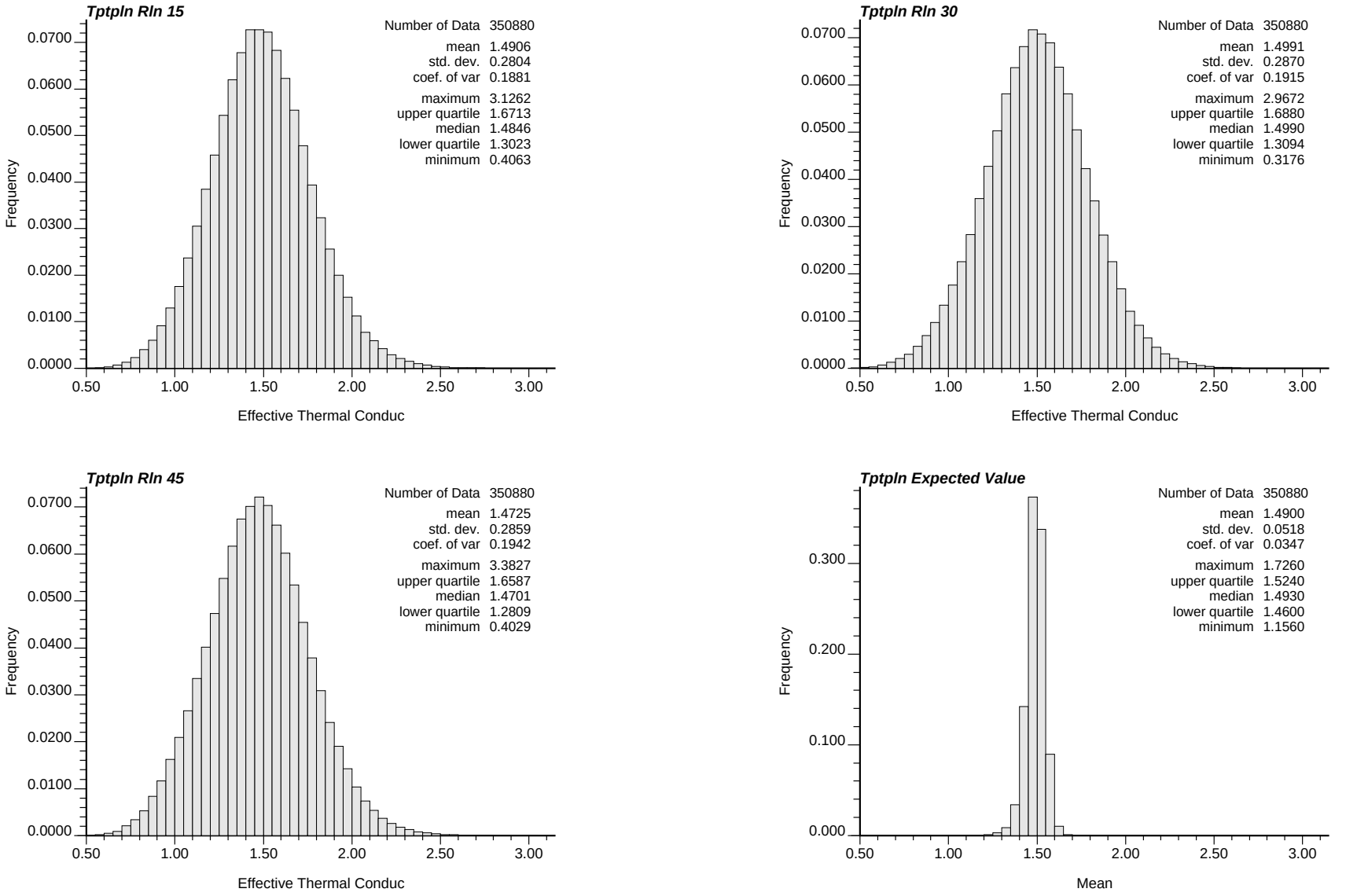

DTN: SN0208T0503102.007

Figure 7-46. Dry Bulk Thermal Conductivity (W m^{-1} K^{-1}) in the Tptpln

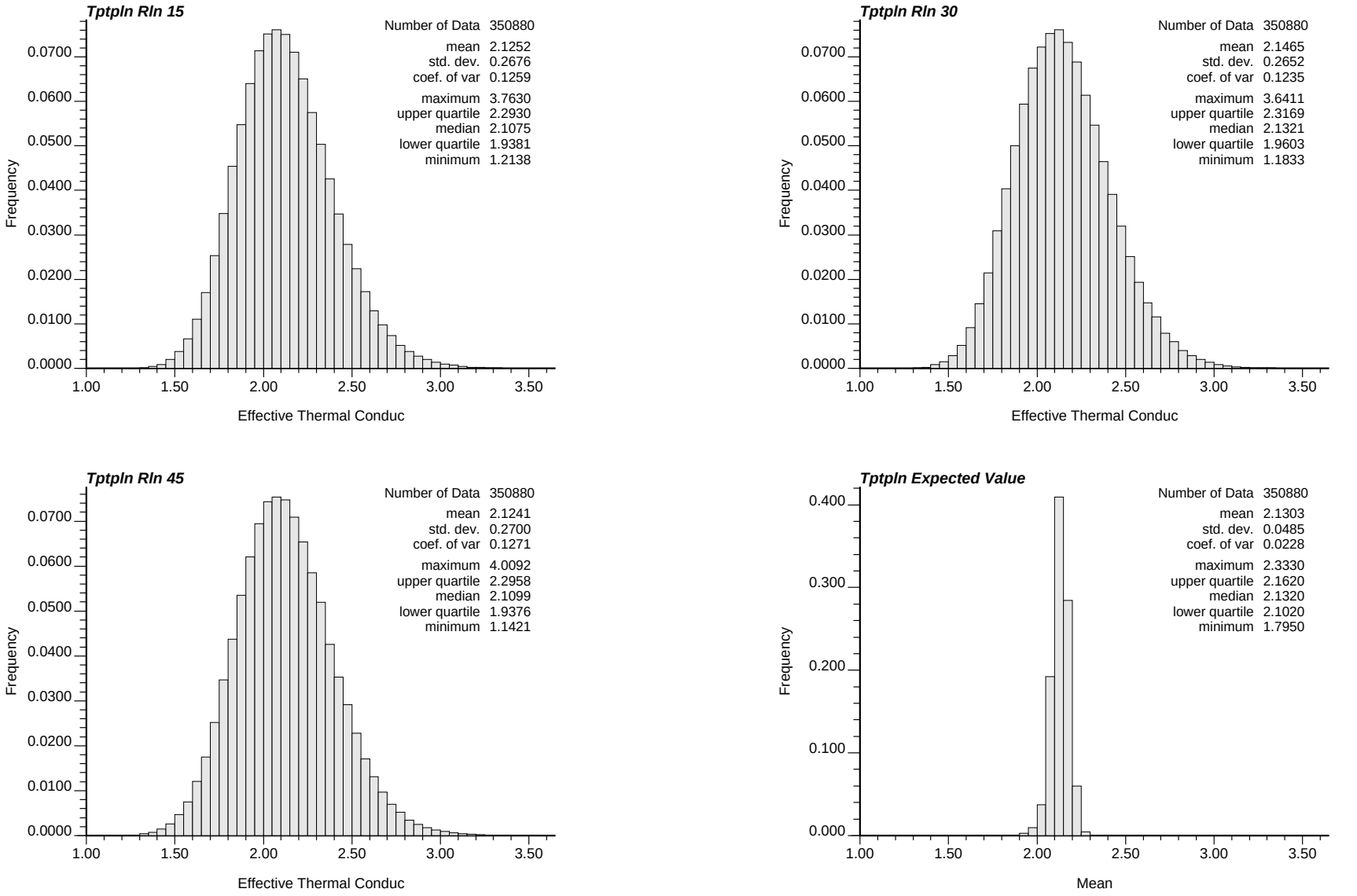

DTN: SN0208T0503102.007

Figure 7-47. Wet Bulk Thermal Conductivity (W m^{-1} K^{-1}) in the Tptpln

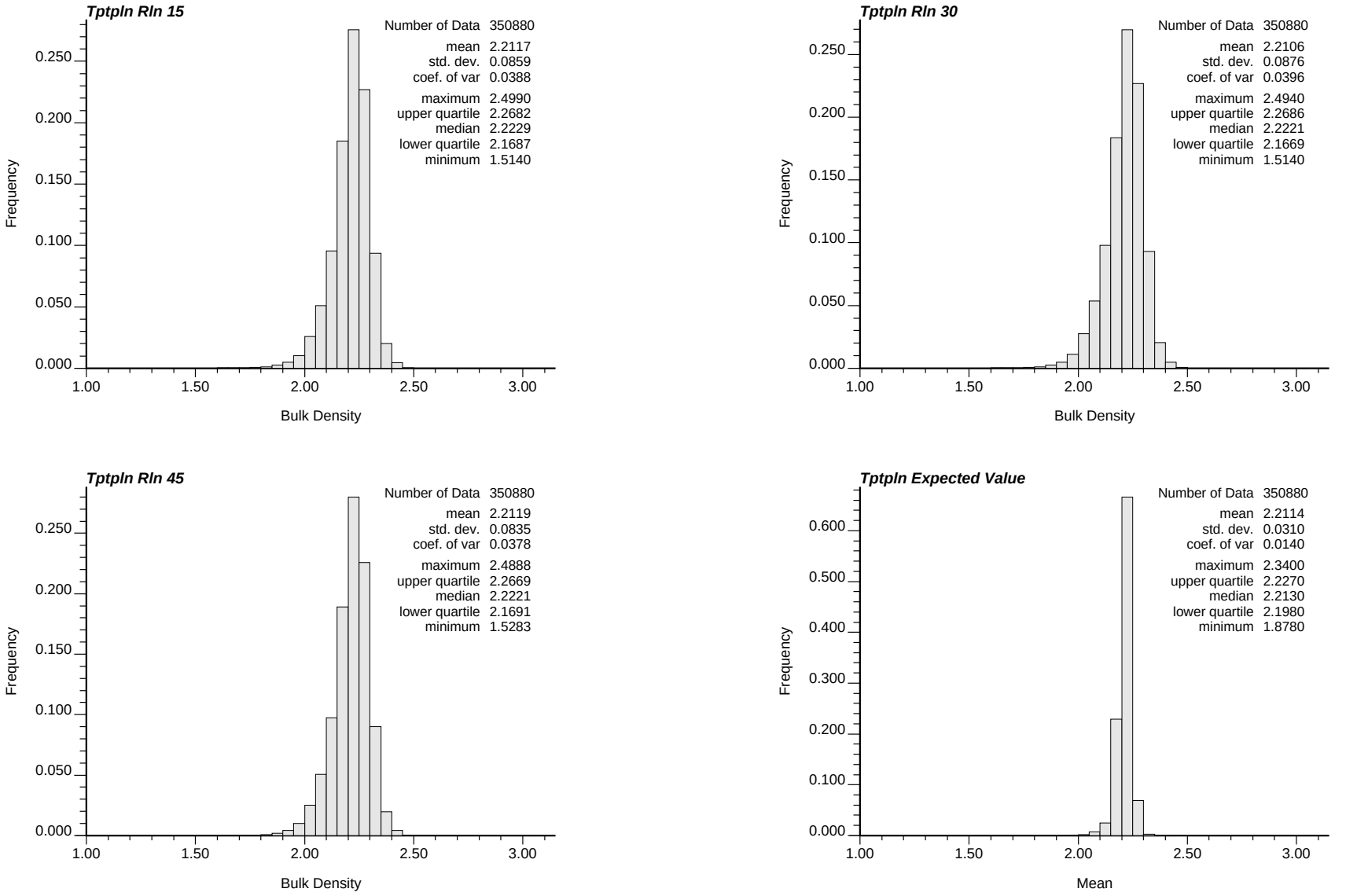

DTN: SN0208T0503102.007

Figure 7-48. Dry Bulk Density (g/cc) in the Tptpln

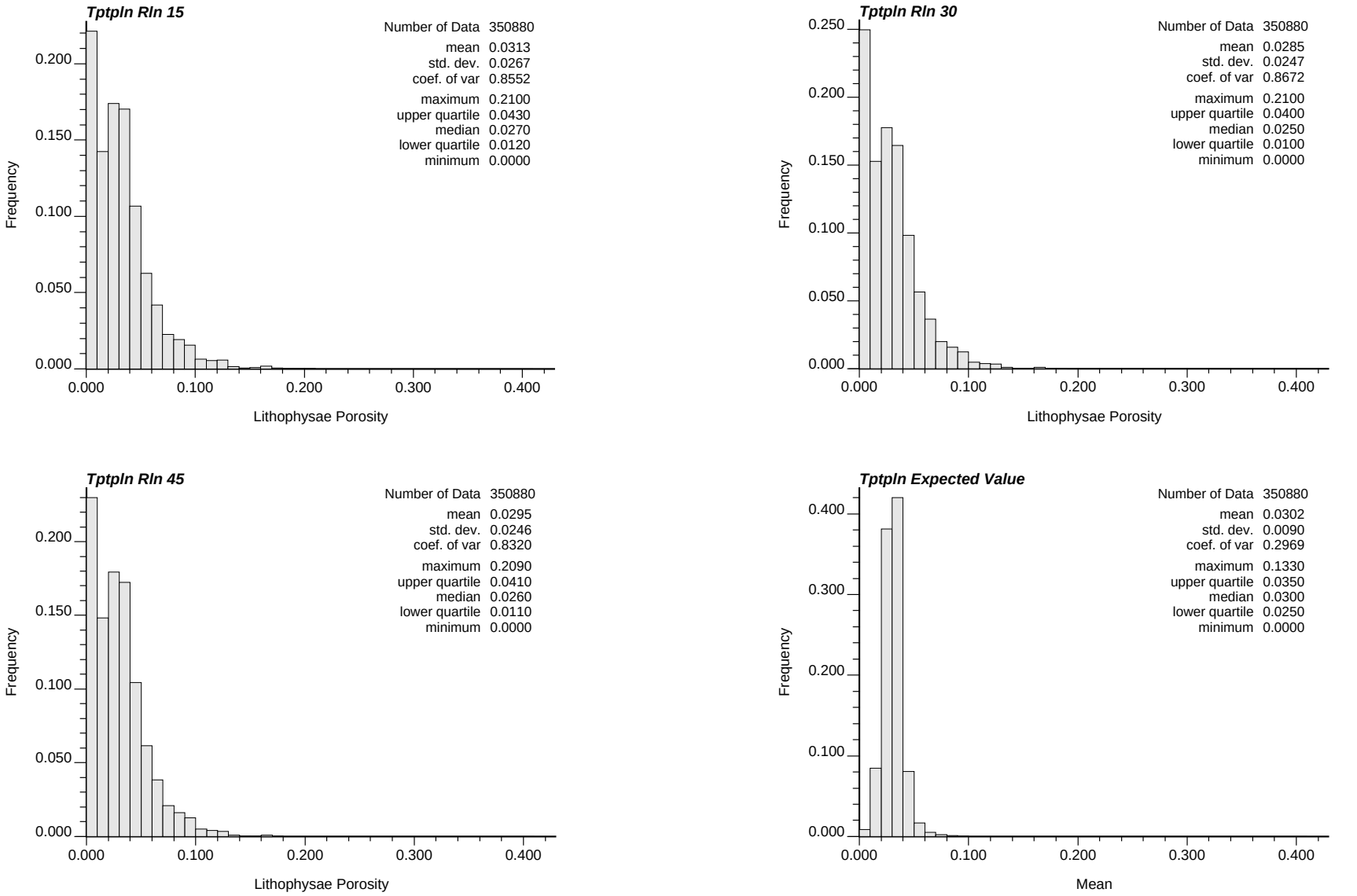

DTN: SN0208T0503102.007

Figure 7-49. Lithophysal Porosity in the Tptpln

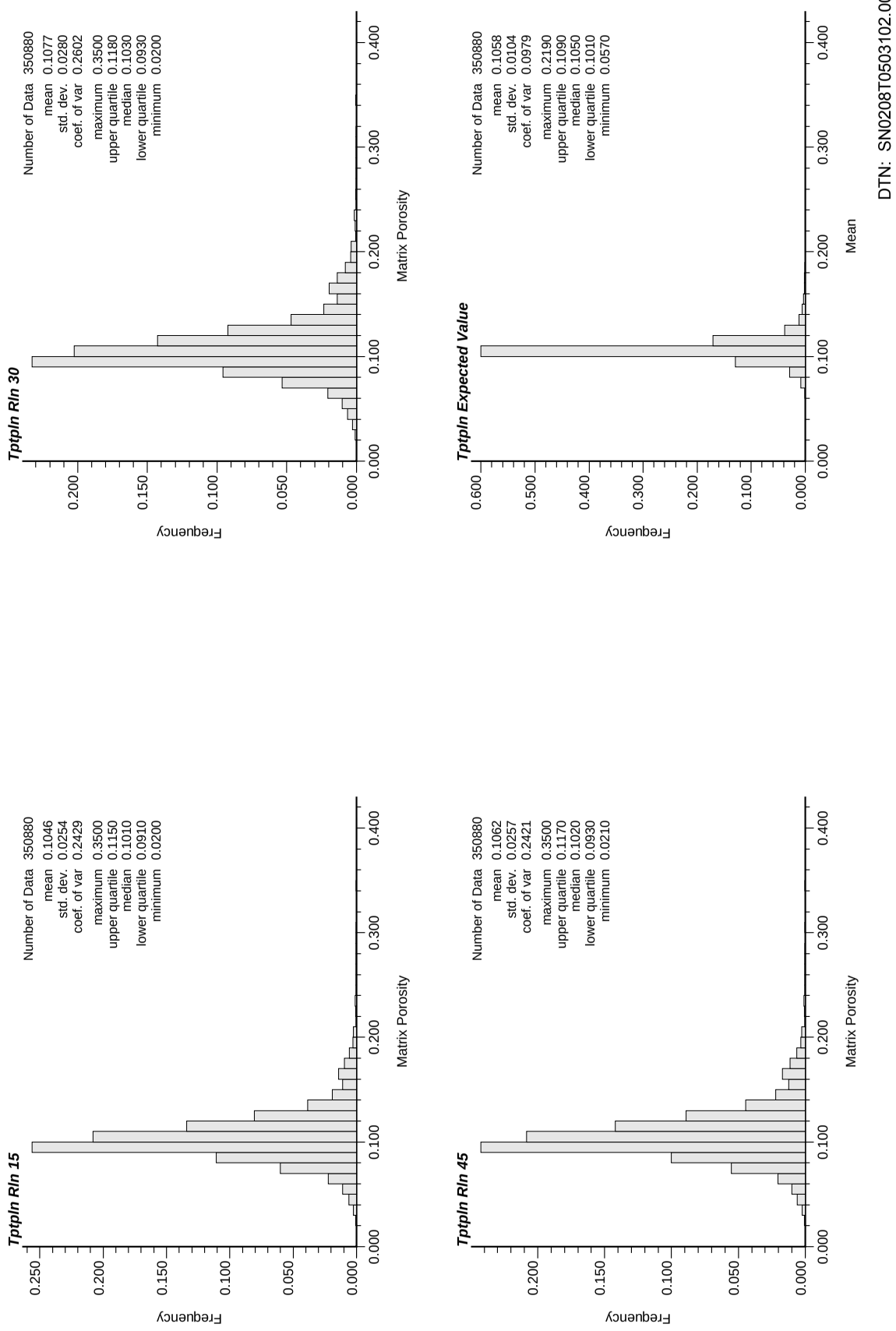

Figure 7-50. Matrix Porosity in the Tptpln

Planned and in progress in situ field thermal conductivity tests can be used to test the appropriateness of the current bulk thermal conductivity model. To date, these results appear to confirm the current model; however, the range of model predictions at the location of these tests sites is rather large. These tests may also be useful in determining the role, if any, of natural convection cells within lithophysae, radiative heat transfer, and vapor diffusion. All are issues that are not addressed in this work.

Aside from the uncertainty concerns raised, the model results are highly satisfactory. The results are internally consistent and reflect all pertinent measurements that have been acquired at Yucca Mountain. Significant effort has gone into collecting, analyzing, and filtering model inputs. The equations developed in Attachment I used to compute matrix and lithophysal porosity from petrophysical measurements of bulk density and neutron porosity are innovative. These equations provide a means of incorporating the relatively vast quantity of borehole petrophysical measurements collected at Yucca Mountain into the model and greatly improve the model's predictive capabilities. The model results are accurate and reflect the current understanding of the thermal conduction properties in the repository horizon.

9. INPUTS AND REFERENCES

9.1 DOCUMENTS CITED

Board, M.; Linden, A.; and Zhu, M. 2002. *Design Evolution Study—Underground Layout.* TDR-MGR-MG-000003 REV 00. Las Vegas, Nevada: Bechtel SAIC Company. ACC: MOL.20020429.0023.

Brodsky, N.S.; Riggins, M.; Connolly, J.; and Ricci, P. 1997. Thermal Expansion, Thermal Conductivity, and Heat Capacity Measurements for Boreholes UE25 NRG-4, UE25 NRG-5, USW NRG-6, and USW NRG-7/7A. SAND95-1955. Albuquerque, New Mexico: Sandia National Laboratories. ACC: MOL.19980311.0316.

BSC (Bechtel SAIC Company) 2001a. *FY 01 Supplemental Science and Performance Analyses, Volume 1: Scientific Bases and Analyses.* TDR-MGR-MD-000007 REV 00 ICN 01. Las Vegas, Nevada: Bechtel SAIC Company. ACC: MOL.20010801.0404; MOL.20010712.0062; MOL.20010815.0001.

BSC 2001b. *Multiscale Thermohydrologic Model.* ANL-EBS-MD-000049 REV 00 ICN 02. Las Vegas, Nevada: Bechtel SAIC Company. ACC: MOL.20020123.0279.

BSC 2002a. *Rock Properties Model Analysis Model Report.* MDL-NBS-GS-000004 REV 00 ICN 03. Las Vegas, Nevada: Bechtel SAIC Company. ACC: MOL.20020429.0086.

BSC 2002b. *Technical Work Plan for: The Integrated Site Model.* TWP-NBS-GS-000003 REV 02. Las Vegas, Nevada: Bechtel SAIC Company. ACC: MOL.20020417.0380.

BSC 2002c. *Mineralogic Model (MM3.0) Analysis Model Report.* MDL-NBS-GS-000003 REV 00 ICN 02. Las Vegas, Nevada: Bechtel SAIC Company. ACC: MOL.20020423.0151.

Buesch, D.C.; Spengler, R.W.; Moyer, T.C.; and Geslin, J.K. 1996. Proposed Stratigraphic Nomenclature and Macroscopic Identification of Lithostratigraphic Units of the Paintbrush Group Exposed at Yucca Mountain, Nevada. Open-File Report 94-469. Denver, Colorado: U.S. Geological Survey. ACC: MOL.19970205.0061.

Carslaw, H.S. and Jaeger, J.C. 1959. *Conduction of Heat in Solids*. 2nd Edition. Oxford, Great Britain: Oxford University Press. TIC: 206085.

CRWMS M&O (Civilian Radioactive Waste Management System Management and Operations) 1996. *Yucca Mountain Site Geotechnical Report.* BAAA00000-01717-4600-00065 REV 00. Las Vegas, Nevada: CRWMS M&O. ACC: MOL.19970425.0062.

CRWMS M&O 2000b. *Mineralogical Model (MM3.0) Analysis Model Report.* MDL-NBS-GS-000003 REV 00 ICN 02. Las Vegas, Nevada: CRWMS M&O. ACC: MOL.20020423.0151.

Deutsch, C.V. and Journel, A.G. 1992. *GSLIB Geostatistical Software Library and User's Guide.* New York, New York: Oxford University Press. TIC: 224174.

Deutsch, C.V. and Journel, A.G. 1998. *GSLIB Geostatistical Software Library and User's Guide.* 2nd Edition. New York, New York: Oxford University Press. TIC: 240101.

Flint, L.E. 1998. *Characterization of Hydrogeologic Units Using Matrix Properties, Yucca Mountain, Nevada.* Water-Resources Investigations Report 97-4243. Denver, Colorado: U.S. Geological Survey. ACC: MOL.19980429.0512.

Hadley, G.R. 1986. "Thermal Conductivity of Packed Metal Powders." *International Journal of Heat and Mass Transfer, 29,* (6), 909-920. [New York, New York]: Pergamon Journals. TIC: 249320.

Hillel, D. 1980. *Fundamentals of Soil Physics.* New York, New York: Academic Press. TIC: 215655.

Holman, J.P. 1997. *Heat Transfer.* 8th Edition. New York, New York: McGraw-Hill. TIC: 239954.

Howard, C. 2002. Thermal K Field Program, Thermal Conductivity Field Measurements. Scientific Notebook SN-SNL-SCI-024-V1. ACC: MOL.20020619.0494.

Hsu, C.T.; Cheng, P.; and Wong, K.W. 1995. "A Lumped-Parameter Model for Stagnant Thermal Conductivity of Spatially Periodic Porous Media." *Journal of Heat Transfer, 117,* (2), 264-269. New York, New York: American Society of Mechanical Engineers. TIC: 252402.

Isaaks, E.H. and Srivastava, R.M. 1989. *Applied Geostatistics.* New York, New York: Oxford University Press. TIC: 200301.

Kaviany, M. 1991. *Principles of Heat Transfer in Porous Media.* New York, New York: Springer-Verlag. TIC: 240655.

Kunii, D. and Smith, J.M. 1960. "Heat Transfer Characteristics of Porous Rocks." *American Institute of Chemical Engineers Journal, 6,* (1), 71-78. [New York, New York: American Institute of Chemical Engineers]. TIC: 249321.

Maxwell, J.C. 1954. *A Treatise on Electricity and Magnetism.* 3rd Edition (unabridged). Two volumes. New York, New York: Dover Publications. TIC: 252475.

Mongano, G.S.; Singleton, W.L.; Moyer, T.C.; Beason, S.C.; Eatman, G.L.W.; Albin, A.L.; and Lung, R.C. 1999. *Geology of the ECRB Cross Drift - Exploratory Studies Facility, Yucca Mountain Project, Yucca Mountain, Nevada.* [Deliverable SPG42GM3]. Denver, Colorado: U.S. Geological Survey. ACC: MOL.20000324.0614.

Paces, J.B.; Neymark, L.A.; Marshall, B.D.; Whelan, J.F.; and Peterman, Z.E. 2001. *Ages and Origins of Calcite and Opal in the Exploratory Studies Facility Tunnel, Yucca Mountain, Nevada.* Water-Resources Investigations Report 01-4049. Denver, Colorado: U.S. Geological Survey. TIC: 251284.

Rohsenow, W.M. and Choi, H.Y. 1961. *Heat, Mass, and Momentum Transfer.* Englewood Cliffs, New Jersey: Prentice-Hall. TIC: 249864.

SNL (Sandia National Laboratories) 1998. *Laboratory Measurements of Thermal Conductivity as a Function of Saturation State for Welded and Nonwelded Tuff Specimens.* Albuquerque, New Mexico: Sandia National Laboratories. ACC: MOL.19980901.0177.

Stephens, H.P. and Sinnock, S. 1979. *Thermophysical Properties of Rock--A Perspective on Data Needs, Sources and Accuracy.* [SAND79-1259C]. Albuquerque, New Mexico: Sandia National Laboratories. TIC: 229997.

YMP (Yucca Mountain Site Characterization Project) 1997. Sample Collection Report for Bulk Rock Sample Collected by A. Mitchell, May 7, 1997. SP000522296. Las Vegas, Nevada: Yucca Mountain Site Characterization Office. ACC: DRC.19970714.0039.

YMP 2001. *Q-List.* YMP/90-55Q, Rev. 7. Las Vegas, Nevada: Yucca Mountain Site Characterization Office. ACC: MOL.20010409.0366.

9.2 CODES, STANDARDS, REGULATIONS, AND PROCEDURES

10 CFR 63. Energy: Disposal of High-Level Radioactive Wastes in a Geologic Repository at Yucca Mountain, Nevada. Readily available.

AP-2.21Q, Rev. 1, ICN 0, BSCN 001. *Quality Determinations and Planning for Scientific, Engineering, and Regulatory Compliance Activities.* Washington, D.C.: U.S. Department of Energy, Office of Civilian Radioactive Waste Management. ACC: MOL.20010212.0018.

AP-2.22Q, Rev. 0, ICN 0. *Classification Criteria and Maintenance of the Monitored Geologic Repository Q-List.* Washington, D.C.: U.S. Department of Energy, Office of Civilian Radioactive Waste Management. ACC: MOL.20020314.0046.

AP-3.15Q, Rev. 3, ICN 2. *Managing Technical Product Inputs.* Washington, D.C.: U.S. Department of Energy, Office of Civilian Radioactive Waste Management. ACC: MOL.20020423.0155.

AP-SI.1Q, Rev. 3, ICN 4. *Software Management.* Washington, D.C.: U.S. Department of Energy, Office of Civilian Radioactive Waste Management. ACC: MOL.20020520.0283

AP-SV.1Q, Rev. 0, ICN 2. *Control of the Electronic Management of Information.* Washington, D.C.: U.S. Department of Energy, Office of Civilian Radioactive Waste Management. ACC: MOL.20000831.0065.

9.3 SOURCE DATA, LISTED BY DATA TRACKING NUMBER

GS980808312242.014. Physical Properties of Borehole Core Samples and Water Potential Measurements Using the Filter Paper Technique for Borehole Samples from USW SD-6. Submittal date: 08/11/1998.

GS991108314224.015. Geology of the ECRB Cross Drift: Tabular Data. Submittal date: 11/05/1999.

MO0004QGFMPICK.000. Lithostratigraphic Contacts from MO9811MWDGFM03.000 to be Qualified Under the Data Qualification Plan, TDP-NBS-GS-000001. Submittal date: 04/04/2000.

MO0010CPORGLOG.002. Calculated Porosity from Geophysical Logs Data from "Old 40" Boreholes. Submittal date: 10/16/2000.

MO0010CPORGLOG.003. Calculated Porosity Values at Depth Derived from Qualified Geophysical Log Data from Modern Boreholes. Submittal date: 10/16/2000.

MO0012MWDGFM02.002. Geologic Framework Model (GFM2000). Submittal date: 12/18/2000.

MO0109HYMXPROP.001. Matrix Hydrologic Properties Data. Submittal date: 09/17/2001.

MO0205GSC02068.000. Alcove #5 Turn Out Samples Exploratory Studies Facilities (ESF). Submittal date: 05/30/2002.

MO0205GSC02070.000. As-Built Enhanced Characterization of the Repository Block (ECRB) Thermal Conductivity Borehole TK1, TK2, TK9, TK10, and TK11 Collars. Submittal date: 05/30/2002.

MO9510RIB00002.004. RIB Item: Stratigraphic Characteristics: Geologic/Lithologic Stratigraphy. Submittal date: 06/26/1996.

MO9906GPS98410.000. Yucca Mountain Project (YMP) Borehole Locations. Submittal date: 06/23/1999.

SN0205F3504502.010. Thermal Conductivity Field Program: Average Values of Abundance of Lithostratigraphic Features for Boreholes THERMK-001 through THERM-011. Submittal date: 05/17/02.

SN0206F3504502.012. Revised Thermal Conductivity, Volumetric Heat Capacity and Thermal Diffusivity Data for ECRB Thermal K Test 1 (Two-Hole Test). Submittal date: 06/07/2002.

SN0206F3504502.013. Revised Thermal Conductivity, Volumetric Heat Capacity and Thermal Diffusivity Data for ECRB Thermal K Test 3 (Three-Hole Test, with Results from 1/22/2002 through 4/9/2002). Submittal date: 06/07/2002.

SN9910T0501399.001. Three-Dimensional Rock Property Models for FY99 (RPM3.1). Submittal date: 10/18/1999.

SNF40060298001.001. Unsaturated Zone Lithostratigraphic Contacts in Borehole USW SD-6. Submittal date: 10/15/1998.

SNL01A05059301.005. Laboratory Thermal Conductivity Data for Boreholes UE25 NRG-4, NRG-5; USW NRG-6 and NRG-7/7A. Submittal date: 02/07/1996.

SNL01A05059301.007. Calculated Porosities for Thermal Conductivity Specimens from Boreholes UE25 NRG-4, UE25 NRG-5, USW NRG-6, and USW NRG-7/7a. Submittal date: 10/14/1998.

SNL22100196001.001. Thermal Expansion and Thermal Conductivity of Test Specimens from the Drift Scale Test Area of the Exploratory Studies Facility at Yucca Mountain, Nevada. Submittal date: 05/14/1997.

SNL22100196001.002. Laboratory Measurements of Thermal Expansion and Thermal Conductivity for Test Specimens from Alcove 5 and 7 and from SD Drill Holes of the Exploratory Studies Facility at Yucca Mountain, Nevada. Submittal date: 08/25/97.

SNL22100196001.006. Laboratory Measurements of Thermal Conductivity as a Function of Saturation State for Welded and Nonwelded Tuff Specimens. Submittal date: 06/08/1998.

9.4 SOFTWARE CODES

EARTHVISION. V. 5.1. Silicon Graphics Indigo R4000. 10174-5.1-00.

Etype. V. 2.01. PC Windows 2000 Server. 10731-2.01-00.

GSLIB. V. 1.0MGAMV2V1.201. 10087-1.0MGAMV2V1.201-02.

GSLIB. V. 1.4MBACKTRV1.20. V1.20. ACC: MOL.19981027.0187.

GSLIB. V. 1.4SGSIMV1.41. STN: 10110-1.4SGSIMV1.41-00.

GSLIB. V. 1.4MNSCOREV1.201. STN: 10109-1.4MNSCOREV1.201-02.

GSLIB. HISTPLT V. 2.01. STN: 10802-2.01-00.

HsuInv. V. 1.0. STN: 10804-1.0-00.

LITHO. V. 1.0. STN: 10800-1.0-00.

MODGEOM. V.1.02. STN: 10597-1.02-01.

POINT. V1.0. 10826-1.0-00.

SMOOTH. V.1.0. STN: 10734-1.0-01.

TCOND. V.1.0. STN: 10801-1.0-00.

9.5 OUTPUT DATA, LISTED BY DATA TRACKING NUMBER

SN0208T0503102.007. Thermal Conductivity of the Potential Repository Horizon, Rev 3. J.L. Ramsey. Albuquerque, New Mexico: Sandia National Laboratories.

10. ATTACHMENTS

I. CALCULATIONS OF MATRIX AND LITHOPHYSAL POROSITY
II INPUT DATA ANALYSIS
III MATRIX THERMAL CONDUCTIVITY DATA
IV STRATIGRAPHIC CONTACTS
V ACRONYMS AND ABBREVIATIONS

ATTACHMENT I
CALCULATIONS OF MATRIX AND LITHOPHYSAL POROSITY

INTENTIONALLY LEFT BLANK

ATTACHMENT I
CALCULATIONS OF MATRIX AND LITHOPHYSAL POROSITY

Method A:

In this section an expression for lithophysal porosity based on matrix porosity, bulk density, particle (grain) density, and matrix water saturation is derived. A representative bulk volume of rock, V_b, can be partitioned into matrix volume, V_m, and lithophysae volume, V_L.

$$V_b = V_m + V_L \quad \text{(Eq. I-1)}$$

The matrix volume, V_m, can be partitioned into a volume of matrix solids, V_{ms}, and a volume of matrix pore-space, V_{mv}. It is assumed that the solids, V_{ms}, occur only in the matrix volume, V_m.

$$V_m = V_{ms} + V_{mv} \quad \text{(Eq. I-2)}$$

Matrix porosity, ϕ_m, is defined as the ratio of the volume of the matrix pore-space, V_{mv}, to the volume of the matrix, V_m.

$$\phi_m = \frac{V_{mv}}{V_m} \quad \text{(Eq. I-3)}$$

Combining Equations I-2 and I-3, the volume of solids, V_{ms}, can be written as follows:

$$V_{ms} = V_m(1 - \phi_m) \quad \text{(Eq. I-4)}$$

Matrix water saturation, S_w, is defined as the ratio of the volume of water in the matrix pores, V_w, to the volume of the matrix pores, V_{mv}. The matrix pore space is assumed to contain water and air, while the lithophysae are assumed to be air filled. The lithophysae are air filled as a result of capillary forces that tend to hold water within the small-scale matrix voids.

$$S_w = \frac{V_w}{V_{mv}} \quad \text{(Eq. I-5)}$$

Using Equations I-3 and I-5 gives:

$$V_w = \phi_m S_w V_m \quad \text{(Eq. I-6)}$$

Grain density, ρ_s, is defined as the ratio of the mass of the solids, m_s, to the volume of solids, V_s, while water density, ρ_w, is the ratio of the mass of water in the matrix pore-space, m_w, to the volume of the water, V_w. Bulk density, ρ_b, is defined as the ratio of the mass of solids, m_s, plus mass of water, m_w, to the bulk volume, V_b. It is assumed that the mass of air occupying

the pore-space is negligible compared to the mass of solids and water in the definition of bulk density.

$$\rho_s = \frac{m_s}{V_{ms}} \quad \text{(Eq. I-7)}$$

$$\rho_w = \frac{m_w}{V_w} \quad \text{(Eq. I-8)}$$

$$\rho_b = \frac{m_w + m_s}{V_b} \quad \text{(Eq. I-9)}$$

Using Equations I-7 through 9, the bulk density, ρ_b, can be written in terms of water and solid densities and volumes as follows:

$$\rho_b = \frac{V_w \rho_w + V_{ms} \rho_s}{V_b} \quad \text{(Eq. I-10)}$$

Substituting Equations I-4 and I-6 into Equation I-10 gives:

$$\rho_b = \frac{\phi_m S_w \rho_w V_m + (1 - \phi_m) \rho_s V_m}{V_b} \quad \text{(Eq. I-11)}$$

Solving for the matrix volume, V_m gives:

$$V_m = \frac{\rho_b V_b}{\phi_m S_w \rho_w + (1 - \phi_m) \rho_s} \quad \text{(Eq. I-12)}$$

Lithophysal porosity, ϕ_L, is defined as the volume of lithophysae pore-space, V_L, to the bulk volume, V_b:

$$\phi_L = \frac{V_L}{V_b} = \frac{V_b - V_m}{V_b} = 1 - \frac{V_m}{V_b} \quad \text{(Eq. I-13)}$$

Substituting the expression for matrix volume, V_m, from Equation I-12 into Equation I-13 gives:

$$\phi_L = 1 - \frac{\rho_b}{\phi_m S_w \rho_w + (1 - \phi_m) \rho_s} \quad \text{(Eq. I-14)}$$

Equation I-14 gives an expression for calculating lithophysal porosity, provided estimates of bulk density, grain density, matrix water saturation, and matrix porosity are available. The bulk density, ρ_b, is obtained from petrophysical logging. The remaining parameters are obtained from laboratory tests on core samples.

Method B:

In this section expressions for matrix and lithophysal porosity based on bulk density, particle (grain) density, volumetric water content, and matrix water saturation are derived.

The volumetric water content, V_{wc}, is defined as the ratio of volume of water in the matrix pores, V_w, to the bulk volume, V_b:

$$V_{wc} = \frac{V_w}{V_b} \quad \text{(Eq. I-15)}$$

Combining Equations I-5 and I-15 gives:

$$V_w = S_w V_{mv} = V_{wc} V_b \quad \text{(Eq. I-16)}$$

Solving Equation I-16 for the volume of matrix voids ($S_w \neq 0, V_{wc} \neq 0$):

$$V_{mv} = \frac{V_{wc} V_b}{S_w} \quad \text{(Eq. I-17)}$$

Using Equations I-3 and I-17 in Equation I-4 gives:

$$V_{ms} = V_m \left(1 - \frac{V_{wc} V_b}{V_m S_w} \right) \quad \text{(Eq. I-18)}$$

Using Equations I-15 and I-18 in Equation I-10 gives:

$$\rho_b = \frac{V_{wc} V_b \rho_w + V_m \rho_s - \frac{V_{wc} V_b \rho_s}{S_w}}{V_b} \quad \text{(Eq. I-19)}$$

Solving Equation I-19 for V_m gives:

$$V_m = \frac{\left(\rho_b - V_{wc} \rho_w + \frac{V_{wc} \rho_s}{S_w} \right) V_b}{\rho_s} \quad \text{(Eq. I-20)}$$

From Equations I-3, I-17, and I-20 and expression for matrix porosity, ϕ_m, is obtained:

$$\phi_m = \frac{V_{mv}}{V_m} = \frac{V_{wc} V_b}{S_w V_m} \quad \text{(Eq. I-21)}$$

$$\phi_m = \frac{\rho_s}{S_w\left(\frac{\rho_b}{V_{wc}} - \rho_w\right) + \rho_s} \qquad \text{(Eq. I-22)}$$

Equation I-22 gives an expression for evaluating matrix porosity, ϕ_m, from knowledge of the grain density, ρ_s, bulk density, ρ_b, matrix water saturation, S_w, and volumetric water content, V_{wc}.

Substituting the expression for matrix volume, V_m, from Equation I-20 into Equation I-13 gives an expression for lithophysal porosity, ϕ_L:

$$\phi_L = 1 - \frac{\rho_b}{\rho_s} + \frac{V_{wc}\rho_w}{\rho_s} - \frac{V_{wc}}{S_w} \qquad \text{(Eq. I-23)}$$

Equation I-23 gives an expression for calculating lithophysal porosity, provided estimates of bulk density, grain density, matrix water saturation, and volumetric water content are available. The bulk density, ρ_b, and volumetric water content, V_{wc}, are obtained from well-logging techniques; in particular, the volumetric water content, V_{wc}, is obtained from the neutron porosity log.

ATTACHMENT II
INPUT DATA ANALYSIS

INTENTIONALLY LEFT BLANK

ATTACHMENT II
INPUT DATA ANALYSIS

This section documents the available core and petrophysical data and any decisions made regarding the use of these data. In addition, matrix and lithophysal porosity are calculated and plotted using the equations developed in Attachment I. Core measurements of volumetric water content are directly compared with petrophysical neutron porosity data when both are available for the borehole. The core measurements of volumetric water content are used to determine when the neutron porosity data appear to be high or low for a borehole. Borehole petrophysical data are also compared for nearby boreholes to determine consistency.

USW G-1

The neutron porosity log data for USW G-1 appear to be high when compared with nearby boreholes USW H-1 and USW UZ-1/UZ-14. In those boreholes the neutron porosity is typically between 0.10 and0.15, while in USW G-1, readings typically exceed 0.2. This borehole was drilled with water, which can lead to higher neutron porosity readings. There were also several regions for which null readings were obtained. Because of the high neutron porosity measurements and null data, the neutron porosity data were not used for this borehole.

The bulk density log for USW G-1 is similar to USW H-1 and USW UZ-1/UZ-14; therefore, lithophysal porosity was computed using Method C, assuming the matrix porosity ($\phi_m = 0.10$) and water saturation $S_w = 1$. The calculated lithophysal porosity looks reasonable except in the middle non-lithophysae zone, where up to 20 percent was calculated near the middle of the zone. The large values of lithophysal porosity around 780 ft occur near the null values of neutron porosity and suggest washout. Therefore, Method C was used to calculate lithophysal porosity except for the middle non-lithophysae zone.

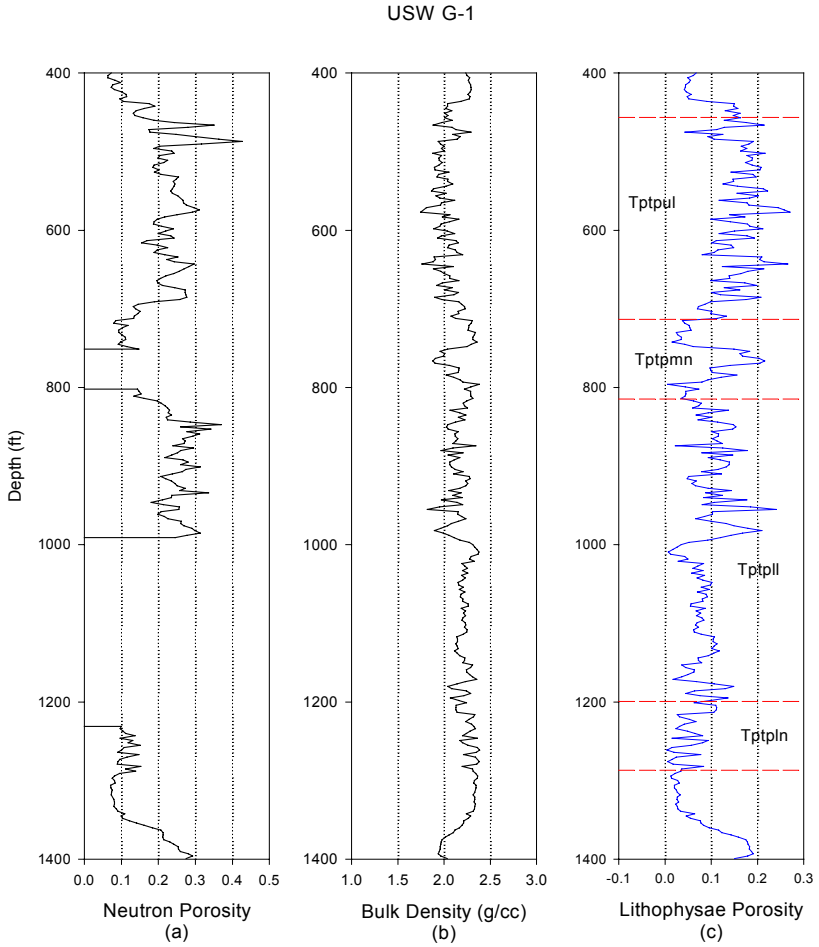

DTN: MO0010CPORGLOG.002 [155229]

Figure II-1. USW G-1

USW G-2

There are two sets of data available for USW G-2. After examining both sets, the choice was made to use the historic era data since the more modern data include many unusual spikes in bulk density, which is characteristic of borehole rugosity (roughness). Both the neutron porosity and the bulk density from the older data set compare well with data from nearby borehole USW WT-24. After applying Method B, the calculated matrix and lithophysal porosity are consistent with the neighboring borehole USW WT-24.

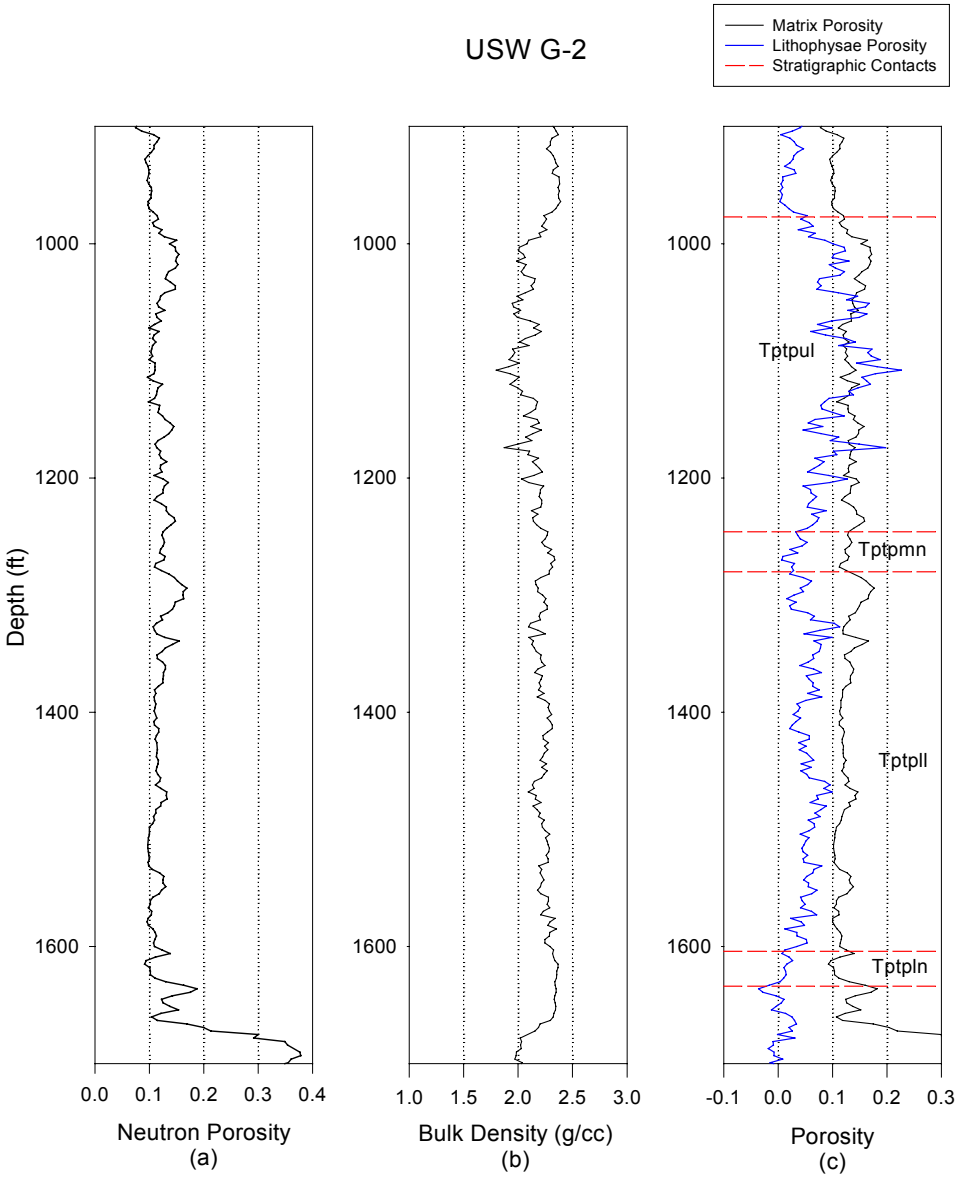

DTN: MO0010CPORGLOG.002 [155229]

Figure II-2. USW G-2

USW G-3

In USW G-3 the neutron porosity log, data look high but are consistent with the neutron porosity logs from neighboring boreholes USW H-3 and USW WT-7. This borehole was drilled with polymer mud as drilling fluid which may explain the higher apparent neutron porosity. Bulk density data compare with nearby boreholes. Method B was applied to this borehole for the calculation of matrix and lithophysal porosity. The method yields very low lithophysal porosity in the lower lithophysae zone.

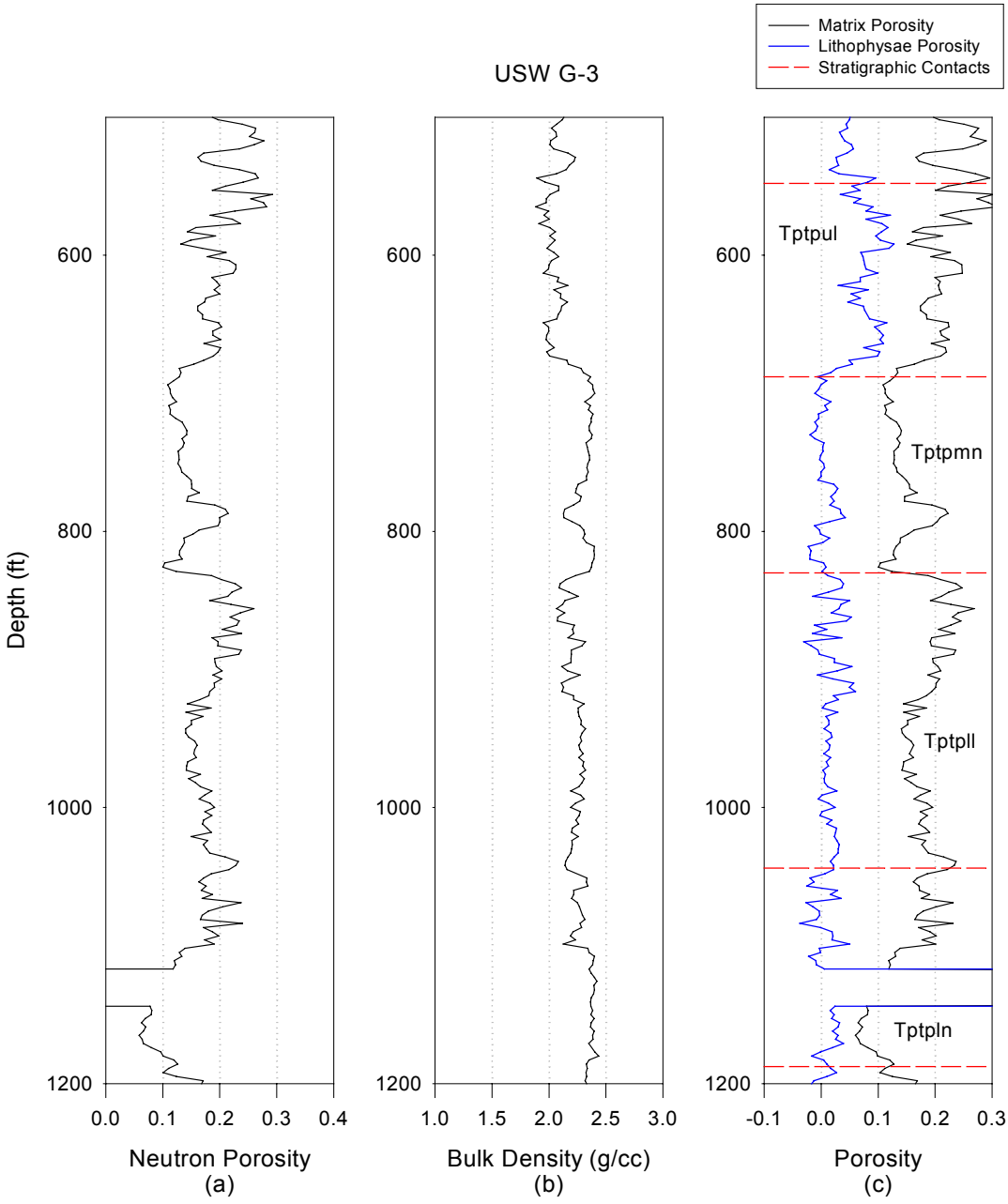

DTN: MO0010CPORGLOG.002 [155229]

Figure II-3. USW G-3

USW G-4

Essentially no neutron porosity data exist in the Tpt for USW G-4; however, the bulk density log is comparable to nearby borehole USW NRG-6. Method C was applied for computing lithophysal porosity.

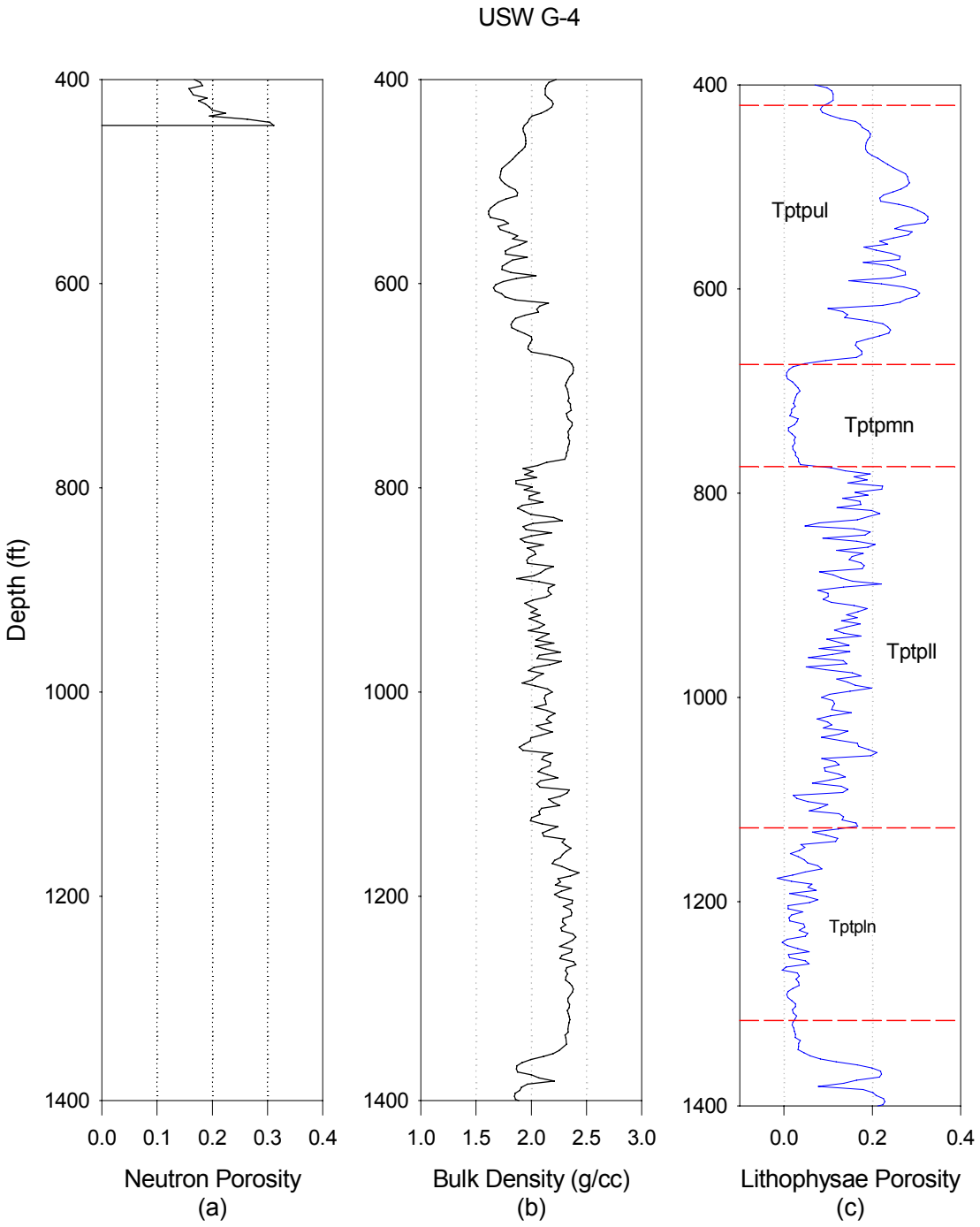

DTN: MO0010CPORGLOG.002 [155229]

Figure II-4. USW G-4

USW H-1

The neutron porosity and bulk density logs for USW H-1 are similar to those from nearby boreholes. Method B is used to calculate matrix and lithophysal porosity.

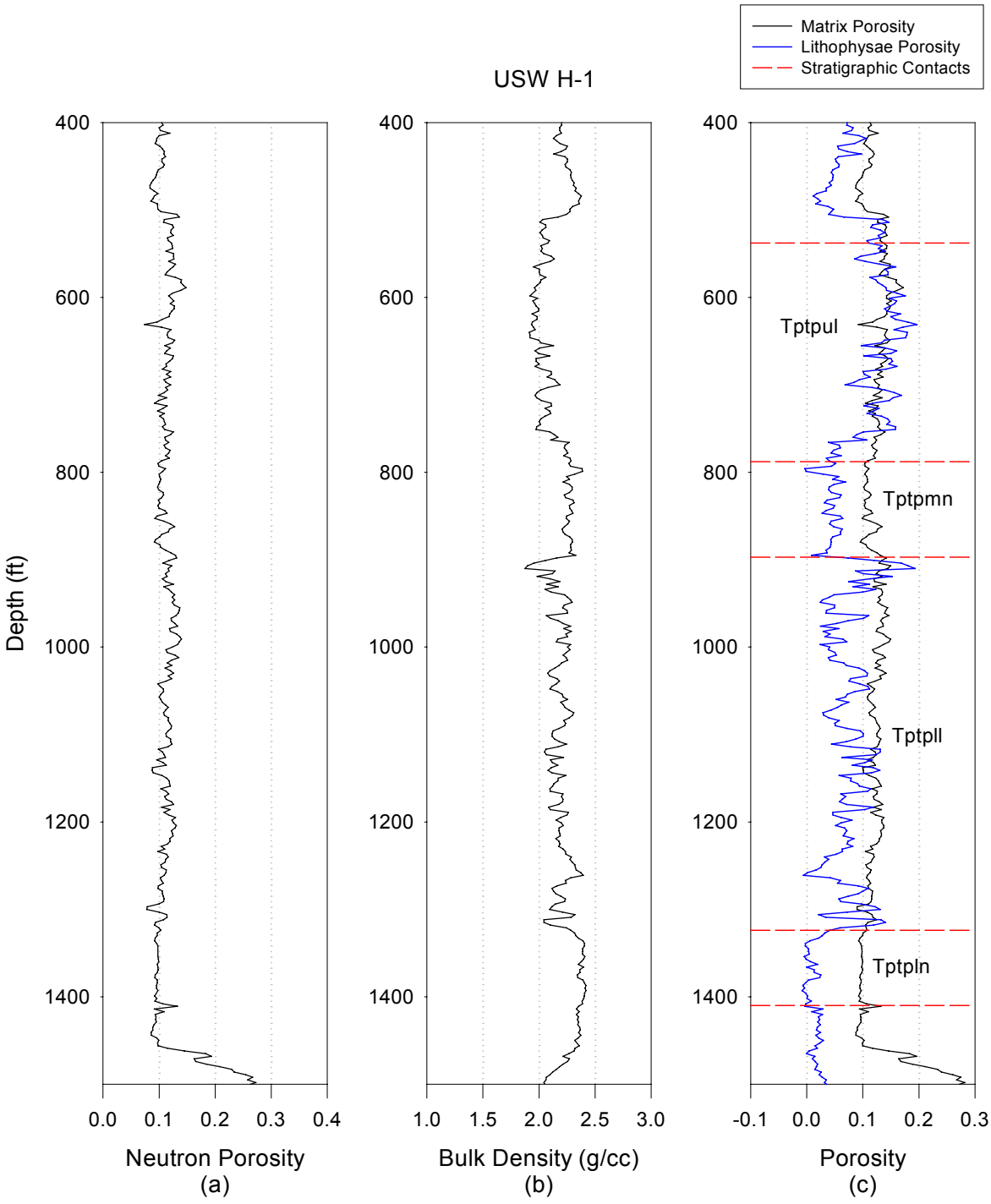

DTN: MO0010CPORGLOG.002 [155229]

Figure II-5. USW H-1

USW H-3

The neutron porosity from borehole USW H-3 looks a little high but is similar to USW H-4. The bulk density data for this well also compare favorably to data from USW H-4. Method B was applied to this borehole. The data below 958 ft, in the lower lithophysae unit, were neglected because of the absence of neutron porosity data.

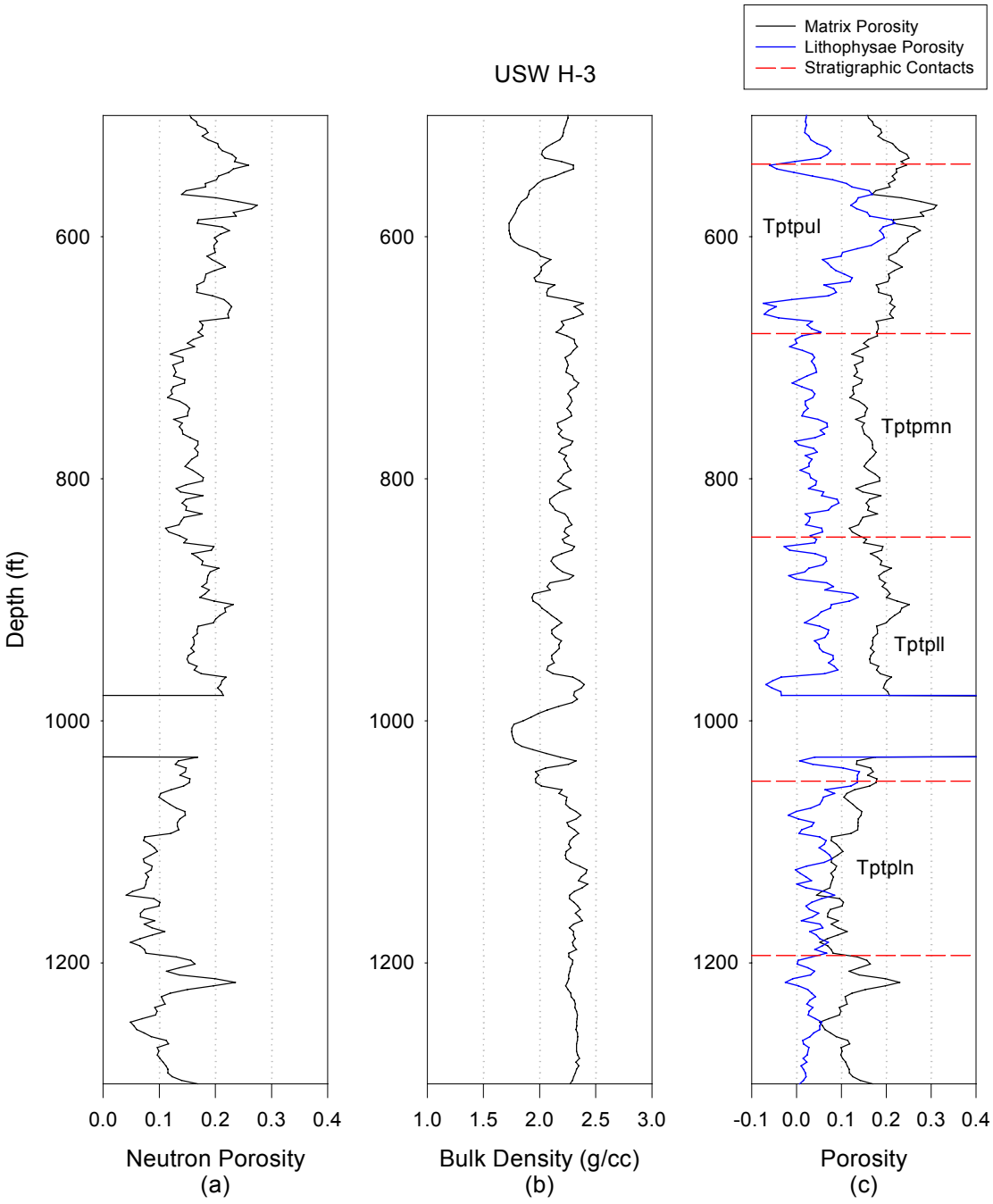

DTN: MO0010CPORGLOG.002 [155229]

Figure II-6. USW H-3

USW H-4

The neutron porosity data in borehole USW H-4 appear high in the lithophysae zones; however, this is the same type of behavior observed in neighboring boreholes USW H-3 and USW SD-12 and confirmed by core measurement. Method B was used for evaluation of matrix and lithophysal porosity for this borehole.

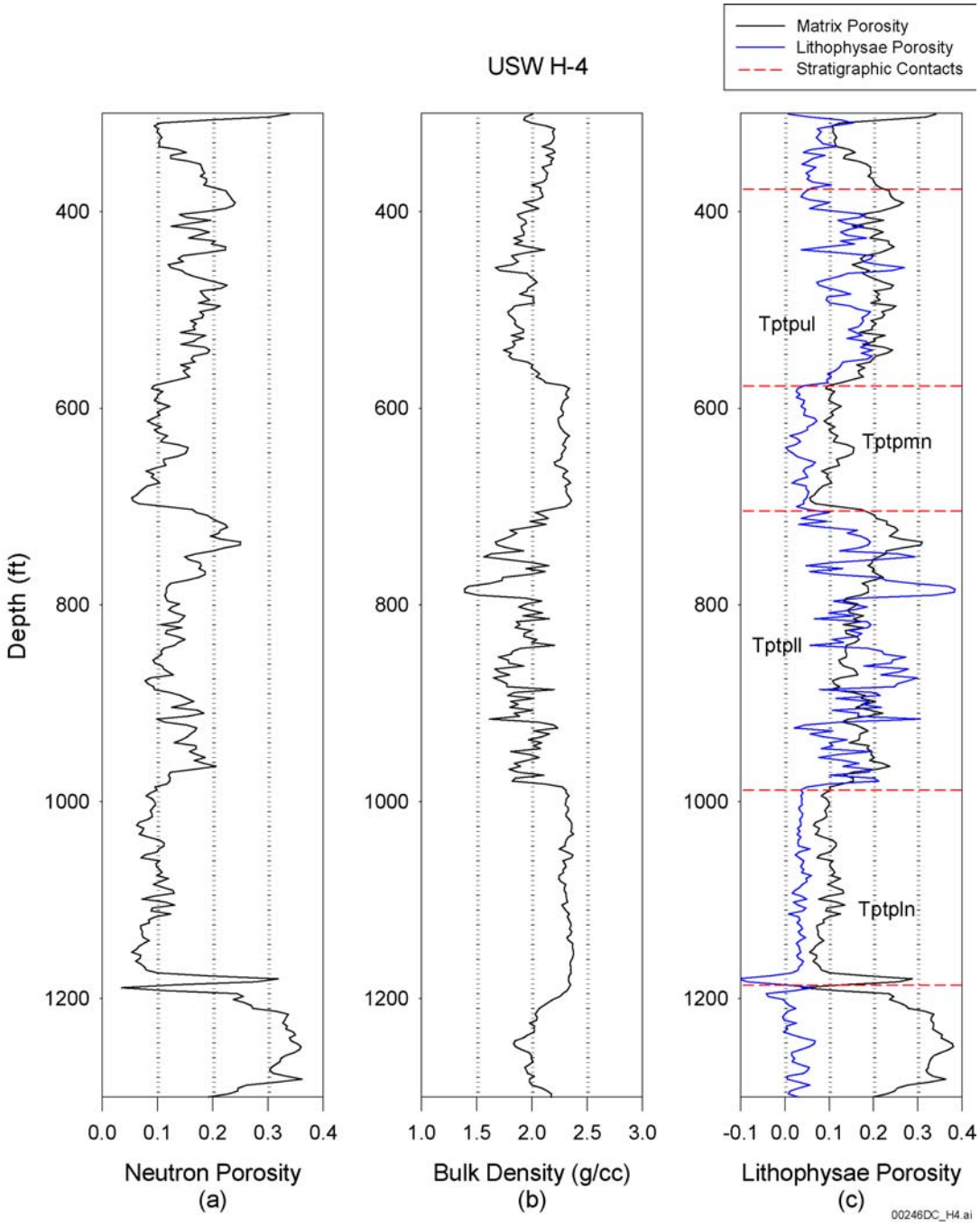

DTN: MO0010CPORGLOG.002 [155229]

Figure II-7. USW H-4

USW H-5

The neutron porosity and bulk density data for USW H-5 are very similar to the data for USW H-4. Method B was used to calculate matrix and lithophysal porosity for this borehole.

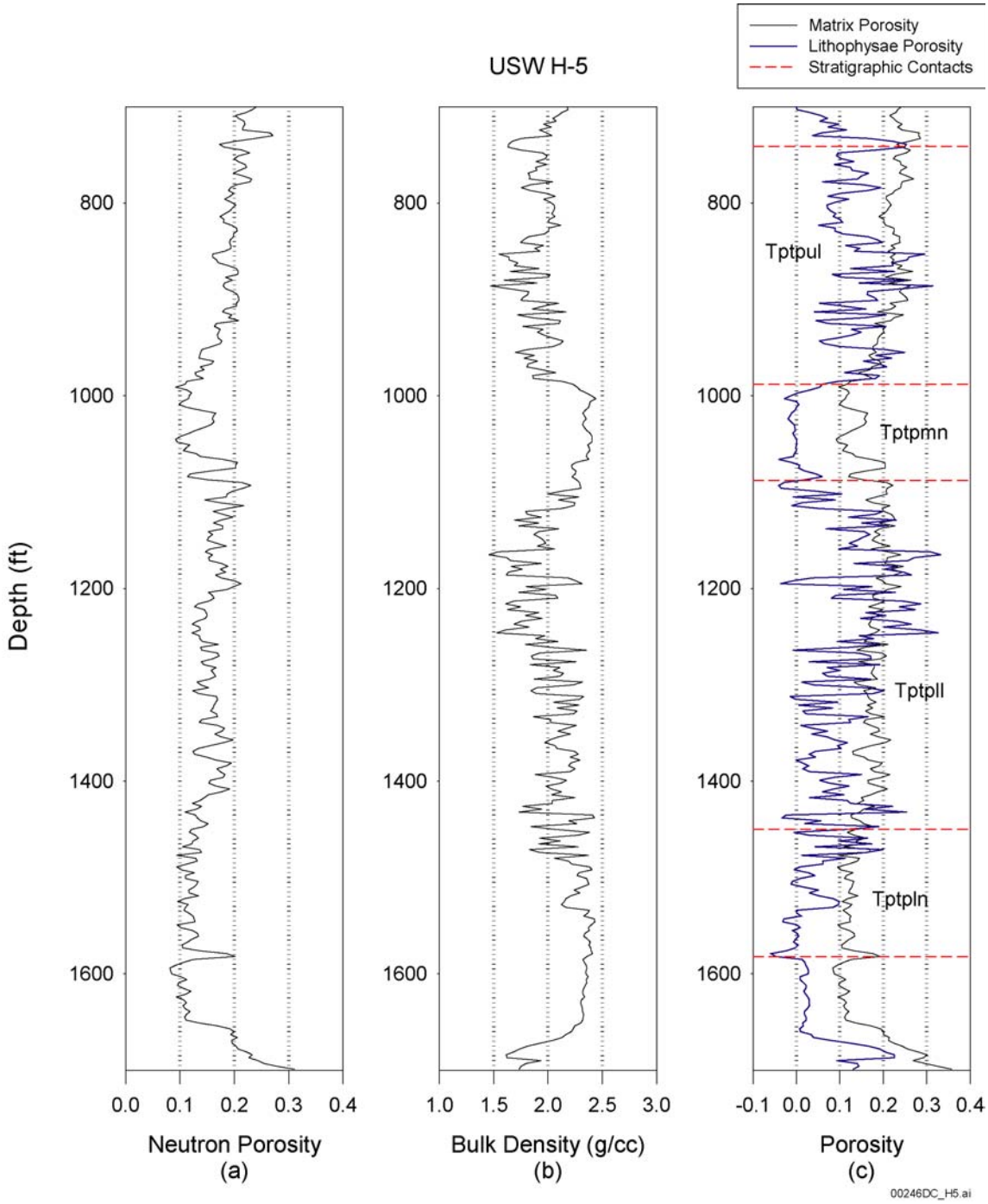

DTN: MO0010CPORGLOG.002 [155229]

Figure II-8. USW H-5

USW H-6

Both the neutron porosity and the bulk density data compare well with neighboring borehole USW H-5. Method B was used to calculate matrix and lithophysal porosity for this borehole.

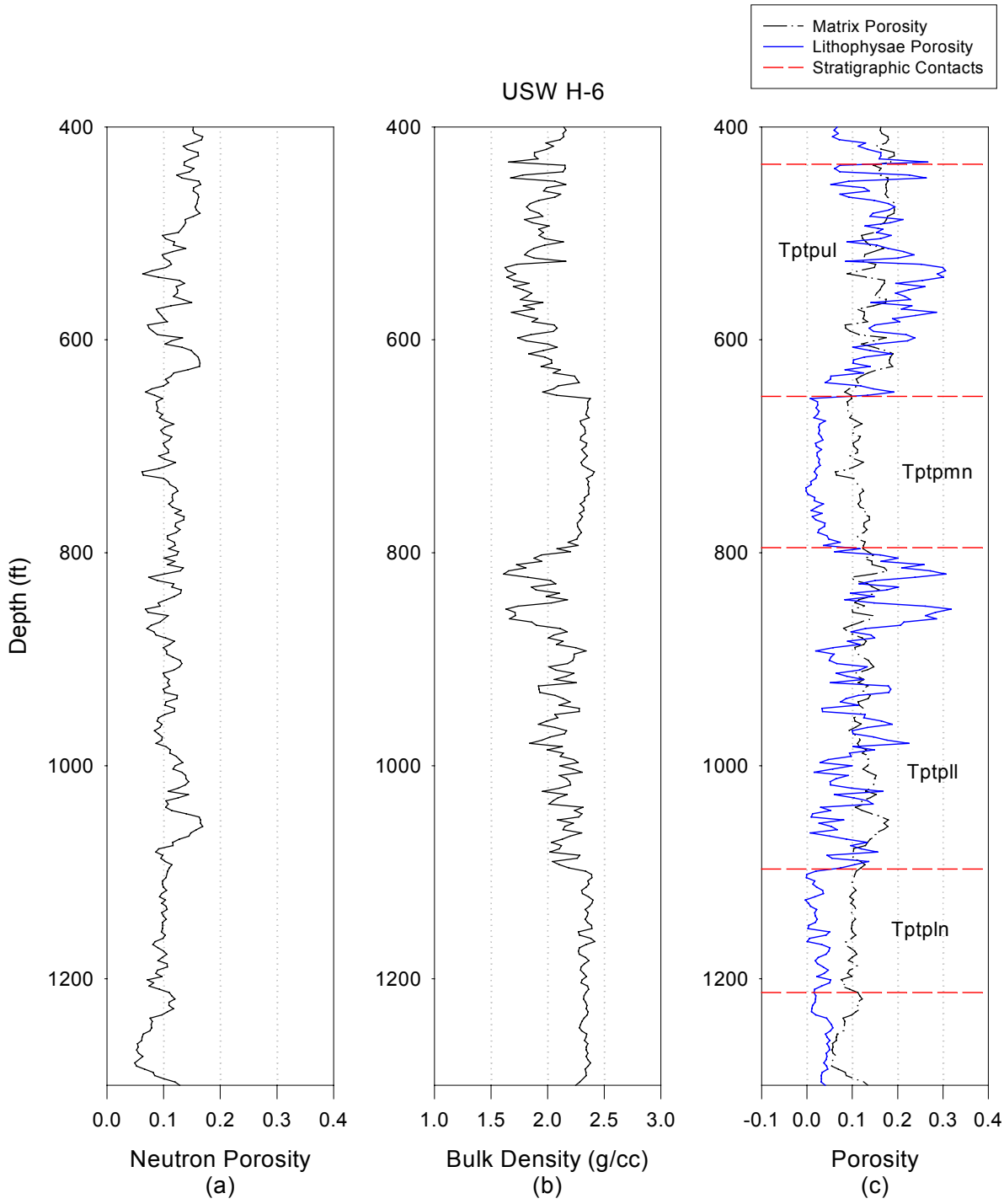

DTN: MO0010CPORGLOG.002 [155229]

Figure II-9. USW H-6

UE-25 NRG #4

There are essentially no data for this borehole; therefore, it was removed from further consideration.

USW NRG-6

Both the neutron porosity and the bulk density data agree with typical readings from nearby boreholes. RH and OD core measurements compare well with calculated values of matrix porosity except for minor differences in the upper lithophysae zone. Given the abundant core data, OD core measurements will be used to represent matrix porosity, and Method A will be used to calculate lithophysal porosity.

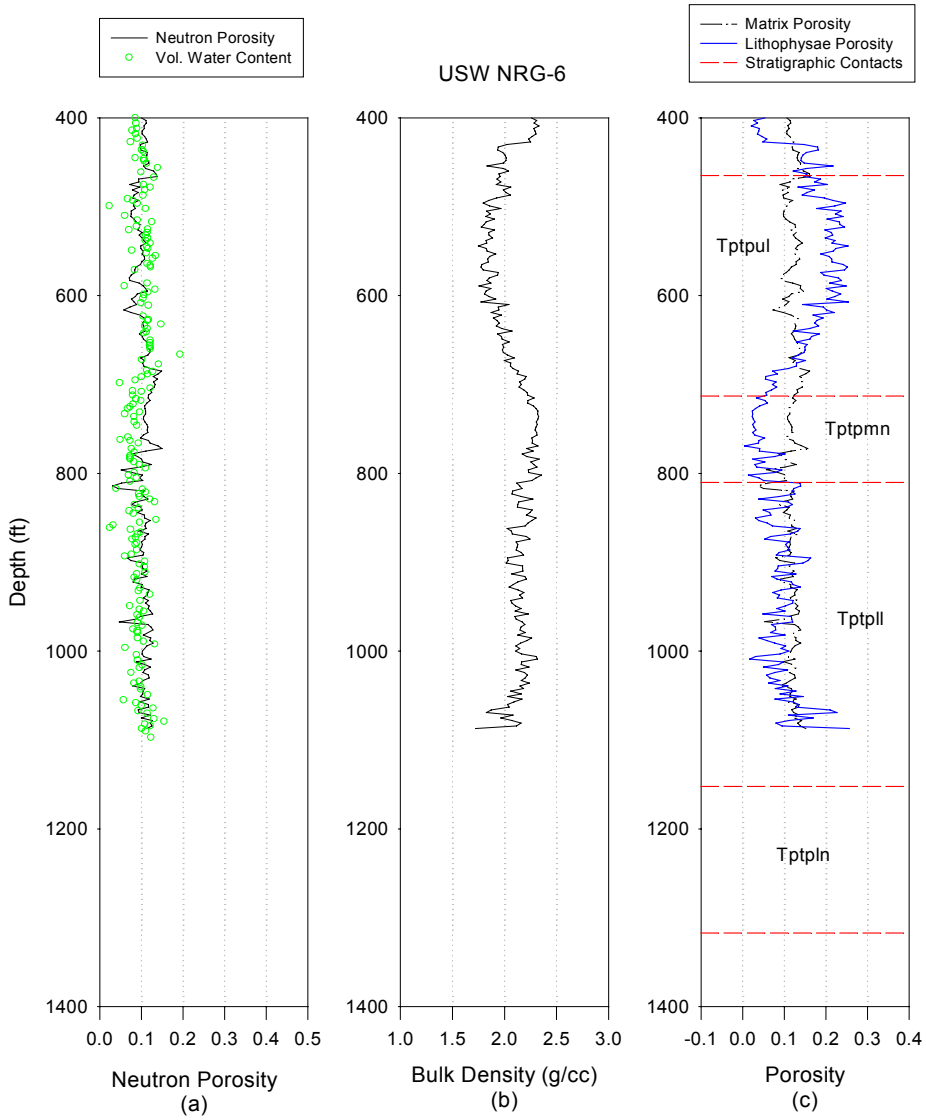

DTN: MO0010CPORGLOG.003 [155959]

Figure II-10. USW NRG-6 Petrophysical

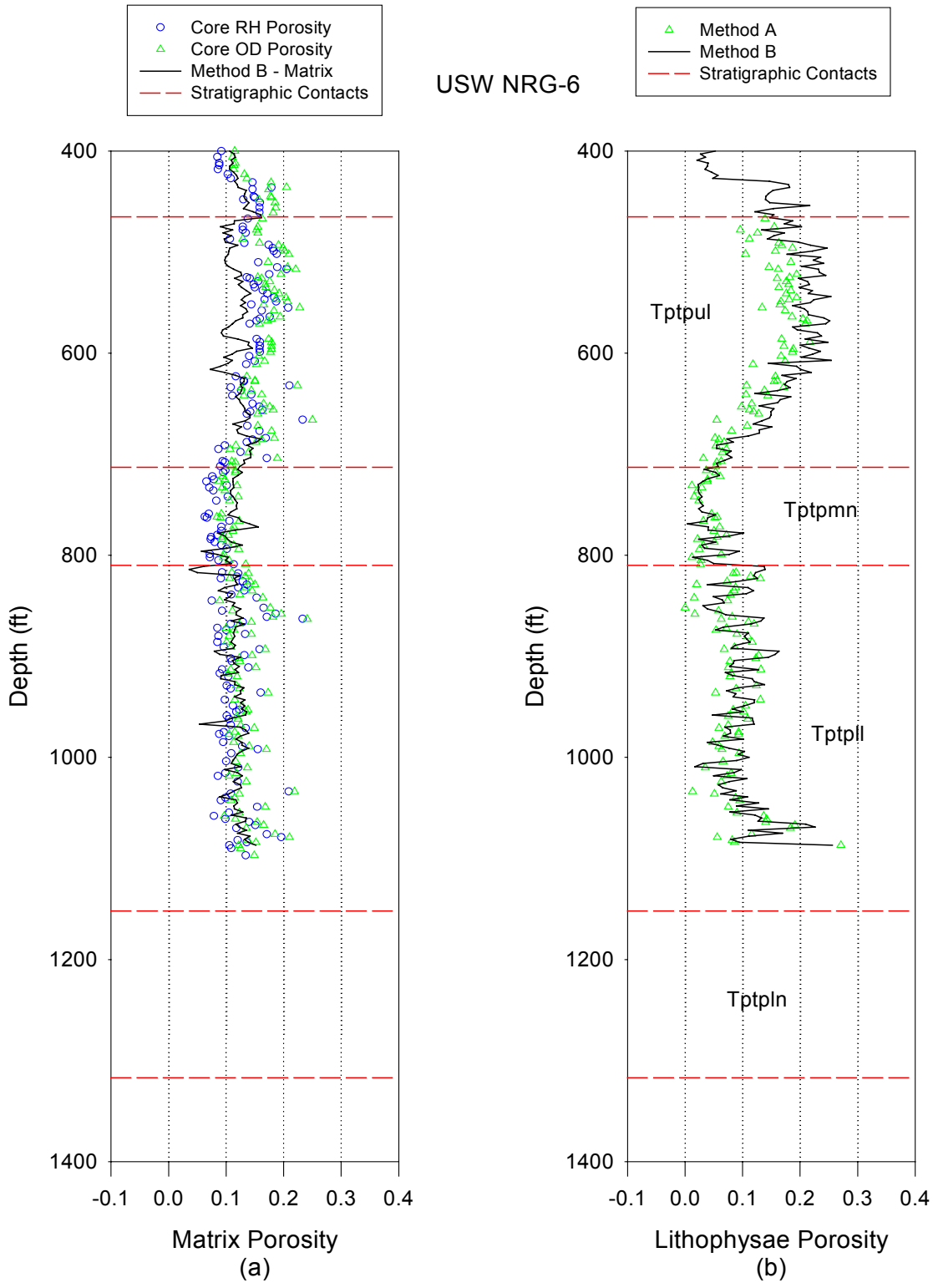

NOTES: OD = oven-dried; RH = relative humidity.

DTN: MO0109HYMXPROP.001 [155989], SN0208T0503102.007

Figure II-11. USW NRG-6 Core

NRG-7/7a

The neutron porosity for this borehole is unusually low, leading to low matrix porosities when calculated via Method B. This is confirmed by comparison with abundant core measurements. The low readings could be attributed to the use of the wrong matrix setting on the compensated neutron tool used to collect the data. The bulk density data compare favorably with the data from nearby borehole USW H-1. Therefore lithophysal porosity is calculated from OD core measurements using Method A.

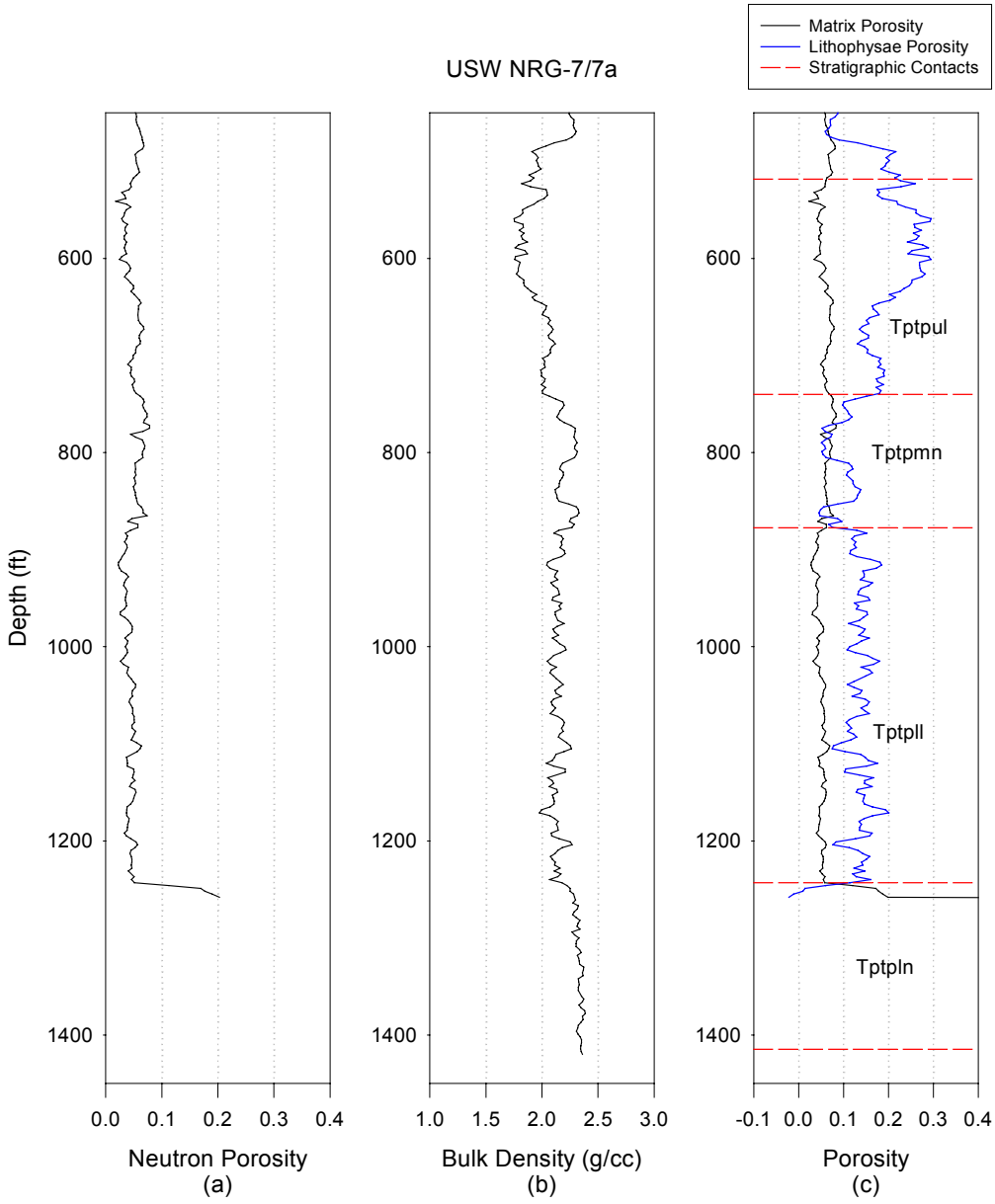

DTN: MO0010CPORGLOG.003 [155959]

Figure II-12. USW NRG-7/7a Petrophysical

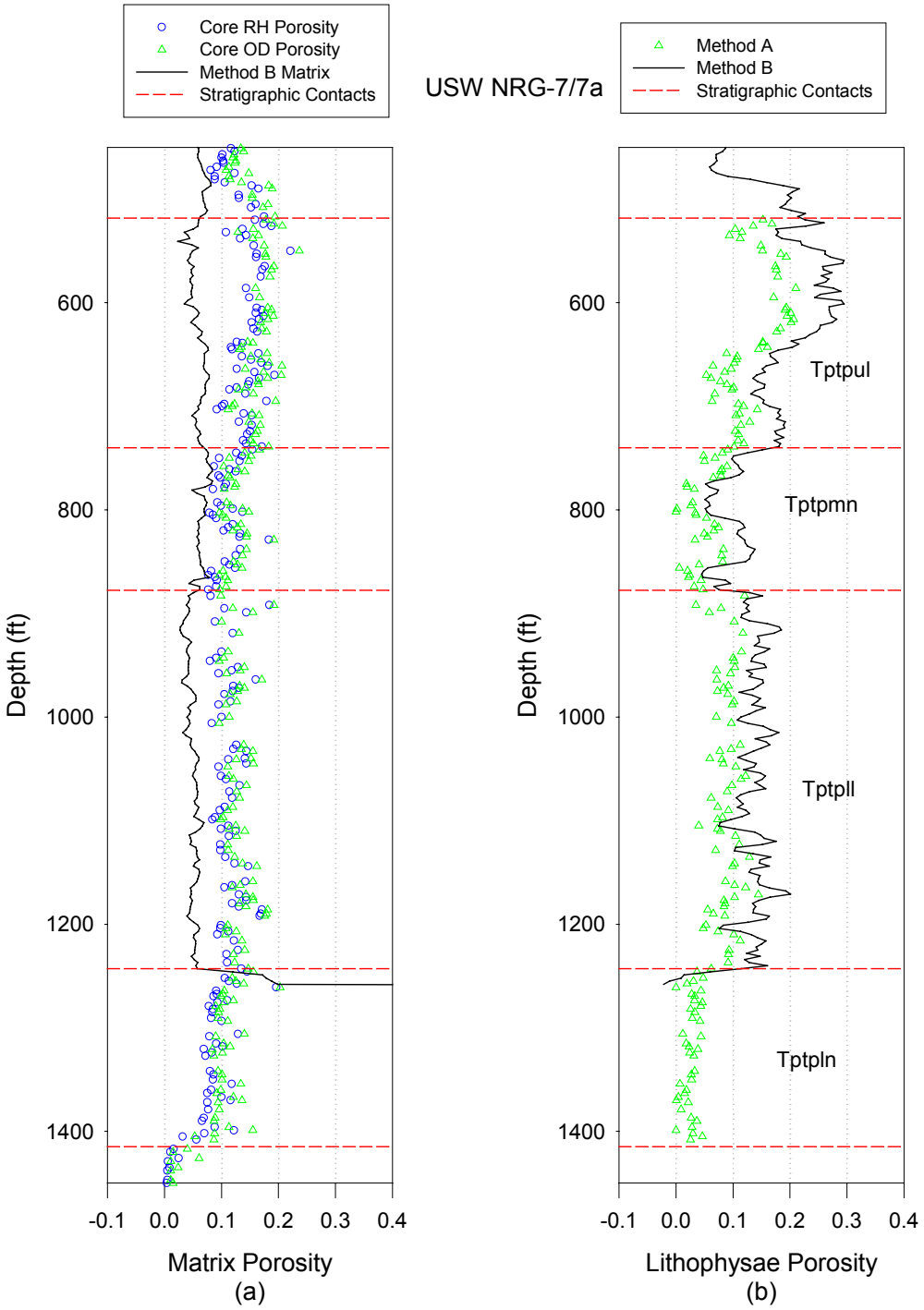

NOTES: OD = oven-dried; RH = relative humidity.

DTN: MO0109HYMXPROP.001 [155989], SN0208T0503102.007

Figure II-13. USW NRG-7/7a Core

UE-25 ONC #1

The neutron porosity data appear low compared to data from nearby boreholes. This is particularly true in the upper lithophysae zone. The bulk density data agree with data from nearby boreholes; therefore, Method C was applied for the calculation of lithophysal porosity.

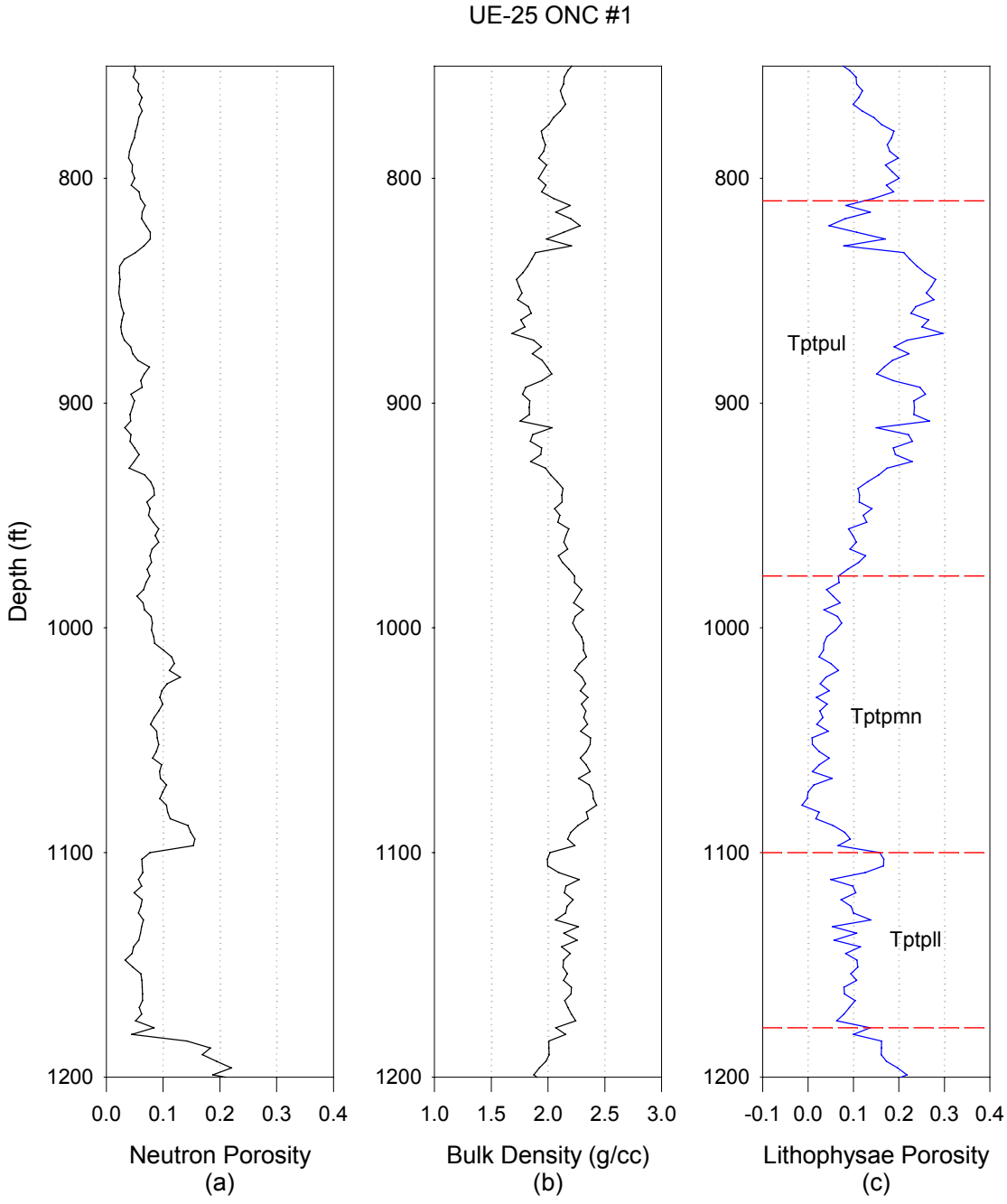

DTN: MO0010CPORGLOG.003 [155959]

Figure II-14. UE-25 ONC #1

UE-25 p #1

The neutron porosity and bulk density logs compare well with the logs from nearby boreholes. There are no core data available for this borehole; therefore, Method B was used to calculate matrix and lithophysal porosity.

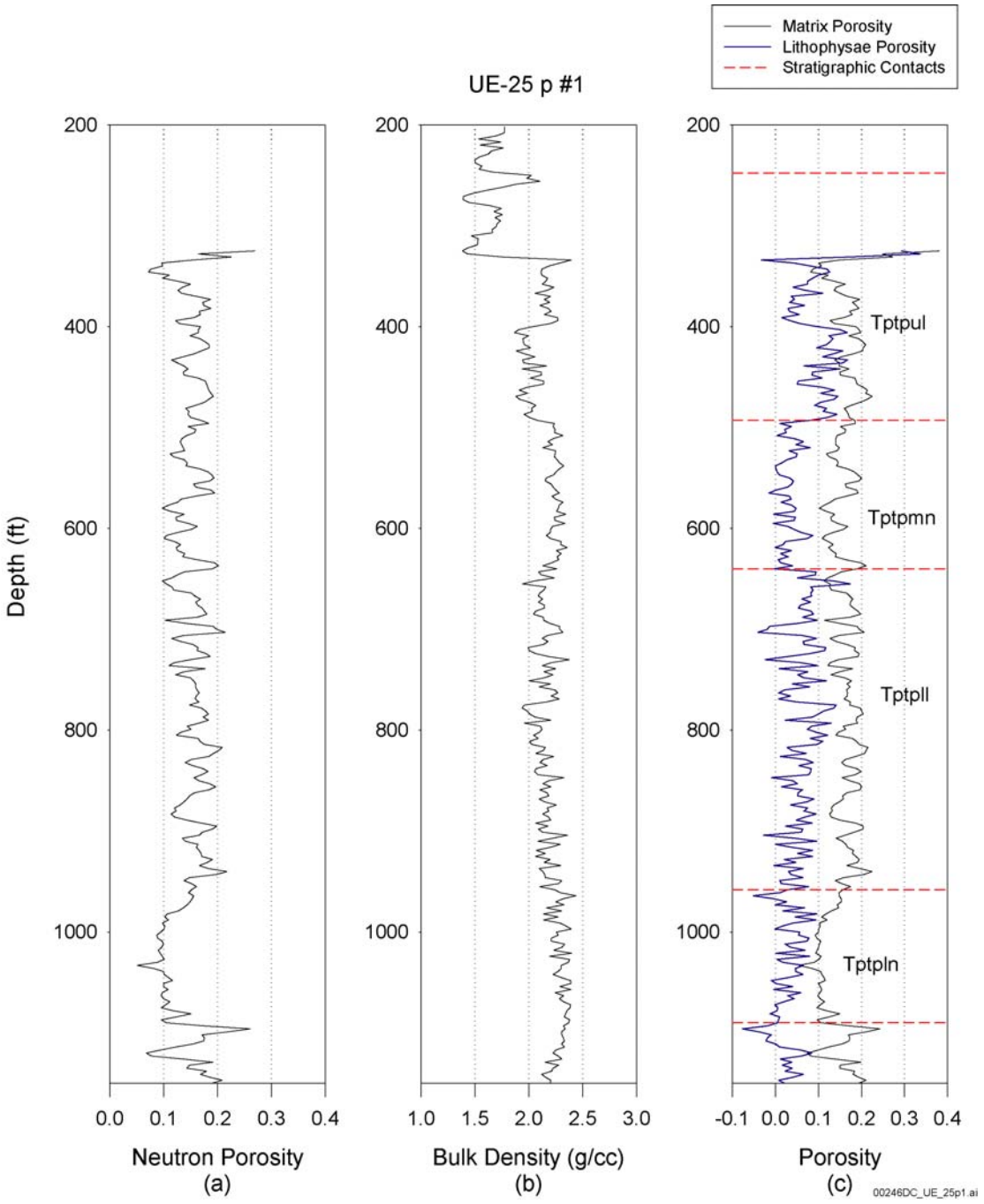

DTN: MO0010CPORGLOG.002 [155229]

Figure II-15. UE-25 p #1

USW SD-6

The neutron porosity data for this borehole compare favorably with data in neighboring boreholes, particularly in lower units. The bulk density measurements show the effect of hole damage (rugosity) when compared to the other boreholes examined. There are a few core samples taken from this borehole in the lower nonlithophysae, which will be used to condition matrix porosity at this location. All other data from USW SD-6 were not used.

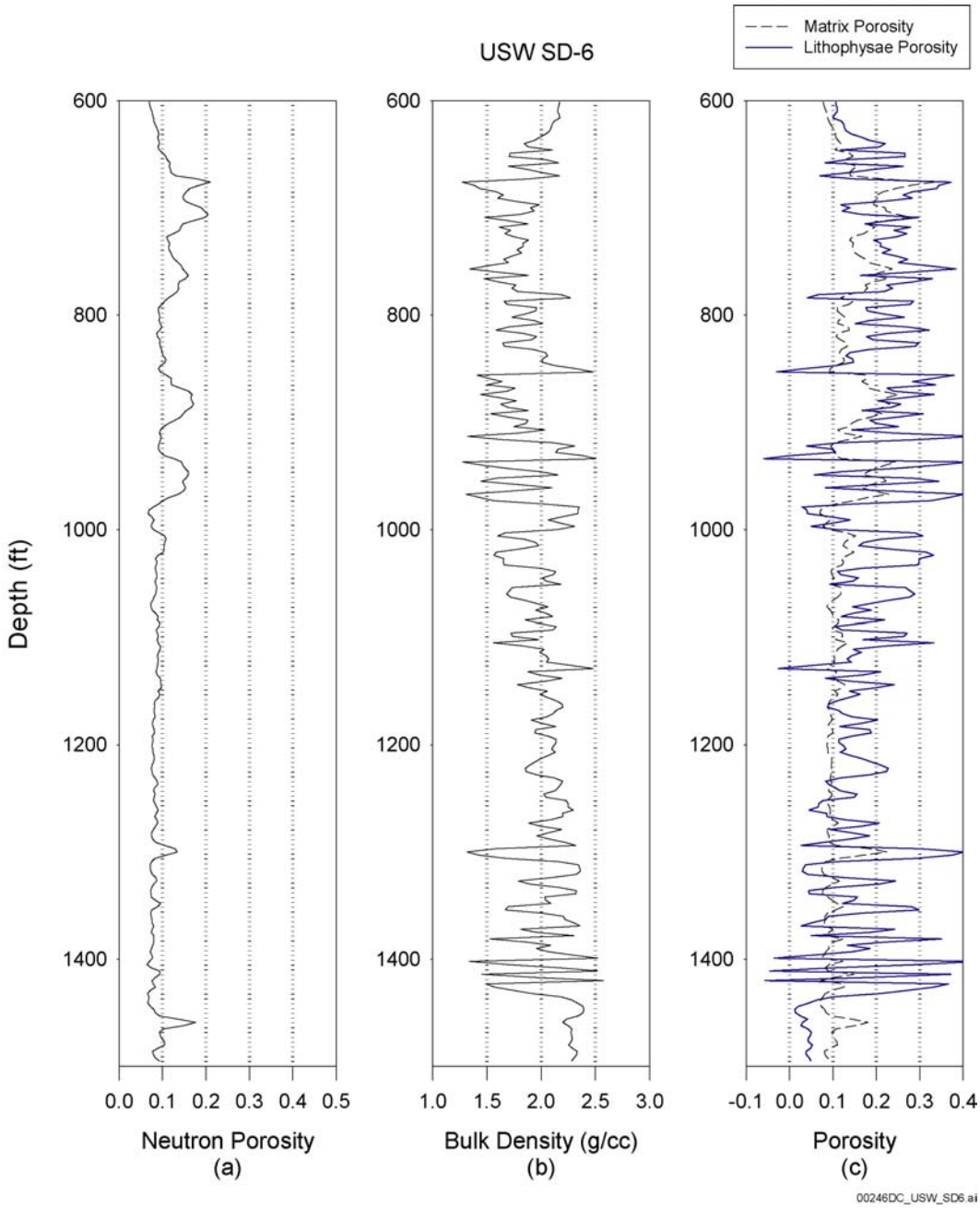

DTN: MO0010CPORGLOG.003 [155959]

Figure II-16. USW SD-6

USW SD-7

The neutron porosity and the bulk density data for this borehole compare well with data from neighboring boreholes. Abundant core data were available for this borehole, and good agreement between the neutron porosity and volumetric water content data was observed. Method A was used to compute lithophysal porosity.

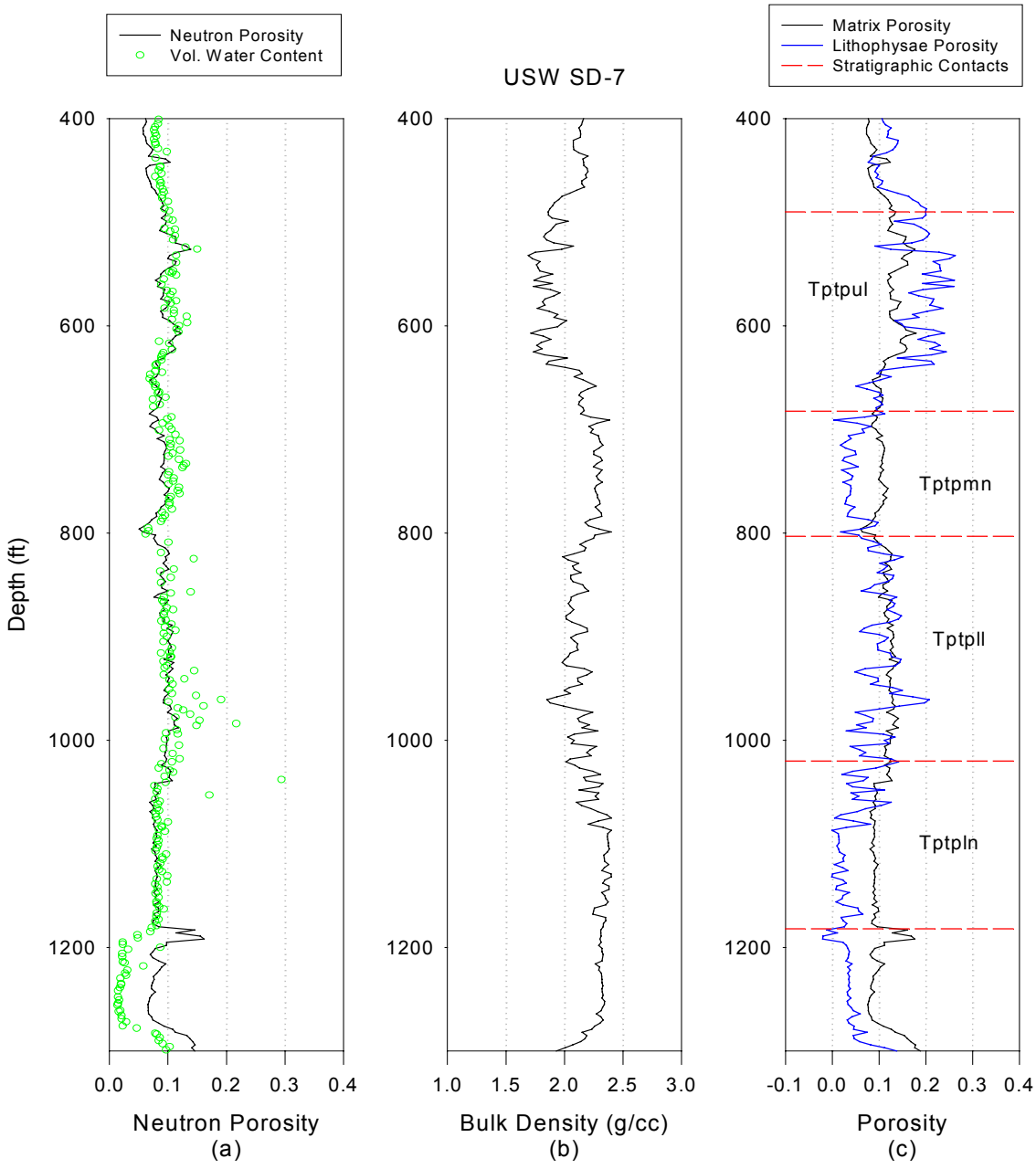

DTN: MO0010CPORGLOG.003 [155959]

Figure II-17. USW SD-7 Petrophysical

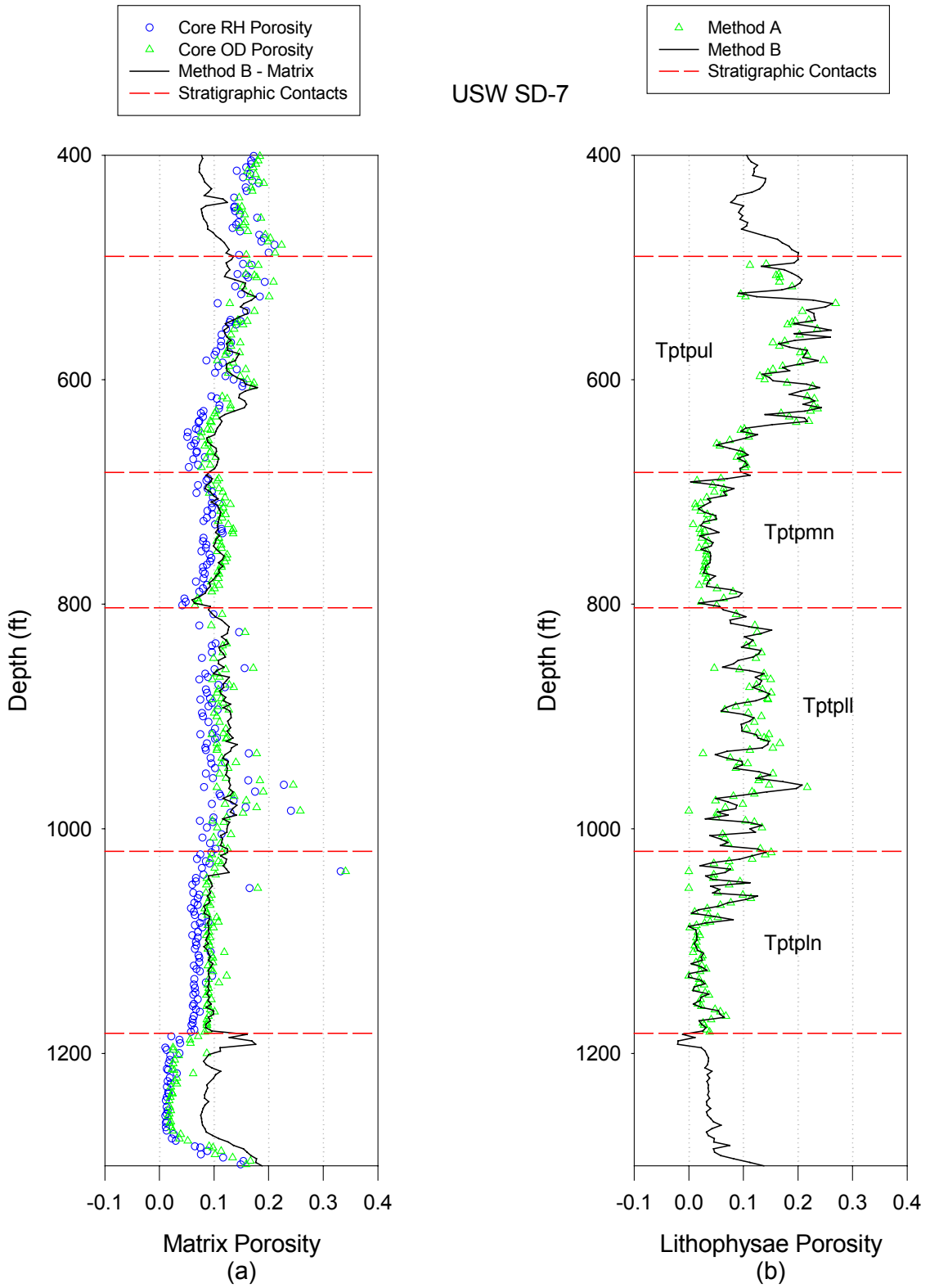

NOTES: OD = oven-dried; RH = relative humidity.

DTN: MO0109HYMXPROP.001 [155989], SN0208T0503102.007

Figure II-18. USW SD-7 Core

USW SD-9

Similar to the neutron porosity data from USW NRG-7/7A, the data for USW SD-9 look low compared to other boreholes. The neutron porosity data are low by the approximate difference between using a limestone porosity matrix and a sandstone porosity matrix. Comparison with the core volumetric water content data confirms this observation. Matrix porosity calculated by Method B is, therefore, also low and will not be used. The bulk density data look reasonable compared to other borehole data and will be applied with the abundant core data to calculate lithophysal porosity using Method A.

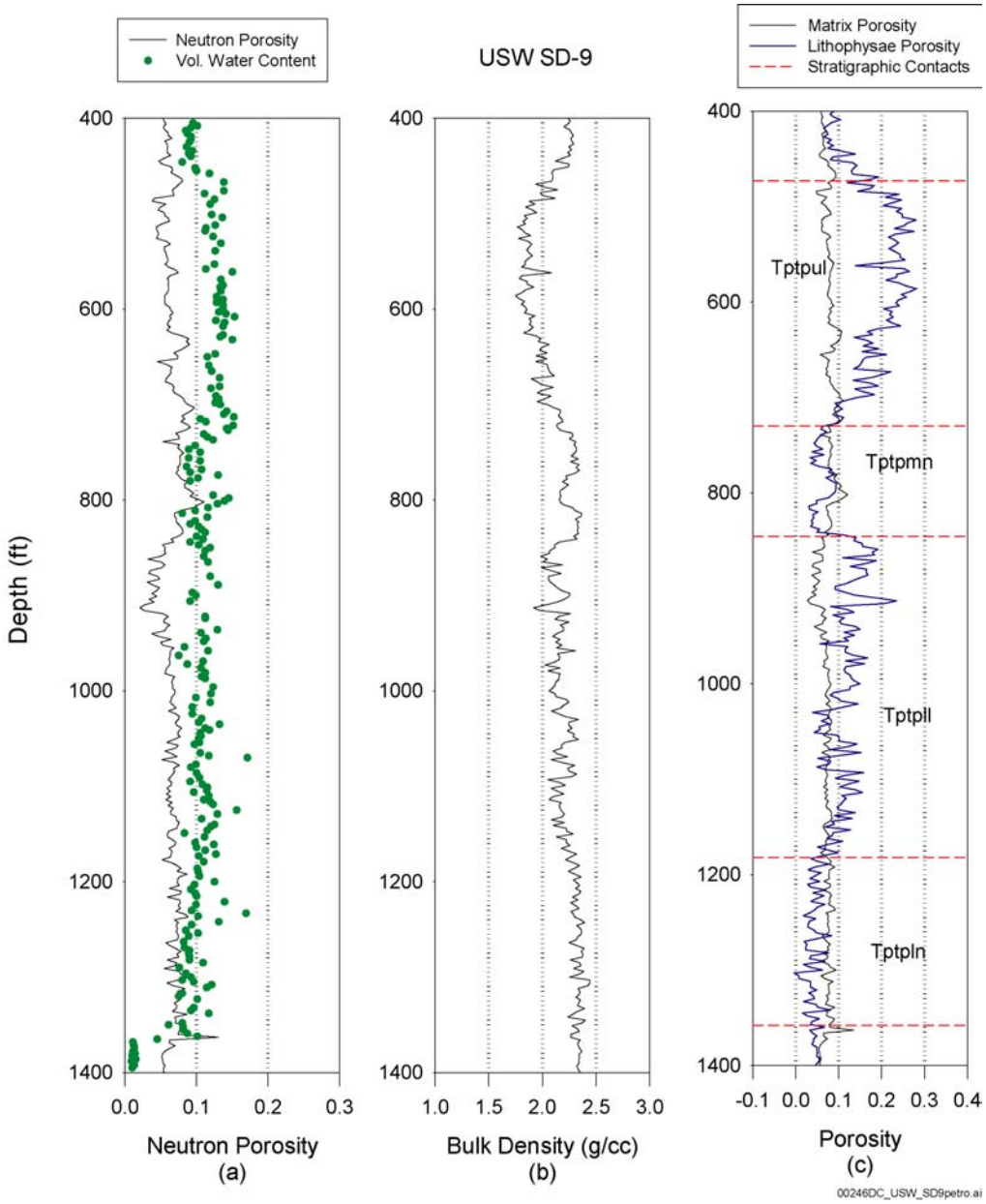

DTN: MO0010CPORGLOG.003 [155959]

Figure II-19. USW SD-9 Petrophysical

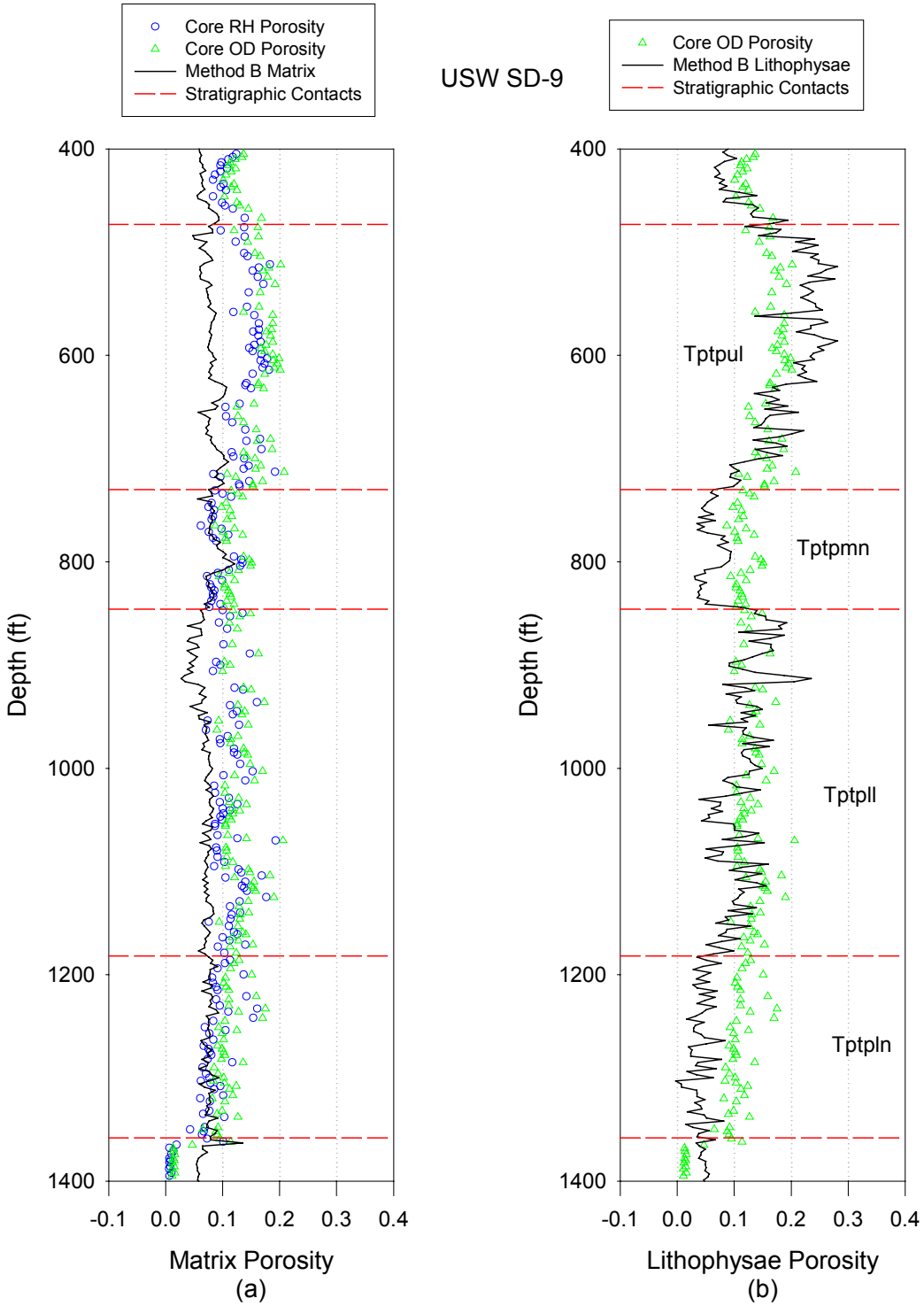

NOTES: OD = oven-dried; RH = relative humidity.

DTN: MO0109HYMXPROP.001 [155989], SN0208T0503102.007

Figure II-20. USW SD-9 Core

USW SD-12

The neutron porosity and the bulk density data for this borehole compare reasonably well with data from nearby boreholes. The volumetric water content determined from core samples agrees very well in the Tptpmn and somewhat less favorably in the other zones. Method A was used to evaluate lithophysal porosity using the bulk density data and core measurements of OD porosity.

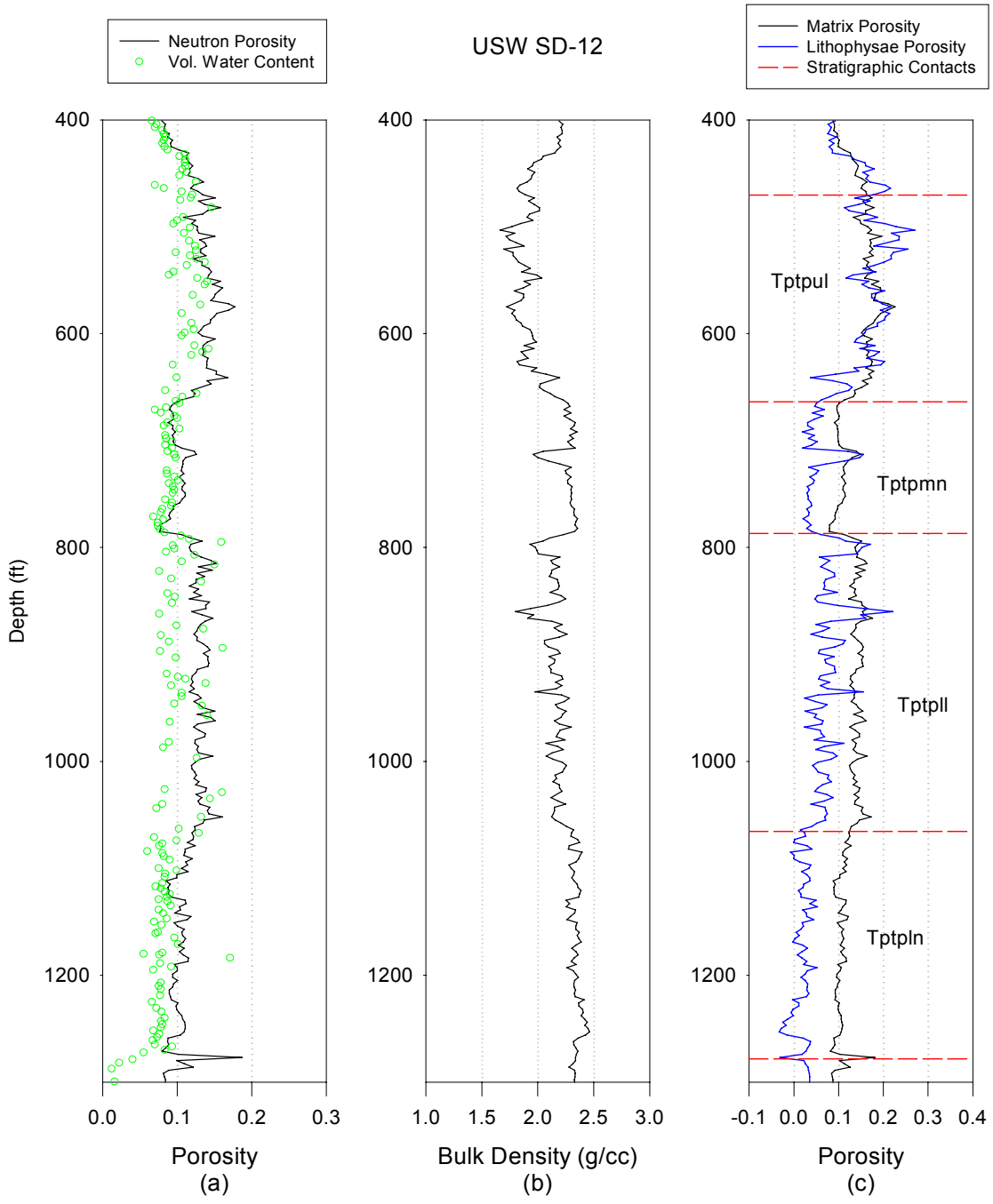

DTN: MO0010CPORGLOG.003 [155959]

Figure II-21. USW SD-12 Petrophysical

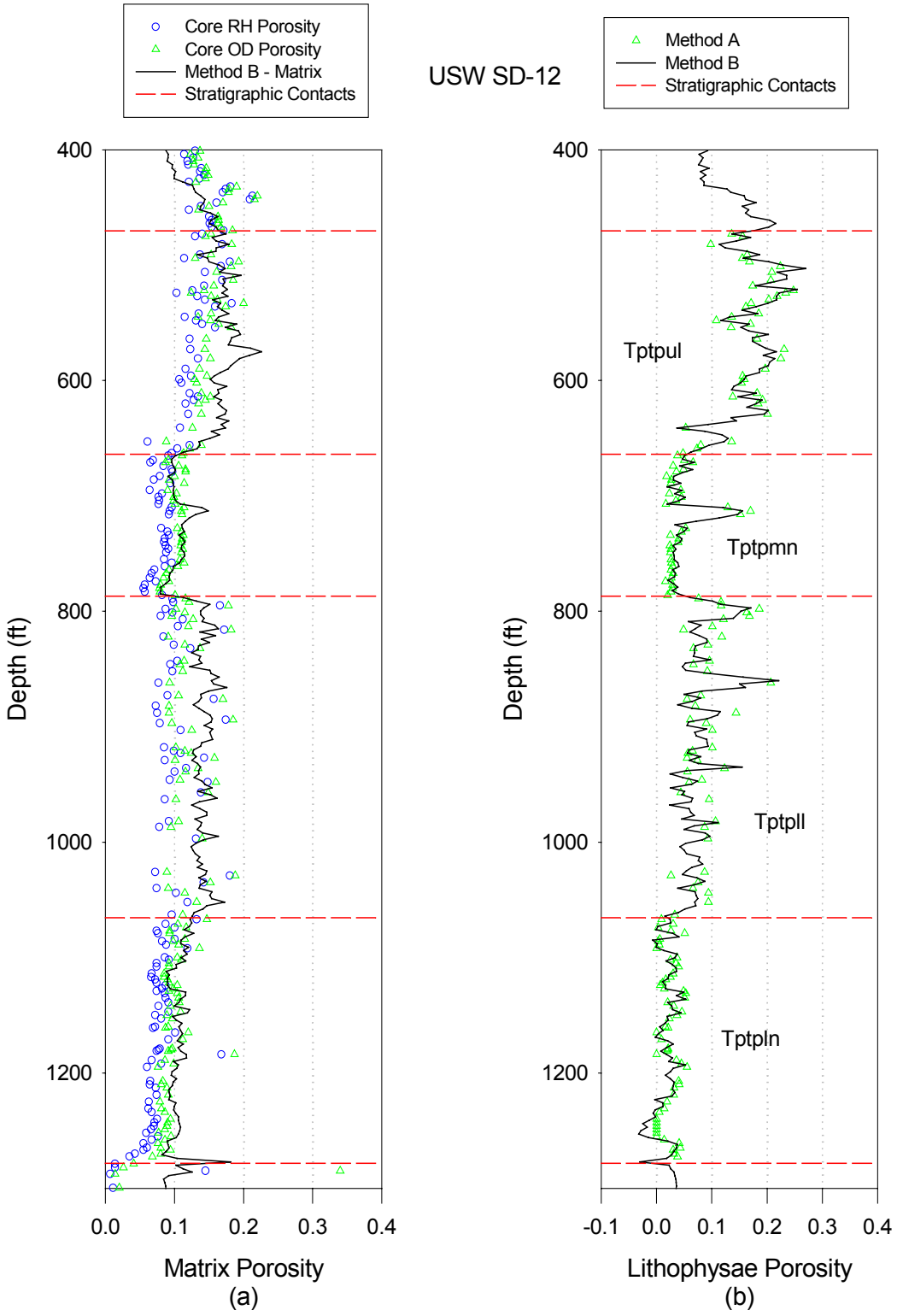

NOTES: OD = oven-dried; RH = relative humidity.

DTN: MO0109HYMXPROP.001 [155989], SN0208T0503102.007

Figure II-22. USW SD-12 Core

USW UZ-1 / UZ-14

Boreholes USW UZ-1 and USW UZ-14 are located very close to one another. The neutron porosity from USW UZ-1 is clearly too high compared to the neutron porosity from USW UZ-14 and to core measurements of volumetric water content from the same borehole. The bulk density log data look better in USW UZ-1 than in USW UZ-14. Consequently, the neutron porosity from USW UZ-14 is combined with bulk density from USW UZ-1 to calculate matrix and lithophysal porosity using Method B. Method A uses the OD core data from USW UZ-14, in conjunction with bulk density from USW UZ-1, to compute lithophysal porosity. The results compare quite well. Method A was ultimately used in the simulations.

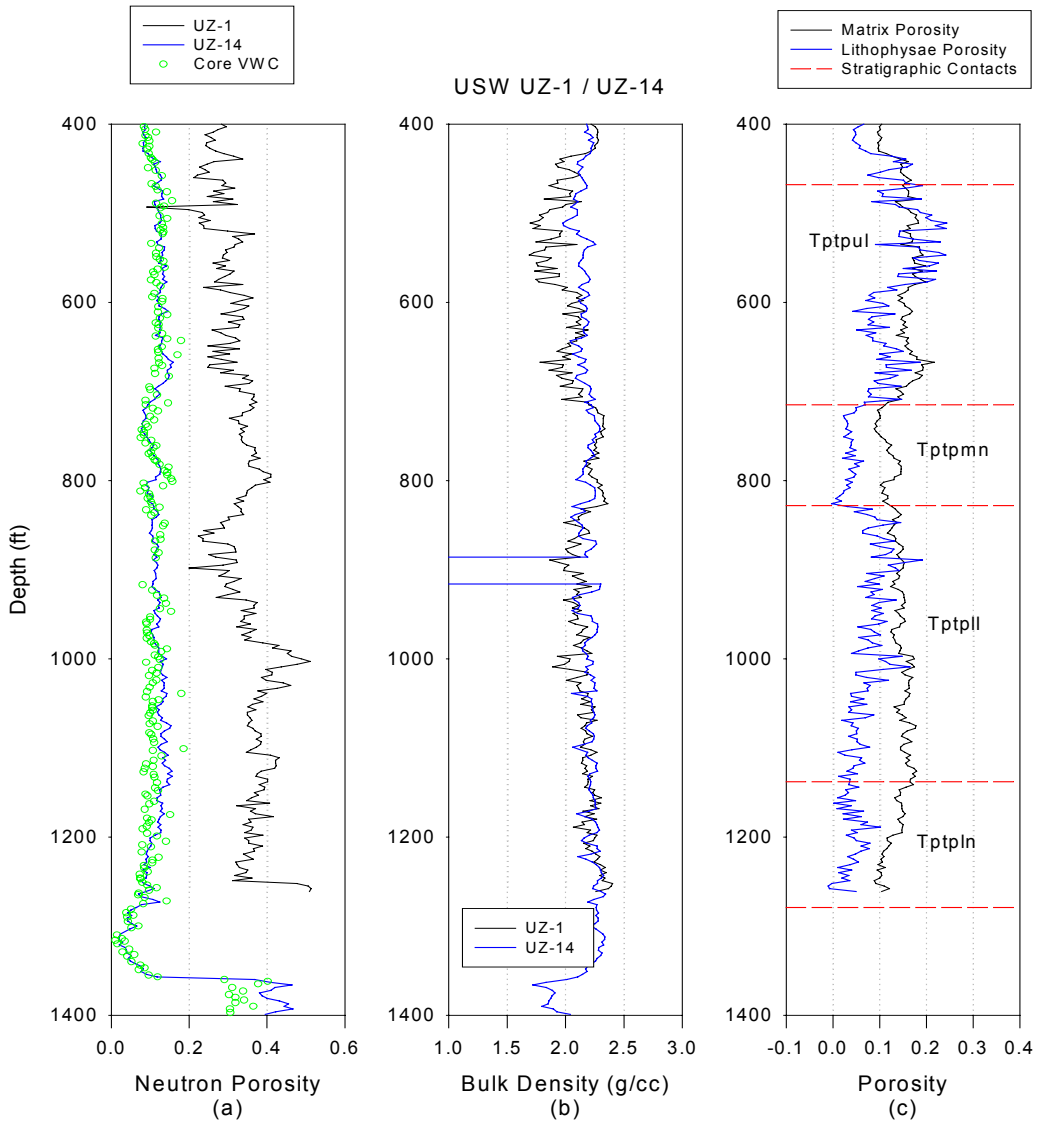

NOTE: VWC = volumetric water content.

DTN: MO0010CPORGLOG.003 [155959]

Figure II-23. USW UZ-1/UZ-14 Petrophysical

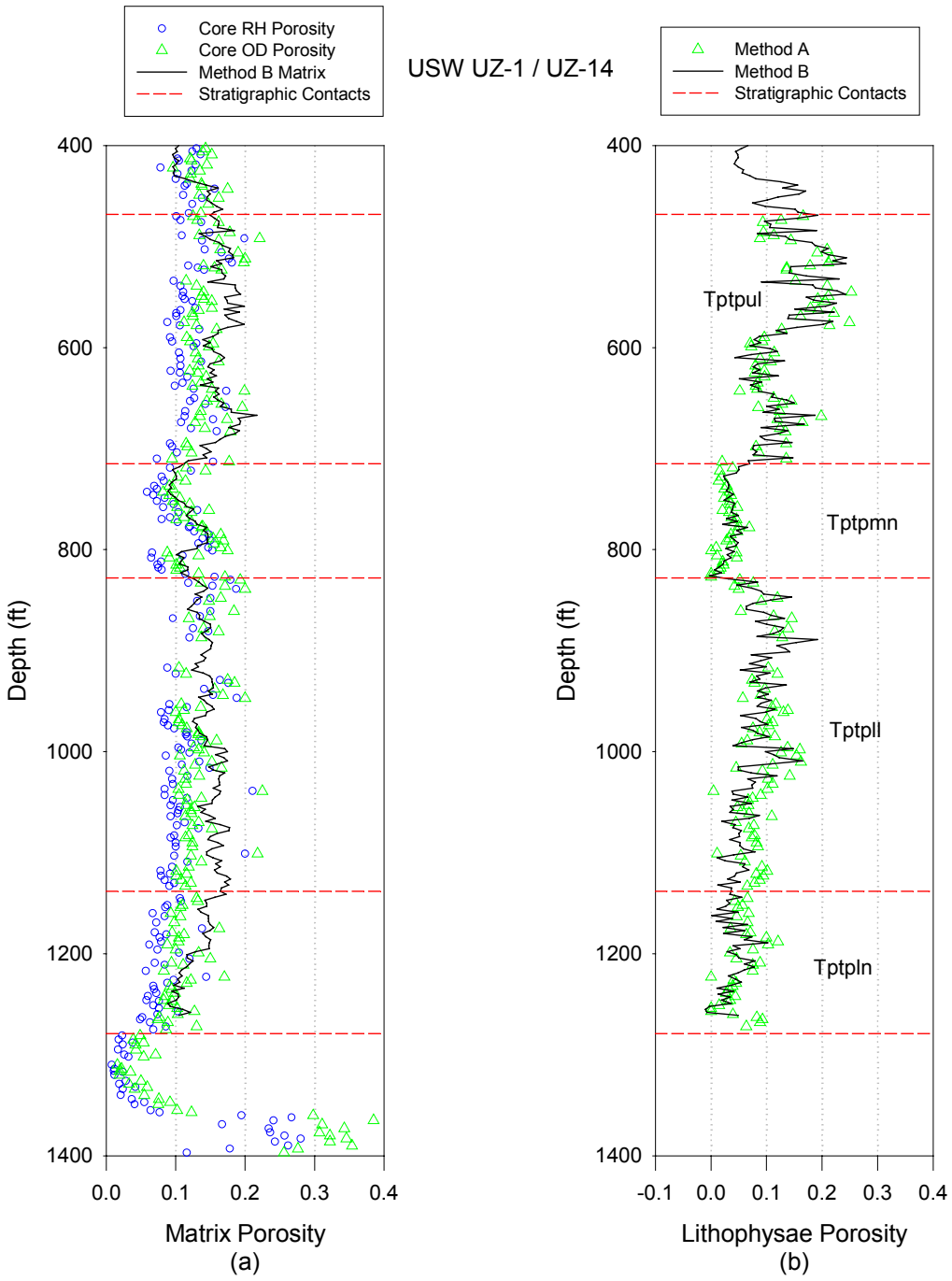

NOTES: OD = oven-dried; RH = relative humidity.

DTN: MO0109HYMXPROP.001 [155989], SN0208T0503102.007

Figure II-24. USW UZ-1/UZ-14 Core

USW UZ-6

The neutron porosity and the bulk density data for this borehole are consistent with data from nearby boreholes. Method B was applied for calculating matrix and lithophysal porosity for this borehole.

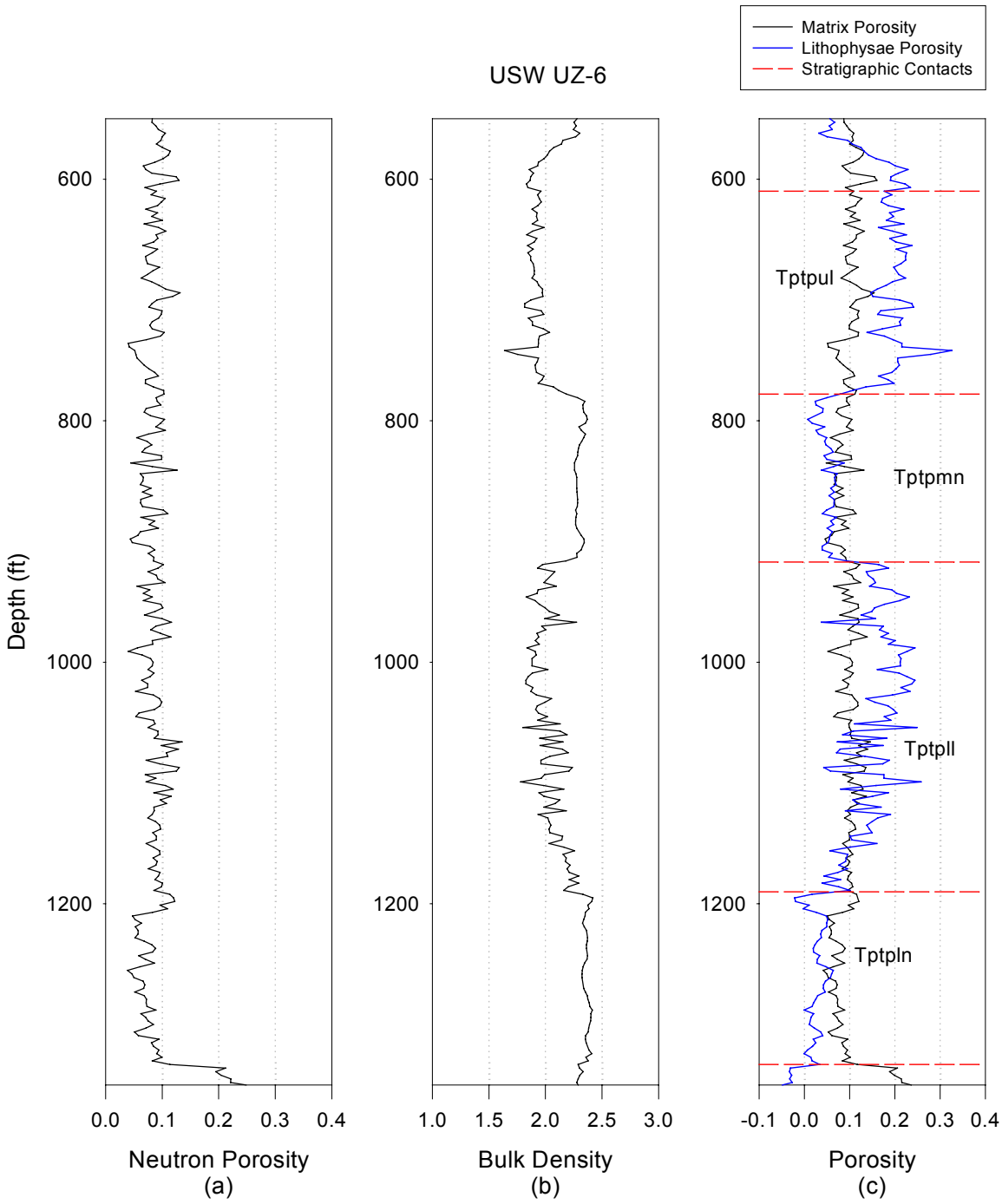

DTN: MO0010CPORGLOG.002 [155229]

Figure II-25. USW UZ-6

USW UZ-16

As observed in the neutron porosity data for boreholes USW NRG-7/7a and USW SD-9, the neutron porosity data are high compared with the volumetric water content measured from core samples. As in these other boreholes, the lower neutron porosity could be the result of using a less accurate porosity matrix. The higher neutron porosity data lead to calculated matrix porosities that are also a little high. The bulk density data compare with the respective data from nearby boreholes. Method A was applied to calculate lithophysal porosity for this borehole. It may be noted that the volumetric water content remains relatively constant in the 8 to 11 percent range regardless of the presence of lithophysae. The core volumetric water content may be the best measure of matrix porosity since it will be largely unaffected by small lithophysae. This seems to be the case for this borehole where core porosity measurements are slightly greater in the lithophysae zones than in the non-lithophysae zones.

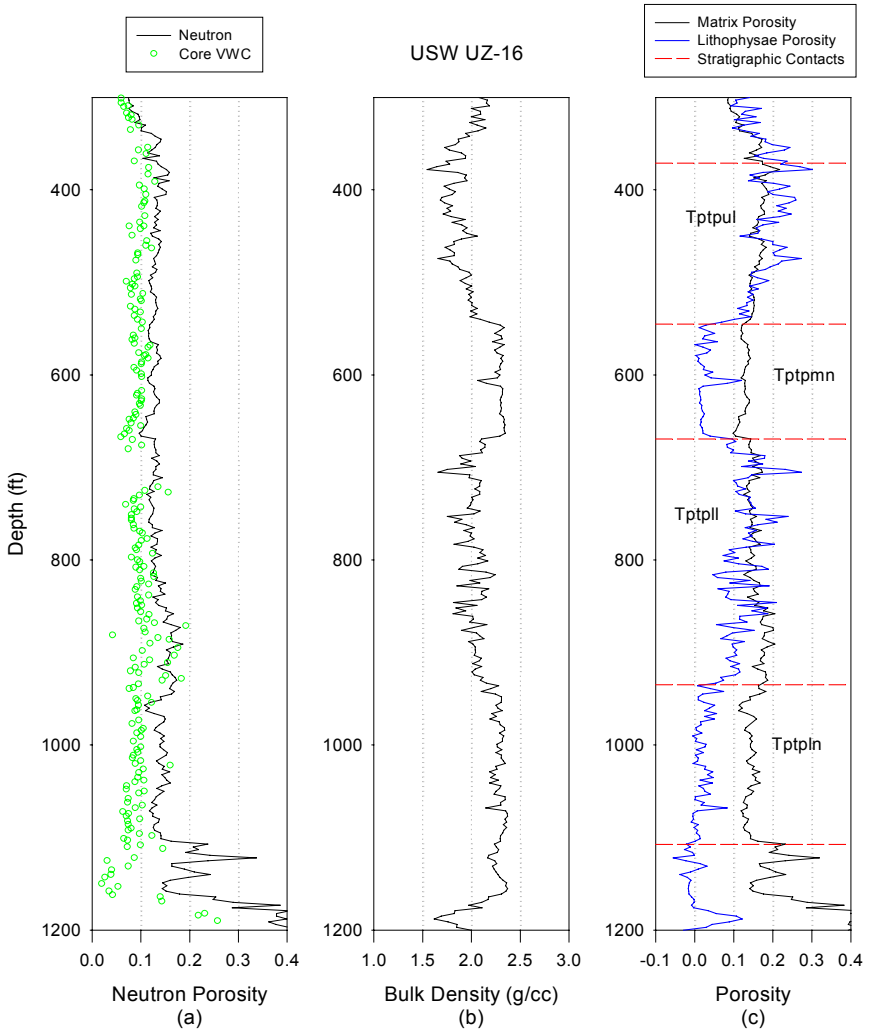

NOTE: VWC = volumetric water content.

DTN: MO0010CPORGLOG.003 [155959]

Figure II-26. USW UZ-16 Petrophysical

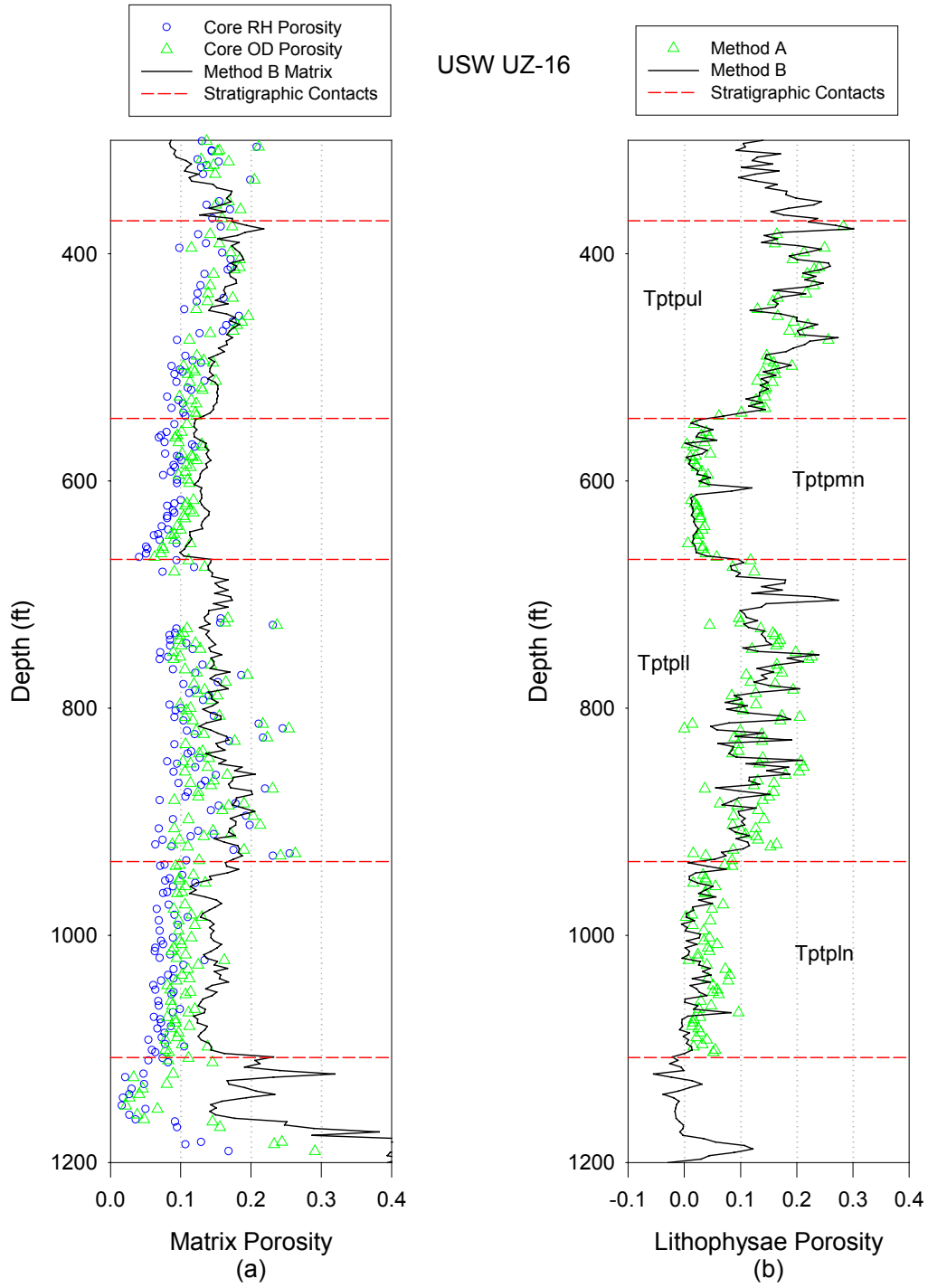

NOTES: OD = oven-dried; RH = relative humidity.

DTN: MO0109HYMXPROP.001 [155989], SN0208T0503102.007

Figure II-27. USW UZ-16 Core

USW UZ-7a

The neutron porosity log for borehole USW UZ-7a is generally high compared with core volumetric water content data. Method A was applied to calculate lithophysal porosity.

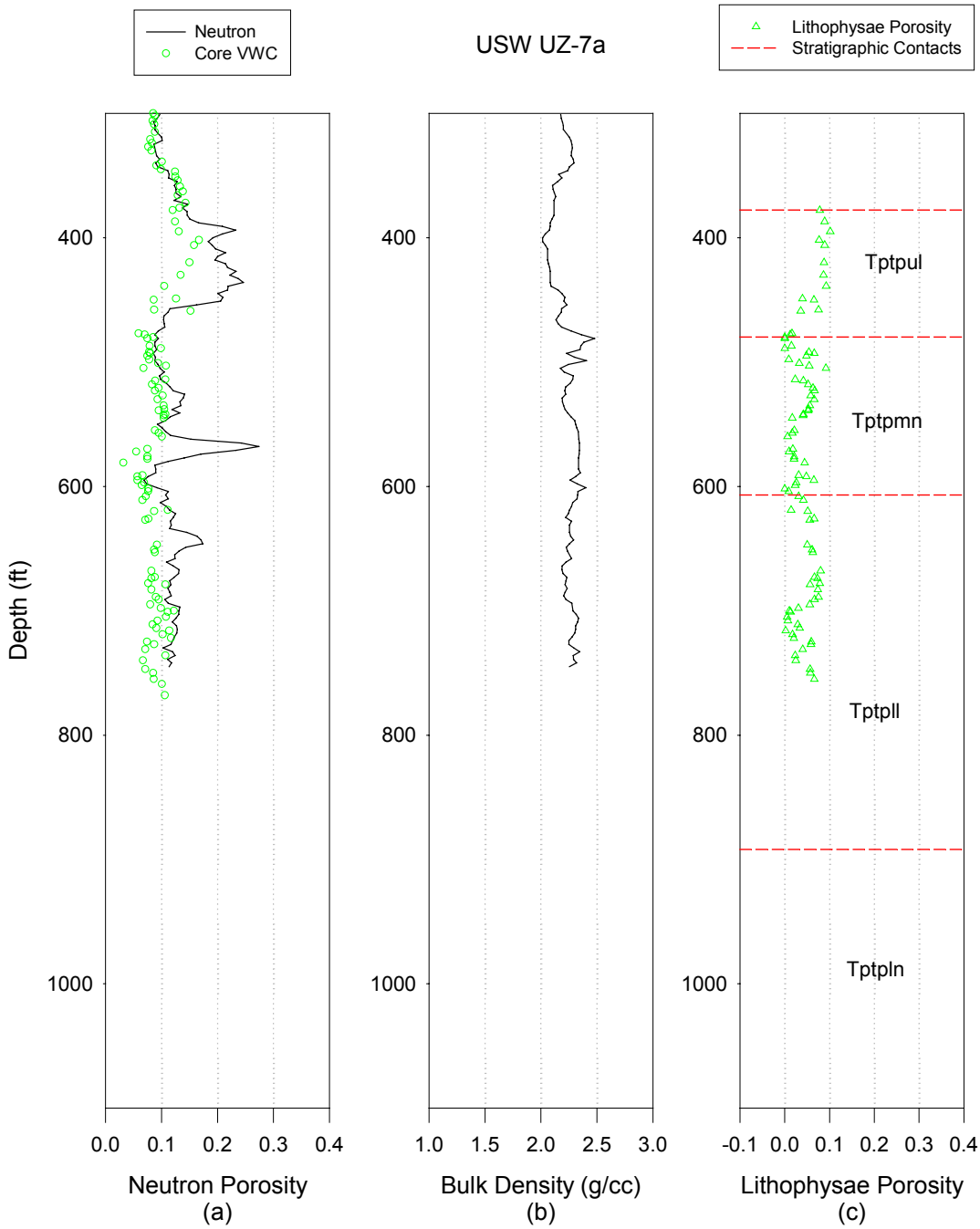

NOTE: VWC = volumetric water content.

DTN: MO0010CPORGLOG.003 [155959]

Figure II-28. USW UZ-7a

USW WT-1

The neutron porosity and bulk density data for USW WT-1 compare reasonably with neighboring boreholes. Method B was used to calculate the matrix and lithophysal porosity for this borehole.

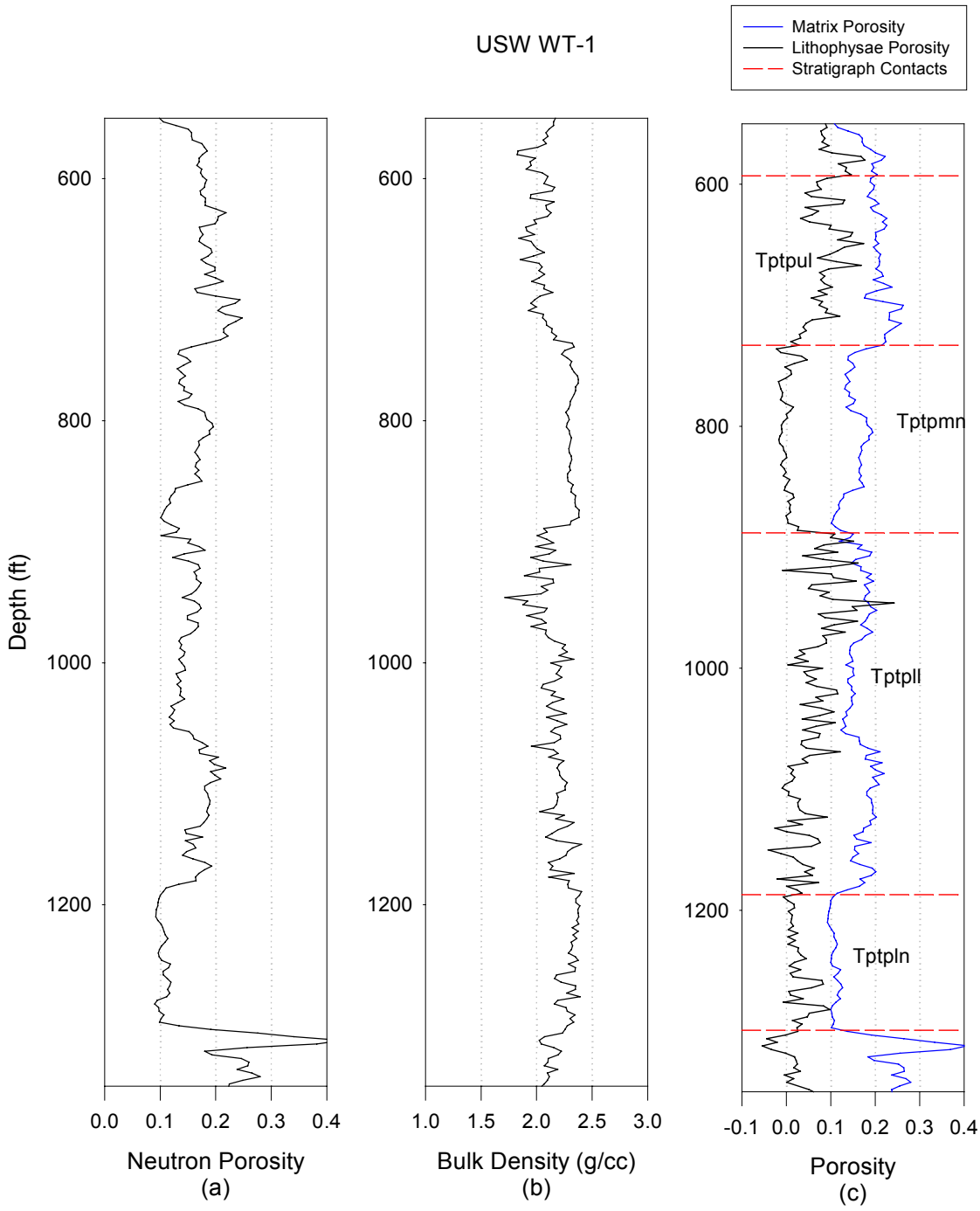

DTN: MO0010CPORGLOG.002 [155229]

Figure II-29. USW WT-1

USW WT-10

The neutron porosity data for USW WT-10 are high over the bottom half of the upper lithophysae zone when compared to other boreholes in the area. Method C was used to calculate lithophysal porosity in this borehole.

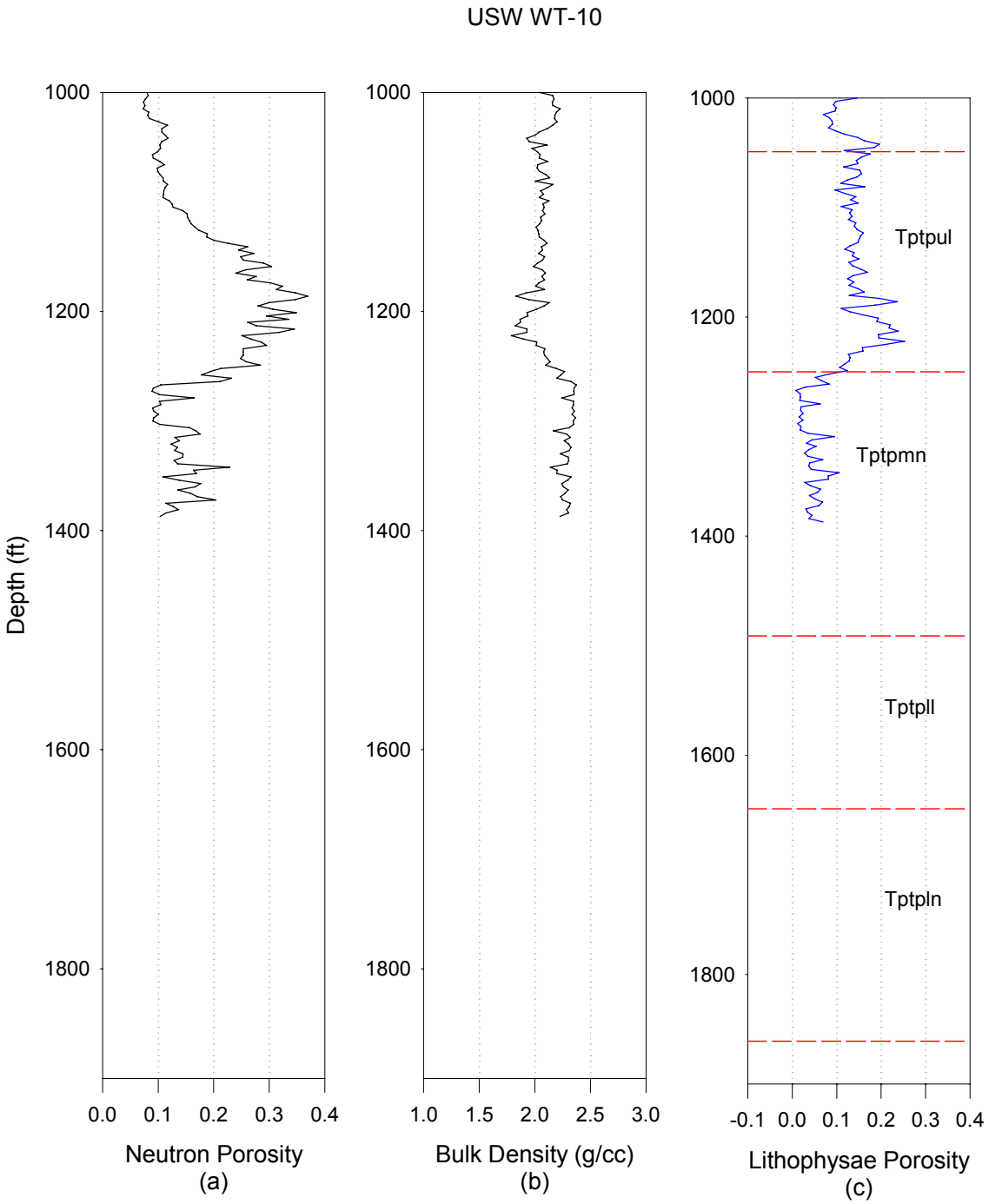

DTN: MO0010CPORGLOG.002 [155229]

Figure II-30. USW WT-10

USW WT-11

The neutron porosity and the bulk density data for borehole USW WT-11 compare favorably with data from other boreholes. Method B was used to calculate matrix and lithophysal porosity for this borehole.

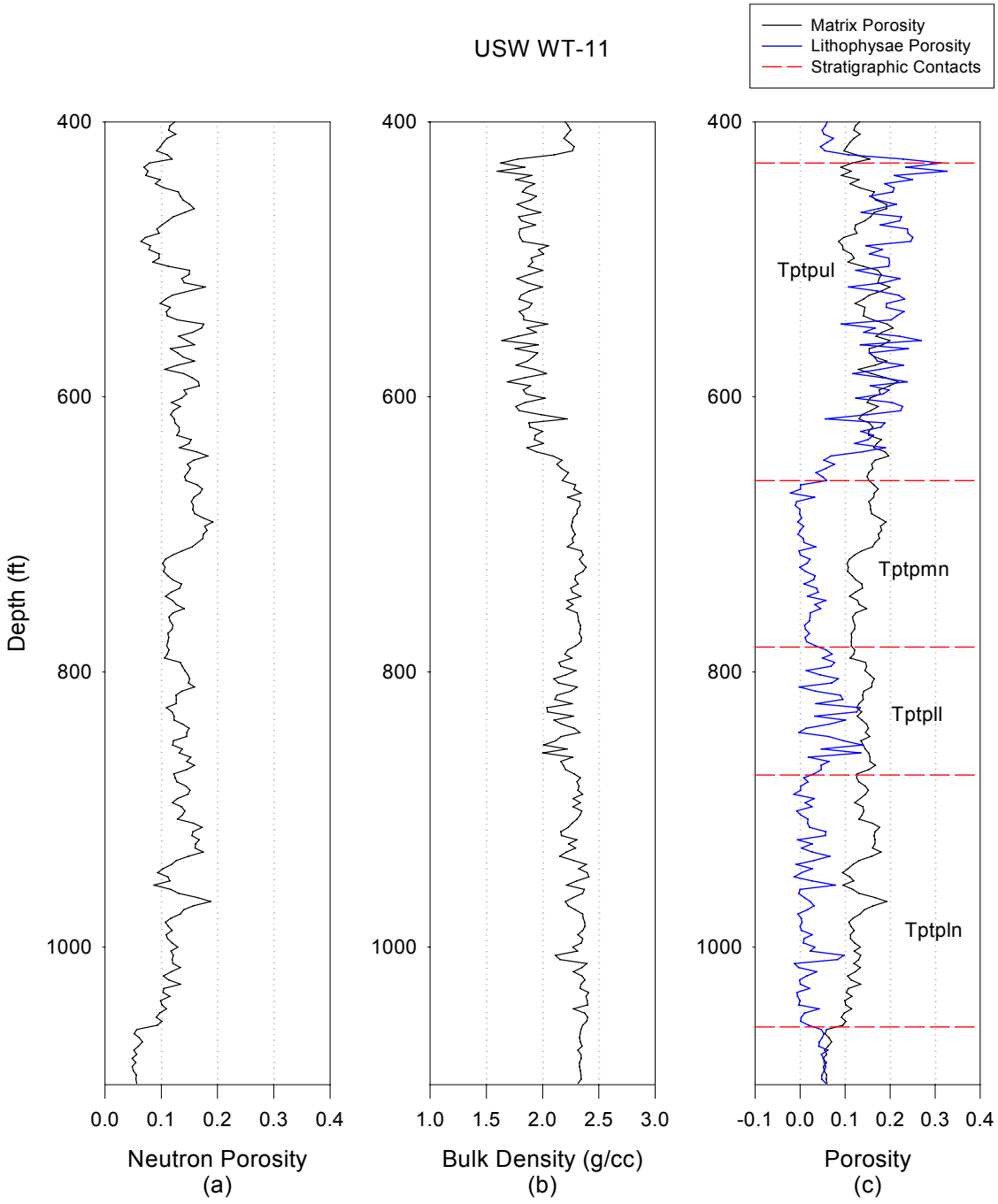

DTN: MO0010CPORGLOG.002 [155229]

Figure II-31. USW WT-11

UE-25 WT #12

The neutron porosity and the bulk density data for UE-25 WT #12 compare favorably with data from other boreholes. Method B was used to calculate matrix and lithophysal porosity for this borehole.

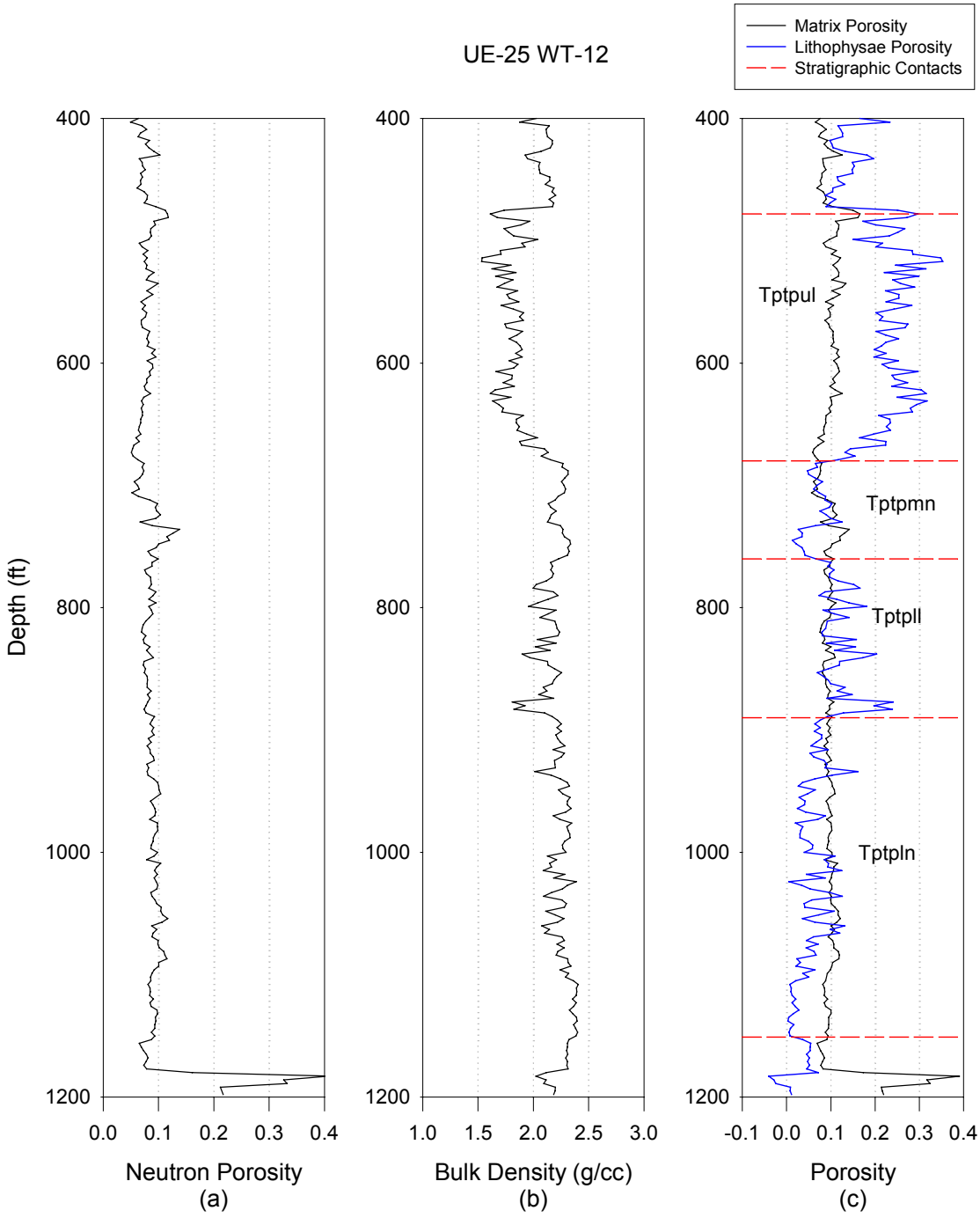

DTN: MO0010CPORGLOG.002 [155229]

Figure II-32. UE-25 WT #12

UE-25 WT #13

The neutron porosity data for UE-25 WT #13 are consistently higher than data from other boreholes, while the bulk density data are consistent with other borehole density recordings. Method C was used to calculate lithophysal porosity for this borehole.

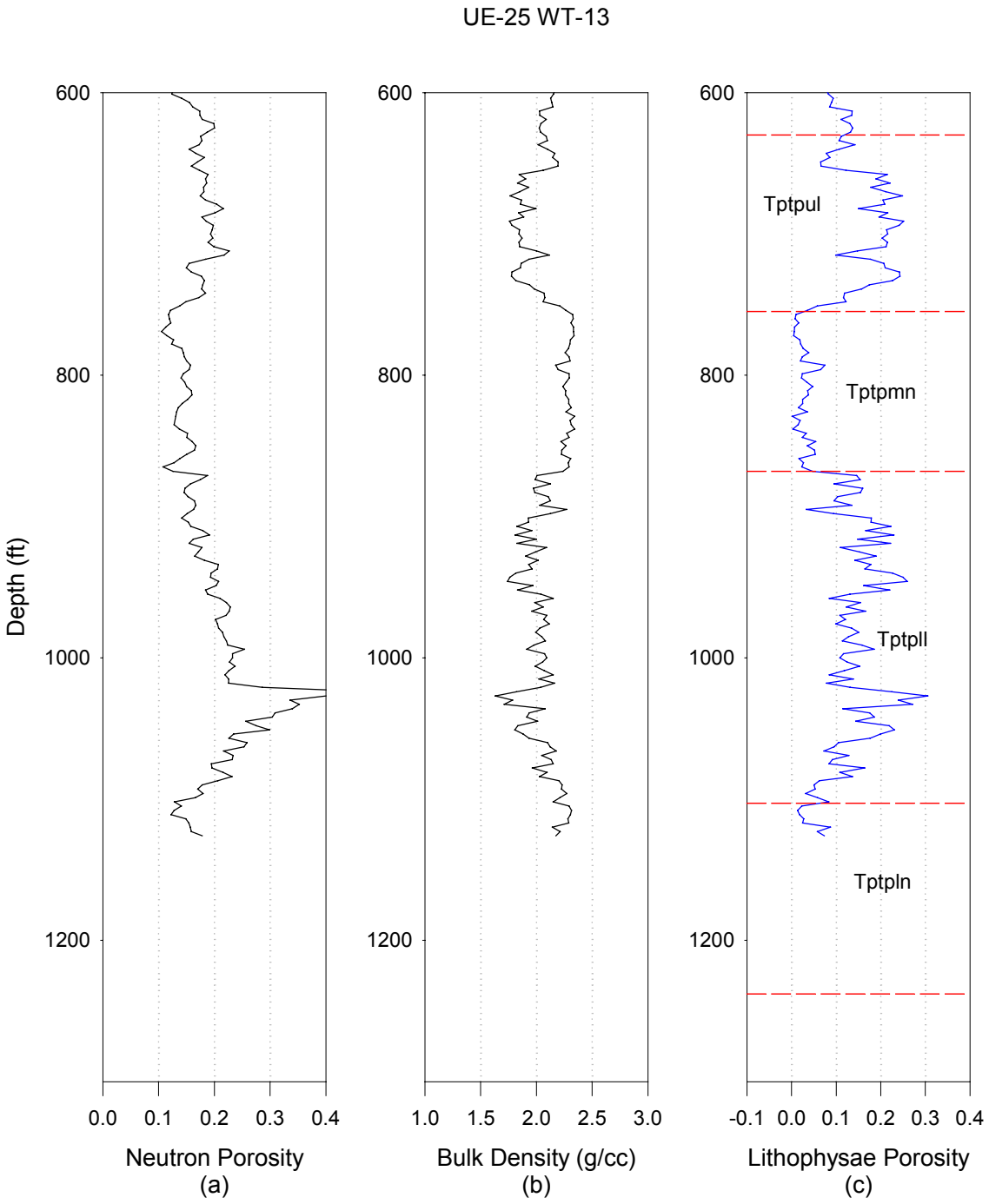

DTN: MO0010CPORGLOG.002 [155229]

Figure II-33. UE-25 WT #13

UE-25 WT #14

The neutron porosity and the bulk density data for borehole UE-25 WT #14 compare favorably with data from other boreholes. Method B was used to calculate matrix and lithophysal porosity for this borehole.

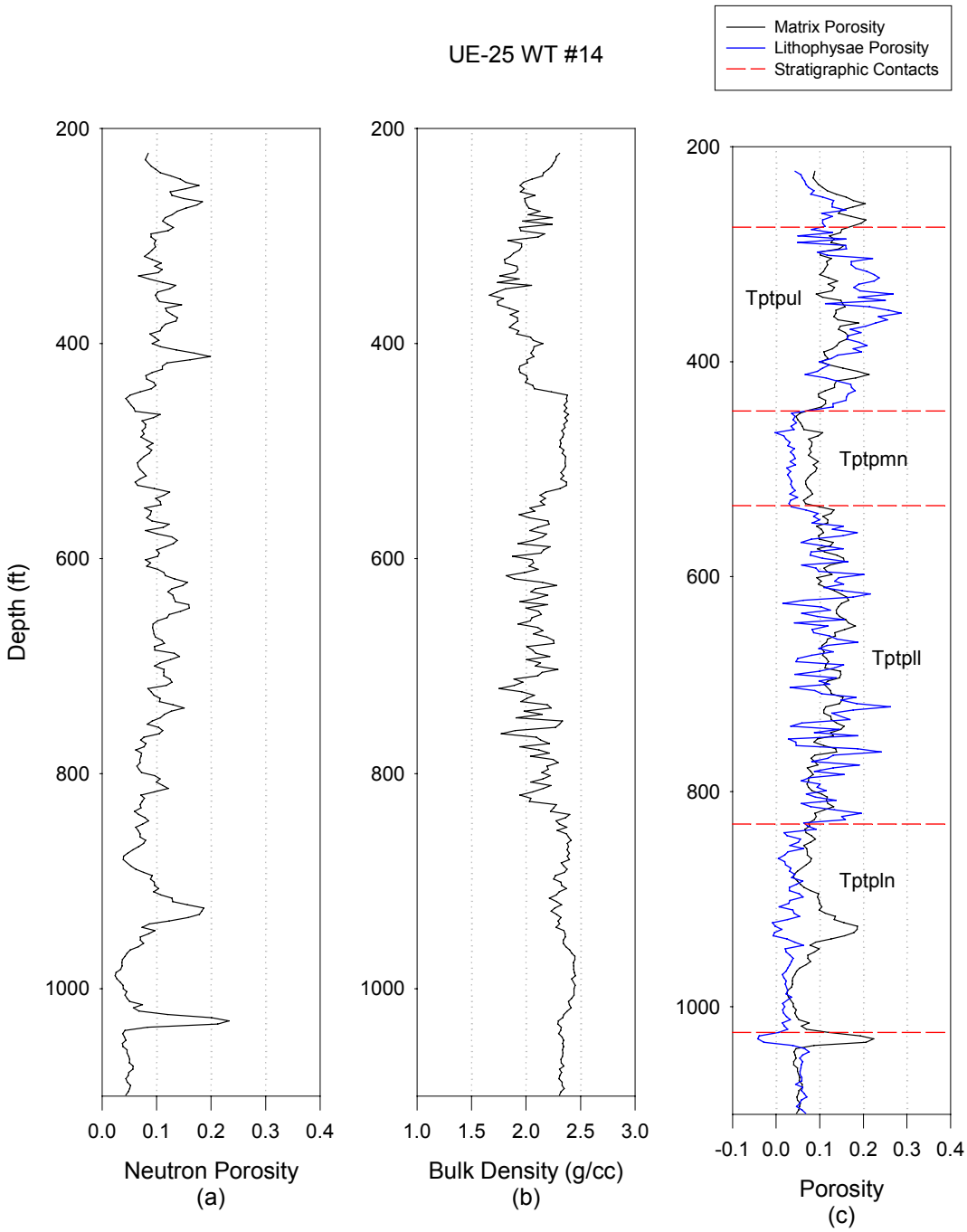

DTN: MO0010CPORGLOG.002 [155229]

Figure II-34. UE-25 WT #14

UE-25 WT #15

The neutron porosity data for UE-25 WT #15 may be a little high compared to other boreholes. Method B was used to calculate matrix and lithophysal porosity for this borehole.

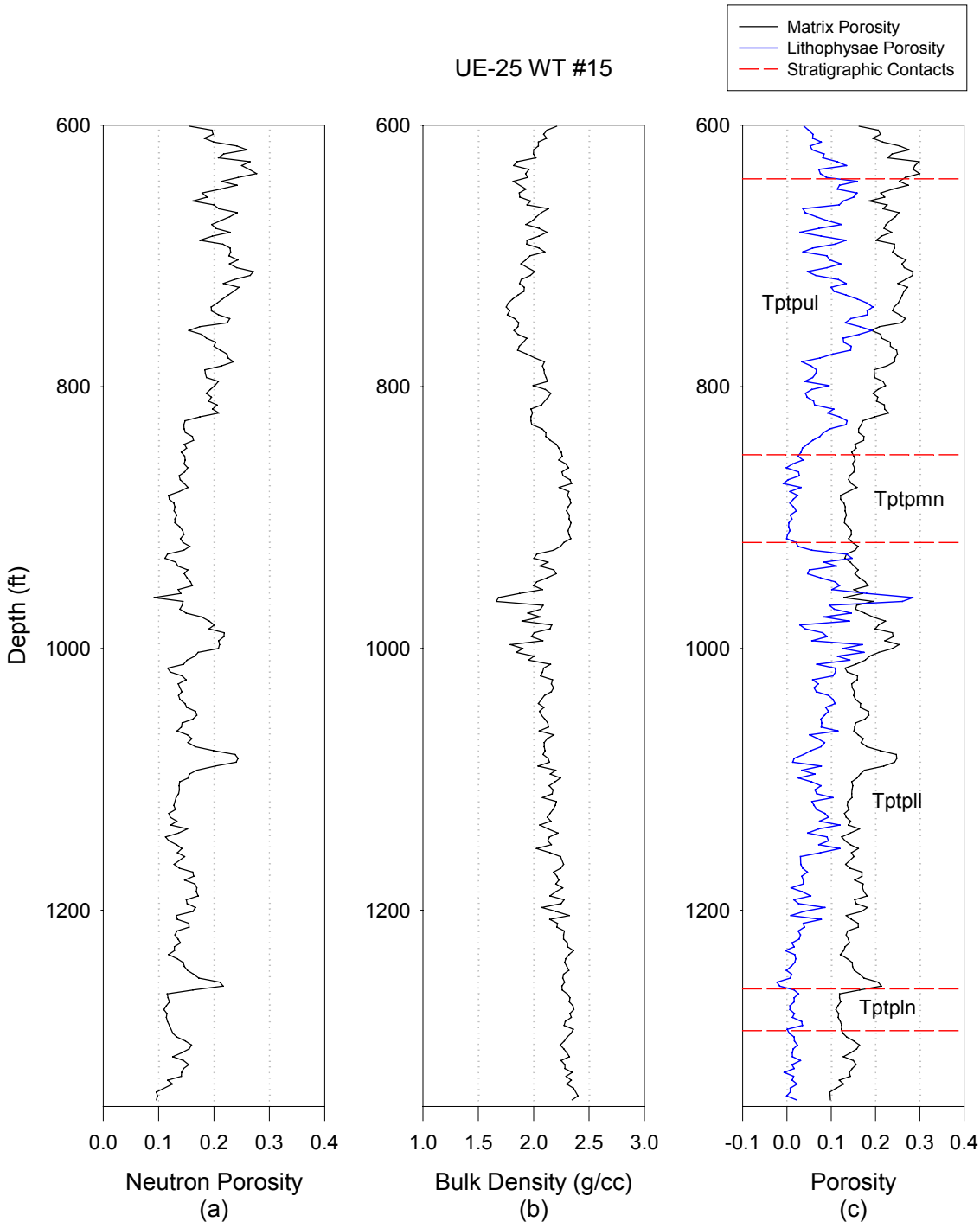

DTN: MO0010CPORGLOG.002 [155229]

Figure II-35. UE-25 WT #15

UE-25 WT #16

The neutron porosity data for UE-25 WT #16 look a little high compared to other boreholes. Method B was used to calculate the matrix and lithophysal porosity for this borehole.

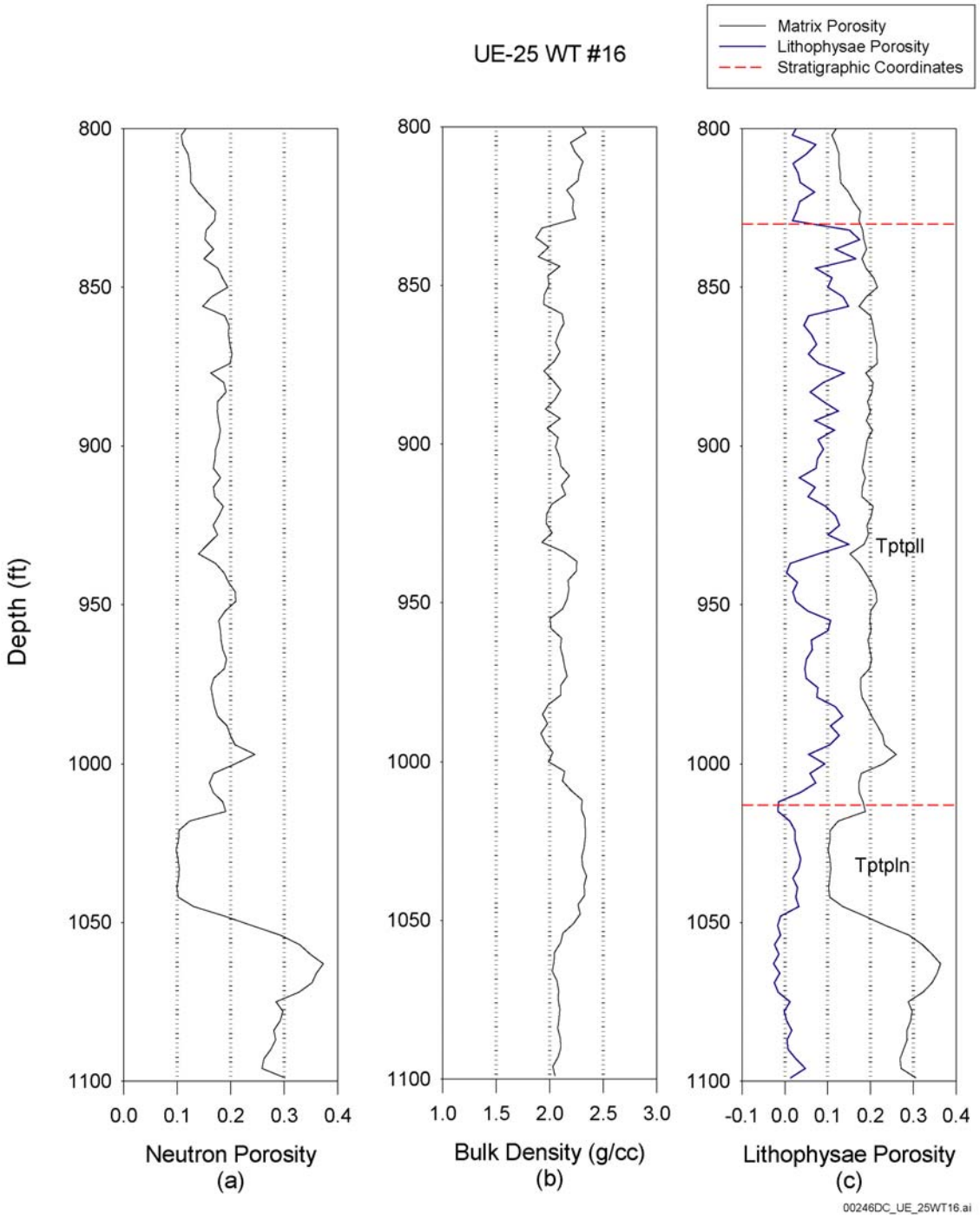

DTN: MO0010CPORGLOG.002 [155229]

Figure II-36. UE-25 WT #16

UE-25 WT #17

The effect of borehole rugosity is reflected in the neutron porosity data for UE-25 WT-#17. The bulk density data are similar to other boreholes, despite reported severe borehole enlargement throughout much of the recording interval. After comparing the calculated porosities from Methods B and C, Method C was chosen. The lower nonlithophysae unit data were not used because negative values were calculated.

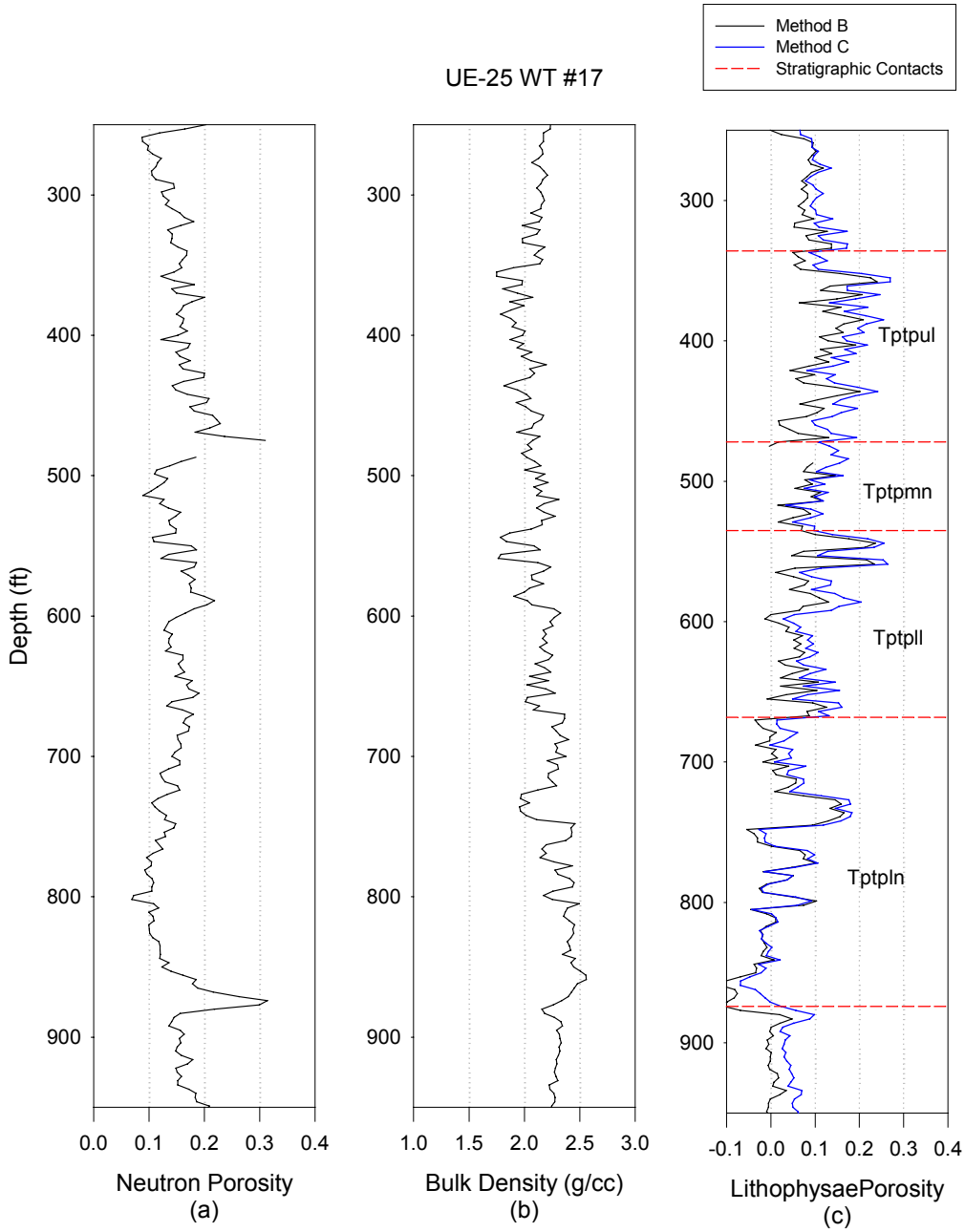

DTN: MO0010CPORGLOG.002 [155229], SN0208T0503102.007

Figure II-37. UE-25 WT #17 Method C

UE-25 WT #18

The neutron porosity data for borehole UE-25 WT #18 may be a little high in the upper lithophysae zone but otherwise match the corresponding data from other boreholes. The bulk density data are also representative of other borehole data. Method B was used to calculate matrix and lithophysal porosity for this borehole.

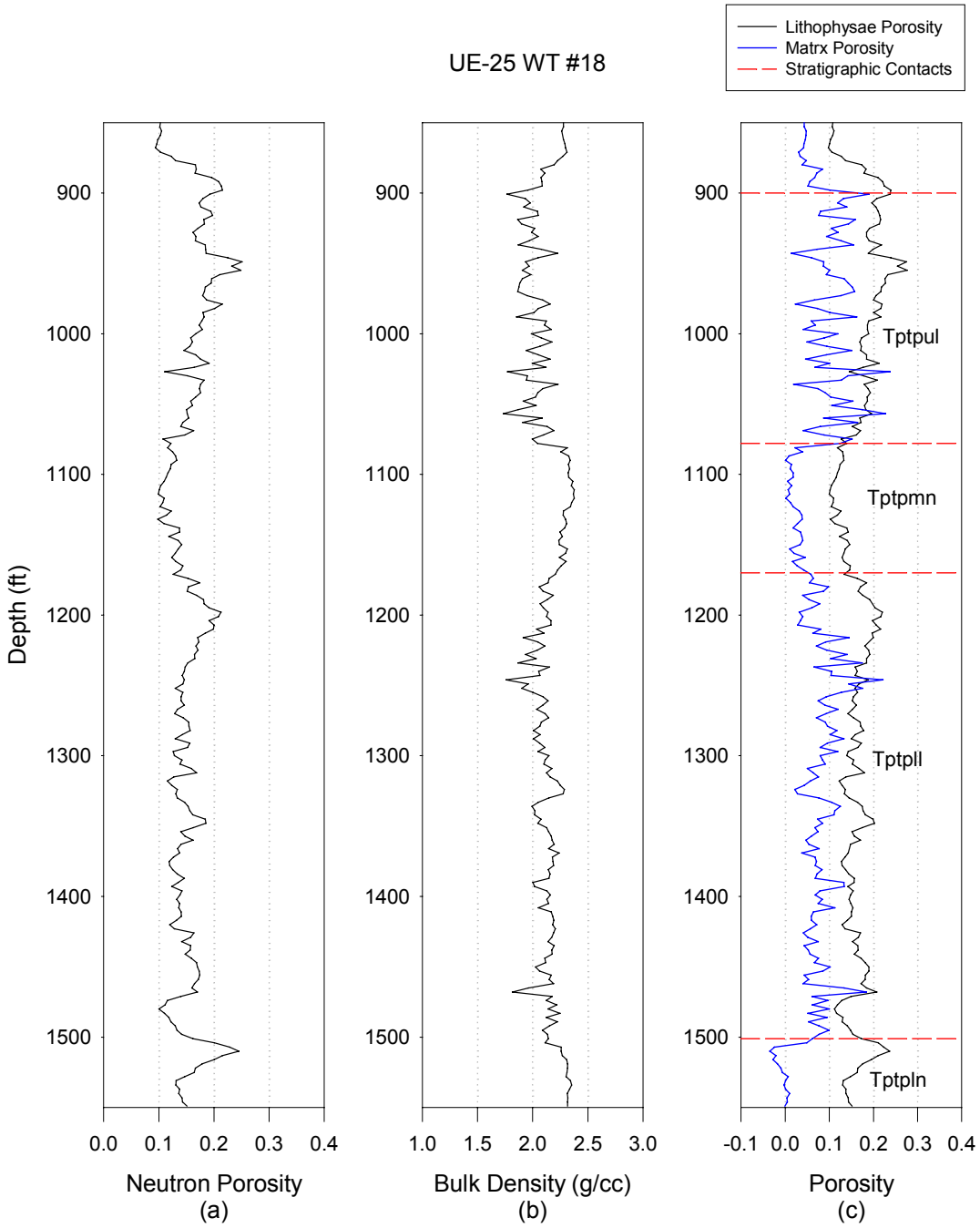

DTN: MO0010CPORGLOG.002 [155229]

Figure II-38. UE-25 WT #18

USW WT-2

The neutron porosity and the bulk density data for borehole USW WT-2 are similar to the respective data from other boreholes. Method B was used to calculate matrix and lithophysal porosity for this borehole.

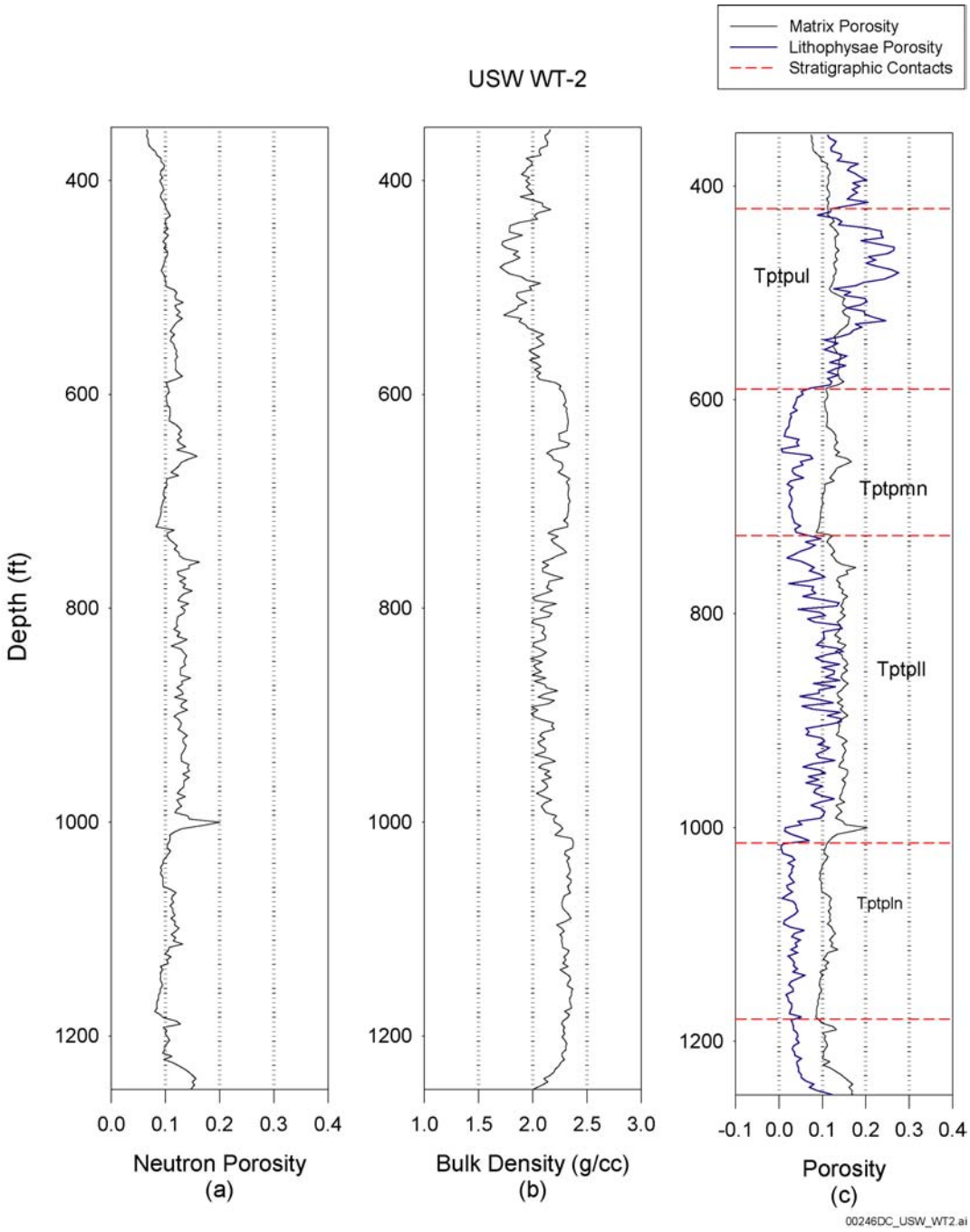

DTN: MO0010CPORGLOG.002 [155229]

Figure II-39. USW WT-2

USW WT-24

The neutron porosity and the bulk density data for borehole USW WT-24 are typical of data from other boreholes. Method B was used to calculate matrix and lithophysal porosity for this borehole.

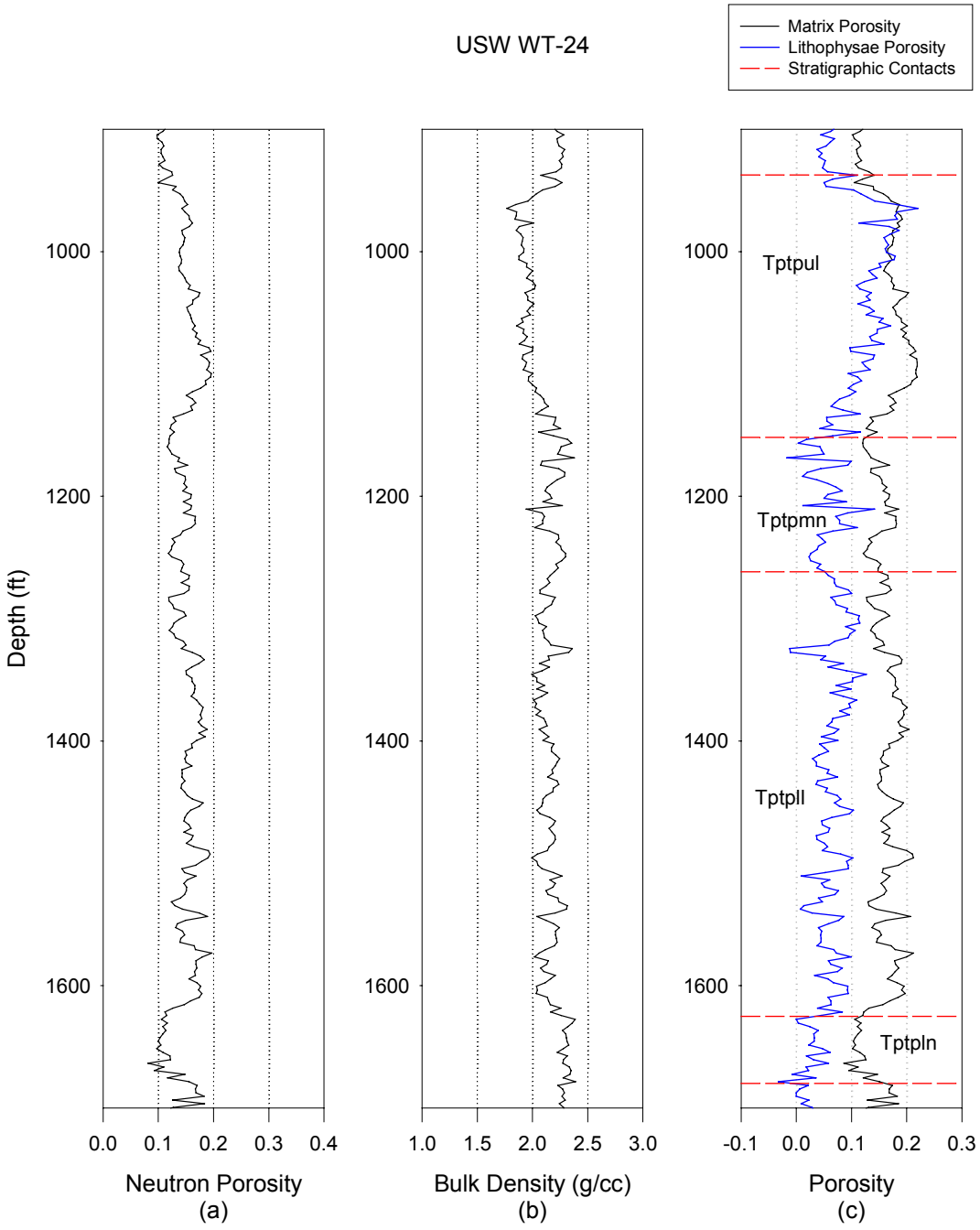

DTN: MO0010CPORGLOG.003 [155959]

Figure II-40. USW WT-24

UE-25 WT #3

Method B was used to calculate the matrix and lithophysal porosity in borehole UE-25 WT #3. According to the stratigraphic picks, the Tptpln should occur between 35 and 189 ft. The value of 189 ft seems reasonable based on the calculated lithophysal porosity. However, a better estimate of the top of the Tptpln appears to be about 130 ft. Therefore, in this work, the range 130 to 189 ft was used to represent the Tptpln. The data above 130 ft were not used.

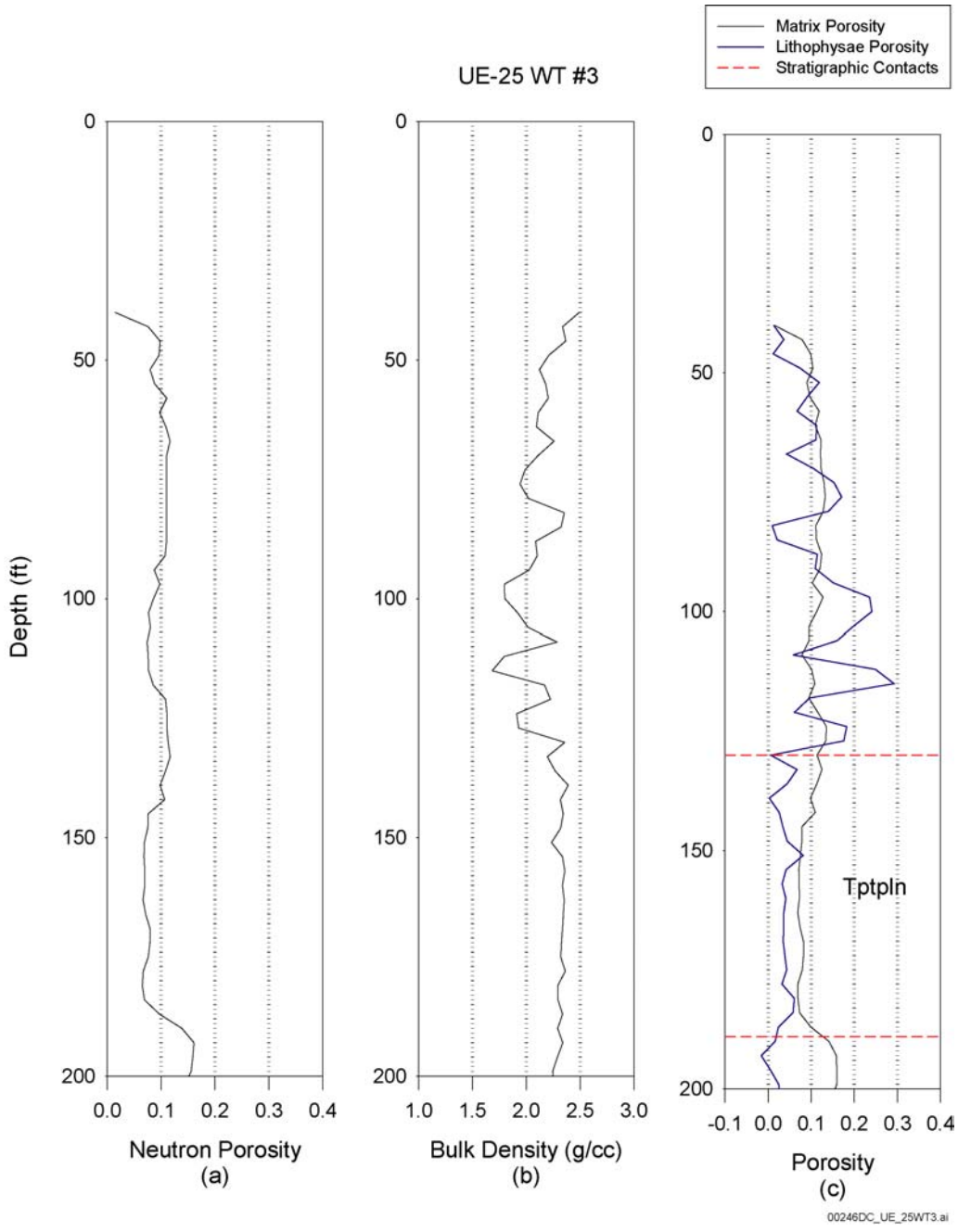

DTN: MO0010CPORGLOG.002 [155229]

Figure II-41. UE-25 WT #3

UE-25 WT #4

The neutron porosity and the bulk density data for borehole UE-25 WT #4 are consistent with other boreholes. Method B was used to calculated the matrix and lithophysal porosity for this borehole.

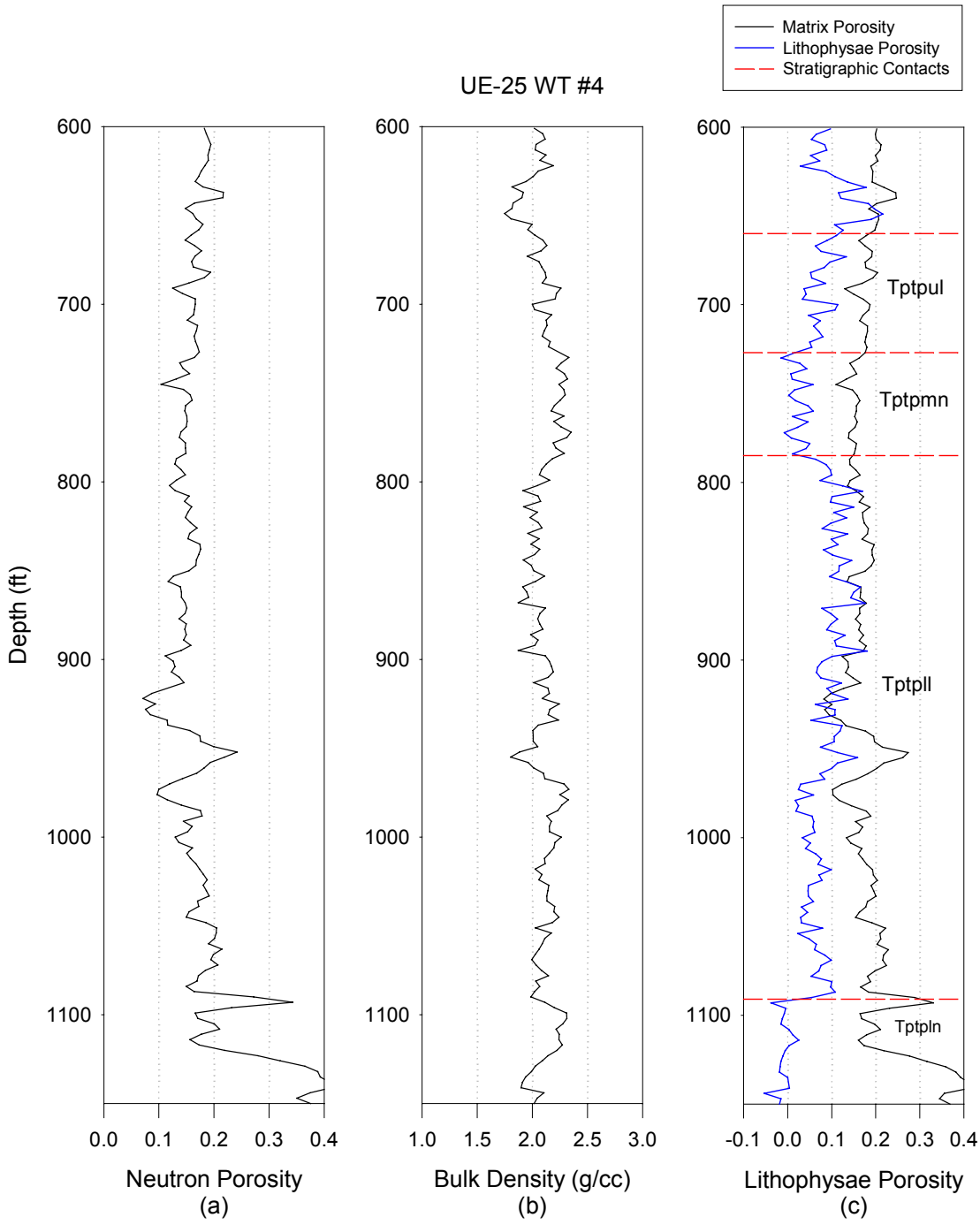

DTN: MO0010CPORGLOG.002 [155229]

Figure II-42. UE-25 WT #4

USW WT-7

The neutron porosity data for borehole USW WT-7 look a little high in the upper lithophysae while the bulk density data are consistent with other boreholes. Using Method B to calculate matrix and lithophysal porosity and gave results that were consistent with neighboring boreholes USW H-3 and USW G-3. Method B was chosen over Method C because there was no clear reason to believe the neutron porosity data were outside the range of other borehole data.

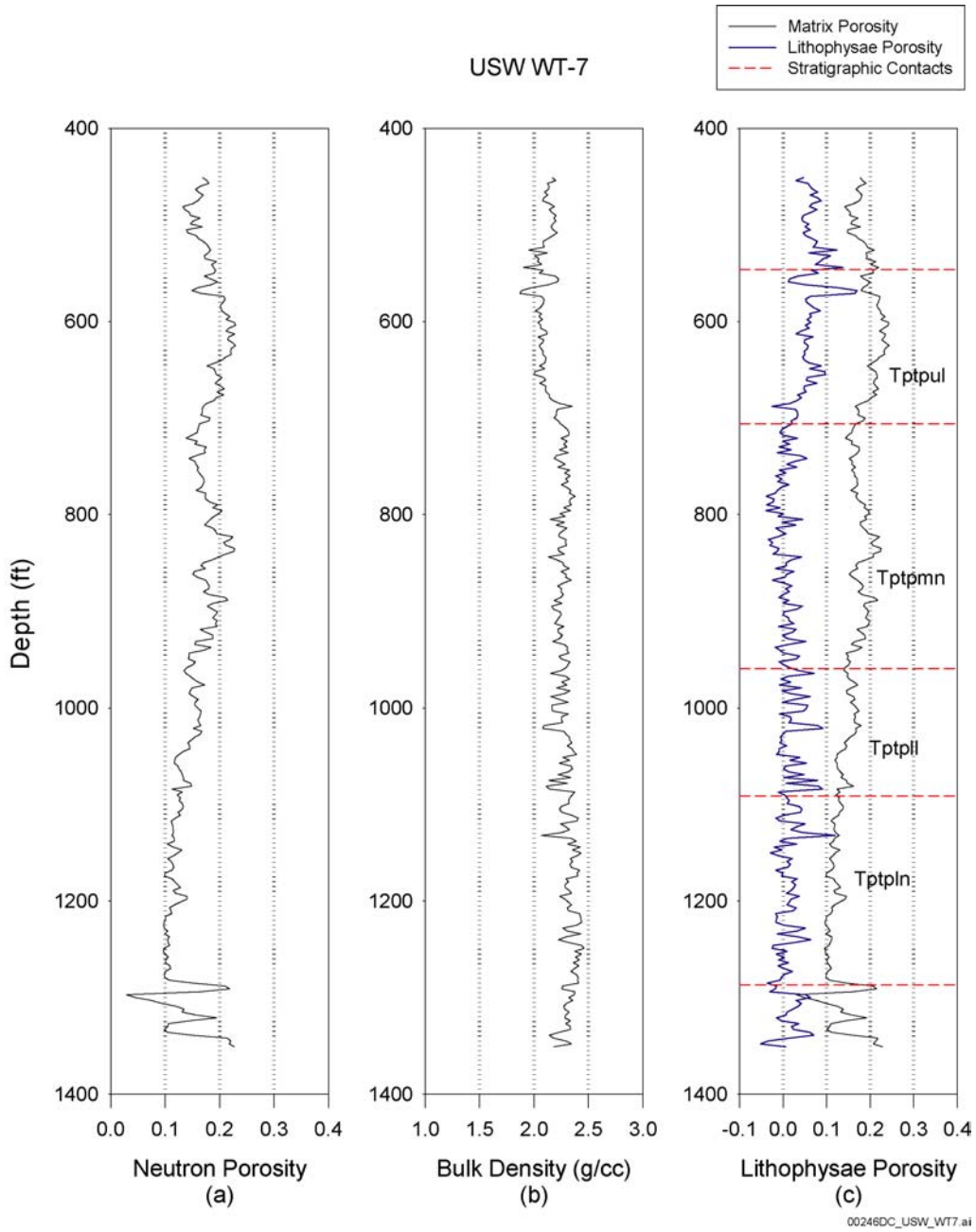

DTN: MO0010CPORGLOG.002 [155229]

Figure II-43. USW WT-7

ATTACHMENT III
MATRIX THERMAL CONDUCTIVITY DATA

INTENTIONALLY LEFT BLANK

ATTACHMENT III
MATRIX THERMAL CONDUCTIVITY DATA

This attachment presents the results of laboratory thermal conductivity measurements considered in the development of model parameter distributions for matrix thermal conductivity. Several data are excluded from model calibration due to inadequate quality assurance pedigree, insufficient analysis, or questionable experimental results. This attachment documents the data considered and describes why certain data are excluded.

All of the data selected for calibration of the matrix thermal conductivity model satisfy the following the three screening criteria:

1. They are fully qualified and verified according to the appropriate procedures.

2. They are appropriate for the model calibration procedure described in Section 6.1.7. This procedure requires the measurement of thermal conductivity under both water-saturated (wet) and air-saturated (dry) conditions. In addition, an estimate of the porosity of the sample is also required.

3. Experimental results must appear to be reasonable and reproducible.

Only two DTNs satisfy all three criteria. The first DTN (SNL01A05059301.005 [109002]) was developed from *Thermal Expansion and Thermal Conductivity Measurements for Boreholes UE25 NRG-4, UE25 NRG-5, USW NRG-6, and USW NRG-7/7A* (Brodsky et al. 1997 [100653]). This report documents the thermal conductivity measurements on core samples extracted from various boreholes. Thermal conductivity measurements from this report are reproduced in Table III-1. For the dry measurements the values reported at 110°C were used, and for the wet measurements, the values reported at 70°C were used. For samples where more than one measurement of thermal conductivity was reported at the specified temperature, the average of the reported values is given in Table III-1. Data that are highlighted in Table III-1 are excluded from this analysis for the reason noted in the table footnotes. Finally, the porosity values for these samples are provided by DTN: SNL01A05059301.007 [108980].

The "dry" thermal conductivity specimens were placed in an oven and heated at $\leq$2 C per minute until the oven reached 110C. They were dried until subsequent weighings 120 to 128 hours apart showed that the masses were stable to within 0.05 percent (Brodsky et al. 1997, pp. 9 to 10 [100653]). The thermal conductivity measurements conducted on the "wet" 70C samples were saturated, then encapsulated in a moisture containment cells to preserve saturation during testing (Brodsky et al. 1997, p. 14 [100653]).

The second DTN (SNL22100196001.006 [158213]) was developed from *Laboratory Measurements of Thermal Conductivity as a Function of Saturation State for Welded and Nonwelded Tuff Specimens* (SNL 1998 [118788]). This data set includes both wet and dry thermal conductivity measurements for six samples extracted from Alcove 5 in the Tptpmn. These data are reproduced in Table III-2.

Table III-1. Borehole Thermal Conductivity Measurements

Location	T/H unit	Specimen ID (dry/wet)	Porosity	Dry Thermal Conductivity at 110°C W/(m K)	Wet Thermal Conductivity at 70°C W/(m K)
NRG4	TSw1	529.0B / 529.0A	0.165	1.16	1.67
NRG4	TSw1	545.0G	0.239	0.895	
NRG4	TSw1	586.2B / 586.2A	0.194	0.945	1.64
NRG4	TSw1	590.5B	0.187	0.995	
NRG4	TSw1	610.5B	0.144	1.095	
NRG4	TSw1	619.9B	0.132	1.14	
NRG4	TSw1	654.0B / 654.0A	0.137	1.155	1.8
NRG5	TSw1	781.8A / 781.8A	0.157	1	1.92
NRG5	TSw1	791.6A / 791.3A	0.246	0.82	1.78
NRG5	TSw2	834.8B / 834.8A	0.089	1.655	1.92
NRG5	TSw2	843.5A / 843.5A	0.088	1.65	2.2
NRG5	TSw2	848.0B / 848.0B	0.121	1.5	2.61
NRG5	TSw2	853.8 / 852.5	0.087	1.705	2.26
NRG5	TSw2	874.9 / 874.3	0.086	1.675	2.32
NRG5	TSw2	879.6A / 879.6A	0.087	1.625	3.09
NRG5	TSw2	886.5 / 886.5	0.124	1.37	2.53
NRG5	TSw2	893.3B / 893.3B	0.113	1.46	2.75
NRG5	TSw2	899.8B / 899.8B	0.110	1.475	2.77
NRG6	TSw1	277.5E / 277.5D	0.100	1.255	1.68
NRG6	TSw1	321.1E / 321.1D	0.150	1.165	1.71
NRG6	TSw1	354.9C / 354.9B	0.150	1.135	1.49
NRG6	TSw1	392.1D / 392.1C	0.040	1.185	1.55
NRG6	TSw1	416.0K / 416.0J	0.090	1.285	1.55
NRG6	TSw1	421.8D / 421.8C	0.127	1.19	1.7
NRG6	TSw1	425.3B / 425.3A	0.138	1.26	1.82
NRG6	TSw1	451.2B / 451.2A	0.185	1.29	1.7
NRG6	TSw1	556.1B / 556.1A	0.277	0.91	2.04
NRG6	TSw1	693.1C / 693.1C	0.136	1.385	1.93
NRG6	TSw2	757.0B / 757.0A	0.096	1.61	2.02
NRG6	TSw2	778.1B / 778.1A	0.084	1.71	1.85
NRG6	TSw2	787.5B / 787.5A	0.112	1.6	1.72
NRG6	TSw2	802.7D / 802.7C	0.095	1.67	1.78
NRG6	TSw2	809.4B / 809.4A	0.092	1.64	1.66
NRG6	TSw2	900.4D / 900.4C	0.145	1.5	2.23

Table III-1. Borehole Thermal Conductivity Measurements (Continued)

Location	T/H unit	Specimen ID (dry/wet)	Porosity	Dry Thermal Conductivity at 110°C W/(m K)	Wet Thermal Conductivity at 70°C W/(m K)
NRG6	TSw2	926.3E / 926.3-D	0.129	1.54	2.15
NRG6	TSw2	987.0B / 987.0A	0.118	1.55	2.04
NRG7	TSw1	312.8D / 312.8C	0.106	1.33	1.63

	Wet thermal conductivity was not measured.
	Measured wet thermal conductivity is outside the calibration range.
	Data from specimen ID 556.1B/556.1A were not used due to ambiguity in one document that cited the data. The data in DTN: SNL01A05059301.005 [109002] are correct. The impact of not including these data is expected to be minimal because specimen ID 556.1B/556.1A data are within the range of the remaining specimen data.
	A measured wet and dry pair is not theoretically possible for the calculated porosity. This statement assumes that a parallel flow model is the limiting case regarding how close two measurements may be to one another.

DTN: SNL01A05059301.005 [109002], SNL01A05059301.007 [108980]

Table III-2. Alcove 5 Thermal Conductivity Data

Alcove 5 Specimen	Saturated Mass (g)	Dry Mass (g)	Porosity	Dry Thermal Conductivity (W/(m K))	Saturated Thermal Conductivity (W/(m K))
SPC00515193-G-H	60.896	58.407	0.0967	1.81	2.3
SPC00515196-G-H	60.856	58.319	0.0986	1.72	2.25
SPC00515199-G-H	60.954	58.497	0.0955	1.87	2.33
SPC00515193-C-V	61.196	58.822	0.0922	1.82	2.28
SPC00515196-C-V	60.946	58.389	0.0993	1.81	2.27
SPC00515199- C-V	60.916	58.305	0.1014	1.8	2.27

DTN: SNL22100196001.006 [158213]

In Table III-2, the values of porosity, ϕ, are computed from the change in mass of the sample that takes place between the saturated and dry states. The equation used to calculate porosity is:

$$\phi = \frac{\left(M_{sat} - M_{dry}\right)/\rho_w}{\pi r^2 l} \qquad \text{(Eq. III-1)}$$

where M_{sat} and M_{dry} are the mass of the water-saturated and OD sample, respectively, ρ_w is the density of water (1.0 g/cc), r is the sample radius (nominally 1.0 cm), and l is the sample length (nominally 0.5 cm).[1]

There are two other qualified DTNs that contain thermal conductivity data for the Tptpmn. Unfortunately, neither satisfies the model calibration procedure screening criteria. The first is DTN: SNL22100196001.001 [109733], which only has water-saturated thermal conductivity measurements, and the second is DTN: SNL22100196001.002 [153138], which only has OD measurements. These data are, therefore, not used in the matrix thermal conductivity model calibration. The data were, however, used to validate the resulting matrix thermal conductivity model as discussed in Section 7.3.

[1] Data from specimen ID 556.1B/556.1A were not used due to an inconsistency between dry thermal conductivity values for this specimen in DTN: SNL01A05059301.005 [109002] and in Brodsky et al. 1997 [100653]. The values given in DTN: SNL01A05059301.005 [109002] are correct; however, some of the values given in Appendix A of Brodsky et al. 1997 [100653] were subject to a typographical error. The data compilations in Brodsky et al. 1997 [100653] are not affected. The impact of not including these data is expected to be minimal because specimen ID 556.1B/556.1A data are within the range of the remaining specimen data.

ATTACHMENT IV
STRATIGRAPHIC CONTACTS

INTENTIONALLY LEFT BLANK

ATTACHMENT IV
STRATIGRAPHIC CONTACTS

Table IV-1. Stratigraphic Contacts

BoreHole	Tptpul	Tptpmn	Tptpll	Tptpln	Tptpv3	Comment
G-1	456.5	713.4	814.8	1199.2	1287	P
G-2	977.2	1246	1280	1604	1633.8	P
G-3	548	688	830	1044	1186.7	P
G-4	420	674	774	1127.9	1316.5	P
H-1	538	788	897	1324	1410	P
H-3	540	680.1	848.1	1049.9	1194	P
H-4	376	576	703	987	1185	P
H-5	741	988	1088	1450	1582	P
H-6	435	653	795	1097	1213	P
NRG-4	700	**875***	**965***	**1302***	**1351***	P
NRG-6	465	713	810	**1152***	**1317***	B
NRG-7	518.4	740	877.6	1243	1414.8	B
ONC-1	810	977	1100	1178	1178	P
P-1	248	493	640	958	1090	P
SD-6	645.7	853	995	1305	1456	C
SD-7	490	682.5	803.3	1020	1182	B
SD-9	473	730	845.8	1182	1358	B
SD-12	470.2	663.7	786.9	1065.5	1278.1	B
UZ-1	470	717	830	**1144***	**1281***	P
UZ-6	610	778	917	1190	1333	P
UZ-14	468	715	828	1138	1279.1	C
UZ-16	371	545	669	935	1107.5	B
UZ-7a	377.8	480	607	**892***	**1060***	B
WT-1	593	733	888	1187	1299	P
WT-10	1049	1250	**1491***	**1649***	**1861***	P
WT-11	430	661	782	875	1058	P
WT-12	478	680	760	890	1151	P
WT-13	630	755	868	1103	**1238***	P
WT-14	275	446	534	830	1024	P
WT-15	641	852	919	1260	**1292***	P
WT-16	830	830	830	1013	1013	P
WT-17	336	472	535	668	874	P
WT-18	900	1078	1170	1501	1501	P
WT-2	421	590	727	1014	1179	P
WT-24	937.4	1151.7	1261.7	1625	1680	P
WT-3	11	11	35	189		P
WT-4	660	727	785	1091	1091	P
WT-7	546	706	959	1091	1287	P

NOTES: B = Both types of data; C = Cored data only; P = Petrophysical data only.
*Indicates depth value (in feet) was modeled or interpolated based on Geologic Framework Model (GFM2000) (DTN: MO0012MWDGFM02.002 [153777]).
The remaining depth values were obtained from DTNs MO0004QGFMPICK.000 [152554], and SNF40060298001.001 [107372]. All depths are measured from ground surface to the top of the unit.

INTENTIONALLY LEFT BLANK

ATTACHMENT V
ACRONYMS AND ABBREVIATIONS

INTENTIONALLY LEFT BLANK

ACRONYMS AND ABBREVIATIONS

Acronyms

3-D	three-dimensional
DTN	Data Tracking Number
ECRB	Enhanced Characterization of the Repository Block
OD	oven-dried
RH	relative humidity
YMP	Yucca Mountain Site Characterization Project

Abbreviations

Tpt	Topopah Spring Tuff
Tptpll	lower lithophysal zone of the Topopah Spring Tuff
Tptpln	lower nonlithophysal zone of the Topopah Spring Tuff
Tptpmn	middle nonlithophysal zone of the Topopah Spring Tuff
Tptpul	upper lithophysal zone of the Topopah Spring Tuff

INTENTIONALLY LEFT BLANK